Bid homeostatically regulates mitochondrial cristae structure and necrotic cell death to protect against cardiac disease and bone marrow failure

By

Christi Therese Salisbury-Ruf

Dissertation

Submitted to the Faculty of the

Graduate School of Vanderbilt University

in partial fulfillment of the requirements

for the degree of

DOCTOR OF PHILOSOPHY

in

Cell and Developmental Biology

May 10, 2019

Nashville, Tennessee

David M. Miller, Ph.D., Chair

Sandra S. Zinkel, M.D., Ph.D. Mentor

William P. Tansey, Ph.D.

David H. Wasserman, Ph.D.

Anne K. Kenworthy, Ph.D.

To loving my parents, Michael and Patricia.

Thank you for instilling in me a passion for learning and the courage to pursue my dreams.

ACKNOWLEDGMENTS

First and foremost, I would like to thank my Ph.D. mentor, Dr. Sandra Zinkel. Dr. Zinkel has been a truly wonderful mentor and I am very grateful for her tireless commitment to my training from the very first day. She challenged me to think critically about science and ask thoughtful and meaningful questions. She has given me independence to pursue my ideas, while also remaining a constant source of professional and personal support. I am infinitely a better scientist because of her dedication to my training and am so thankful to her for her guidance and support.

I would like to thank my thesis committee: my chair, Dr. David Miller and members Dr. William Tansey, Dr. David Wasserman, and Dr. Anne Kenworthy. I am very grateful for their support and scientific input throughout the past six years. They challenged me to defend my ideas and reach my goals.

I also thank past and present members of the Zinkel laboratory, including former graduate students Dr. Clint Bertram and Dr. Patrice Wagner for their help and friendship. Clint made the early findings that initiated the mitochondrial project, contributed to metabolic studies and made several of the Bid mutants. Patrice extensively characterized the bone marrow failure phenotype in TKO mice and her work led to my studies into the role of Ripk1 in inflammation and erythropoiesis. I thank former senior research scientist Qiong Shi, who taught me invaluable protein and molecular biology skills. My thanks also go to current lab members Yuliya Hassan and Teresa Dugger. Yuliya is wonderful source of support; her management of the lab's mouse colony and friendship has been invaluable. Teresa Dugger worked with me to optimize and characterize inflammation in bone marrow

by immunofluorescence. Teresa is a remarkable person, and I'm immensely grateful to have had the opportunity to work.

Thank you to the many collaborators we worked with over the years. First and foremost, Dr. Eric Gamazon whose expertise in human genetics directly contributed to the success of my research. I learned so much from him and have a new appreciation for genetic science. I am very grateful for his input and patience. I would also like to thank Dr. Josh Fessel whose expertise in mitochondrial biology was invaluable. He went above and beyond to support me, both scientifically and personally. I am also grateful to Dr. Quinn Wells who directly contributed to the rare variant analysis in Bid. I thank Dr. Javid Moleshi and his lab for their assistance with Doxorubicin experiments. I thank Dr. Daniel Lark for teaching me his expertise in mitochondrial physiology and experimental assistance. Lastly, I thank Niki Fortune, who performed *Bid-/-* echocardiograms and suggested quantitative analysis of fibrotic staining. Her ideas directly contributed to the success of this project.

I especially thank Dr. Jennifer Pietenpol and the Pietenpol lab. Our joint lab meetings were incredibly helpful in both developing my critical thinking and presentation skills. Dr. Pientepol's input has been instrumental in helping me to grow, and I truly appreciate her time and comments over the years.

I would like to thank the individuals who work in Vanderbilt Cores. The Cell Imaging Shared Resource (CISR) core, including Dr. Jenny Schafer, Dr. Janice Williams, Dr. Mary Dawes, Dr. Robert Matthews, and Dr. Jay Jerome. I thank the translational pathology shared resource core (TPSR), especially Dr. Kelli Boyd for her scientific expertise and Sherry Smith for her assistance with my samples. I also thank the flow cytometry shared resource core and lab manager David Flaherty for his assistance.

Lastly, I would like to thank my family, including my parents Michael and Patricia Ruf, my sisters Katie and Clare, my husband Matthew Gurniak, and my mother and father-in-law, Paula and John Gurniak. They have been my rock throughout this process, and unwavering in their support. I am eternally grateful to them for their love.

TABLE OF CONTENTS

LIST OF TABLES

LIST OF FIGURES

Figure Page

LIST OF ABBREVIATIONS

53BP1	TP53-binding protein 1
aa	Amino acid
AA	Aplastic anemia
Acetyl-CoA	Acetyl coenzyme A
ActD	Actomyosin D
ADP	Adenosine diphosphate
AGM	Aorta-gonad-mesonephros
ALL	Acute lymphocytic leukemia
AML	Acute myeloid leukemia
APAF1	Apoptotic protease activating factor 1
ASXL1	Addition of sex combs-like1
ATM	Ataxia telangiectasia mutated
ATP	Adenosine triphosphate
ATR	ATM and rad-3 related
ATRIP	ATR-interacting protein
Bad	Bcl-2 associated death promoter
Bak	Bcl-2-associated X protein
Bax	Bcl-2-antagonist/killer
Bcl-2	B-cell lymphoma 2
Bcl-w	Bcl-2 like protein 2
Bcl-XL	B-cell lymphoma extra large
BFU-E	Burst forming unit-erythroid
BH	Bcl-2 homology

BH3	Bcl-2 homology 3 domain
Bid	BH3 interacting death domain agonist
Bim	Bcl-2 interacting mediator of cell death
BM	Bone marrow
BMF	Bone marrow failure
BMT	Bone marrow transplant
BN-PAGE	Blue-native polyacrylamide gel electrophoresis
BRCA1	Breast cancer type 1
CAD	Coronary artery disease
CASP8	Caspase-8
CASP9	Caspase-9
Caspase	Cysteine-dependent aspartate-specific protease
cBid/tBid	Cleaved Bid/Truncated Bid
CCUS	Clonal cytopenia of undetermined significance
CD	Clusters of differentiation
Cdk	Cyclin dependent kinase
cDNA	Complimentary DNA
Ced-3	Cell death 3
Ced-4	Cell death 4
Ced-9	Cell death 9
cFLIPL	Cellular FLICE-like inhibitory protein long
CFU-E	Colony forming unit-erythroid
CFU-GEMM	Colony forming unit-granulocyte, erythrocyte, macrophage, megakaryocyte
CHIP	Clonal hematopoiesis of indeterminate potential
CJ	Cristae junction

CL	Cardiolipin
CLL	Chronic lymphocytic leukemia
CLP	Common lymphoid progenitor
CML	Chronic myeloid leukemia
CMML	Chronic monomyelocytic leukemia
CMP	Common myeloid progenitor
CS	Cardiolipin synthase
CYLD	Cylindromatosis
Cyt c	Cytochrome c
DKO	Double-knock out
DMNT3A	DNA methyltransferase 3 alpha
Drp1 (Dnm1l)	Dynamin-1-like protein
EHR	Electronic health record
EM	Electron microscopy
EndoG	Endonuclease G
Epo	Erythropoietin
eQTL	Expression quantitative trait loci
ER	Endoplasmic reticulum
EryA	Erythroid A
EryB	Erythroid B
EryC	Erythroid C
ETC	Electron transport chain
FADD	Fas-associated death domain protein
FAO	Fatty acid oxidation
FAS/APO-1	Apoptosis antigen 1 (also known as CD95)

FASL	FAS-ligand
GM-CSF	Granulocyte-macrophage colony stimulating factor
GMP	Granulocyte-macrophage progenitor
GWAS	Genome wide association study
HMGB1	High mobility group box 1
HSC	Hematopoietic stem cell
HSPC	Hematopoietic stem and progenitor cell
HtrA2/Omi	High-temperature requirement protein A2
HU	Hydroxyurea
I/R	Ischemia/Reperfusion
IAP	Inhibitor of apoptosis
ICUS	Idiopathic cytopenia of undetermined significance
IFNγ	Interferon-gamma
Ig	Immunoglobulin
IKK	IκB kinase
IL-1β	Interleukin-1beta
IL-3	Inteleukin-3
IL-6	Interleukin-6
IMJ	Inter-membrane junctions
IMM	Inner mitochondrial membrane
IMS	Inner membrane space
IP3R	Inositol triphosphate receptor
LDL	Low-density lipoprotein
LPS	Lipopolysaccharide

LSK	Lin-Sca-1-c-Kit+
LUBAC	Linear ubiquitin chain assembly complex
MAF	Minor allele frequency
Mcl-1	Myeloid cell leukemia sequence 1
MDS	Myelodysplastic Syndrome
MEP	Megakaryocyte-erythroid progenitor
Mfn1/2	Mitofusin 1/2
MI	Myocardial Infarction
MICOS	Mitochondrial contact site and cristae organizing system
MLKL	Nixed lineage kinase domain like protein
MOMP	Mitochondrial outer membrane permeabilization
MPC	Myeloid progenitor cell
MPP	Multi-potent progenitor
MTCH2	Mitochondrial carrier homolog 2
mtDNA	Mitochondrial DNA
MTX1	Metaxin-1
NADHN	Nicotinamide adenine dinucleotide
Nec-1	Necrostatin-1
NEMO	NF-kB essential modulator
NF-kB	Nuclear factor kappa-light-chain-enhancer of activated B cells
NK	Natural killer cells
NMR	Nuclear magnetic resonance
Nrf2	Nuclear factor (erythroid-derived-2)-like 2
OMM	Outer mitochondrial membrane
Opa-1	Optic atrophy 1

p53	Tumor protein 53
PCD	Programmed cell death
PDX	Patient derived xenograph
PG	Phosphatidylglycerol
PheWAS	Phenome-wide association study
PINK1	PTEN-induced kinase 1
Poly I:C	Polyinosine-polycytidylic acid
ProE	Proerythroblast
PRX2	Peroxiredoxin 2
Puma	p53 upregulated modulator of apoptosis
qPCR	Quantitative PCR
RBC	Red blood cell
RIPK1/RIP1	Receptor-interacting serine/threonine-protein kinase 1
RIPK3/RIP3	Receptor-interacting serine/threonine-protein kinase 3
RNA-Seq	RNA sequencing
ROS	Reactive oxygen species
RPA	Replication protein A
sAML	Secondary acute myeloid leukemia
SCF	Stem cell factor
SD	Synthetic Derivative
SERCA1	Sarcoplasmic/endoplasmic reticulum calcium ATPase 1
SF3B1	Splicing factor 3b subunit 1
SLAM-HSC	SLAM-Hematopoietic stem cell
Smac/Diablo	Second mitochondria-derived activator of caspases/direct inhibitor of apoptosis (IAP)-binding protein with low pI

SNP	Single nucleotide polymorphisms
SRSF2	Serine and arginine rich splicing factor 2
TCA	Tricarboxylic acid
TET2	Ten-eleven translocation-2
TGF-β	Tumor growth factor beta
TIM/TOM	Translocase of the inner/outer membrane
TKO	Triple-knock out
TLR	Toll-like receptor
TM	Transmembrane
TNFα	Tumor necrosis factor alpha
TNFR	Tumor necrosis factor receptor
TRADD	TNF-receptor associated death domain
TRAIL	TNF-related apoptosis inducing ligand
tRIPK1	Truncated-RIPK1
VAF	Variant allele frequency
VDAC	Voltage-dependent anion-selective channel
VLCAD	Very long-chain acyl-CoA dehydrogenase
WES	Whole exome sequencing
WT	Wild-type

Chapter I

Introduction

Early after its discovery, the Bcl-2 protein Bid was extensively characterized for its role as a mitochondrial cytochrome c releasing factor. Its activation of the pore-forming proteins Bax and Bak have dominated studies of its function at the mitochondria. However, among BH3-only family members Bid is very unique, both in its structure, which is similar to anti-apoptotic proteins, and in its functions independent of apoptosis. Despite this, it's role at the mitochondria beyond cell death had not been characterized. This thesis directly investigates a role for Bid at the mitochondria in a non-apoptotic setting. Taking a multifaceted approach that combines biochemical data and mouse models with human genetics, our studies reveal that full-length Bid is necessary for the maintenance of mitochondrial cristae structure. We find that this function for Bid is essential for normal mitochondrial metabolism, especially in the setting of cardiomyocyte function. We find Bid can localize to the mitochondrial matrix and interact with matrix Mcl-1 through helix-6. Genetic analysis using Vanderbilt University's DNA biorepository BioVU determined decreased BID expression associates with risk for myocardial infarction. We propose this is directly related to Bid's function in regulating cristae and maintaining mitochondrial health. Complimentary to this study, this thesis also includes work investigating the role of Bid in the regulation of necrotic cell death in the setting of bone marrow failure. Additional studies using an integrative genetic and biological approach also examine the consequences of necrotic death on anemia and inflammation. Together, this work highlights the role for Bid as sensor of cell fitness and emphasize the importance of examining basic biological processes that may reveal insight about our understanding of human disease.

The Bcl-2 Family: Gate keepers of Programmed Cell Death (PCD)

The term “apoptosis” from the Latin “falling off” was first used to described cell death as a way to distinguish necrotic, or perceived mechanical cell death, from “natural” or programmed death (1). While this early description was the first to propose that apoptosis was a regulated process, it was not fully accepted until seminal discoveries were made in cell and cancer biology that converged on a family of genes.

When the fate of all cells in the nematode *C. elegans* was mapped out by Sulston et al., it was discovered that in every worm, the same 131 cells died during development (2). In 1986, Robert Horvitz found that the loss of the *ced-3* and *ced-4* genes in *C. elegans* (orthologous to the human genes CASP9 and APAF1), prevented cell death (3). Concurrently, the breakpoint translocation t(14;18) found in human follicular lymphoma was cloned and identified as the fusion of the BCL-2 (B-cell lymphoma) gene with immunoglobulin heavy chain Ig resulting in the overexpression of BCL-2 (4–6). Studies investigating hematopoietic cell survival with retrovirally transfected bone marrow from E mu-myc mice and transgenic mice expressing the Bcl-2-Ig fusion gene revealed its role as an anti-apoptotic protein (7, 8).

Over the next decade, pioneering work by the Korsmeyer laboratory and others identified the role for Bcl-2 as a 25 kDa anti-apoptotic protein residing at the mitochondria, as well as a potent proto-oncogene in multitude of hematopoietic cancers. Investigation into the precise mechanism of Bcl-2’s function revealed interacting partners, the first of

which was identified as the pro-apoptotic protein Bax (9). Identification of additional proteins with pro- and anti-apoptotic functions revealed a Bcl-2 family of genes that share conserved regions called BH (Bcl-2 homology)-domains, of which there are four. In 1994, Hengartner et al. discovered that over-expression of Bcl-2 in *C. elegans* could protect against cell death due to loss of *ced-9*, the Bcl-2 ortholog, revealing the evolutionary conservation of programmed cell death (10).

Consisting of approximately 12 core proteins, the Bcl-2 family is divided primarily into three groups: multi-domain anti-apoptotics, multi-domain pro-apoptotics, and BH3-only pro-apoptotics (11, 12). All family members share a BH3 domain which consists of the amino-acid sequence LXXXGD. This motif facilities Bcl-2 family protein-protein interactions as the alpha-helix on which it resides can bind to a hydrophobic groove on another family member. For example, the Bax BH3 domain binds to the hydrophobic grove of Bcl-2 and this sequesters Bax, preventing apoptosis. The BH3 domain of Bid however binds the Bax hydrophobic grove and promotes apoptosis. While many of the anti-apoptotic proteins have multiple binding partners, some interactions are specific. For instance, the anti-apoptotic protein Mcl-1 can bind the BH3-only proteins Bid, Bim, Puma, and Noxa, but only weakly to Bad (13, 14). The pro-apoptotic protein Noxa only binds to Mcl-1, while Bid and Bim can associate with all anti-apoptotics, although they themselves lack hydrophobic grooves (Figure 1-1).

Importantly, the binding affinity of BH3 peptides with recombinant anti-apoptotic proteins is now leveraged for use in cancer biology. Termed BH3-profiling, the activation or failure to active mitochondrial cell death by BH3-only peptides can be used to classify cells in order to predict response to chemotherapy (15, 16). Furthermore, small molecule BH3-mimetics, such as ABT-737, have been used for many years to inhibit cell death (17).

The next generation of these drugs, particularly Venetoclax are now successfully in clinical use for CLL (Chronic Lymphocytic Leukemia) and in clinical trial for AML (Acute Myeloid Leukemia) (18, 19).

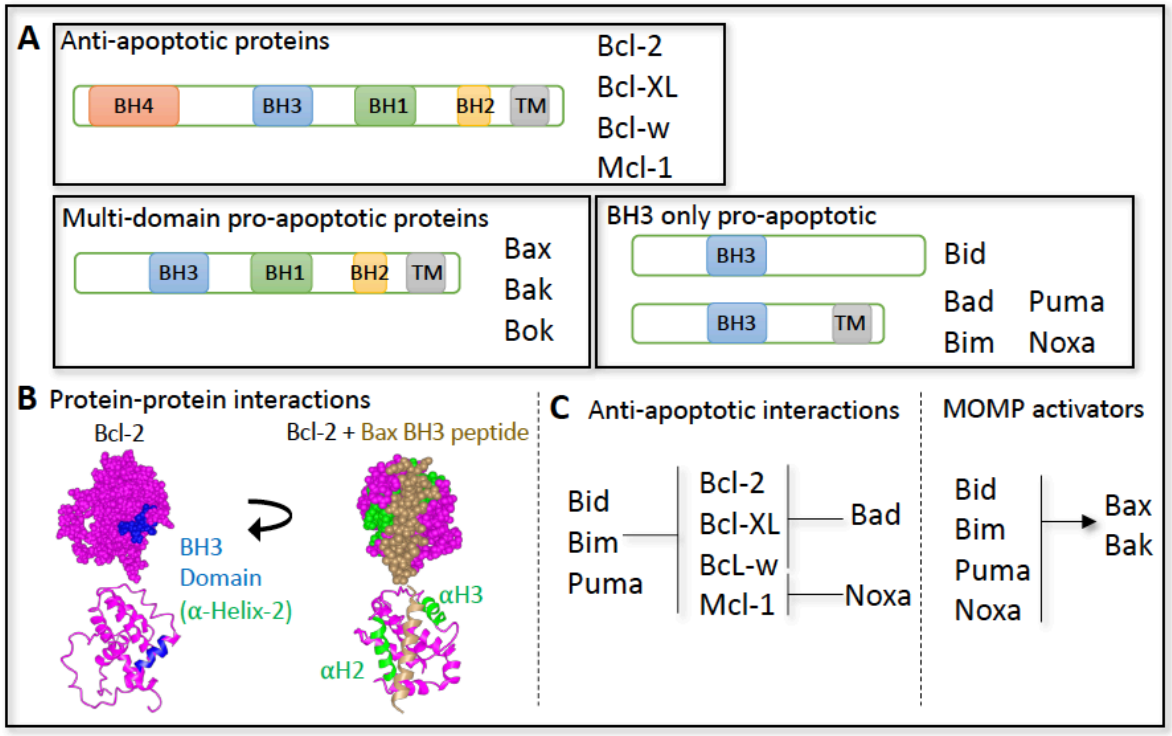

Figure 1-1. The Bcl-2 family.
A. The Bcl-2 family is divided into 3 categories based on the BH (Bcl-2 homology) domains and protein functions: anti-apoptotic, multi-domain pro-apoptotic and BH3-only pro-apoptotic groups B. Bcl-2 family members interact through the binding of their BH3-domains into hydrophobic grooves or pockets. Shown here is the BH3-domain of Bcl-2, which can bind to and inhibit Bax or Bak (left), as well as the Bax BH3-peptide (brown) bound to the hydrophobic groove of Bcl-2, flanked by alpha-helices 2 and 3 (αH2 and αH3). C. Interactions between the Bcl-2 family members have specificity. For example, Bad has very low affinity for Mcl-1. Furthermore, mitochondrial outer membrane permeabilization (MOMP) through Bax and Bak pore formation is activated by subset of BH3-only proteins, termed direct activators. This includes Bim, Bid, Puma, and Noxa.

Apoptosis

The primary site of action for the Bcl-2 family converges on the mitochondria, which serves to amplify death signaling through mitochondrial outer membrane permeabilization (MOMP). Death signals can originate intrinsically within the cell from

DNA damage, or extrinsically due to receptor mediated signaling. Death receptors include tumor necrosis factor receptor (TNFR), FAS (CD95 or APO-1), or TNF-related apoptosis inducing ligand receptor (TRAIL). Additionally, Toll-like receptors (TLRs), which recognize innate pathogen associated molecular patterns, also converge on the same initiator cysteine protease, caspase-8, leading to apoptotic death.

When a death stimulus occurs, the pro-apoptotic BH3-only proteins Bid, Bim and Puma, termed "direct activators", bind to and promote the formation of Bax and Bak homo-oligomers to create pores. Other BH3-only proteins including Bad, however are considered to be "sensitizers;" whose role is to inactivate the anti-apoptotics by binding to their hydrophobic grooves. The model for how these proteins work together to execute MOMP is not completely understood but is dependent on their local concentrations and affinity with the mitochondrial outer membrane, termed the 'embedded together' model (12).

Once the BH3-only Bid is cleaved by caspase-8 (cBid), as well as other proteases discussed below, its association with the outer mitochondrial membrane (OMM) facilitates a conformation change that results in its interaction with Bax and/or Bak. Homo-oligomers of Bax and Bak then form pores, releasing cytochrome c. In addition to pore formation, cBid also reorganizes inner mitochondrial membrane (IMM) loops called cristae (20, 21). This mobilizes cytochrome c from cristae sequestration and increases the pool available within the inner membrane space (IMS) to be released.

Once MOMP occurs and cytochrome c is released, the cell is committed to apoptosis through subsequent activation of the apoptosome (Caspase-9, Apaf1, and cytochrome c) and executioner caspases including caspase-3, 6 and 7 (22). Caspase-3 itself can then subsequently feedback on caspase-8 as well as Bid itself, amplifying the apoptotic signal (23) (Figure 1-2).

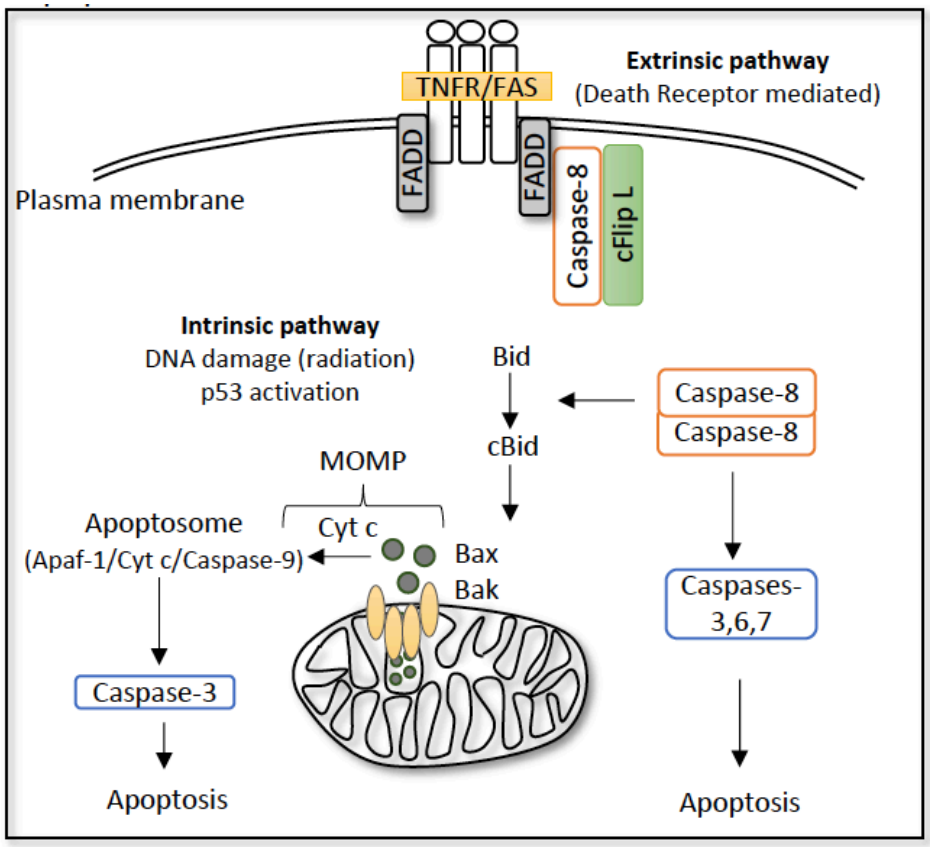

Figure 1-2. Apoptosis.
Apoptosis can occur through death receptor activation by extracellular ligands (such as TNFα binding to TNFR), termed extrinsic apoptosis, or from internal signals, such as DNA damage or ROS through the activation of p53, termed intrinsic apoptosis. Both pathways can converge on the mitochondria which serves to amplify the death signal in a feed-forward manner (Type II cell death). The BH3-only protein can Bid trigger MOMP when it is cleaved by the initiator protease caspase-8. Cleaved Bid can then bind to pro-apoptotic proteins Bax and Bak, resulting in their formation of pores on the outer mitochondrial membrane (OMM). This releases cytochrome c and other pro-apoptotic proteins. Cytochrome c is necessary to build the apoptosome, which triggers executioner caspases such as caspase-3. Caspase cascades can also result in apoptotic death in the absence of mitochondrial amplification (Type I cell death). Morphologically, apoptotic death is characterized by cell shrinkage, membrane blebbing, and condensation and fragmentation of chromatin. MOMP=Mitochondrial outer membrane permeabilization.

The IMS of the mitochondria also harbors additional proteins to promote cell death. These include the second mitochondria-derived activator of caspases (Smac, also called Diablo) high-temperature requirement protein A2 (HtrA2, also called Omi), Endonuclease G, and Apoptosis-inducing factor (AIF). Smac and HtrA2 prevent inhibitor of apoptosis

proteins (IAPs) from degrading caspases, and EndoG and AIF facilitate DNA fragmentation (24–26).

Independent of mitochondrial amplification, apoptosis can also occur as a result of a caspase cascade known as Type I apoptotic death. This type of cell death occurs for example in hepatocytes while Type II cell death, which involves mitochondrial amplification, occurs for example in thymocytes (27, 28). Like Type II death, Type I death also relies on caspase-8 activity (describe in more detail below). Caspase-8 can directly cleave executioner caspases such as caspase-3, leading to chromatin condensation and DNA fragmentation and ultimately cell death (29, 30).

Regulation of the Bcl-2 family

In addition to protein-protein interactions, regulation of the majority of Bcl-2 proteins occurs by post-translational processes. For example, phosphorylation results in very different outcomes depending on the site and protein. Mcl-1 and Bcl-XL are known to be phosphorylated by cyclin dependent kinase 2 (Cdk2), which promote their stability and inhibit their anti-apoptotic functions (31, 32). Phosphorylation of Bcl-2 however has been reported to be related to several non-apoptotic functions. For example, non-phosphorylatable Bcl-2 protein (BCL-2^{AAA}) is unable to regulate calcium ER, and cardiac and skeletal muscle from BCL-2^{AAA} mice show deficiencies in exercise endurance due to inhibition of Beclin-2 mediated autophagy (33, 34).

Pro-apoptotic proteins are also phosphorylated. Recently it has been shown that phosphorylation of Bax inhibits its apoptotic function (35). In other cases, phosphorylation promotes non-apoptotic roles for these proteins altogether such as Bid in the DNA damage response or Bad in the regulation of glucose homeostasis (36–38).

Cleavage by proteases is also a common regulatory mechanism. Bid, Bad, and Bcl-XL are all cleaved by proteases, especially cysteine-dependent aspartate-specific proteases called caspases (39–41). Cleavage of Bid and Bad promote cell death while this results in inhibition of the anti-apoptotic function of Bcl-XL. Lastly, Bim and Puma are known to be regulated at the level of transcription. This occurs in response to signals such as cytokine withdrawal or p53 activation and ER stress, respectively (42–44).

Necroptosis

Necrotic cell death was originally thought to be a consequence of injury, disease, or infection and occur in an unregulated manner. However, it was found that signaling through death receptors could also result in morphological features such as osmotic swelling and membrane disintegration that appeared necrotic (45). Identified in a yeast cDNA screen to study the events following Fas ligation, the receptor-interacting serine/threonine (Rip1)-protein kinase was shown to interact with the intracellular domains of TNFR and FAS (46) and its kinase function was shown to be necessary for these necrotic features (47, 48). Work by Hitomi et al. revealed that indeed necrotic death was mediated by the Ripk1, and this occurred in a regulated manner (49). Necroptosis is now appreciated to occur in many physiological contexts including viral infection, ischemia/reperfusion injury, atherosclerosis, and sepsis.

Unlike apoptosis, necrosis does not depend on caspases or the release of mitochondrial proteins, although generation of damaging reactive oxygen species (ROS) is thought to facilitate this process (49–51) . Necrosis relies on Ripk1, and in some cases Ripk3 (52), which associate with the cytosolic portion of the TNFR in conjunction with death domain proteins FADD or TRADD, TRAF2, and ubiquitinases. This is termed

complex I. Upon ligand association with the death receptor, a cytosolic complex, the necrosome, can form preventing caspase-8 from cleaving and inactivating Ripk1. Ripk1 can phosphorylate itself and Ripk3, and Ripk3 recruits and phosphorylates the mixed-lineage kinase domain-like protein (MLKL). MLKL, trimerizes with itself, a process found to be dependent on inositol phosphate kinases, and localizes to the plasma membrane (53, 54). In concert with additional proteins, it facilitates the pinching off of plasma membrane through the formation of bubbles, rupturing the cell (55) (Figure 1-3A).

In addition to its kinase function, Ripk1 also serves as a protein scaffold (56). Ligand stimulation of TNFR can also result in a complex composed of the adaptor protein TRADD (TNF-receptor associated death domain) that directly interacts with the death domain of Ripk1. Ripk1 can subsequently be ubiquitylated at Lys63 by inhibitor of apoptosis proteins (IAPs), which has recently been shown to also suppress Ripk1-kinase auto-activation (and thus necrosis) (57). These ubiquitin (Ub) chains further support the recruitment of the E3 ligase linear Ub chain complex called LUBAC, linearly ubiquitylating Ripk1. This creates a scaffold for subsequent activation of the IKK complex and canonical activity of NF-κB. However, if Ripk1 is de-ubiquitylated by CYLD or if IAPs are inhibited by Smac (or smac mimetics), Ripk1 will form the necrosome to promote necroptosis (58) (Figure 1-3B).

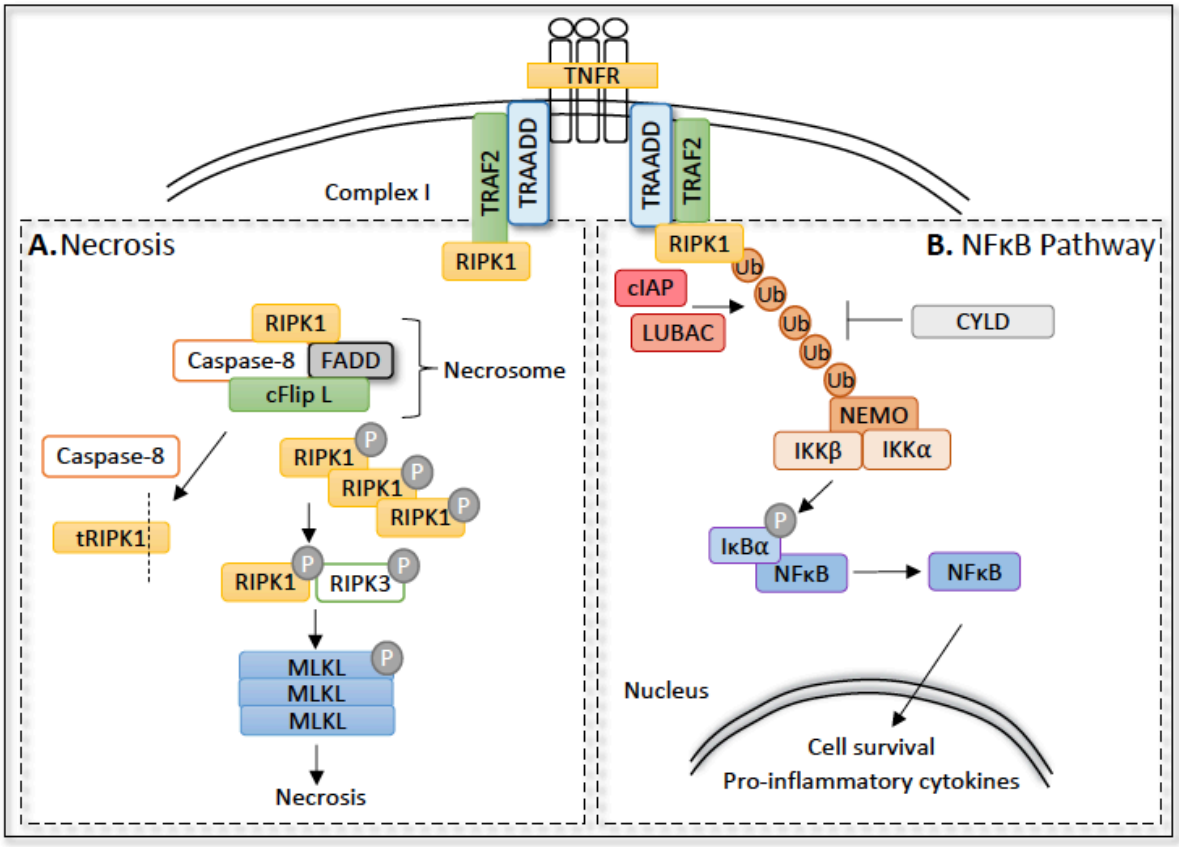

Figure 1-3. Necrosis and NFκB.
A. Necrotic cell death occurs upon stimulation of death receptors and subsequent formation of the necrosome which includes Ripk1, Caspase-8, FADD, and c-FLIP. This complex inhibits caspase-8 from cleaving and degrading Ripk1, allowing for its autophosphorylation. Ripk1 can phosphorylate Ripk3 and MLKL which trimerizes and mediates the plasma membrane breakdown. Unlike apoptosis, necrotic cell death does not rely on a caspase cascade. Morphologically, it results in cellular and organelle swelling followed by rupture and release of pro-inflammatory cytosolic contents into the periphery. B. Ripk1 can also participate in canonical NFκB signaling. Within complex I, which includes the cytoplasmic domain of TNFR, FADD/TRADD, and TRAF2, Ripk1 can be ubiquitylated by cIAP and LUBAC. LUBAC creates linear ubiquitin chains providing a docking platform for the activation of IKKs (IκB kinases) which phosphorylate IκBα. These chains also inhibit Ripk1's necrotic function. This results in proteasomal degradation of IκBα unmasking of the nuclear localization signal and DNA binding site of NFκB.

While apoptosis and necrosis both ultimately result in cell death, the physiological consequences of these two types of cell death are very different. Apoptotic cell death does not initially lead to plasma membrane permeability. Instead, apoptotic cells bleb and

fragment, and are consequently cleared by surrounding phagocytic cells such as macrophages. If this process however is not cleared, eventual inflammation is possible.

Loss of membrane integrity during necrosis conversely results in the release of intracellular content such as DNA, HMGB1, S100 proteins, heat shock proteins, and cytokines among others (59–61). These molecules can then associate with TLRs on adjacent cells resulting in the release of additional pro-inflammatory molecules including cytokines and chemokines. If this acute inflammation is not resolved, it can become chronic. Chronic inflammation is known to be involved in the pathogenesis of a variety of diseases especially cancer.

It is important to note that the mechanisms and consequences of necrotic cell death pathway highly depend on the cell and tissue type in which they occur. For example, FADD prevents Ripk3-mediated necrosis and inflammation in the intestine and skin and Ripk1-mediated necrosis can result in long-term neuroinflammation (62–64). However, *Ripk1* knockout mice die shortly after birth due to cell death in lymphoid and adipose tissues (65). Furthermore, within the bone marrow microenvironment, cytokines can impair hematopoietic stem cell function (66). In contrast, adult mice with liver specific deletion of *Ripk1* however do not exhibit damage despite a reported Ripk1 pro-survival role in this tissue. These data highlight the complexity of necrosis regulation and execution in different tissue types and point to the importance of careful interpretation of results observed in immortalized cell line *in vitro*.

Cross-talk between Apoptosis and Necroptosis

As described, apoptosis and necroptosis can both occur downstream of death receptors, however cell fate ultimately relies on several key protein-protein interactions. The first of these is the initiator cysteine-dependent aspartate-specific protease, caspase-8.

Caspase-8 was first identified to not only have a role in execution of apoptosis, but also a pro-survival function as loss of *Casp8* was found to be embryonically lethal in mice (67). This pro-survival function was attributed to inhibition of necroptosis as *Casp8-/-* mice could be rescued by additionally knocking out *Ripk3* (68, 69). It was further shown that the lethality observed in *Ripk1* knock-out mice could also be rescued by additional deletion of both *Ripk3* and *Casp8* (70). This was consistent with the finding that both Ripk1 and Ripk3 had been identified as caspase-8 cleavage targets (71).

Caspase-8 also has a homolog, the cellular Flice inhibitor protein, cFLIP, which arose from a gene duplication of caspase-8. The long form of cFLIP, $cFLIP_L$ can also dimerize with caspase-8, activating it, but also altering its activity towards downstream targets. In particular, caspase-8 homodimers have a catalytic efficiency of 10.3 kcat/km for Bid, while heterodimers with FLIPL are <<0.01 kcat/km. Interestingly, the caspase-8 kcat/km for Ripk1 is virtually unchanged regardless of its interacting partner (72). Thus, caspase-8 is directly involved both in apoptotic and necroptotic cell death and its specific activity is regulated by its cellular location such as at the mitochondria (73, 74) and its association in various molecular complexes. Regulation of caspase activity can now begin to be uncovered with the availability of new, highly specific molecular probes (75).

In addition to caspase-8, Ripk1 itself has been proposed to have a role in regulating apoptosis, but in very precise contexts. It has been shown that in mice with parenchymal cell (LPC)-specific deletion of the NF-κB pathway protein NEMO (NF-κB essential modulator) ($NEMO^{LPC\text{-}KO}$) develop chronic steatohepatitis due to apoptosis. Loss of Ripk1 kinase function by crossing to $Ripk1^{D138/D138N}$ mutated mice can rescue apoptosis, but not

loss of the entire Ripk1 protein itself (*Ripk1*$^{LPC\text{-}KO}$), separating its scaffolding function from its role in cell death (76).

In sum, the proteins that regulate cell death rely on both a complicated combination of protein-protein interactions and signaling cascades that balances survival and death. How these signals are regulated relies not only on this biochemical dance but is also specific to the cell type and signal that is received.

The BH3-only protein Bid

Among the BH3-only pro-apoptotic proteins, Bid, or Bcl-2 interacting domain death agonist, is unique as it is the solitary BH3-only to remain structured in solution (77). Identified using labeled Bcl-2 and Bax fusion probes, it shares a BH3 domain necessary for its canonical interactions with other Bcl-2 proteins including Bax, Bak, Bcl-2, Bcl-XL and Mcl-1, but lacks other BH domains or a hydrophobic carboxy-terminus (78). Soon after Bids discovery, it was revealed that its apoptotic mechanism of action was dependent on its cleavage by caspase-8 (39, 79, 80). This cleavage results in Bid's association with and integration into the OMM, necessary for the release of cytochrome c through its activation of the pore forming proteins Bax or Bak (81–83).

The structure of Bid was revealed in solution by NMR (84, 85). Bid consists of 8 alpha-helices with a disordered loop between helices 2 and 3 that harbors both Bid's cleavage sites at D59 and phosphorylation sites at S61, S64, S66 and S78, described below (Figure 1-4 A, B). It was also found to lack the hydrophobic groove necessary for other BH3-domains to associate with it. Despite differences in protein sequence, Bid was unexpectedly found to have high structural similarity with Bcl-XL and Bax. As a group,

these proteins were classified as being structurally similar to membrane binding regions of diphtheria toxin (77, 84).

The structure of membrane-associated p15 cleaved Bid was later determined by EPR in vitro (86). Helix 6 and 7 associate with the membrane but rather than spanning it, are integrated peripherally and maintain their helical conformation. Specifically, helix-6 is tilted down into the membrane at an approximately 25-degree angle, and this is conformation thought to be due to lysine residues 157 and 158 that interact with the head group of the bilayer while hydrophobic residues further down stabilize the helix (Figure 1-4 C, D).

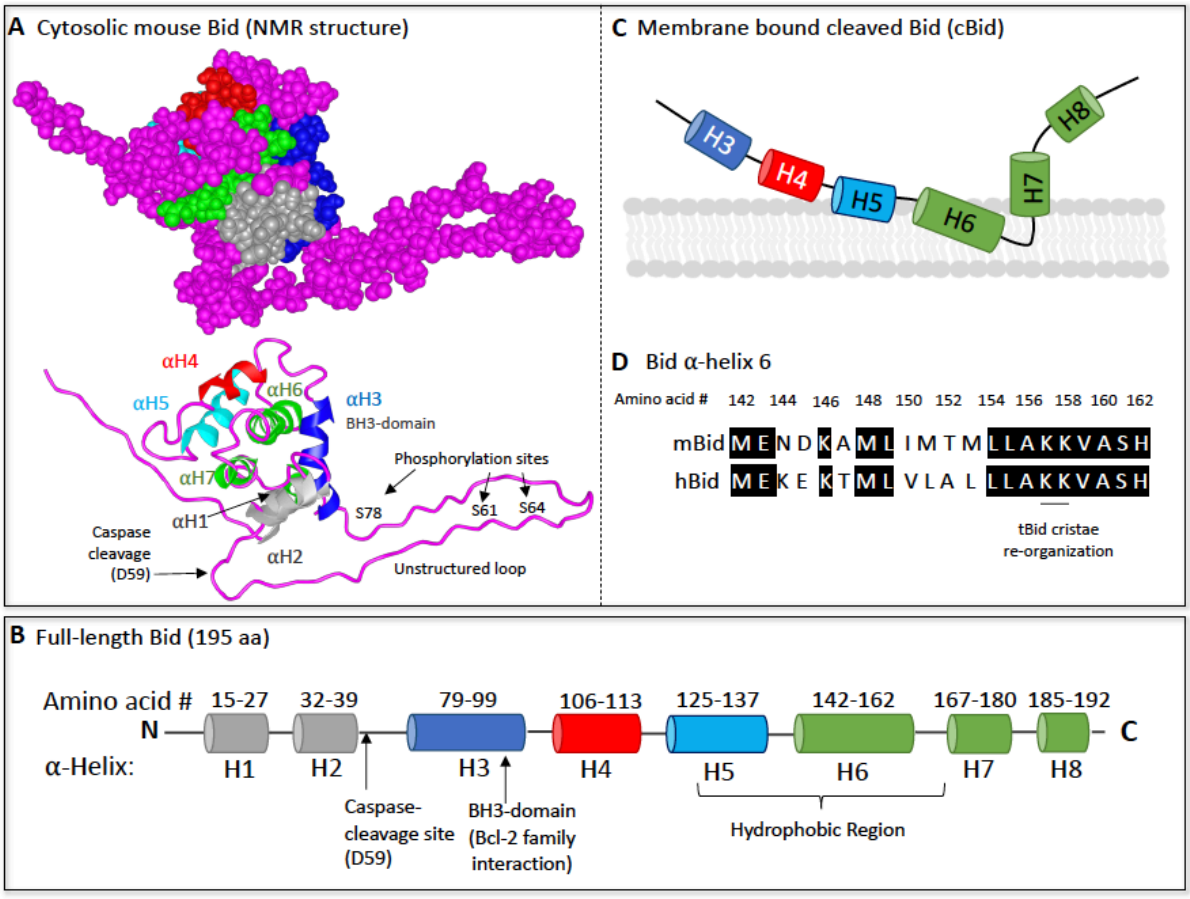

Figure 1-4. Bid protein structure.
A. Sphere (top) and ribbon (bottom) structure of cytosolic mouse Bid determined by NMR. Grey regions correspond to alpha-helices 1 and 2 (αH1 and αH2,) which are removed after cleaved Bid interacts with membranes, exposing αH3 (BH3-domain) which binds the

Figure 1-4 Continued.
hydrophobic grooves of other Bcl-2 family proteins. In solution, αH6, 7, and 8 form a hydrophobic core. B. Line-diagram of full-length with colors corresponding to A. C. EPR structure of membrane bound cBid. Helix-6 and 7 partially integrate into the membrane. (Diagram based on (87)). D. Detailed amino acid sequence of mouse (mBid) and human (hBid) helix 6. Residues highlighted in black are conserved between mice and humans. Lysines 157 and 158 were previously found to be necessary for cleaved Bid mediated cristae reorganization.

These results, including data from additional groups, support the idea that helix-6 is necessary for Bid's targeting and binding membranes. Bid is stabilized in part on the OMM by the phospholipid cardiolipin (CL) (88, 89). Cardiolipin is phospholipid found exclusively in the mitochondria. It is composed of four fatty acid acyl chains, predominately linoleic acid (18:2), connected by a glycerophosphate backbone. This unique structure of CL provides not only a platform on which Bid (as well as caspase-8) can dock, but also is essential for the structure and function of cristae discussed in more detail below. This interaction is BH3-independent, and Bid's mitochondrial localization is not inhibited by overexpression of Bcl-2 or Bcl-XL (20, 90).

In addition to cardiolipin, Bid is also stabilized on the OMM by the mitochondrial carrier homolog 2 (Mtch2). Mtch2 is transmembrane protein structurally similar to other mitochondrial carriers but lacks the helices necessary for carrier function. Upon apoptotic stimulation, cleaved Bid as well as Bax associate with Mtch2 (91). The residues for this association have been partly mapped, although not in the context of a membrane (92). It has been shown that Mtch2 facilitates a conformation change in tBid that promotes insertion of helices into the membrane and subsequently enables its activation of Bax (87). Additional roles for Mtch2 in regulating mitochondria structure and function have been proposed, however it is unknown if these also involve Bid (93).

Interestingly, Bid was also shown to be involved in remodeling of the IMM loops termed cristae in an apoptotic context (20, 94). Isolated liver mitochondria treated with

truncated Bid (tBid) resulted in complete cytochrome c mobilization due to cristae remodeling as observed by electron microscopy (EM). This was also shown to dependent in part on Bid's helix-6 but not BH3-domain, and its interaction with CL at contact sites between the inner and outer mitochondrial membranes (89). Additional lines of investigation into Bid's role in cristae re-organization presented conflicting results. Using a BH3-domain peptide of Bid, it was observed that mitochondria did not appear to have any gross morphological changes, but instead Bid peptide narrowed cristae junctions (21). These distinct experimental approaches, tBid versus BH3-peptide, likely account for the difference and demonstrate the importance of helix-6 , highlighting that Bid is more than its BH3-domain.

Insight into the physiological role for Bid was further revealed by the generation of *Bid-/-* mice (95). These mice were initially characterized as resistance to Fas-induced hepatocyte cell death despite activation of caspases. This was consistent with the earlier finding that Bcl-2 also protected hepatocytes from anti-Fas injury (96).

Further characterization of aging *Bid-/-* mice revealed that they developed the bone marrow disorder chronic monomyelocytic leukemia (CMML) due to loss of myeloid lineage homeostasis. These mice also presented with increased chromosomal aberrations (97). Loss of Bid was subsequently found to sensitize cells to DNA-damaging agents, and loss of S-phase checkpoint regulation. Bid was revealed to be phosphorylated at Serine 78 by the DNA-damage response proteins ataxia telangiectasia mutated (ATM) (36, 37). Investigation into its role in DNA damage identified Bid as component of a nuclear complex, directly associating with the DNA repair proteins ATRIP and RPA (98–100).

This role for Bid was also shown to be involved in progression of T-cell leukemia. Loss of ATM-kinase results in increased DNA damage during T-cell development. As a

substrate of ATM, additional loss of Bid increased thymocyte cell death. This was due to an inability to repair damage as well as inhibited cell cycle checkpoint activation, and thus delayed progression of leukemia (101).

The multiple functions for Bid in cell death as well as hematopoietic homeostasis, are regulated primarily by post-translation modifications. As described, Bid is cleaved by the cysteine protease, caspase-8. Bid can also be cleaved by caspase-3, which occurs after MOMP and serves to amplify the apoptotic signal (23). Additionally, Bid can also be cleaved by several other proteases depending on the specific cell type as well as stimuli. These proteases include granzyme B (102), calpains (103), and cathepsins (104) which also cleave Bid in its unstructured loop between helix-2 and 3. In addition to cleavage, its apoptotic function was also proposed to be regulated by N-terminal myristylation (105).

Bid's nuclear localization and involvement in the DNA damage response however is regulated by phosphorylation. During the DNA-damage response, Bid can be phosphorylated by ATM and ATR-kinases at Serine 61, 64, and 78 (36, 37). These phosphorylation sites facilitate Bid's pro-survival function in two ways; firstly, by promoting its non-apoptotic function and secondly by preventing Bid's cleavage as they are adjacent to the caspase-cleavage site D59 physically hindering its accessibility. Bid can also be phosphorylated in the cytosol by casein kinases 1 and 2 in order to prevent its apoptotic cleavage (106). Lastly, phosphorylation of Bid has also been shown to be important for targeting of Bid to the mitochondria during mitotic failure. This phosphorylation at S66 also occurs in Bid's unstructured loop, but it is unclear as to the kinase or role this phosphorylation site plays in regulating death (107).

In sum, these data suggest that Bid is an essential regulator of cellular homeostasis with clear functions in execution of apoptosis while also promoting cell survival in the

context of DNA-damage. Studies presented in the next few chapters will reveal additional pro-survival roles for Bid in the context of both mitochondrial homeostasis and hematopoiesis cell fate. To begin to explore these novel findings, the known roles for the Bcl-2 family in mitochondrial and hematopoietic regulation will first be explored.

Beyond death: Day jobs of the Bcl-2 family

Bcl-2 family overview

While cell death is necessary for development and homeostasis, it is a terminal process that occurs only once per cell. Bcl-2 family members however are expressed in cells at all times, posing the question as to their function when the cell is not dying. Recently, alternative functions for each family member are being revealed (Table 1). A few of these key findings will be explored.

Among the BH3-only proteins, alternative functions for Bad, Bid, Noxa, and Bim have all been uncovered, revolving around cell survival and metabolism. Bad was identified in 1995 as a binding partner for Bcl-XL and Bcl-2, and soon after was found to be phosphorylated at the mitochondria (108). Proteomic analysis revealed that Bad also associated with hexokinase IV (HK) and Bad phosphorylation was necessary for HK activity (38). Subsequently Bad has been shown to play an essential role in insulin secretion and beta cell survival as well as hepatocyte metabolism (109, 110). In addition to Bad, Noxa, which is the specific Mcl-1 interacting protein, was also shown to have a role in metabolism. Phosphorylation by Cdk5 in the presence of glucose results in cytosolic localization and increased glycolytic flux through the pentose phosphate shunt, independent of its apoptotic activity (111). Lastly, loss of the BH3-only Bim protein has been shown to decrease release of Ca^{2+} from the ER (112).

In addition to regulation of cell metabolism, the DNA damage response pathway also involves Bcl-2 proteins. As described above, *Bid-/-* mice were found to display increased sensitivity to DNA damaging agents due to loss of association with ATR/ATRIP and RPA (98–100). Recently, it has also been proposed that Mcl-1 supports the DNA damage in response to hydroxyurea (HU), as loss of this protein increases molecular association of 53BP1 and inhibits recruitment of BRCA1 (113).

As with the pro-apoptotics, the subcellular localization of the anti-apoptotics also partially dictates their various homeostatic functions. Bcl-2 for instance, while found on the OMM, also resides at the endoplasmic reticulum (ER). Here it was shown to bind to and inactive the calcium pump SERCA decreasing Ca^{2+} import into the ER (114). ER localized Bcl-2 protein is predominantly phosphorylated, which inhibits its antiapoptotic function, and contributes to its regulation of Ca^{2} concentration in the ER (33). Bcl-2's role at the ER is additionally thought to extend to its role in the regulation of autophagy as it was found to bind to the autophagy protein Beclin-1 and inhibiting its function (115) . Interestingly, additional anti-apoptotics including Bcl-XL and Mcl-1 have also been shown to bind to and inhibit Beclin-1 (116, 117).

Protein	Subcellular location	Non-apoptotic function
Bad	Cytosol, OMM	Glucose metabolism
Bak	OMM	Mitochondrial dynamics
Bax	Cytosol, OMM, ER	Mitochondrial dynamics
Bid	Cytosol, Nucleus, OMM, Matrix	DNA damage response, Cristae structure and metabolism
Bim	Cysotol, ER	ER stress response
Bcl-2	OMM, ER	Ca^{2+} flux, Mitochondrial fusion, autophagy, cell cycle checkpoint
Bcl-XL	OMM, ER, IMM	Ca^{2+} flux, ATP synthase stability, mitochondrial fusion, cell cycle, autophagy
Mcl-1	Cytosol, Nucleus, Matrix	Cristae structure and metabolism, cell cycle checkpoint, DNA replication
Noxa	Cytosol	Glucose metabolism

Table 1-1. Summary of non-canonical functions for the Bcl-2 family.

Regulation of mitochondrial homeostasis

Given that the Bcl-2 family resides or transiently interacts with the mitochondria, many of the characterized non-apoptotic roles for these proteins involve regulating mitochondrial physiology (Figure 1-5). For multi-domain apoptotics, this has been highly informed by knockout cell lines. It was observed that double knock-out (DKO) Bax and Bak deficient MEFs have disrupted mitochondrial homeostasis, particularly loss of elongated tubule mitochondria (118). Bax associates with the GTPase Mitofusin2 (Mfn2), overexpression of which could restore normal mitochondrial morphology in DKO cells (119). In addition to mitochondrial fusion, Bax has also been found to co-localize with the dynamin-GTPase protein Drp1 (120). Drp1 association with the mitochondria creates oligomers that form a contractile ring. This results in local changes in membrane structure

favorable for Bax insertion and pore formation. Importantly, as an example of the evolutionary conservation of these non-apoptotic functions in *C. elegans*, *ced-9* (Bcl-2 homolog) also interacts with Mfn1, Mfn2 and Drp1 (121).

The anti-apoptotics have also extensively been shown to be involved in mitochondrial physiology. In particular, Bcl-XL has been shown to be associated with inner mitochondrial membrane. Here, Bcl-XL associates with the beta-subunit of the ATP synthase complex increasing the efficiency of ion flux (122, 123). This interaction has been shown to be particularly important in neurological disorders, particularly Alzheimer's disease (124).

Mcl-1 has also been found to localize to the mitochondrial matrix, however unlike Bcl-XL, it has a mitochondrial localization signal. Once imported through outer and inner mitochondrial translocases (TOM and TIM), it is subsequently cleaved to a shorter, 36 kDa matrix form. This form of Mcl-1 (Mcl-1^{Matrix}) stabilizes the ETC and cristae (125). Loss of Mcl-1 disrupts both mitochondrial cristae structure as well as energy homeostasis, leading to a cardiomyopathy phenotype in mice (126, 127). Recently, it was shown that BH3-domain of Mcl-1 interacts with the very long-chain acyl-CoA dehydrogenase (VLCAD) enzyme involved in fatty acid oxidation (FAO) (128).

Thus, the Bcl-2 family, through post-translational modifications and changes in subcellular localization, have functions that reach well beyond cell death. The next sections will focus specifically on mitochondrial structure and disease.

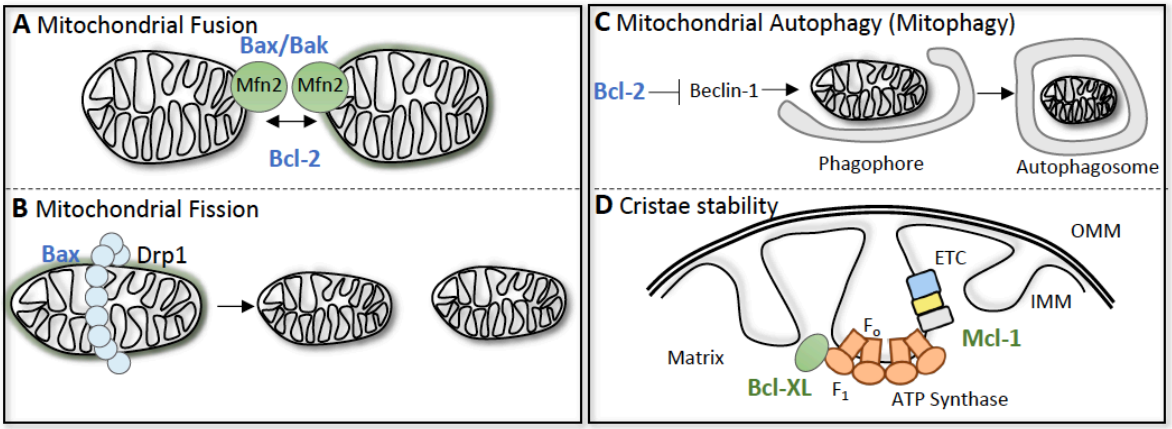

Figure 1-5. The Bcl-2 family and mitochondrial homeostasis.
A. Mitochondrial fusion can occur to increase energy output or in conditions of stress (such as mtDNA damage). This process is regulated by the Mitofusin proteins (and Opa-1 in the inner membrane). *Bax-/-Bak-/-* cells have increased fragmented mitochondria and Bax mediated Mfn2 homotypic interactions. B. Bax can also localize to Drp1 (dynamin protein) rings which constrict mitochondria which is thought to induce MOMP during apoptosis but has been also found to occur in the absence of cytochrome c release. **C.** ER localized Bcl-2 inhibits the association of autophagy protein Beclin-1 with its core complex components preventing the formation of phagophores. D. Bcl-XL has been shown to associate with beta F_1 subunit of ATP synthase increasing efficiency. Mcl-1 has a mitochondrial matrix isoform, Mcl-1^{Matrix}. Loss of Mcl-1 disrupts mitochondrial cristae structure, the electron transport chain (ETC) and ATP synthase, resulting in decreased oxygen consumption.

Mitochondria: form dictates function

Mitochondria structure

Mitochondria are much more than energy powerhouses; they regulate the supply of essential metabolic building blocks, oxidation-reduction (Redox) cycles, cell death, production of hemoglobin, immune responses, and contain their own DNA. Their origins as endosymbiotic bacteria account for their unique structure; composed of an outer and inner member separated by an inner membrane space. Within their internal compartment called the matrix, they contain circular mitochondrial DNA (mtDNA) which encode 37 different genes, 13 of which encode proteins that form the electron transport chain (ETC).

The inner mitochondrial membrane is structurally unique, composed of invaginations or loops termed cristae. Cristae junctions (CJs), where the lumen of the top of

the cristae meets the inner membrane boundary, are the site a large protein complexes thought to stabilize the structure of these loops. These junctions are thought to be narrow, 10-15 nm in rat liver (129) allowing the diffusion of small metabolites but limiting free diffusion of larger proteins such as cytochrome c. The primary purpose of cristae is to harbor components of the ETC within the membrane, sequester the electron carrier cytochrome c, and create a uniform proton gradient, resulting in a proton motor force across their length for generation of ATP (130).

Variation in the number, density and size of cristae between cells and tissues and reflects differences in metabolic requirements. Some cristae are tubular, others are dense and lamellar such as in hematopoietic cells and muscle, and even triangular in shape in astrocytes (131). Cristae can also remodel depending on the energetic needs of the cell and were proposed to exist in two states: condensed and orthodox. Increased respiratory demand, modeled by the addition of excessive ADP to isolated mitochondria, results in a transition from a condensed state (referring to the density of the matrix), to an orthodox state in which the cristae become compact and the matrix less dense (132). Electron tomography revealed that during the condensed state, cristae were also interconnected to one another through tubules, while this state was lost during inter-conversion to an orthodox state (133). Interestingly, cristae may also communication between mitochondria. Inter-mitochondrial junctions (IMJs) have been found in the heart between cristae of adjacent mitochondria. These adjacent cristae have been proposed to couple electrochemical gradients of adjacent mitochondria, increasing bioenergetic efficiency (134).

Cristae structure has been shown to be maintained by a number of proteins and protein complexes located at the CJs as well as the fusion protein Opa-1, ATP synthase

dimerization, Mcl-1 as previously discussed, and the mitochondrial-specific phospholipid cardiolipin (CL). At the junctions resides the mitochondrial contact site and cristae organizing system, termed MICOS (previously named MitOS or MINOS). This complex is highly evolutionarily conserved, as the components were originally discovered in yeast simultaneously by multiple groups (135–137). MICOS is composed of at least seven different subunits with two core components, Mic60, which contacts the outer mitochondrial membrane and Mic10, which stabilizes cristae shape.

In addition to MICOS is the dynamin-related protein optic atrophy protein-1 (Opa-1) (138, 139). Opa-1 forms high molecular weight oligomers within the luminal space of the cristae to narrow and stabilize them, promoting ATP synthase dimerization, proper respiratory complex associations, and ultimately increase ATP production. These oligomers are ultimately controlled by mitochondrial proteases including Yme1 and OMA1. Importantly in the context of apoptosis, it has been shown that cleaved Bid can reorganize the inner membrane structure, resulting in Opa-1 cleavage (20, 94).

ATP synthase is also key for establishing cristae shape. Cryo-electron tomography revealed ATP dimers arranged in rows around the loops of the cristae while oxidative phosphorylation (OxPhos) complexes and supercomplexes reside on the sides of the cristae (140, 141). Loss of dimer-subunits resulted in absent or balloon-shaped cristae (142). Thus, cooperation between MICOS, Opa-1, ATP synthase is thought to stabilize cristae, rather than the other way around. Loss of cristae structure results in failure of supercomplex assembly and consequently respiration (94).

In addition to these critical protein complexes, CL is equally important for maintaining cristae curvature due to four fatty acid chains it possesses rather than the two normally present on most phospholipids. Its synthesis is dependent on the conversion of

other phospholipids, particularly phosphatidylglycerol (PG) by cardiolipin synthase (CS). Cardiolipin not only serves as a docking platform for cleaved Bid and binds and sequesters cytochrome c but is also required for respiratory supercomplex formation and Opa-1 self-assembly (143). Furthermore, in flies, the supramolecular organization of ATP synthase also relies on cardiolipin(144) and in yeast, the MICOS subunit mic27, which contains a lipid-binding domain, has been shown to mark the site of cristae junctions, a process dependent upon cardiolipin (145). These features of mitochondrial cristae structured are illustrated in Figure 1-6 below.

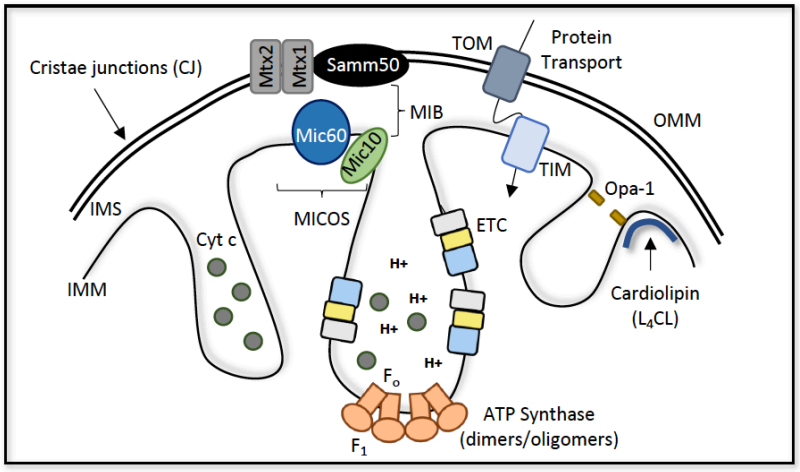

Figure 1-6. Overview of mitochondrial cristae structure.
Mitochondrial cristae are highly specialized inner membrane invaginations that sequester inner membrane space proteins (IMS) creating protein gradients and harbor the components of the electron transport chain. Cristae are stabilized by a number of protein complexes including the MICOS at cristae junctions (CJs) which facilitates the tethering of the OMM to the inner membrane. Opa-1, an IMS protein, creates bridges to stabilize cristae openings. ATP synthase dimerization and oligomerization creates bends within the membrane forming loops. Electron transport chain components can associate with themselves creating supercomplexes (respiratory complexes I, III, IV) that are found along the sides of cristae. Lastly, the phospholipid composition of the IMM is highly specific for cardiolipin (CL), which with its four fatty acid acyl chains, facilitates curvature of the membrane.

Questions that remain in regard to cristae shape is the nature of the process which initiates the formation of these structures, particularly in mammalian systems, as well as how the cristae are dynamically regulated. One possibility is that cristae are the result

inner membrane fusions during mitochondrial network dynamics, especially given that Opa-1 is also involved in mitochondrial fusion (146, 147).

Alternative models propose cristae form as energetically favorable invaginations which are stabilized by junction protein complexes, or a conversely a balloon model proposes that CJs form first, followed by membrane invagination (131). Interestingly, it has been proposed that fission and fusion events between the cristae themselves can occur. In yeast, these internal fission-fusion events have been proposed to be spontaneous and reversible and are promoted by mitochondrial matrix swelling due to changes in osmolarity (148). It is unclear however if this spontaneous fission-fusion can occur similarly in mammals.

Cardiac mitochondria and disease

The energetic demand that is met daily by cardiac mitochondria is enormous, producing 6 kg of ATP per day in humans, and occupying approximately one-third of the volume of a myocyte (149). The majority of this ATP is produced by fatty acid oxidation (FAO), however during states of stress such as fasting, starvation, diabetes, or hypertrophy, the heart can metabolize carbon from glycolysis and amino acids. Defects in mitochondrial function resulting from improper fission-fusion dynamics, metabolic signaling, electron transport, or increased generation of ROS can lead to a multitude of cardiac diseases and ultimately cardiomyocyte cell death (150, 151).

Many mitochondrial cardiac diseases are myopathies presenting with muscle dysfunction and weakness, and many known mutations within both mtDNA as well as nuclear encoded DNA are known to be involved (152, 153). Interestingly, the interaction between mtDNA haplogroup, or groups of related haplotypes, and nuclear encoded genes

add an additional layer of genetic complexity that affects disease penetrance (151). Some of the known associations between mitochondrial dysfunction and myopathy are summarized in Figure 1-7 below.

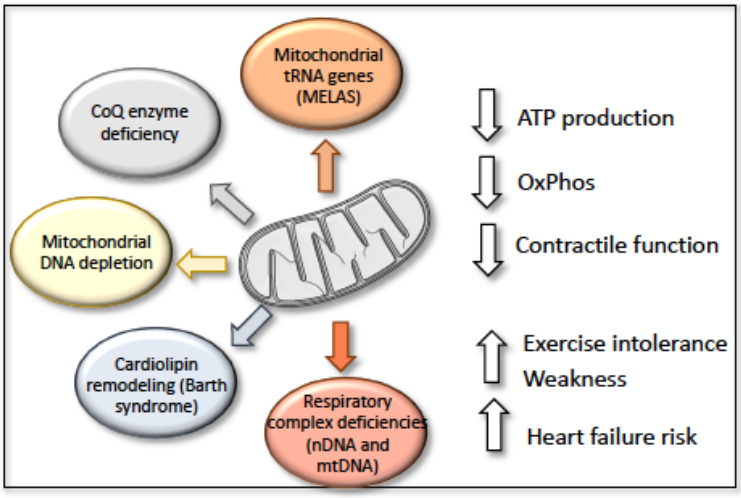

Figure 1-7. Mitochondrial dysfunction and cardiomyopathy.
Known causes of mitochondrial cardiomyopathies include: respiratory chain complex defects due to mtDNA deficiency or mutations and mutations in mtDNA for tRNA encoding genes such as in mitochondrial encephalopathy with lactic acidosis and stroke (MELAS). Furthermore, mutations in the X-linked cardiolipin remodeling gene Tafazzin results in Barth Syndrome. Dysfunctional mitochondria contribute to overall cardiac weakness and ultimately predisposes to individuals to heart failure.

In addition to cardiomyopathies, extensive genetic analysis has been done to evaluate potential risk loci for predisposition to coronary artery disease (CAD) and myocardial infarction (MI), or heart attack. CAD is characterized by arterial atherosclerotic plaques and cause a blockage in the blood flow to the heart, leading to ischemic tissue damage. In 2016, it was estimated by the American Heart Association that 15.5 million Americans have CAD, and an individual will have an MI every 42 seconds (154). While single-nucleotide polymorphisms (SNPs) in genes impacting low-density lipoprotein cholesterol (LDL-C) have been validated, including *ApoE*, *ApoB*, *LDLR,* the most common risk allele on chromosome 9p21.3 has an undetermined mechanism (155).

Recent genome wide association study (GWAS) meta-analysis by the CARDIoGRAMplusC4D Consortium however has expanded the coverage of genetic variation, revealing 10 new CAD-associated loci (156). One of these significant loci included 23 SNPs found in linkage disequilibrium (LD) within an intron of the nitric-oxide-associated 1 (*REST-NOA1*) gene locus ($p<1x10^{-6}$). Noa1 is a mitochondrial cristae-associated protein that interacts with complex I and regulates oxygen consumption and mitochondrial dynamics (157). How these SNPs impact mitochondria however is still unknown.

Given the apparent difficulty in measuring mitochondrial physiology in human heart tissue prior to an MI, the link between mitochondrial dysfunction as a predisposing factor for an MI, rather than as a consequence of atherosclerosis, is limited. Evidence from *ApoE-/-* knockout mice crossed to mitochondrial antioxidant superoxide dismutase 2 haploinsufficient mice (*SOD+/-*) revealed increased atherosclerosis as well as mtDNA lesions, compared to *ApoE-/-* mice alone (158). In a complementary study, *ApoE-/-* mice crossed to *ATM+/-* mice, lacking proper DNA repair, presented with enhanced clinical features of atherosclerosis, and some mitochondrial metabolic defects (159). These results suggest both mitochondrial function and ROS handling may be important for the pathogenesis of MI.

In addition to atherosclerosis, the highest risk factor for poor outcome after an MI is aging (160). Mitochondria structure and function are compromised in aged hearts due to decreased numbers of mitochondria, increased peroxidation of cardiolipin, ETC chain defects especially in complexes III and IV, and a corresponding increase in ROS production (161). Consumption of the anti-oxidant β-carotene in an aged population

without a prior MI decreased the risk of a future MI event (162) however clinical trials with anti-oxidants have not been successful, suggesting ROS is only one of multiple factors involved in MI risk (163).

While these studies begin to address the role of mitochondria in atherosclerosis, they do not take into account the role of mitochondrial function in the cardiac tissue itself. This consideration is especially important as approximately 8.8% of all MI events are not linked to arterial plaque formation (164). In mouse models, loss of Mfn1 and 2 expression in adult myocytes results in fragmented mitochondria, rapidly leading to respiratory defects and cardiomyopathy (165). Conversely, Opa-1 transgenic mice have increased mitochondrial cristae and are resistant to apoptotic remodeling, cytochrome c release, and damage following ischemia-reperfusion (I/R) (139). Furthermore, evidence from a recent study in humans revealed that despite the presence of coronary calcification, men who exercise have a decrease in cardiovascular related mortality compared to men do not exercise (166). This is consistent with findings that exercise promotes mitochondrial fitness and resistance to ischemic damage (167, 168).

In sum, these results highlight that MI risk is not solely due to atherosclerotic build-up. Overall decreased heart fitness prior to an MI event due to underlying mitochondrial dysfunction is a virtually unexplored area of potentially great risk.

The Bcl-2 family and heart

The role for the Bcl-2 family in cardiac disease has almost exclusively been studied in the context of cell death regulation after ischemia-reperfusion (I/R) injury. After an ischemic event, oxidative damage occurs during reperfusion resulting in cardiomyocyte

cell death. Many of the pro- and anti-apoptotic have been shown to play a role in this process (169). For example, overexpression of Bcl-2 reduces cardiac apoptosis and dysfunction in mice, while Bax is activated during oxidative stress (170, 171). Cleavage of Bid by calpains also promotes apoptotic death and cleavage-resistant Bid however can protect from ischemic damage (172, 173).

In addition to apoptosis, cardiomyocyte death after an I/R event is often described as necrotic. This is due to an earlier study describing the morphological appearance of the heart tissue after I/R (174). However, despite the wide use of necrotic terminology, no evidence yet connects Ripk1 or Ripk3 signaling after an ischemic event (175). It has been shown however, that treatment with the Ripk1 specific inhibitor necrostatin-1 (Nec-1) does confer protection after I/R injury in both WT mice (176, 177).

Given the roles for Mcl-1 and Bcl-XL in mitochondrial structure and function, especially cardiomyopathy observed in deficient Mcl-1 mice, it is likely that Bcl-2 family is also important for mitochondrial fitness (126, 127). In particular, Bid is an especially interesting candidate for homeostatic cristae regulation. It associates at the mitochondria inner and outer-membrane contact sites with cardiolipin (CL) and both can reorganize cristae independent of its apoptotic BH3-domain (20). Results in Chapter III explore the role for Bid in mitochondrial homeostasis and reveal a novel role for the maintenance of the cristae structure. Results from mice, with evidence from human genetics studies, reveal loss of Bid or BID gene expression increases propensity to mitochondrial damage, due in part to Bid's association with the mitochondrial matrix form of Mcl-1.

Hematopoiesis

Given the discovery of Bcl-2 as an oncogenic translocation in B-cell lymphoma, one most well characterized roles for these proteins is in the regulation of blood cell formation, or hematopoiesis. Hematopoiesis is a highly ordered process in which a small

number of stem cells (HSCs) give rise to multipotent progenitor cells and ultimately terminally differentiated, lineage-committed cells. This process is regulated by a fine balance between progenitor cell expansion during infection or injury and contraction after resolution. Normal homeostasis requires programmed cell death, highlighted by numerous mouse models in which loss of one or more PCD genes results in severe hematopoietic phenotypes. Imbalances in homeostasis can lead to bone marrow failure disorders such as myelodysplastic syndrome (MDS) and promote clonal expansion, which has potential to transform to cancer.

In mice, the aorta-gonad-mesonephros (AGM) tissue, specifically the dorsal aorta, harbor the first HSCs at embryonic day 10 (E10) (178). HSCs from the AGM colonize the fetal liver by E11 and can be found in the marrow by E17.5. In humans, HSCs also arise in the AGM and populate the bone marrow by day 70 of gestation (179). Once in the marrow, HSCs mature and are generally quiescent, asymmetrically dividing to self-renew while also giving rise to multi-potent progenitors (MPPs) and two main lineages: myeloid and lymphoid.

Lymphoid cells comprise the adaptive immune system including T-cells and B-cells, as well as innate cells such as natural killer (NK) and antigen presenting (APC) dendritic cells. These cells clear infections through release of cytotoxic granules, enzymes, or antibodies. The myeloid lineage is composed of granulocytes including neutrophils, macrophages, platelet-forming megakaryocytes, and erythroid, or red blood cells. Neutrophils are the most abundant granulocytes and the front-line defense after an injury or infection, while phagocytic macrophages, are responsible for pathogenic clearance. Within the bone marrow these cells occupy their own regions, termed niches. For example, HSCs reside adjacent to sinusoids, enriched in the chemokine CXCL12, while B-cell progenitors

are highly supported by osteoclasts (180, 181). A diagram of the major lineages discussed is included below (Figure 1-8). As hematopoietic cells mature, they express surface markers, or clusters of differentiation (CDs) and receptors. Targetable by antibodies, these allow for immunophenotyping by flow cytometry to distinguish between cell types and maturation stage. Frequently studied populations include SLAM-HSCs with a surface marker profile of $CD150^{+}$, $CD244^{-}$, $CD48^{-}$ (182), stem-cell enriched LSK cells, progenitor cells (Lin-Sca-1-c-Kit+), and lineage-specific markers such as CD71 and Ter119 for erythroid cells, CD3 for T-cells, and B220 for B-cells.

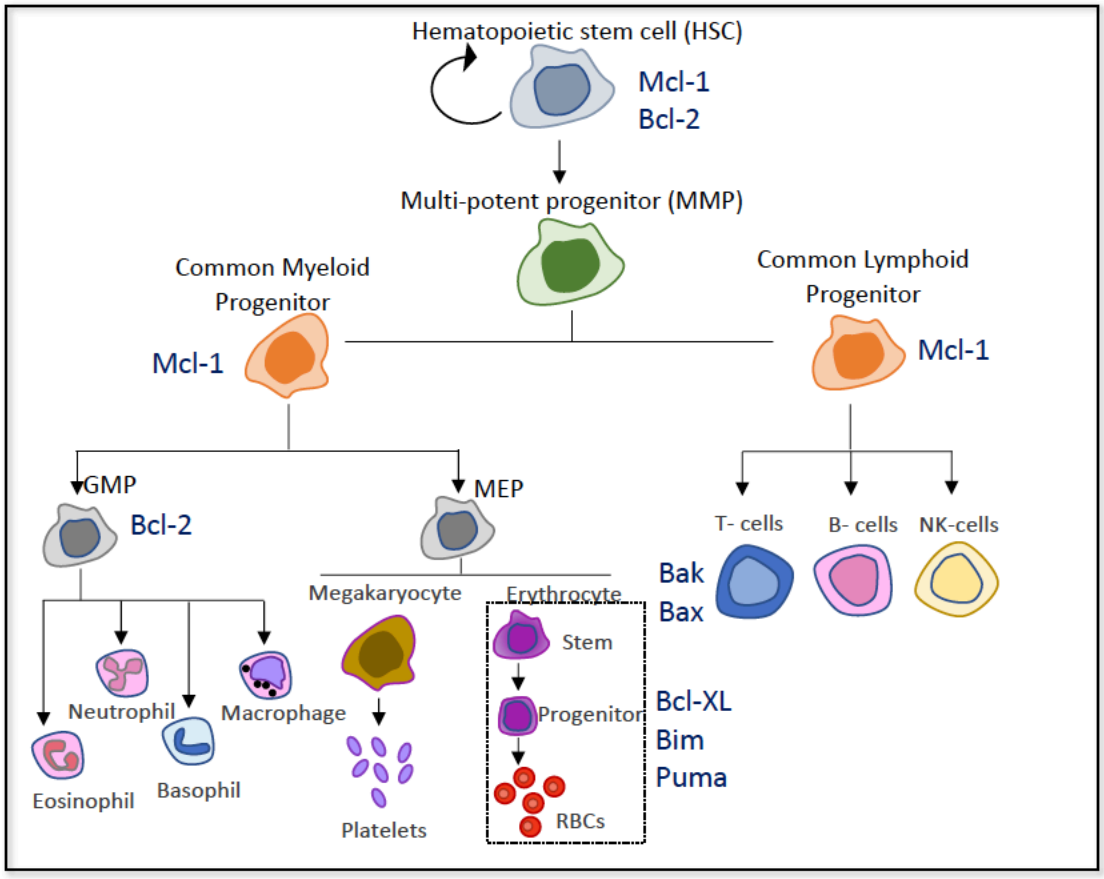

Figure 1-8. Hematopoiesis.
The process of blood cell formation or hematopoiesis occurs primarily in the long bones of adult mammals. A hematopoietic stem cells, which reside in bone marrow called niches, are generally quiescent but can self-renew and divide into more differentiated cells, giving rise to two main lineages, lymphoid and myeloid. Both lineages have a common progenitor cell that differentiates into more mature, committed cells. The myeloid compartment consists of

Figure 1-8 Continued.
antigen presenting as well as platelet forming macrophages and red blood cells. White blood cells, or lymphoid cells, complete their maturation process outside of the marrow in the spleen and thymus for B- and T-cells, respectively. Indicated are also some of the key Bcl-2 family proteins that have implicated in various stages of hematopoietic maturation. NK=Natural killer cell, GMP=Granulocyte-monocyte progenitor, MEP=Megakaryocyte-erythroid progenitor

The Bcl-2 family and hematopoiesis

Cell death genes have been implicated in the normal maturation of both myeloid and lymphoid lineages, especially the anti-apoptotic proteins Mcl-1, Bcl-2 and Bcl-XL. Bcl-2 knockout mice are unable to maintain hematopoiesis due to T and B-cell death and loss of Mcl-1 in mice is embryonically lethal while its over-expression increases hematopoietic stem cell survival (183, 184). Bcl-XL knockout-mice are also embryonically lethal due to massive hematopoietic stem cell death while conditional knock-out animals have severe anemia (185, 186).

Further studies have revealed that the hematopoietic lethality of these mouse models in part is due to loss of inhibition of pro-apoptotic proteins. For example, *Puma-/-* mice rescues bone marrow failure observed in lethality irradiated *Mcl-1+/-* mice, suggesting it is the key player of death in this context (187).

One of the most well characterized roles for Bcl-XL is in the regulation of erythropoiesis or red blood cells. During erythropoiesis, cells mature from de-differentiated blasts through multiple precursor stages before extruding their nuclei, mitochondria, and organelles forming mature red cells (Figure 1-9). This process is regulating by transcription factors such as KLF, the hormone erythropoietin (EPO) in early blasts (mainly in CFU-Es and ProE), adherence to erythroid precursors to macrophages, termed erythroblastic islands, and Bcl-XL (188–191). A direct role for Bcl-XL was first uncovered in *Stat5a* and *5b* deficient mice which had decreased Bcl-XL levels and substantial red cell death in the

bone marrow (192). Further work defined the precise role for Bcl-XL during late stages of maturation during heme synthesis (193) and more recently it has been shown that Bcl-XL can rapidly increase during conditions of stress mediated by EPO (194).

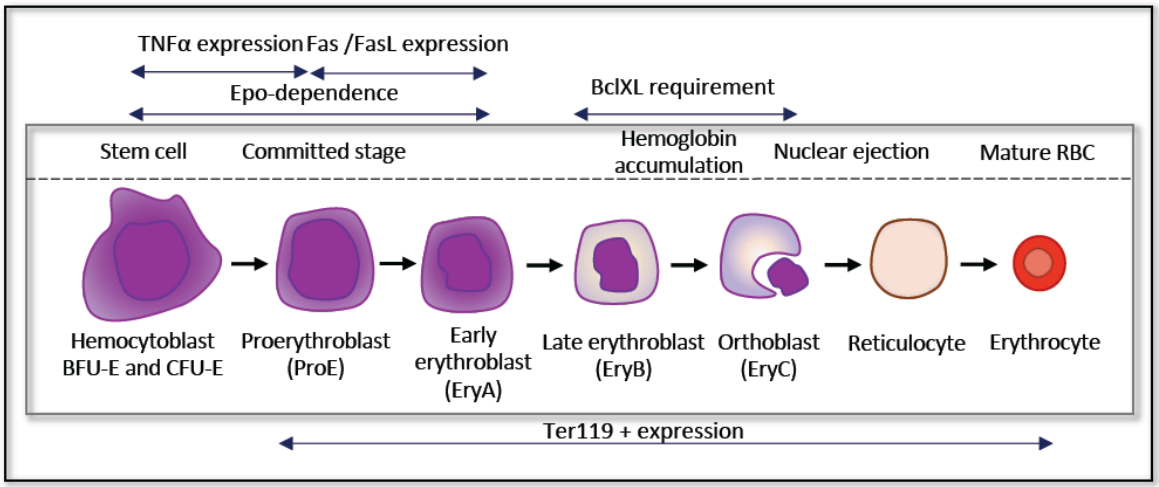

Figure 1-9. Erythropoiesis.
The first committed red cell progenitors can be detected *in vitro* by methylcellulose assay which include immature Burst-forming units-erythroid (BFU-E) and Colony-forming units-erythroid (CFU-E). In the presence of growth factors such as Erythropoietin (EPO), IL-3, and SCF (stem cell factor), cells expand and differentiate, decreasing in size. Between the orthochromatic (orthoblast) and mature reticulocyte stages, red cells extrude their nuclei. This process occurs in a red cell specific niche in the marrow termed erythroid islands. Islands consist of a central macrophage which are essential for phagocytosis of nuclei and also transfer iron as ferritin to maturing red cells. Fully mature erythrocytes then extravasate into the periphery, where they circulate for approximately 120 days before they are recycled by resident macrophages in the red pulp of the spleen. In mice under conditions of stress such as hypoxia, erythropoiesis can also occur in the spleen, termed extramedullary or emergency hematopoiesis.

In addition to anti-apoptotic proteins, the pro-apoptotics also contribute to hematopoietic homeostasis by inhibiting inappropriate cell expansion. *Bid-/-* mice present with CMML as they age (36) and *Bim-/-* mice have an increased myeloid cells as well as erythrocytes in the spleen. While *Puma-/-* mice have no hematopoietic phenotype on their own, loss of Puma in addition to Bcl-XL can partly restore red cell numbers after competitive BMT (195).

Necrotic genes have also been implicated in hematopoiesis however these roles are less well understood. Loss of germline *Ripk1* results failure to thrive in mice, however this is due to Ripk1 scaffolding function as mice harboring mutations in the kinase domain are viable (65, 196, 197). Conditional loss of Ripk1 in the hematopoietic compartment however results in bone marrow failure, partially rescued by additional loss of *Ripk3* (198). It is unclear however, if and how necrotic cell death plays a role in normal hematopoietic homeostasis. This is of particular interest given the highly inflammatory nature of necrotic cell death, and potential for contribution of this process in disease pathogenesis.

Bone marrow failure and clonal hematopoiesis

Bone marrow failure (BMF) disorders comprise a group of diseases, both inherited and acquired, in which cells predominantly of the myeloid lineage fail to constitute the blood system. The most common inherited syndrome is Fanconi anemia (FA), caused by mutations in genomic DNA repair genes. Other disorders are the result of mutations in telomere maintenance and mutations in ribosomal proteins (199). Acquired BMFs syndromes include aplastic anemia (AA) and myelodysplastic syndrome (MDS) both of which can present with anemia, leukopenia, and thrombocytopenia among other symptoms.

In particular, MDS is a pathologically and clinically difficult disease to diagnose and treat, with less than a 20% response rate to current therapies. Prevalence of MDS increases with age and is more common in men. Prior exposure to DNA-damaging therapeutics is also a common risk factor. Diagnosis of MDS is based on a combination of peripheral blood analysis, marrow aspirates to determine dysplastic morphologies, changes in bone marrow cellularity, especially excess blasts, as well as cytological abnormalities such a 5q deletions. Disease severity is stratified using an international prognostic scoring

system (IPSS-R), separating patients into low-risk, intermediate and high-risk disease (200).

Regardless of risk type, therapies for MDS are extremely ineffective, particularly for those individuals who have refractory disease. The only curative therapy is allogeneic bone marrow transplant (BMT) (201). Most patients with low risk MDS succumb to infection due to cytopenia (202), while patients with high risk MDS can progress to secondary acute myeloid leukemia (sAML).

The peripheral cytopenia observed in MDS is often in contrast to the normal or hyper-cellularity in the marrow. This is attributed to increased apoptotic cell death (203). However, these studies used general markers of death such as DNA laddering, and do not take into account precise signaling pathways such as caspase activation. Furthermore, MDS is extremely difficult to culture, and any observed death *in vitro* is likely not be related to the disease itself (204). Improved understanding of PCD prompts revisiting of these findings, especially given that inflammation has also been shown to be involved in disease progression and is not a hallmark of apoptotic cell death (205). This is especially important as anti-apoptotic proteins are now being proposed as therapeutic targets (206).

Recently, whole-exome sequencing has identified increased numbers of molecular abnormalities associated with MDS. Common mutations are found in mRNA splicing genes SF3B1 and SRSF2, epigenetic regulators such as TET2 and DMNT3A, and chromatin remodeling genes such as ASXL1. The frequency of these mutations directly corresponds to increased patient age (207). Importantly however these abnormalities are also found in healthy individuals with normal blood counts and no presence of dysplasia despite clonality and are thus referred to as having clonal hematopoiesis of indeterminate potential (CHIP). Individuals with CHIP are thought to progress at a rate of 0.5-1% per

year to MDS or other neoplasms, highlighting rarity in which CHIP actually results in cancer (208). While approximately 85% of individuals diagnosed with MDS have mutations in one or more of these genes, currently the presence of these mutations does not directly impact treatment decisions nor are they used to definitively diagnose MDS. Other idiopathic syndromes however such ICUS and CCUS (idiopathic cytopenia and clonal cytopenia of undetermined significance), do present with cytopenia and have elevated rates of disease progression to cancer suggesting cytopenia in combination with clonality is particularly detrimental (208). Overall, the major question that remains is the identify of other risk factors that contribute to the progression of disease in some individuals versus others.

CHIP and coronary artery disease

One of associations identified in CHIP patients was increased risk of CAD and ischemic stroke (207, 209). The link between the hematopoiesis and atherosclerotic lesions has been known from some time, identified first in patients with peripheral leukocytosis with increased risk for MI (210). Circulating monocytes develop into pro-inflammatory macrophages in plaques promoting inflammation and calcification of arterial walls. States of hypercholesteremia, particularly high low-density lipoprotein (LDL), induces both monocytosis, increased monocyte expression of chemokine receptors, and increased proliferation of HSPCs (211).

CHIP genes, particularly DNMT3A, TET2, and ASXL1 were found to be present in 17% of individuals with CAD compared to 10% of patients without CAD. Early-onset myocardial infarction patients also had significantly increased CHIP gene enrichment (2% of patients versus <1%). Measurement arterial calcification in CHIP carriers without

incident CAD was also 3.3 times that of non-CHIP patients, linking the incident of MI with plaque burden (209). A complementary mouse study also tested these findings. BMT with donor marrow from TET2 knockout-mice or macrophage specific TET2 knockout marrow (Mye-Tet2-KO) was transplanted into radiated *Ldlr-/-* mice. *Ldlr-/-* mice are particularly prone to atherosclerotic plaques (212, 213). High fat diet after hematopoietic engraftment accelerated atherosclerotic plaque lesions and enhanced macrophages inflammatory cytokine production, particularly IL-1β compared to controls (214).

In addition to CHIP genes, other hematopoietic genes have been linked to CAD such as the LNK/SH2B gene locus. LNK suppresses thrombopoietin signaling which activates platelet formation. BMT of *Lnk-/-* bone marrow into *Ldlr-/-* recipients also increased atherosclerotic lesion size due to increased myeloid cell infiltrate (215). Furthermore, it was recently shown that MDS also corresponds with increased risk of death due to CAD. This was particularly true of patients with intermediate and high-risk MDS 5 years post-diagnosis (216). CHIP mutational burden in these patients however is unknown, and complications from treatment and disease course, such as transfusions and EPO, likely confound this association.

One of the factors that link CHIP, MDS, and CAD is inflammation. TET2 in particular has been associated with inflammation in multiple studies. During acute inflammation, Tet2 associates with the NFκB transcription factor IκBζ repressing IL-6 expression and loss of Tet2 promotes inflammation (217). Bone marrow derived macrophages derived from *Tet2-/-* mice stimulated with LPS *in vitro* showed an acute increase in inflammatory cytokine (218). Treatment of marrow with either a Shp inhibitor or Ape1 inhibitor, involved in inflammatory signaling downstream of IL-6, decreased

clonal expansion of *Tet2-/-* cells after BMT in mice, although whether this response can be sustained remains to be determined (219). Lastly, BMT of *Tet2-/-* marrow into recipient mice with previous coronary artery ligation (CAL) worsened cardiac function and increased IL-1β expression (214).

In sum, these studies strongly support a link between clonal hematopoiesis and CAD. However, the directionality of this association has yet to be determined. For example, CD34+ bone marrow isolated from patients during coronary bypass have decreased numbers of burst-forming unit-erythroid (BFU-E) colonies *in vitro* and increased death compared to marrow from healthy controls. This was associated with severity of heart failure but not anemia (220). It is unclear then if clonal hematopoiesis drives CAD in a feed-forward manner, or conversely if CAD promotes an inflammatory response detrimental to normal hematopoiesis. Thus, determining the timing and type of therapeutic intervention in early MDS or clonal hematopoiesis, before transformation or onset of CAD, remains a true challenge. The identification of additional risk factors to improve prognosis will help answer these essential questions, addressed in Chapter IV of this thesis.

Using human genetics to inform biological questions

The goal of genome wide-association studies (GWAS) is to connect genetic variants, namely single nucleotide polymorphisms (SNPs), with traits or phenotypes observed in populations. The predictive value of GWAS relies on how many genetic loci influence a trait, variant allele frequency (VAF), sample size, and the heterogeneity of the trait itself (221). Most complex traits or diseases are highly polygenic, involving many genetic loci, and consequently one of the challenges of GWAS has been translating these

findings into mechanistic understanding of disease. This is made particularly more complex as most variation is found in non-coding regions of the genome.

PheWAS, or phenome-wide association studies, is a reverse genetic approach in which a genetic variant of interest can be connected to many phenotypes (222, 223). The framework for this type of analysis was made possible in in 2007 when Vanderbilt University Medical Center began to collect discarded blood from clinical tests with patent consent. Extracted DNA from these samples was used to create a biorepository called BioVU (224). This connected sequencing information with electronic heath records (EHRs) and consequently disease information. Importantly, EHRs are de-identified, given a unique ID that cannot be traced to the original medical record. The EHRs linked to BioVU are a part of Vanderbilt's larger Synthetic Derivative (SD). The SD contains just under 3 million records of clinical data which can also be mined but are not connected to genome level analysis. These two approaches PheWAS and GWAS are highly complementary, identifying all phenotypes associated with a particular variant and all of the variants of a particular phenotype, respectively.

To connect findings in GWAS studies to the more mechanistic understanding of disease, genetic variation has been linked to mRNA expression. Termed expression quantitative trait loci or eQTLs, variation in a gene can impact expression of either genes locally, or in cis, or distantly, called trans eQTLs (225). The Genotype-Tissue Expression (GTEx) project established in 2013 has led the effort to build a resource of eQTLs and gene expression data in a tissue-specific manner from deceased donors (226, 227). This searchable database is a powerful resource and has been recently used to shed light on disease and trait variation that is shared across tissues (228).

Another approach that has been developed to connect the genetic variation to phenotype is PrediXcan. Developed by Gamazon et al., it estimates genetically determined gene expression (229). This estimation is based on reference transcriptome data that is available through GTEX which is then used to impute gene expression. PrediXcan analysis can then be applied to whole-genome sequencing data such as BioVU. Combining BioVU with PrediXcan is extremely powerful. Unlike CHIP gene mutations which are somatic, PrediXcan's approach, which relies on germline SNPs rather than somatic variability, can begin to identify genes, or gene pathways, involved in genetic predisposition.

In addition to GWAS level analysis, whole exome sequencing (WES) level-chip analysis can also be informative. This is particularly useful in the identification of low-frequency or rare variants which have minor allele (second most common allele) frequencies (MAF) of less than 1% (in contrast to common variants which have MAFs generally >1%). Exome sequencing platforms in particular can identify SNPs which may have consequences at the protein-level. For example, WES of patients with elevated low-density lipoprotein cholesterol (LDL-C) identified new low-frequency variants in lipid hydrolase, PNPLA5, not found in larger GWAS studies (230). Depending on the nature of the SNP, these findings may have implication for protein structure of function. In Chapter III, data from both WES and PrediXcan analysis of GWAS studies including BioVU are used to inform and integrate experimental results from *in vitro* and *vivo s*tudies. This approach is highly complementary, and sheds light on a new role for Bid in human disease (231).

Chapter II

MATERIALS AND METHODS

*Mitochondrial Methods**

Mice

All mice were housed, and experiments performed with approval by the IACUC of Vanderbilt University Medical Center in compliance with NIH guidelines. WT (*Bid*+/+) and *Bid-/-* mice were back-crossed onto a C57BL/6 background at least nine generations in addition to being re-derived to mice with a pure C56BL/6 background. Age and sex of mice used for experiments are indicated where applicable.

Cell culture and Bid mutants

Hox11-immortalized MPCs were cultured in IMDM medium with 20% FBS, 100 U/ml penicillin-streptomycin, 2 mM glutamine, 0.1 mM b-mercaptothionβ, and 10% WEHI conditioned medium as a source of IL-3. Cell lines were mycoplasma tested and negative. Cell lines were also authenticated by genotyping. To generate MPCs expressing exogenous wild type or mutant Bid, Bid was cloned into pOZ-FH-C-hCD25 using XhoI and NotI restriction sites (232). BH3 mutant Bid has amino acids 93–96 of mouse Bid mutated from IGDE to AAAA (78). The D59A mutant Bid is mutated at the caspase eight cleavage site. M148T, E120D, R123Q, and BH3S61AS78A (BH3AA) were designed according to the Quickchange II Site-directed mutagenesis Kit (Agilent Technologies) using the pOZ-FH-C-Bid-BH3-mut-hCD25 as a template (see Table 2-1 below). Stable cell lines were generated with retroviral transduction using Fugene 6 (Promega) or Lipofectamine 2000 (Thermo Fisher Scientific). See Table 2-1 and Table 2-2 for primer sequences and additional information.

**Methods described here correspond to Chapter III and have been published as reference (203)*

Primer	Sequence
M148T	Fwd: 5'GGAGAACGACAAGGCCATGCTGATAATGACAATGC 3'
	Rev: 5' GCATTGTCATTATCAGCATGGCCTTGTCGTTCTCC 3'
E120D	Fwd: 5' GAATGGCAGCCTGTCGGATGAAGACAAAAGGAAC 3'
	Rev: 5' GTTCCTTTTGTCTTCATCCGACAGGCTGCCATTC 3'
R123Q	Fwd: 5' GTCGGAGGAAGACAAAAGGAACTGCC GGCCAAAG 3'
	Rev: 5' CTTTGGCCAGGCAGTTCCTTTTGTCTTCCTCCGAC 3'
S78A	Fwd: 5'CCAGATTCTGAAGCTCAGGAA GAAATCATCCACAACATTGCC 3'
	Rev: 5'GGCAATGTTGTGGATGATTTCTTCCTGAGCTTCAGAATCTGG 3'
S61A	Fwd: 5'CAGACAGACGGCGCCCAGGCCAGCCGC 3'
	Rev: 5'GCGGCTGGCCTGGGCGCCGTCTGTCTG 3'

Table 2-1. Primers for site-directed mutagenesis

Reagent type (species) or resource	**Designation**	**Source or reference**	**Identifiers**	**Additional information**
Strain, strain background (*mus musculus*, C57BL/6)		The Jackson Laboratory	Stock No: 000664 (Black 6) RRID: IMSR_JAX:000664	
Strain, strain background (*mus musculus*, C57BL/6)	*Bid-/-*	PMID: 10476969		
Cell line (mouse)	Myeloid Progenitor Cells (MPCs)	PMID: 16122425		
Gene (mouse)	BID (BH3 interacting death domain agonist)	PMID: 8918887 NCBI Reference	MGI: 108093 NM_007544.4	
Transfected construct	pOZC-FH-C-hCD25	PMID: 14712665		Available from Addgene (plasmid #32516)

Transfected construct (pOZ-FH-C-hCD25 vector)	FHA-Bid	PMID: 16122425		
Transfected construct (pOZ-FH-C-hCD25 vector)	FHA-BidBH3	PMID: 16122425		
Transfected construct (pOZ-FH-C-hCD25 vector)	FHA-BidD59A	PMID: 12519725		
Transfected construct (pOZ-FH-C-hCD25 vector)	FHA-BidBH3AA	This paper		Mutant made with site directed mutagenesis of FHA-BidBH3 construct; Zinkel Laboratory; See Methods Table 2-1 for primer sequences
Transfected construct (pOZ-FH-C-hCD25 vector)	FHA-BidBH3/M148T	This paper		Mutant made with site directed mutagenesis of FHA-BidBH3 construct; Zinkel Laboratory; See Methods Table 2-1 for primer sequences
Transfected construct (pOZ-FH-C-hCD25 vector)	FHA-BidM148T	This paper		Mutant made with site directed mutagenesis of FHA-Bid construct; Zinkel Laboratory; See Methods Table 2-1 for

				primer sequences
Transfected construct (pOZ-FH-C-hCD25 vector)	FHA-BidBH3/E120D	This paper		Mutant made with site directed mutagenesis of FHA-BidBH3 construct; Zinkel Laboratory; See Methods Table 2-1 for primer sequences
Transfected construct (pOZ-FH-C-hCD25 vector)	FHA-BidBH3/R124Q	This paper		Mutant made with site directed mutagenesis of FHA-BidBH3 construct; Zinkel Laboratory; See Methods Table 2-1 for primer sequences
Antibody	Bid (goat polyclonal)	R and D Systems	AF860 RRID: AB_2065622	1:1000 (5% milk, Western Blot (WB))
Antibody	Bid (rabbit polyclonal)	PMID: 8918887	Antibody generated by S. Korsmeyer Lab	1:1000 (5% milk, WB)
Antibody	Bim (H-5, mouse monoclonal)	Santa Cruz Biotechnology	sc-3743589 RRID: AB_10987853	1:100 (5% milk, WB)
Antibody	Bad (Clone 48, mouse)	BD Bioscience	610391 RRID: AB_397774	1:500 (5% milk, WB)
Antibody	Puma/bbc3, N-terminal (rabbit)	Sigma-Aldrich	P4743 RRID: AB_477351	1:1000 (5% milk, WB)

Antibody	Anti-HA (rabbit polyclonal)	Sigma-Aldrich	H6908 RRID: AB_260070	1:1000 (5% milk, WB)
Antibody	VDAC1 (rabbit polyclonal)	Abcam	ab15895 RRID: AB_2214787	1:1000 (5% milk, WB)
Antibody	β-Actin (AC-15, mouse monoclonal)	Sigma-Aldrich	A5441 RRID: AB_476744	1:200,000 (5% milk, WB)
Antibody	Anti-GAPDH (FL-335, rabbit polyclonal)	Santa Cruz Biotechnology	sc-25778 RRID: AB_10167668	1:1000 (5% milk, WB)
Antibody	Bak, NT (rabbit polyclonal)	EMD Millipore	Cat #06–536 RRID: AB_310159	1:1000 (5% milk, WB)
Antibody	MnSOD (rabbit polyclonal)	Stressgen	ADI-SOD-111 RRID: AB_10631750	1:1000 (5% milk, WB)
Antibody	Mcl-1 (rabbit polyclonal)	Rockland Immunochemicals, Inc	600-401-394S RRID: AB_2266446	1:1000 (5% milk, WB)
Antibody	Opa-1 (Clone 18, mouse)	BD Bioscience	612606 RRID: AB_399888	1:1000 (5% milk, WB)
Antibody	Calreticulin (D3E6, XP, rabbit monoclonal)	Cell Signaling Technology	12238 RRID: AB_2688013	1:1000 (5% milk, WB)
Antibody	Anti-pyruvate dehydrogenase E2/E3 (mouse monoclonal)	Abcam	ab110333 RRID: AB_10862029	1:1000 (5% milk, WB)
Antibody	Amersham ECL anti-rabbit IgG, HRP-linked (from donkey)	GE Healthcare	NA934 RRID: AB_772206	1:10,000 (5% milk, WB)
Antibody	Goat anti-mouse IgG, HRP-conjugate	Novex	A16072 RRID:AB_2534745	1:10,000 (5% milk, WB)
Antibody	Donkey anti-goat IgG HRP	Santa Cruz Biotechnology	sc-2020 RRID:AB_631728	1:10,000 (5% milk, WB)
Chemical compound, drug	Doxorubicin HCl (Dox)	APP Fresenius Kabi USA, LLC	NDC 63323-883-05	
Chemical compound, drug	Epinephrine (Epi)	BPI Labs, LLC	NDC 54288-103-10	
Chemical compound, drug	Fugene 6 Transfection Reagent	Promega	E2691	

Chemical compound, drug	Lipofectamine 2000 Transfection Reagent	ThermoFisher Scientific	11668027	
Commercial assay or kit	QuikChange XL Site-Directed Mutagenesis Kit, 10 rxn	Agilent Technologies	200521	
Commercial assay or kit	GeneJET Plasmid Miniprep Kit	ThermoFisher Scientific	K0503	
Commercial assay or kit	GenElute HP Plasmid Maxiprep Kit	Sigma-Aldrich	NA0310-1KT	
Commercial assay or kit	PureLink HiPure Plasmid Maxiprep Kit	ThermoFisher Scientific (Invitrogen)	K210006	
Software, algorithm	PrediXcan	PMID: 26258848 and other		https://github.com/hakyimlab/PrediXcan
Software, algorithm	S-PrediXcan	Other		https://github.com/hakyimlab/MetaXcan
Other	CARDIoGRAM plus C4D	Other		www.CARDIOGRAMPLUSC4D.ORG
Other	GTEx Consortium (v6p)	PMID: 29022597 and other		http://www.gtexportal.org

Table 2-2. Key Resources.

Cell death and proliferation assays

At the indicated times cells were, washed, incubated with Annexin V-FITC (BioVision) in 1X Annexin V staining buffer (10 mM HEPES, pH 7.4, 140 mM NaCl, 2.5 mM $CaCl_2$). Immediately prior to analysis, propodeum iodide (Sigma) was added to a final concentration of 1 mg/ml. TNFα/Actinomycin D death assays were performed by treating cells with 25 ng/ml TNFα and 50 ng/ml Actinomycin D in complete IMDM growth medium Samples were analyzed on a Becton-Dickinson flow cytometer and FlowJo analysis software. Cell growth was determined by trypan blue viability.

Electron microscopy and image quantitation

Cells were washed with 0.1 M cacodylate buffer ($Na(CH_3)2\ AsO_2 \bullet 3H_2O$) and fixed in 2.5% glutaraldehyde/0.1M cacodylate for 1 hr at room temperature and left at 4°C overnight. The samples were post-fixed in 1% osmium tetroxide and washed 3 times with 0.1 M cacodylate buffer. The samples were dehydrated through a graded ethanol series followed by incubation in 100% ethanol and propylene oxide (PO) as well as 2 exchanges of pure PO. Samples were embedded in epoxy resin and polymerized at 60°C for 48 hr.

For each sample, 70–80 nm ultra-thin sections were cut and mounted on 300-mesh copper grids. Two sections per sample were stained at room temperature with 2% uranyl acetate and lead citrate. Imaging was done on a Philips/FEI Tecnai T-12 high resolution transmission electron microscope with a side mounted 2k _ 2 k AMT CCD camera. For initial cell line analysis, a total of 40 images were captured per cell type. Images were quantified at 30,000x. LV cardiac tissue was harvested from WT or Bid-/- mice at 18 hours with or without Epinephrine (0.5 mg/kg) and immediately fixed and processed as described above. All images were acquired in the Vanderbilt Cell Imaging Shared Resource.

Quantitation was done with FIJI (Fiji Is Just ImageJ) software using a stereology plugin (Version 0.1) to create a multipurpose stereological grid (233). Horizontal grid lines were overlaid on each image using the same tile density setting for all samples. The end of each line was counted as a point and points on the grid were counted as nucleus, extracellular space, cytoplasm or mitochondria. Total reference points per image were everything except nucleus and extracellular space. Cristae were counted when intersecting the grid line or point, and each crista was counted twice to account for double membranes. Data is represented as either area density (equivalent to volume density), which is the

number of mitochondria divided by the number of reference points. Length density (which is equivalent to surface density) was calculated as two times the number of cristae intersections divided by the total length of line for all possible intersections. For LV tissue cristae quantitation, 150 individual cristae were measured per treatment condition using the measurement tool in ImageJ software.

Western Blot and Co-immunoprecipitation

MPCs were treated as indicated and clarified cell extracts were prepared by lysis in RIPA buffer (50 mM Tris HCl pH 8, 150 mM NaCl, 0.5% sodium deoxycholate, 0.1% SDS, 2 mM EDTA) supplemented with protease (Complete Mini, Roche) and phosphatase (PhosSTOP, Roche) inhibitor followed by centrifugation at 12,000 rcf. Heart tissue extract was also prepared in the same way. Proteins were resolved by SDS-PAGE and transferred to PVDF membrane. Immunoblots were probed with the indicated antibodies and developed using chemiluminescent HRP substrate and autoradiography film. Co-immunoprecipitation was performed on 293T cells transfected by Fugene 6 (Promega) with the following Bid constructs: FlagHA-Bid, FHA-BidD59A, FHA-BidM148T and the following Mcl-1 constructs (a kind gift from Dr. Joseph Opferman): pMSVC-puro (empty vector), Mcl-1 (WT), Mcl-1OM, Mcl-1Matrix. Input was removed from equal concentrations of whole cell lysate, followed by immunoprecipitation with Flag-M2 agarose beads (Sigma).

Antibodies used: anti-Bid goat (R & D Systems) or anti-Bid rabbit polyclonal antibody (78), anti-Bim H-5 (Santa Cruz), anti-Bad Clone 48 (BD Biosciences), anti-Puma/bbc3 (Sigma), N-terminal (Sigma), anti-HA tag (Sigma), anti-VDAC1 (Abcam), anti-b-Actin (Sigma), anti-GAPDH (Santa Cruz), anti-Bak, NT (EMD Millipore), anti MnSOD (Stressgen), anti-Mcl-1 (Rockland Immunochemicals Inc) anti-Opa1 (BD Biosciences),

anti-Calreticulin (Cell Signaling Technology), anti- PDH E2/E3 (Abcam), anti-HRP conjugated anti-rabbit (GE Healthcare), and HRP conjugated anti-mouse (Novex), and HRP conjugated anti-goat (Santa Cruz). See Table 2-2 above for antibody catalog numbers and dilutions.

Mitochondrial isolation

Mitochondria were isolated by differential centrifugation from both tissue and cell lines. Unless stated otherwise, all isolations were done at 4°C. Mouse liver mitochondria were isolated using a protocol adapted from Brookes et al. (234) and heart mitochondria were isolated based on a protocol by JW Palmer et al. (235).

Liver tissue: harvested livers were placed in ice cold isolation buffer (IB) (200 mM sucrose, 5 mM HEPES-KOH, pH 7.4, and 1 mM EGTA) and homogenized in a glass-glass dounce homogenizer. The homogenized tissue was centrifuged at 1,000 g and clarified supernatant was centrifuged at 10,000g to pellet mitochondria followed by two wash spins in IB at 10,000 g to obtain a final crude mitochondrial pellet. Light membrane was removed based on the protocol by Wieckowski et al. (236). After a crude pellet was obtained, mitochondria were resuspended in MRB buffer (250 MM mannitol. 5 mM HEPES (pH 7.4) and 0.5 mM EGTA) and further purified in 30% Percoll gradient (vol/vol), spun for 30 min at 95,000 g. Purified mitochondria were isolated with a Pasteur pipette from the bottom of the tube followed by two wash spins at 6,3000 g for 10 min. Mitochondria were resuspended in MRB buffer and stored at -80°C.

Heart tissue: Hearts were dissected, rinsed with buffer A (220 mM mannitol, 70 mM sucrose, 5mM MOPS, 2 mM EGTA and 0.1% BSA, pH 7.4) and minced into small pieces. Tissue was homogenized in a glass-glass dounce homogenizer. Tissue was then centrifuged at 500 g, supernatant was retained, and the pellet was washed and repeated.

Supernatant from both spins were combined at 3,000 g to obtain a final mitochondrial pellet.

MPCs: MPC mitochondria were prepared based upon the protocol by Wieckowski et al. (236). At least 2 x 10^8 cells were harvested, rinsed in cold PBS buffer and resuspended in isolation buffer (225 mM mannitol,75 mM sucrose, 0.1 mM EGTA, and 30 mM Tris-HCl, pH 7.4) containing 20 mg/ml digitonin to permeabilize the outer membrane. After a 25 min incubation on ice, cells were homogenized with a glass-glass dounce homogenizer until >90% of the cells were damaged (determined by trypan blue visualization). Cell debris was removed with two 5 min spins at 600 g followed by a 7,000 g spin for 10 min. The mitochondrial containing pellet was washed in buffer, and spun at 7,000 g, washed and followed by a final spin at 10,000 g. The mitochondrial pellet was stored in MRB buffer at -80°C. Cytosolic proteins were retained from the supernatant after debris removing spins and spun at 100,000 g for 1 hr to separate light membranes. Protein concentration for all isolations was determined by Bradford reagent.

Proteinase K treatment

Mitochondria were isolated from WT mouse liver, with fragmented mitochondria removed from the pellet after the first fast spin. Isolated mitochondria (4 mg/ml) were then treated with 0.5 mg/ml Proteinase K (Macherey-Nagel GmbH and Co. KG) in the presence or absence of 1% SDS for 20 min on ice followed by quenching with 5 mM PMSF.

Mitochondrial subfractionation

Crude liver mitochondria were isolated from two WT mice, and fragmented mitochondria were removed from the pellets after the first fast spin. Pellets were combined and treated as described in (125) with the following modification: 1. The mitoplast fraction was washed

2x in buffer (10 mM KH2PO4 with one-third volume of 10 mM MgCl2) to remove contaminating OMM and2. isolated OMM was resuspended in buffer followed by a second spin at 100,000 g for 1 hr for further purification.

Echocardiography and Epinephrine treatment

Echocardiograms on male *Bid* +/+ (WT) and *Bid*-/- C57BL/6 mice were performed under 2–3% isoflurane anesthesia using an a VisualSonics Vevo 770 instrument housed and maintained in the Vanderbilt University Institute of Imaging Science core lab. Measurements of the left ventricular internal diameter end diastole (LVIDd) and the left ventricular internal diameter end systole (LVIDs) were determined from M-mode tracings in triplicate for each mouse. Mice were echoed before (baseline), and 18 hr (stress condition) and 5 days after (recovery) an IP injection of Epinephrine at 0.5 mg/kg per mouse.

Doxorubicin treatment

Female WT (*Bid*+/+) and *Bid*-/- C57BL/6 approximately 12–18 weeks of age were treated with 3 doses of Doxorubicin at 7.5 mg/kg 5 days apart. Echocardiogram was performed three days after the final dose. Echocardiography was performed using the VEVO2100 digital ultrasound system (Visual Sonics; Toronto, Ontario). Studies were performed using the MS400 18–38 MHz transducer. M-mode images were then processed using the Visual Sonics Software ver2.2. All measurements were made in at least duplicate using the LV trace function.

Histology and fibrosis quantitation

Hearts were excised from mice, weighed, and fixed for a minimum of 12 hr (overnight) in 10% formalin and embedded in paraffin. Coronal sections of hearts were cut and stained using H and E and Masson trichrome blue stain by the Translational Pathology Shared Resource (TPSR) at Vanderbilt University. Trichrome stained slides were scanned at 40X magnification using the Aperio CS2 Brightfield Scanner or whole slide imaging was performed in the Digital Histology Shared Resource at Vanderbilt University Medical Center (www.mc.vanderbilt.edu/dhsr). Representative 2x and 60x, H& E and Trichrome images were acquired on an Olympus BX43 brightfield microscope with a Spot Insight camera.

Aperio Imagescope software version 12.3.28013 was used to define regions of within the left ventricle, excluding edges where stain uptake may have been falsely increased or any visible artifact within the section. Slides were run through a positive pixel algorithm and input parameters were adjusted to detect aniline blue staining and positive pixels are counted and grouped as weak, medium, or strong intensity. Positivity is defined as the total number of positive pixels divided by the total number of pixels in the region of interest.

Multidimensional protein identification technology (MudPIT)

Equal amounts of Bid +/+ and Bid-/- MPC mitochondrial protein were isolated and frozen. Samples were trypsinized and analyzed by MudPIT. MS/MS spectra were identified using SEQUEST software which queried a Uniprot-mouse-reference-canonical_20121112_rev database (Unknown version, 86222 entries). Results were visualized in Scaffold 4.5.1 software (Proteome Software Inc.) and protein identification was limited to two unique peptides per protein and a 5% FDR (false discovery rate) for both peptides and proteins.

For analysis, samples were ranked based upon Fisher's exact test done in Scaffold with a significance value of $p<0.05$. The Mouse MitoCarta 2.0 (237)(Broad Institute) was used to verify genes encoding mitochondrial proteins.

Native-PAGE and In-gel activity assay

Mitochondria from heart and liver tissue were prepared as described. Complexes were extracted based on the protocol by Wittig, et al. (238) and run on native gels followed by incubation with complex specific substrates.

Specifically, mitochondrial protein was extracted with digitonin at a 6.0 g/g detergent/protein ratio for complexes I and IV extraction and 2.5 g/g ratio for complex V. After solubilization, samples were spun at 20,000 g for 20 min. Supernatant was retained and protein concentration was determined by Bradford reagent (BioRAD). Samples were supplemented with 50% glycerol and 5% Coomassie blue G-250 dye. Equivalent protein concentrations were then loaded onto pre-cast NativePAGE 4–16% Bis-Tris gel (Invitrogen by ThermoFisher Scientific). Samples were run at 4°C for 30 min at 100V and 2 1/2 hr at 300V. Cathode and anode buffers per Wittig, et al. For Coomassie band visualization, gels were stained with NOVEX Colloidal blue staining kit (Invitrogen) and destained overnight. All in gel activity assays were performed at room temperature. Complex I was developed in 5 mM Tris-HCl buffer (pH 7.4) supplemented with 10 mg/ml NADH (Roche Diagnostics) and 25 mg of Nitro Blue Tetrazolium (Sigma) for 10 min. Complex IV was developed in 50 mM Sodium Phosphate buffer (pH 7.2) supplemented with 5 mg of Diaminobenzidine (DAB) (Sigma) and 100 ml of horse heart cytochrome c (Sigma) for at least 30 min. Complex V activity was determined by equilibration of native gels in a 35 mM Tris/270 mM Glycine buffer (RPI) (pH 8.3) for 1 hr followed by addition of 14 mM $MgSO_4$ (Fisher), $Pb(NO3)_2$ (Sigma) and 8 mM ATP (Roche), adjusted to pH 8.6

and incubated until a precipitate appeared. Reactions were quenched with fixation in methanol and gels were scanned for quantitation. Quantitation was done on replicate samples (n = 3 WT and *Bid-/-* mice for CI and CIV, n = 4 WT and *Bid-/-* for CV) run on t the same gel for accuracy, however experiments were done a minimum of three independent times. Analysis was done using the gel tool function of ImageJ software and graphs were generated with GraphPad Prism.

High resolution respirometry

MPCs: To determine the basal respiration rate of MPCs, oxygen consumption rates (OCR) were measured in an Oroboros O2K oxygraph (Oroboros Instruments). For each genotype, 2 x10^6 viable cells, determined by trypan blue exclusion, were added to oxygraph chambers containing 2 ml of culture medium. The average OCR was measured over an interval of stable oxygen flux following addition of cells to the chamber.

Cardiac fibers: Initial basal respiration of cardiac myocytes was performed on 2–3 mg of heart fibers extracted from the left ventricle of *Bid* +/+ and *Bid-/-* mice (239). Fibers were prepared in ice-cold relaxation and preservation solution (2.77 mM CaK_2EGTA, 7.23 mM K_2EGTA, 6.56 mM $MgCl_2$, 5.7 mM Na_2ATP, 14.3 mM phosphocreatine, 20 mM taurine, 0.5 mM dithiothreitol, 50 mM K-MES and 20 mM imidazole, pH 7.1). Fibers were permeabilized by incubation at 4°C for 20 min in relaxation and preservation solution containing 50 mg/ml saponin. Fibers were transferred into mitochondrial respiratory solution (MiRO5: 0.5 mM EGTA, 3 mM $MgCl_2$, 60 mM K-lactobionate, 20mM taurine, 10 mM KH_2PO_4, 20 mM HEPES, 110 mM Sucrose, and 1 g/L BSA, adjusted to pH 7.1with KOH) Oroboros O2K oxygraph chambers containing MiRO5 buffer were supplemented with 10mM glutamate, 4 mM malate, and 2 mM ADP. Respiration rate was determined during stabilized oxygen flux.

ATP/O of cardiac fibers: Mitochondrial ATP production and O_2 consumption were determined as described previously (240). Briefly, the left ventricle was excised and placed in ice-cold Buffer X containing (in mM): 7.23 K_2EGTA, 2.77 CaK_2EGTA, 20 Imidazole, 20 Taurine, 5.7 ATP, 14.3 Phosphocreatine, 6.56 $MgCl_2$-$6H_2O$ and 50 MES (pH 7.1, 295 mOsm). Under a dissecting microscope, valves and wall muscle were removed and remaining muscle separated into small bundles and weighed. Less than 3 mg wet weight of tissue was used for each experiment. Fiber bundles were incubated in Buffer X supplemented with 40 mg/ml saponin for 30 min. PmFBs were then washed in ice-cold Buffer Z containing (in mM): 110 K-MES, 35 KCl, 1 EGTA, 5 K_2HPO_4, 3 $MgCl_2$-$6H_2O$, and 5 mg/ml Bovine serum albumin (BSA, pH 7.4, 295 mOsm) and remained in Buffer Z on a rotator at 4°C until analysis (<4 hr).

O_2-equilibrated Buffer Z was supplemented with: 5 U/ml HK, 5 U/ml G6PDH, 5 mM D-Glucose, 2 mM NADP+ and 20 mM Creatine Monohydrate. This buffer permitted coupling of glucose-dependent, HK-catalyzed ATP hydrolysis to G6PDH-catalyzed reduction of NADP+ to NADPH in a 1:1 stoichiometry. To measure ATP synthesis, auto-fluorescence of NADPH (340/460 ex/em) was measured continuously at 30°C simultaneously with O_2 consumption using a customized system integrating monochromatic fluorescence (FluoroMax-4, Horiba Jobin Yvon, Edison, NJ) via a fiber optic cable (Fiberguide Industries) with high-resolution respirometry (Oroboros Oxygraph-2k, Innsbruck, Austria). Complex I-supported respiration was established with glutamate (10 mM) and malate (4mM). ADP (75 mM) was added to determine Complex I-supported ATP synthesis and O_2 consumption. Rotenone (0.5 mM) was added to inhibit Complex I, followed by the addition of succinate (10 mM) to assess Complex II-supported respiration. Rates of ATP synthesis (JATP) were quantified by applying a standard curve generated

from ATP titrations in the presence of the enzyme-coupled system and the respiratory substrates.

For each step of the experimental protocol, JO_2 or JATP were obtained from identical time points and are reported as the mean of >20 s of steady-state data (>10 individual data points). Instrumental background rates (prior to any substrate additions) were subtracted from all subsequent values for JO_2 and JATP and data were normalized to PmFB weight. ATP:O ratio was calculated by dividing the rate of ATP synthesis by the rate of atomic oxygen consumed using the formula: $ATP/O = JATP/(JO_2*2)$

Measurement of cellular ROS and membrane potential

Intracellular ROS was determined by staining MPCs with either 2 mM MitoSOX or 5 mM DHE for 30 min followed by washing and analysis by flow cytometry. As a positive control, cells were also treated with Antimycin A for 1.5 hr prior to staining with MitoSOX. Membrane potential was measured by staining for 30 min with 50 nM TMRE. For Bid-/- + FHA-BidBH3 and Bid-/- + FHA-Bid^{BH3AA} MPCs. Cells were also stained for human CD25 and measurements were obtained from CD25 + cells. All samples were analyzed on a Becton-Dickinson flow cytometer and FlowJo analysis software.

PrediXcan

We performed PrediXcan analysis (229) to evaluate potential roles for Bid in myocardial infarction. PrediXcan proposes gene expression as a mechanism underlying disease risk by testing the genetically determined component of expression for association with disease risk. An observed association implies a likely causal direction of effect from the gene expression trait to disease risk since, as can be reasonably assumed, disease risk does not

alter germline genetic profile. The genetic component of BID expression was estimated from an imputation model (Elastic Net (229)) with mixing parameter a = 0.5) trained on a reference transcriptome data set (the Genotype-Tissue Expression (GTEx) project (226, 228)). Imputation performance for each analyzed tissue was evaluated using 10-fold cross-validation (between imputed expression and directly measured expression), as previously described (229).

The imputation model derived from GTEx left heart ventricle was then applied to genome-wide association study data from BioVU, a Vanderbilt University resource that links human DNA samples and genetic data to de-identified electronic health records (EHRs). The development of BioVU has been previously described (224). We applied PrediXcan on 29,366 individuals (of whom 5146 are MI cases) to impute the genetically determined BID expression and to test for correlation with the phenotype of interest. We performed logistic regression with disease status as the response variable and the inferred genetic component of gene expression as predictor. We also evaluated the patients with the lowest BID expression, that is, in the bottom 5% of the expression distribution and closest to a BID 'knockout', to test for enrichment of MI and to directly validate the observed increased fibrotic damage akin to human MI observed in *Bid-/-* mice. To determine whether the observed association implicated a specific pathophysiology, we applied summary-statistics based PrediXcan (241) with atrial fibrillation using a recently released GWAS data in more than 1 million patients (242). In a secondary analysis, we also tested the other members of the BH3-only Bcl-2 family as well as the BID-interacting protein MTCH2. The connection of MTCH2 with obesity has been explored in the literature (243), prompting us to evaluate the PrediXcan association with BMI using the GIANT Consortium dataset (244).

Comorbidity analysis in the Synthetic Derivative

The Synthetic Derivate consists of approximately 2.8 million de-identified records that contain basic clinical and demographic information of individuals seen at Vanderbilt University Medical Center. This resource was used to determine the number of patients with the following ICD-9 codes as well as their basic demographic information (age, sex, and ethnicity): Burn (949), Headache (784), Myocardial Infarction (410), Cardiomyopathy (425), Hypertension (401.9), Diabetes mellitus (250), Hypercholesteremia (272). Caucasian patient numbers were then used to create a 2 x 2 contingency table binned by age group to determine the relative risk (RR) of each ICD-9 code with MI. Raw RR risk scores and patient numbers are as indicated in the figure.

Replication of gene-level association and search for cardiac phenotype associated regulatory variation

The CARDIoGRAMplusC4D Consortium consists of multiple large-scale genetic association studies (e.g., 14 CAD GWAS studies) of individuals of European descent totaling 22,233 cases and 64,762 controls and a later (larger but more heterogeneous) meta-analysis of GWAS studies of European, South Asian, and East Asian decent totaling 60,801 cases and 123,504 controls. These data provide a resource to identify new SNP associations with coronary artery disease or myocardial infarction and facilitate replication of the gene-level (PrediXcan) associations (156, 245).

BioVU BID coding SNP analysis

The human clinical cohort was derived from BioVU. Genotyping was performed with the Illumina Human Exome BeadChip v1 by the Vanderbilt DNA resources core (VANTAGE) using standard quality control procedures.

Pre-specified clinical syndromes of cardiac injury were heart failure and MI. Phenotypes were defined by extraction of International Classification of Disease (ICD9) billing codes and application of a code translation table used for phenome-wide association scanning (Pews), a validated method of mapping ICD9 codes to clinical phenotypes within the EMR environment (222, 246, 247). Analyses of genotype-phenotype associations from the coding SNPs were performed using the R statistical package. Due to the individual rarity of variants, SNPs were collapsed prior to association testing. Pre-specified SNP groupings were: (1) presence of one or more of any genotyped missense variants in the BID gene, and (2) presence of one or more genotyped SNPs in the MBD. Association testing between SNPs and clinical phenotypes was performed using multivariable logistic regression with age, gender, systolic blood pressure, cholesterol levels, body mass index (BMI), and hemoglobin A1C included as covariates (in the case of heart failure, prior MI was also included as a covariate). A Bonferroni correction was applied to account for multiple testing, resulting in an adjusted p-value for significance of 0.0125. We also utilized the recent meta-analysis of exome-chip studies of MI, involving 42,335 cases and 78,240 controls to replicate the coding SNP associations (248).

Additional statistical methods

Within each experiment, all pairwise comparisons were made by the indicated statistical test and all relevant and significant comparisons are indicated on the figures or in figure legends. All biological replicates (denoted as n) are defined as the same experimental method independently tested on different samples of the same type of cell or mouse model. It should also be noted that one *Bid-/-* mouse was not included in the statistical analysis of echocardiogram data at 18 hr as it was a statistical outlier (Grubbs' outlier test, $p<0.05$).Graphs and statistical analysis were completed using GraphPad Prism software

and the following denote statistical significance: ns = not significant, *p<0.05, **p<0.01, ***p<0.005,****p<0.001. All error bars indicate SEM (standard error of the mean).

*Hematopoietic Methods***

Mice

VavCreBaxBak null mice were generated through crossing $Bax^{F/F}$ $Bak^{-/-}$ mice with *VavCre+* mice. *VavCreBaxBakBid* mice were developed by crossing *VavCre*$Bax^{F/F}$ $Bak^{-/-}$ mice to *Bid-/-* mice. to generate *VavCreBaxBakBid* mice were also crossed with $Ripk1^{K45A}$ mice which harbor loxP sites flanking exon 4 of *Ripk1* (obtained as a kind gift from Peter Gough (197)). Mice were backcrossed 9 generations with C57BL/6J mice from The Jackson Laboratory. Mice were also rederived into a C57/BL6 background from Jackson Laboratories in order to move them into the Vanderbilt barrier facility. The Vanderbilt University Institutional Animal Care and Use Committee approved all experiments (IACUC # M16000037).

For erythropoiesis studies, *VavCreBaxBakBid* mice were also crossed to transgenic $Ripk1^{D138N/D138N}$ mice (obtained as kind gift from Michelle Kelliher (196). $Tet2^{F/F}$ mice (obtained as a kind gift from Omar Abdel-Wahab (249)) were crossed with mice harboring both *VavCre+ and* $Ripk1^{D138N/D138N}$.

Flow cytometry

Stem and progenitor bone marrow characterization: For examination of hematopoietic stem and progenitor cell populations, analysis was performed on whole bone marrow. A power analysis was done to calculate the number of animals needed to analyze from each

***Methods described here correspond to Chapter IV and V and have been published as reference (295)*

genotype. Cell suspensions were obtained by flushing the femurs and tibia with media. Erythrocytes were lysed using erythrocyte lysis buffer (100μM Tris pH 8, 157mM NH_4Cl) and then samples were stained with biotinylated antibodies obtained from BD Pharmingen (as above). The following fluorescent conjugated antibodies were used from eBioscience: CD117 (17-1171), Sca-1 (25-5981), Flt3 (15-1351), CD48 (11-0481), Streptavidin eFluor 450 (48-4317), and CD150 (12-1501). Samples were run on a BD LSRII flow cytometer with FACSDiva software and analyzed using FlowJo software.

For examination of mature populations, single-cell suspensions were obtained from bone marrow and spleen (through filter dissociation). Cells were stained with the following antibodies from BD Pharmingen: CD3 (553062), B220 (553090), CD11b (553311), and Gr-1 (553127). Samples were run on a BD FACScalibur and analyzed using FlowJo.

Intracellular flow cytometry: For intracellular cleaved caspase-3, MPCs were treated as in death assays, collected at designated time points and fixed, permeabilized, and stained per manufacturer's instructions (BD Biosciences). Cells were then stained with rabbit polyclonal Cleaved Caspase-3 antibody (Asp175) (9661; Cell Signaling), followed by anti-Rabbit Alexa Fluor488 (A11008; Invitrogen) Samples were run and analyzed as above.

For intracellular TNFα, single-cell suspensions of bone marrow were obtained and cultured overnight in IMDM 20 WEHI. Cells were re-plated the next day with fresh media and treated with 200ng/ mL lipopolysaccharide (L4391; Sigma) and Golgi Plug per manufacturer's instructions (BD Biosciences) or Golgi plug alone for five hours. Cells were then fixed, permeabilized, and stained with TNFα according to the manufacturer's instructions (554419; BD Pharmingen). Samples were then run and analyzed as above.

Numbers of cells were calculated through back-calculation of percentages from FlowJo analysis to the total number of cells counted when isolated.

For intracellular Ripk1, whole bone marrow was fixed immediately after isolation in 3% PFA/2% Sucrose. After lineage depletion, samples were stained for surface markers at 1:100 (eBioscience as above), permeabilized, and stained for Ripk1 (Cell Signaling Technology, RIP (DC94C12) XP) or isotype control (Cell Signaling Technology, Rabbit IgG) at 1:100 followed by Alexa Fluor 488 anti-rabbit secondary antibody (Invitrogen Molecular Probes) at 1:800. Isotype and secondary only controls were done on marrow combined from all genotypes. Samples were run on the BD LSR Fortessa (150,000 events/sample). LSK and progenitor populations were analyzed for intracellular Ripk1 using FlowJo.

For erythropoiesis evaluation: Single cell suspension of isolated bone marrow and spleens were obtained as described (but without red cell lysis) and cells were immediately counted were counted, diluted and stained for 15 minutes on ice at 1:200 with CD16/CD32 (Fc Block) (553142; BD Pharmingen). Red blood cell surface makers were then added at 1:200 for 30 minutes on ice in the dark. Samples were washed two times and flow was run (without fixation) within approximately an hour of staining. The following antibodies were used? APC Rat anti-mouse CD44 (IM7) (559250; BD Pharmingen), FTIC Rat anti-mouse CD71 (C2) (561936; BD Pharmingen), PE Rat anti-mouse TER-119 (553673; BD Pharmingen). Immediately prior to analysis, samples were stained with Propdium Iodide (P4864; Sigma-Aldrich). Samples were run on a BD LSRII flow cytometer with FACSDiva software, and analyzed using FlowJo software, gating on viable cells. At least 50,000 events per sample were collected.

Colony forming unit assays

Bone marrow and splenocytes were harvested as previously described, and single cell suspensions were lysed for red blood cells and counted. $3x10^5$ bone marrow cells and $5x10^5$ splenocytes were resuspended in MethoCult™ M3134 supplemented with FBS, BSA, SCF, IL3, IL6, EPO, Apo-transferrin, and insulin. Samples were plate in triplicate in 35 mm dishes and incubated at 37°C in 5% CO_2. Plates were counted 48-72 hours after plating to evaluate CFU-E colonies and 10 days after plating to evaluate all other colonies, including BFU-E.

Competitive Reconstitution Assay

Whole bone marrow (femur and tibia) from CD45.2 Bid +/+, *VavBaxBak* DKO, and *VavBaxBakBid* TKO, and CD45.1 *Bid* +/+ mice was isolated, and erythrocytes were lysed as above. Bone marrow was mixed in a 1:1 ratio with *Bid* +/+ CD45.1 bone marrow: CD45.2 experimental bone marrow, then injected retro-orbitally into lethally irradiated CD45.1 *Bid* +/+ mice. Irradiation was performed in two doses five hours apart for total dose of 9 Gy. Approximately 1 million cells were injected after irradiation and reconstitution was examined every 4 weeks beginning at 8 weeks post-transplantation by retro-orbital bleeding and separation of nucleated cells using lymphocyte separation medium. Nucleated cells were stained with antibodies for CD45.1 (553776) and CD45.2 (553772) from BD Pharmingen and analyzed as above. Upon sacrifice, organs were fixed in 10% formalin and were embedded in paraffin.

Secondary transplantation was performed with bone marrow from primary transplanted animals as above. Percent 45.2 positivity was determined and then number of cells needed to have 1:1 ratio with Bid +/+ 45.1 positive cells was calculated. For secondary transplantation of leukemic *VavBaxBak* DKO bone marrow, bone marrow was collected from a leukemic *VavBaxBak* DKO. *Bid* +/+ mice were sub-lethally irradiated at a dose of 5 Gy. Mice were retro-orbitally injected with 5 million leukemic bone marrow cells.

In Vivo BrdU Assay

A power analysis was utilized to determine the number of animals needed to analyze from each genotype. Mice were injected three times with BrdU over the course of 36 hours (once every 12 hours) with a total of 4mg of BrdU (550891; BD Pharmingen) injected. Whole bone marrow was isolated from mice four hours after the last injection and then lineage-depleted using antibodies for CD3, B220, Ly-6G, CD127, and Ter119 from BD Pharmingen (as mentioned above) with Dynabeads (#11035; Life Technologies). All remaining cells were stained for stem and progenitor surface stains from eBioscience (CD117, Sca-1, Flt3, and CD150 as described above) and CD48 from BioLegend (103432). Cells were lastly treated with DNase type I (#D5025; Sigma) for 1hour at 37°C and then stained for BrdU (556028; BD Pharmingen). All remaining cells were run on a LSRII flow cytometer and analyzed using FlowJo software.

LPS injection of mice

Mice were intraperitoneally injected with 1.5 mg/kg LPS (L4391; Sigma) and monitored for at least 6 hours following injection (provided with IP-saline when needed). Animals were sacrificed 18 hours later, and bone marrow, spleen and sternums were harvested for flow cytometry and immunofluorescence analysis respectively.

Immunofluorescence

Mouse bone marrow: Paraffin-embedded samples of whole tibia were fixed in formalin solution (10% formaldehyde) and decalcified before embedding. Embedded sections were stained with either Ripk1 (H-207)(sc-7881; Santa Cruz Biotechnology) with no antigen retrieval required or Cleaved Caspase-3 (9661; Cell Signaling Technologies). Signal was amplified utilizing Fluorescein-conjugated Tyramide Sample amplification kit (SAT701001EA; Perkin Elmer), an Avidin/Biotin blocking kit (SP-2001; Vector Laboratories), and a biotinylated anti-Rabbit antibody (BA-1000; Vector Laboratories). Samples were mounted with Prolong Gold with DAPI (P36941; Life Technologies) or stained with Hoescht (H21492; Life Technologies) and mounted (P10144; Life Technologies).

Mouse spleens: Paraffin-embedded sections of mouse spleen fixed in formalin solution were stained for Ripk1 as described above using Ripk1 (H-207) (sc-7881; Santa Cruz Biotechnology) with antigen retrieval followed by Tyramide sample amplification (Cy5) as described. Images were acquired on a Zeiss upright widefield Axioplan microscope (Hamamastu OCRA-ER monochrome digital camera) with MetaMorph Software. Images were equivalently enhanced using and scale bars added using Adobe

Photoshop. Corresponding H&E sections of spleen (stained by VUMC Translational Pathology Shared Resource) were imaged on an Olympus BX4 microscope (DP72 Olympus camera) using CellSens standard (Version 1.11, Olympus) software.

Mouse Sternums: Sternums were harvested, fixed in 10% formalin, and decalcified with 13% formic acid for 1 hour. Samples were then paraffin-embedded and sectioned approximately 3μm thick. For Ripk1 staining, samples were deparaffinized in xylene, rehydrated in an ethanol series, an antigen retrieval was performed with Sodium Citrate buffer pH 8 for 10 minutes. Samples were quenched with 3% hydrogen peroxide, followed by Biotin and Avidin blocking (SP-2001; Vector Laboratories) and primary Ripk1 antibody (H-207) (sc-7881; Santa Cruz Biotechnology) at 1:120. Biotinylated secondary antibody at 1:1500 was followed by Streptavidin-HRP at 1:100 then Cyanine 5 Tyramide Sample amplification (Cy5 TSA) kit (SAT705A001KT; Perkin Elmer) at 1:250 for 2 minutes in the dark.

For 1L-1β staining, samples were stained as described for with the following exceptions. Antigen retrieval was done for 20 minutes with Sodium Citrate buffer, pH 6. 1L-1β antibody was diluted at 1:500 overnight followed by secondary at 1:1000, Streptavidin-HRP at 1:500 followed by Cy5 TSA at 1:100 for 4 minutes in the dark.

For TNFα staining, samples were deparaffinized as above, blocked for 1 hour at room temperature (1% BSA, 10% Normal goat serum, and 0.3% Triton X-100), and treated with TNFα (ab9739; Abcam) antibody overnight at 7.5 μg/ml followed by anti-mouse AlexaFluor546 secondary (1:1500) for 1 hour. All staining was also done in combination with Ter119 (550565: BD Pharmingen) at 1:50 primary overnight and 1:200 secondary

AlexaFluor488 as well as Dapi. Sternums were imaged on an LSM 710 Meta inverted confocal microscope and evaluated with Zeiss ZEN imaging software.

3T3 cells: WT or *Ripk1-/-* 3T3 cells (a kind gift from Dr. Michelle Kelliher) were grown on coverslips, fixed and permeabilized with 3:1 methanol to acetone, following by peroxidase quench with 3% H_2O_2, Avidin/Biotin blocked (SP-2001; Vector Laboratories) in 2% BSA for 1 hour each, and stained with anti-Ripk1 (H-207) (sc-7881; Santa Cruz Biotechnology), followed by 1:1500 Biotinylated secondary antibody, and TSA Amplification (Cyanine 3 Tyramide Reagent; PerkinElmer) at 1:50 for 2 minutes. Slides were mounted with Prolong Gold with DAPI (P36941; Life Technologies) and imaged on a Zeiss upright widefield Axioplan microscope (Hamamastu OCRA-ER monochrome digital camera) with MetaMorph Software. Images were equivalently enhanced using ImageJ software, and scale bars added with Adobe photoshop.

Human bone marrow: Paraffin-embedded samples of human bone marrow aspirate were stained as above as well as with phosphoMLKL (S358) (Ab187091; Abcam). Samples were imaged on a Nikon AZ100 microscope and images were captured using a Nikon DS-Ri1 color camera or on a Zeiss upright widefield Axioplan microscope (Hamamatsu ORCA-ER monochrome digital camera).

Immunoblot

Cells and tissue were lysed utilizing Lysis Buffer (25mM HEPES pH 7.5, 250mM Sodium Chloride, 2mM EDTA, 0.5% NP-40, 10% Glycerol, 1X Complete Mini Protease Inhibitor, EDTA free (Roche), 10mM β Glycerophosphate, 0.1 mM Sodium Orthovanadate, 10mM Sodium Fluoride, 1mM Sodium Pyrophosphate). Samples were denatured by boiling in

Laemmli Buffer (containing β-mercaptoethanol), and then run utilizing SDS-PAGE.
For MLKL trimerization, cells were lysed as above, and lysates were prepared under nondenaturing conditions or lysates were treated with BMH crosslinker (#22330; Thermo Scientific) for 45 minutes on ice (125 μM in DMSO) and quenched with 50 mM of DTT (D11000; Research Products International) for 10 minutes. Stimulation was completed with LPS as indicated (L4391; Sigma) and treatment with Z-IETD-FMK (550380; BD Pharmingen), Z-VAD-FMK (sc-311561; Santa Cruz Biotechnology), and MG132 (BMLPI102; Enzo Biologicals). The following antibodies were used: Bid (gift from S. Korsmeyer laboratory (78)) or Bid (AF860; R&D Systems), CYLD (GTX100228; GeneTex), Ripk1 (610459; BD Pharmingen), pRipk1 (#31122; Cell Signaling Technology), Ripk3 (NBP1-77299; Novus Biologicals), MLKL (LS-C323026; LifeSpan Biosciences), pMLKL (#37333, Cell Signaling Technology), Caspase-8 (#4927S; Cell Signaling Technology), Cleaved Caspase-8 (Asp387) (#8592S; Cell Signaling Technology), TNFα (ab9739; Abcam), GPx-4 (sc-166570; Santa Cruz Biotechnology), PRX II (sc-515428; Santa Cruz Biotechnology), β-Actin (A5441;Sigma) and GAPDH (FL-335) (sc-25778; Santa Cruz Biotechnology).

Retroviral Transduction

Retroviral supernatants were generated through transient transfection of 293T cells using Fugene (11814443001; Roche) to introduce a FLAG-HA-tagged *Bid* +/+ expression vector with a retroviral packaging vector. Bid was introduced into *BaxBakBid* knockout MPCs by infection and was over-expressed.

Reverse- Transcription PCR to examine Bax and Ripk1 deletion

RNA isolation was completed utilizing Trizol reagent (15596; Invitrogen) from single-cell suspensions of bone marrow and spleen prepared as above. Isolation was completed according to manufacturer's instructions. cDNA was prepared using GoScript Reverse Transcription System (A5000; Promega) or SuperScript III First Strand synthesis system (Invitrogen). PCR was performed using the following Bax primers: Forward: ACAGATCATGAAGACAGGGG and Reverse: CAAAGTAGAAGAGGGCAACC. To confirm knockdown of Ripk1 the following primers were used:
Forward: CCAGACATGTCCTTGGAC and Reverse: GCCCTTCTCCATGTACTC, with an expected band size of approximately 288 base pairs.

CRISPR-Cas9 mediated deletion of Caspase-8

Caspase-8 deletion was performed utilizing the CRISPR-Cas9 system. Two guide RNAs: CCATCGAGGATGCCCAGAAGCT and CCCAAATGTAAGCTGGAAGATG were used to flank and excise CASP8 (MISSION CRISPR; Sigma-Aldrich).
MISSION Lentiviral Packaging Mix (SHP001-0.25 ml; Sigma-Aldrich) and was used to deliver the guide RNA sequences to 293T cells. Lenti CRISPR Universal Non-target control plasmid (pLV-U6g-EPCG) (CRISPR12-1EA; Sigma-Aldrich) was used as a non-specific control.

Human genetic analysis

Comorbidity analysis in the Synthetic Derivative: Comorbidity analysis was performed using the Vanderbilt University Medical Center Synthetic Derivate (consists of approximately 2.8 million de-identified records that contain basic clinical and demographic

information of individuals seen at Vanderbilt University Medical Center). Analysis was done as described in Salisbury-Ruf et al. (231). Also refer to description in mitochondrial methods above. All ICD9 and ICD10 codes used are described in the corresponding figure or supplemental figures. PrediXcan analysis was performed as previously described (231).

Statistical Analysis

All analyses were completed using either GraphPad Prizm (GraphPad Software) or with the help of the Vanderbilt University Medical Center (VUMC) Center for Quantitative Sciences. Analysis of survival curve was determined through Kaplan-Meier log-rank test between all genotypes and DKO versus TKO to examine difference between all genotypes and specifically DKO and TKO. Analysis of cell numbers from mouse experiments (Lymphocyte, progenitor, and stem cell populations) was analyzed by one-way ANOVA to examine differences between genotypes. Examination of percent 45.2 reconstitution in competitive reconstitution assay (Primary and Secondary) was determined by two-way analysis of variance to examine differences in 45.2 reconstitution between genotypes at different timepoints after transplantation. Comparison of necrotic death by transmission electronic microscopy in bone marrow and MPCs was determined utilizing a chi-squared test on the proportions of the type of cell death. Analysis of intracellular cleaved Caspase-3 was completed utilizing a two-way ANOVA to compare differences between genotypes at different timepoints post-stimulation.

Chapter III

BID MAINTAINS MITOCHONDRIAL CRISTAE STRUCTURE AND FUNCTION AND PROTECTS AGAINST CARDIAC DISEASE IN AN INTEGRATIVE GENOMICS STUDY

Data in this chapter are from:

Salisbury-Ruf CT, Bertram CC, Vergeade A, Lark DS, Shi Q, Heberling ML, Forutne NL, Okoye GD, Jerome WG, Wells QS, Fessel J, Moleshi J, Chen H, Roberts LJ 2nd, Boutaud O, Gamazon ER, and Zinkel SS. Bid maintains mitochondrial cristae structure and function and protects against cardiac disease in an integrative genomics study. Elife. 2018 Oct 3;7. piie40907.

Project Contribution: Note that all contributions to experiments shown in each figure are noted in the captions.

Introduction

The critical function for Bcl-2 family proteins during apoptosis transpires at the mitochondria and involves remodeling of both the inner and outer mitochondrial membranes to mobilize cytochrome c and release it into the cytosol. In addition to cell death, mitochondrial membranes can reorganize with changes in metabolic conditions (129, 250). Regulation of the inner mitochondrial membrane (IMM) into highly organized loops known as cristae is necessary for a multitude of metabolic processes (251, 252). Cristae harbor respiratory chain complexes embedded within and peripheral to the membrane and this tight organization is critical for efficient electron transfer (253) and cytochrome c sequestration (81). Inefficient oxidative phosphorylation due to disruption of the respiratory chain can lead to mitochondrial disease, which range widely in organ systems and severity (254–256).

During apoptosis, the BH3-only protein Bid, is cleaved by caspase-8 (cBid) to facilitate both mitochondrial cristae reorganization (20, 94, 138) and outer membrane permeability cBid associates with the multidomain Bcl-2 proteins Bax and Bak through its BH3-domain at the outer mitochondrial membrane (OMM), triggering mitochondrial outer membrane pores (MOMP) (39, 77–79, 256).

Bid's role in regulating cristae structure has been limited to in vitro studies focusing on isolated mitochondria and cBid. cBid's interaction with the mitochondrial membrane is stabilized in part through an interaction with MTCH2 as well as cBid's membrane binding domain (MBD), consisting of alpha-helices 4,5, and 6 (90). Alpha- helix-6 partially embeds within the membrane and has been shown to be necessary for apoptotic cristae reorganization (86, 94).

In addition to its apoptotic function, Bid is also known to be involved in the regulation of other essential cellular processes such as DNA damage and metabolism, acting as rheostat for cell health (Reviewed in (110, 257, 258)). Interestingly, several studies have shown full-length Bid can also localize to the mitochondria (107, 259). These findings are intriguing for several reasons. Firstly, Bid's role in cristae reorganization has been shown to be independent of its BH3-domain and thus canonical Bcl-2 protein-protein interactions (94). Secondly, Bid's structure is unique among Bcl-2 family members in that it more highly resembles Bax in structure. Bax also transiently interacts with the outer mitochondrial membrane in the absence of apoptosis (260). Along with Bax, Mcl-1 and Bcl-XL also reside at the mitochondria have been shown to play critical roles in mitochondrial cristae function and ATP synthase stability respectively (123, 125). We

therefore hypothesized that these observations suggest a potential homeostatic role for Bid at the mitochondria that is independent of cell death.

We tested this idea with an approach that integrates cell biology with human genetic studies (Figure 3-1). We observe that loss of Bid impairs proper cristae formation in the absence of an apoptotic stimulus both in myeloid cells and left ventricular (LV) cardiomyocytes. This function is independent of Bid's caspase-8 cleavage site (D59A), and BH3-domain. We demonstrate decreased respiration in *Bid-/-* cells and decreased respiration coupled with decreased ATP production in LV fibers. These deformations become more pronounced in the heart when it is exposed to various cardiac stressors including Epinephrine and Doxorubicin, in both cases leading to decreased LV function in *Bid-/-* mice. In the case of Epinephrine, these changes correspond to increased cristae damage and fibrosis, phenotypically similar to damage caused by a myocardial infarction (MI) in humans.

Given the known association between mitochondrial dysfunction, especially respiratory chain deficiencies, and heart disorders (261), we use two human genetics approaches to interrogate an association for BID with human cardiac diseases. We first use PrediXcan, which estimates the genetically determined component of gene expression (228, 229), applied to a cohort of Vanderbilt University's de-identified genetic database called BioVU (224). We reveal a highly significant association between decreased BID expression and MI. We also find that patients with the lowest 5% of BID expression have a > 4 fold increase in MI susceptibility. BID's role in cardiac diseases is further validated through an investigation of additional independent cohorts including the large-scale CARDIoGRAMplusC4D GWAS data- sets (156, 245). Secondly, using BioVU exome-chip data, we uncover a gene-level association with MI from low-frequency

nonsynonymous variation. Of significance, coding single nucleotide polymorphism (SNP) M148T lies within Bid's membrane binding domain (MBD), that includes alpha-helix-6. We then demonstrate that the double Bid mutant $Bid^{BH3/M148T}$ fails to support proper mitochondrial respiratory function or restore cristae in *Bid-/-* cells.

The Bcl-2 family member, Mcl-1, has been shown to localize to the mitochondrial matrix ($Mcl\text{-}1^{Matrix}$) and facilitate maintenance of respiratory complexes (125). We also observe a pool of Bid localized to the matrix and find that while WT Bid can interact with $Mcl\text{-}1^{Matrix}$, this matrix association is diminished with Bid^{M148T}. Using PrediXcan, we find MCL-1 and MTX-1, a mitochondrial transporter that associates with the mitochondrial contact site and cristae reorganizing complex (MICOS) (262) are significantly associated with MI, linking susceptibility to MI to two additional genes involved in cristae regulation.

Our study provides an integrative approach, summarized in Figure 3-1, that spans observations in tissue culture and mice to independent human genetics studies providing direct relevance for our findings in human disease. We shed light on the regulation of mitochondrial cristae and consequently oxidative phosphorylation and reveal an important role for Bid's alpha-helix-6 in regulation of mitochondrial function under homeostatic conditions. Furthermore, this approach provides a model for elucidating previously unrecognized proteins that impact complex genetic diseases.

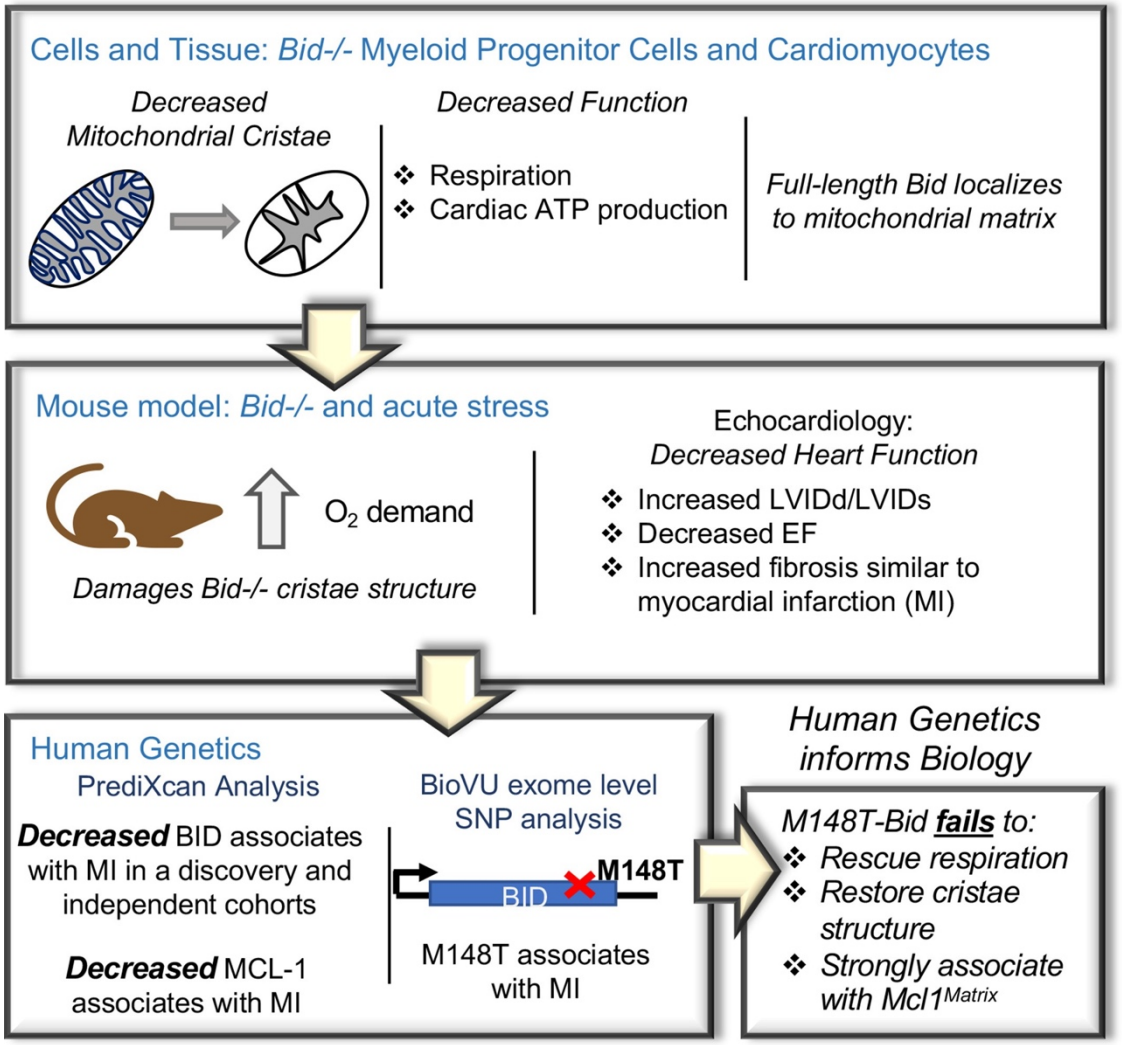

Figure 3-1. An integrated approach combining cells and mice with human genetics uncovers a novel role for Bid in the regulation of mitochondrial cristae. Diagram of the approach used to uncover Bid's novel function in regulating mitochondrial cristae structure. *Bid-/-* myeloid progenitor cell (MPCs) and left ventricular (LV) heart mitochondria have cristae structure abnormalities that result in functional defects. These defects are enhanced under conditions of stress in a *Bid-/-* mouse model. Human genetics analysis using PrediXcan reveals decreased BID gene expression associated with MI and BID exome level variation identifies coding SNP M148T, which is directly linked to Bid's mitochondrial function. This SNP fails to restore cristae structure, respiration, and association with Mcl-1^{Matrix}.

Results

Bid-/- cells have a cristae defect that can be rescued with BH3-mutated or D59-mutated Bid

Consistent with a pro-survival function, *Bid-/-* myeloid progenitor cells (MPCs) display decreased growth rates not due to altered proliferation, but instead as a result of decreased viability ($p<0.05$) (Figure 3-2). Given the critical apoptotic role for Bid at the mitochondria, we evaluated mitochondrial structure in *Bid-/-* MPCs by transmission electron microscopy (TEM) (Figure 3-3A, B and Figure 3-4A). Compared to *Bid* +/+ MPCs, mitochondria in *Bid-/-* MPCs were highly abnormal. Quantitation of the average number of cristae per mitochondrion revealed a significant decrease in the number of cristae in *Bid-/-* MPCs compared to *Bid* +/+ MPCs ($p<0.0001$) (Figure 3-3C). This function is independent of Bid's apoptotic role, as *Bid-/-* MPCs stably expressing Flag-HA-tagged full-length Bid mutated in either in its BH3-domain (FHA-Bid^{BH3}) or caspase-8 cleavage site D59 (FHA-Bid^{D59A}) could rescue cristae structure ($p<0.0001$) (Figure 3-3C). Furthermore, quantitation of the area density of mitochondria per cell revealed a slight decrease in density in the *Bid-/-* cells compared to *Bid*+/+ cells ($p<0.05$), while FHA-Bid^{D59A} expressing cells had increased mitochondrial density compared to all other cell lines (Figure 3-3D).

Several groups have reported that cleaved Bid (cBid) reorganizes cristae (20, 94) or Bid BH3-peptide narrows cristae junction size (21) in the presence of isolated mitochondria. Given that myeloid cells have high endogenous protease activity, we anticipated that reintroduction of WT FHA-Bid into *Bid-/-* MPCs by retroviral transduction may not rescue mitochondrial structure (Figure 3-3 A-D). Indeed,

overexpression of full-length WT Bid (*Bid-/-* + FHA Bid) but not FHA-Bid^{BH3} or FHA-Bid^{D59A} results in the production of endogenous cBid in the absence of a death stimulus (Figure 3-3E). Thus, in a myeloid cell line, we observe that Bid's apoptotic domains must be mutated to fully restore cristae.

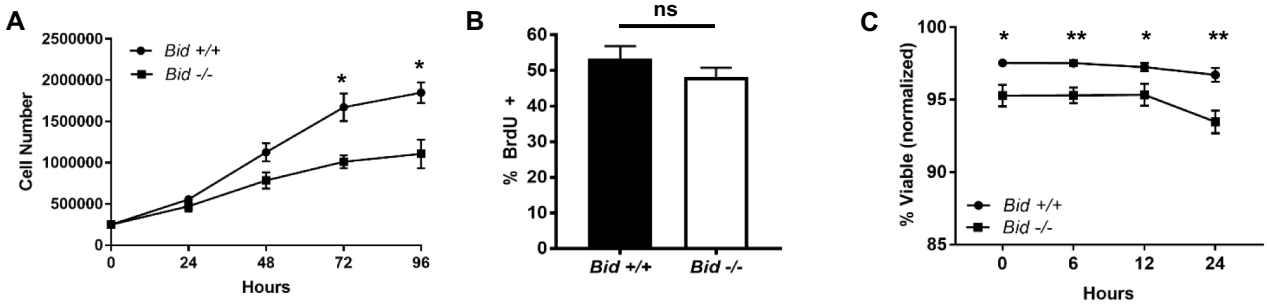

Figure 3-2. Loss of Bid results in increased cell death in the absence of an apoptotic stimulus. (A) *Bid* -/- MPCs display decreased growth rates (n=4) but not proliferation rates (B) in complete media (n=3). (C) Viability assay of *Bid* +/+ and *Bid-/-* cells in complete media (n=7). Data were normalized to no treatment. P-values were determined by unpaired Student's t-test for A-C. Error bars indicate +/- SEM for all data. ns=not significant, *p<0.05 and **p<0.01. Contribution: All experiments shown performed by Salisbury-Ruf CT.

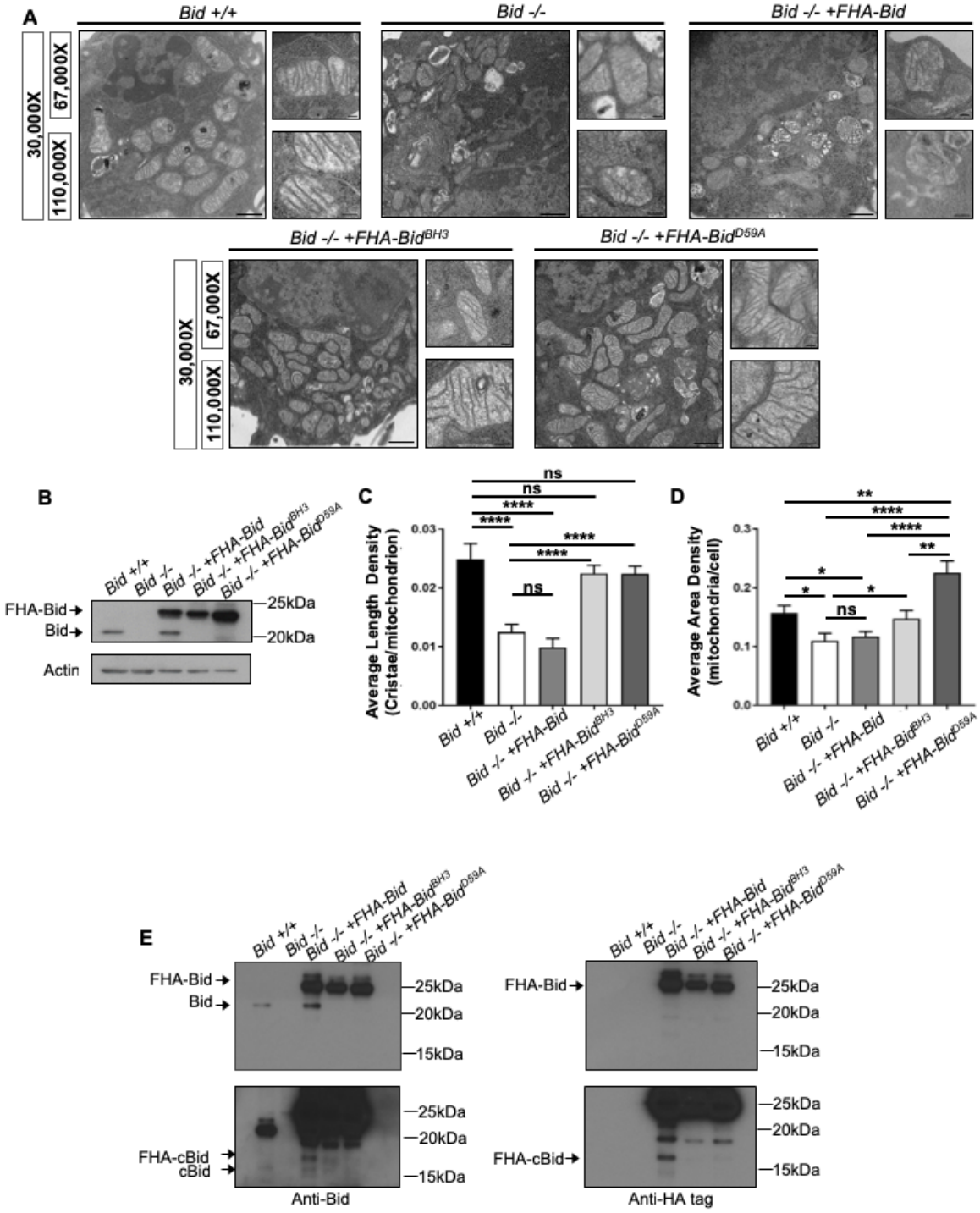

Figure 3-3. The Bcl-2 family protein Bid is required for normal mitochondrial cristae formation, independent from its apoptotic function. (A) Transmission electron microscopy (TEM) of mitochondria from MPC cell lines including: *Bid* +/+ (WT), *Bid-/-, Bid-/- + FHA* Bid, *Bid-/- + FHA-Bid*^{BH3} and *Bid-/- + FHA-Bid*^{D59A}. Representative images at 30,000X (scale bar = 500 nm), 67,000X and 100,000X magnification (scale bar = 100 nm). (B) Western blot of expression levels of Bid for the indicated genotypes. Note that

Figure 3-3. Continued
full-length Bid is observed in *Bid-/-* + *FHA* Bid cells due to cleavage of the FlagHA-epitope tag. (C) Quantitation of the number of cristae per mitochondria (represented by the average length density) and (D) the mitochondrial density per cell (represented by the average area density) of the MPC lines shown in (A). A total of 40 images were quantified at 30,000X for each cell line. (E) Western blot of Bid (left) and HA-tag (right) indicating increased presence of cleaved Bid (cBid) in *Bid-/-* + *FHA* Bid cells (lower blots are darker exposure). FlagHA-tagged expressing cells were loaded for equal Bid expression. P-values were determined by one-way ANOVA ($p<0.0001$) with unpaired Student's t-test (C, D). Error bars indicate ±SEM for all data. ns = not significant, *$p<0.05$, **$p<0.01$, ***$p<0.001$, and ****$p<0.0001$. Contribution: All experiments shown performed by Salisbury-Ruf CT with TEM quantitation methodology assistance from Jerome WG.

We next analyzed expression of other BH3-only apoptotic proteins as we anticipated they may be upregulated in the absence of Bid and considering the known role of Bim in disassembly of mitochondrial Opa-1 oligomers (21). We evaluated *Bid-/-* cellular extracts as well as lysate from left ventricular (LV) cardiac tissue which are highly enriched in mitochondria, and find no compensatory upregulation of Bim, Bad, or Puma to account for the observed loss of cristae structure in *Bid-/-* cells (Figure 3-3 B, C).

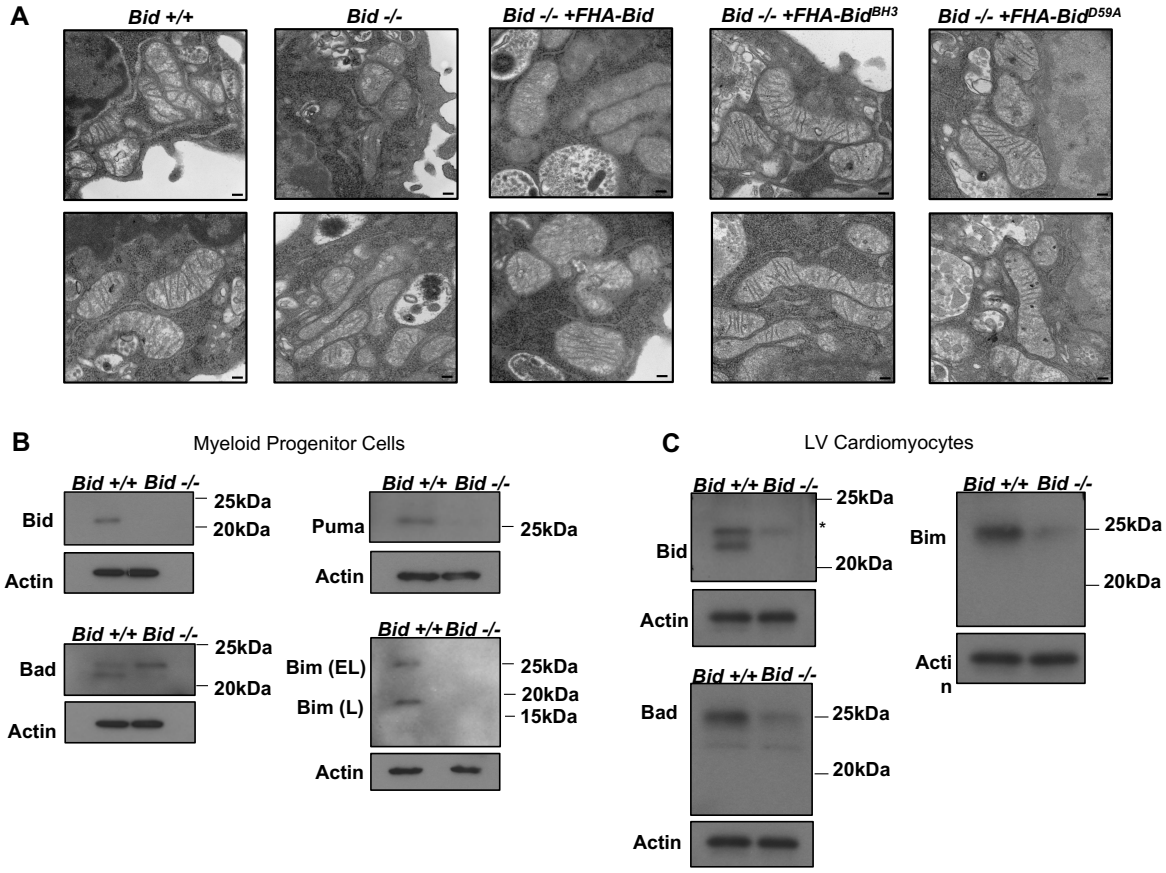

Figure 3-4. Loss of Bid results in a mitochondrial structural defect not compensated for by upregulation of Bad, Puma, or Bim. (A) Transmission electron microscopy images of the indicated MPC cell lines. Images were taken at 67,000X, scale bar =100 nm. (B) Western analysis of BH3-only proteins including Bad, Puma, and Bim from *Bid* +/+ and *Bid-/-* MPCs or (C) LV Cardiomyocytes. Loss of Bid does not lead to a compensatory increase in expression of these apoptotic proteins. * indicates cross reacting band. Contribution: All experiments shown performed by Salisbury-Ruf CT.

Full-length Bid localizes to multiple-mitochondrial subcompartments in the absence of cell death

It has previously been shown that full-length Bid can localize to mitochondria in the absence of an apoptotic stimulus (107, 259). To confirm this result, we first evaluated Bid in subcellular fractions of *Bid-/-* and WT MPCs. We find full-length Bid in a heavy

membrane, mitochondrial-enriched fraction absent of cytosolic contamination (Figure 3-5A). We also observe full-length Bid in mitochondria isolated from liver tissue, both in a crude mitochondrial fraction as well as in a Percoll purified fraction (Figure 3-5B).

To determine the submitochondrial localization of full-length Bid, isolated liver mitochondria were treated with Proteinase K (PK) in the presence or absence of SDS. We observe that a pool of Bid remains uncleaved with PK, under conditions in which we observe cleaved Bak (Figure 3-5C), a protein associated with the OMM. Furthermore, we used an osmotic shock approach to separate and enrich for OMM and mitoplast (inner membrane and matrix containing fractions) from isolated liver mitochondria. We find an enrichment of Bid in the mitoplast-containing fraction compared to the OMM (Figure 3-5D). Taken together, the above results suggest that full-length Bid can localize to the mitochondria during non-apoptotic conditions and is found both at the OMM as well as in the mitoplast.

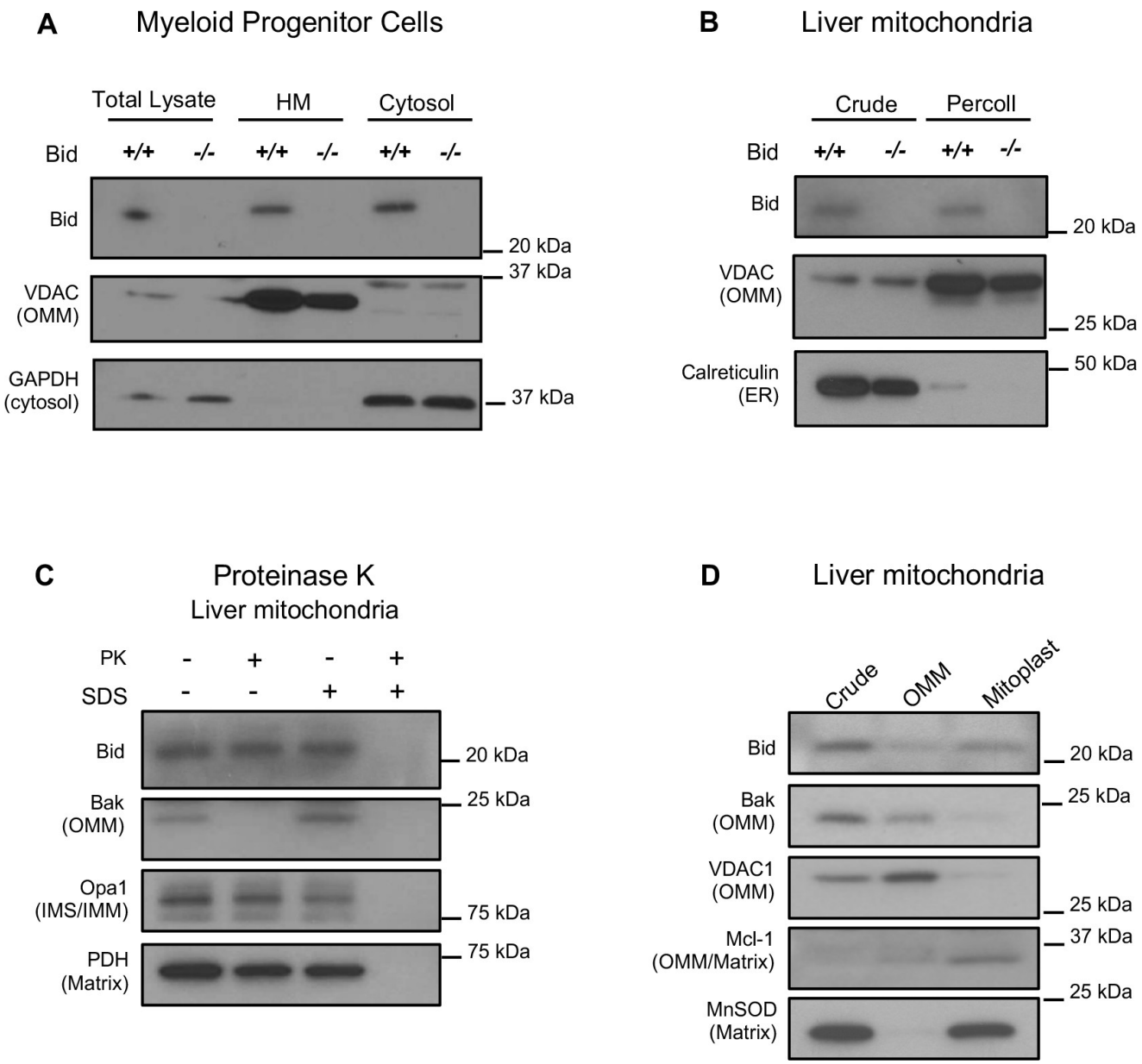

Figure 3-5. Full-length Bid localizes to the mitochondria in the absence of apoptosis and is found within a mitoplast fraction. (A) Subcellular fractionation of WT and *Bid-/-* MPCs showing whole cell lysate (WCL), a mitochondrial- containing heavy membrane (HM) (VDAC) and cytosolic fraction (GAPDH). (B) Crude and Percoll purified liver mitochondria from WT and *Bid-/-* mice shows the presence of full-length Bid in the purified fraction in the absence of light membrane contamination. (C) Proteinase K (PK) treatment of isolated liver mitochondria reveals Bid in a PK resistant fraction. (D) Crude liver mitochondria from WT mice were fractionated into OMM and mitoplast (IMM/ matrix) containing fractions and probed for OMM and matrix markers. Full-length Bid can be observed in the mitoplast rich fraction. OMM = outer mitochondrial membrane, IMS = inner membrane space, IMM = inner mitochondrial membrane. Contribution: All experiments shown performed by Salisbury-Ruf CT.

Bid-/- mice have abnormal left ventricular mitochondrial cristae exacerbated by acute cardiac stress

Mitochondria cristae defects in humans can result in severe abnormalities in multiple organ systems, especially the heart (263, 264). We were interested to know if *Bid-/-* mice also display cristae abnormalities beyond myeloid cells. TEM of left ventricular tissue isolated from *Bid-/-* mice revealed striking irregularities both in gross mitochondrial organization between myofibrils as well as loss of normal lamellar cristae structure (Figure 3-6A). Specifically, without treatment, *Bid-/-* tissue had overall decreased mitochondrial electron density corresponding to significantly increased cristae width ($p<0.0001$) (Figure 3-6B). To test how *Bid-/-* mice respond to an acute stress, we used Epinephrine (Epi) to increase the energetic demand on the mitochondria. We assessed both *Bid+/+* and *Bid-/-* mitochondria 18 hours after a dose of 0.5 mg/kg Epi and find that while both *Bid+/+* and *Bid-/-* tissues are damaged, the *Bid-/-* cristae are significantly more deformed ($p<0.0001$) (Figure 3-5A, B). Interestingly, these damaged cristae are structurally similar to mitochondria observed after induction of an acute myocardial infarction (MI) (265). Thus, *Bid-/-* mice have a severe cardiac cristae defect that results in increased susceptibility to acute stress-induced damage.

Acute cardiac stress results in a functional defect in Bid-/- mice

To determine whether the mitochondrial cristae defect in *Bid-/-* mice translates to decreased cardiac function, we performed echocardiograms on mice. In the absence of a clear mouse model of heart failure (266), we chose Epi as an acute pharmacological stress due to the fact it causes both a rise in blood pressure with increased left ventricular (LV) afterload as well as increased myocardial contractility (267). This results in maximal

oxygen demand with potential to reveal a phenotype driven by mitochondrial dysfunction.

Bid+/+ and *Bid*-/- mice were evaluated at baseline (without treatment), 18 hours after acute-intraperitoneal (IP) Epi (0.5 mg/kg), and 5 days after Epi treatment to evaluate recovery. Cardiac function does not differ at baseline. However, we find a significant increase in left internal ventricular diameter during diastole (LVIDd) ($p<0.01$) as well as during systole (LVIDs) ($p<0.05$) 18 hours after Epi (Figure 3-6C, D). This corresponds to a significant decrease in Ejection Fraction (EF) for *Bid*-/- mice ($p<0.01$) (Figure 3-6E) and a trend for decreased fractional shortening (FS) ($p=0.1564$) (Figure 3-7A). Furthermore, we also observe an increase in both end diastolic ($p<0.01$) and end systolic volume ($p<0.05$) (Figure 3-6 F, G) with stress. This is consistent with our findings by EM indicating a decreased ability of *Bid*-/- hearts to maintain proper mitochondrial structure under stress. Decreased LV cardiac function observed in *Bid*-/- mice is phenotypically similar to observations made by echo in patients during the acute phase of MI (LV wall dilation and decreased ejection fraction) (268). Interestingly, at 5 days post-Epi, both the *Bid*+/+ and *Bid*-/- mice had restored cardiac function and we find no difference in heart weights at sacrifice (Figure 3-6 C-G, Figure 3-7B).

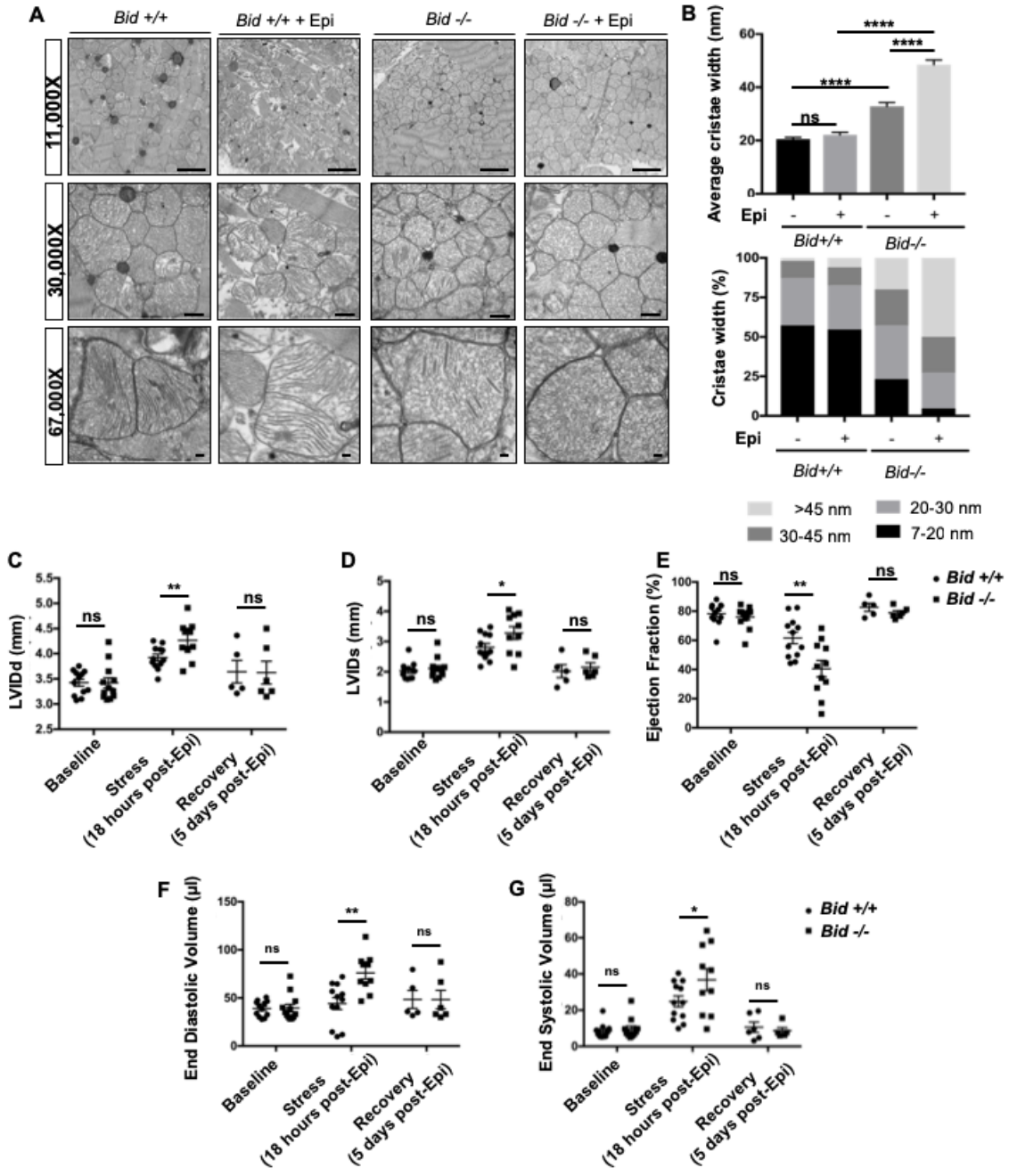

Figure 3-6. Left ventricular cardiomyocytes from *Bid-/-* mice have abnormal cristae, which are structurally and functionally exacerbated with acute Epinephrine stress. (A) Transmission electron microscopy (TEM) of left ventricle cardiomyocyte mitochondria from *Bid* +/+ and *Bid-/-* 18 hours with or without 0.5 mg/kg Epinephrine treatment. Representative images at 11,000X (scale bar = 2 *m*m), 30,000X (scale bar = 500 nm), and 67,000X (scalebar = 100 nm). (B) (Top) Quantitation of average cristae width (nanometers) corresponding to (A). n = 150 cristae per genotype, measured at 67,000X. (Bottom) Percent of cristae corresponding to the indicated widths (nm). (C) Echocardiogram analysis of left-ventricular internal diameter diastole (LVIDd, mm) and (D) LVID systole (LVIDs, mm) of *Bid* +/+ and *Bid-/-* mice at the indicated

Figure 3-6. Continued
time points. (E) Ejection fraction (%) from *Bid* +/+ and *Bid-/-* mice without treatment (Baseline), 18 hr after 0.5 mg/kg Epinephrine, and 120 hr post Epinephrine (recovery). (F) End diastolic volume (*m*l) and (G) End systolic volume (*m*l) at the indicated time points. n = 12, 12, 5 *Bid* +/+ mice and n = 12, 10, 6 for *Bid-/-* mice for baseline, 18 hr, and 120 hr time points, respectively for (C–G). P-values were determined by one-way ANOVA with unpaired Student's t-test (B), and unpaired Student's t-test (C–G). Error bars indicate ± SEM for all data. ns = not significant, *p<0.05, **p<0.01 and ****p<0.0001. Contribution: All experiments shown performed by Salisbury-Ruf CT with TEM assistance by Mary Dawes (Panel A), and echocardiography and experimental design assistance by Fortune NL and Fessel J (Panels C-G).

Lastly, we also employed an additional pharmacological myocardial stress in the form of Doxorubicin (Dox) (3 doses of 7.5 mg/kg), a chemotherapy drug with heart mitochondrial toxicity (269). Dox also resulted in a significant decrease in FS and EF (p<0.01) (Figure 3-7C, D) in *Bid-/-* mice. Thus, using two different models, Epinephrine, which directly results in increased oxygen demand, as well as the mitochondrial toxic drug Doxorubicin, we find that Bid plays a role in maintaining LV function under stress.

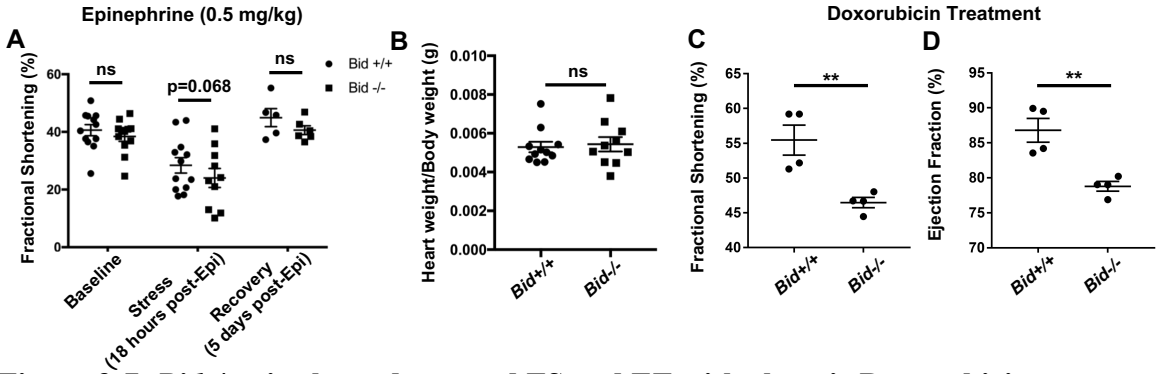

Figure 3-7. *Bid-/-* mice have decreased FS and EF with chronic Doxorubicin.
(A) Fractional shortening (%) from mice corresponding to Figure 4. (B) Heart weight to body weight ratio from mice in Figure 4. (C) Fractional shortening (%) from *Bid* +/+ and *Bid-/-* mice after 3 doses of 7.5 mg/kg of Doxorubicin every 5 days (n=4 mice per group). (D) Ejection fraction (%) of Doxorubicin treated mice as in C. Measurements for FS and EF were made in at least duplicate using the LV trace function using the Visual Sonics Software ver2.2. P-values were determined by two-way ANOVA with unpaired Student's t-test A and unpaired Student's t-test B-D. Error bars indicate +/- SEM for all data. ns=not significant, * p <0.05, **p<0.01. Contribution: All experiments shown performed by Salisbury-Ruf CT with assistance by Fortune NL (Panel A) and Okoye GD and Moslehi J (Panels B-D).

Bid-/- hearts have increased fibrotic damage after acute stress, similar to post-MI damage observed in human patients

Myocardial fibrosis due to cardiomyocyte remodeling after damage is a prominent sequelae of MI, and directly contributes to loss of cardiac function (270). To determine the extent of fibrotic damage, we used Masson's trichrome staining and quantitatively evaluated whole heart tissue sections (Figure 3-8). We find that *Bid-/-* tissue has significantly increased fibrosis both at the 18 hour and the recovery time point, 5 days post treatment ($p<0.05$) (Figure 3-8 B, C). Interestingly, WT mice display no increase in fibrosis at 18 hours post-Epi; fibrosis developed in WT hearts at 5 days post-Epi. Thus, *Bid-/-* mice have more fibrosis and increased susceptibility to damage after stress. This result recapitulates the response to cardiomyocyte damage in human MI and suggests that although the *Bid-/-* mice are able to recover functionally, the long-term damage is more severe.

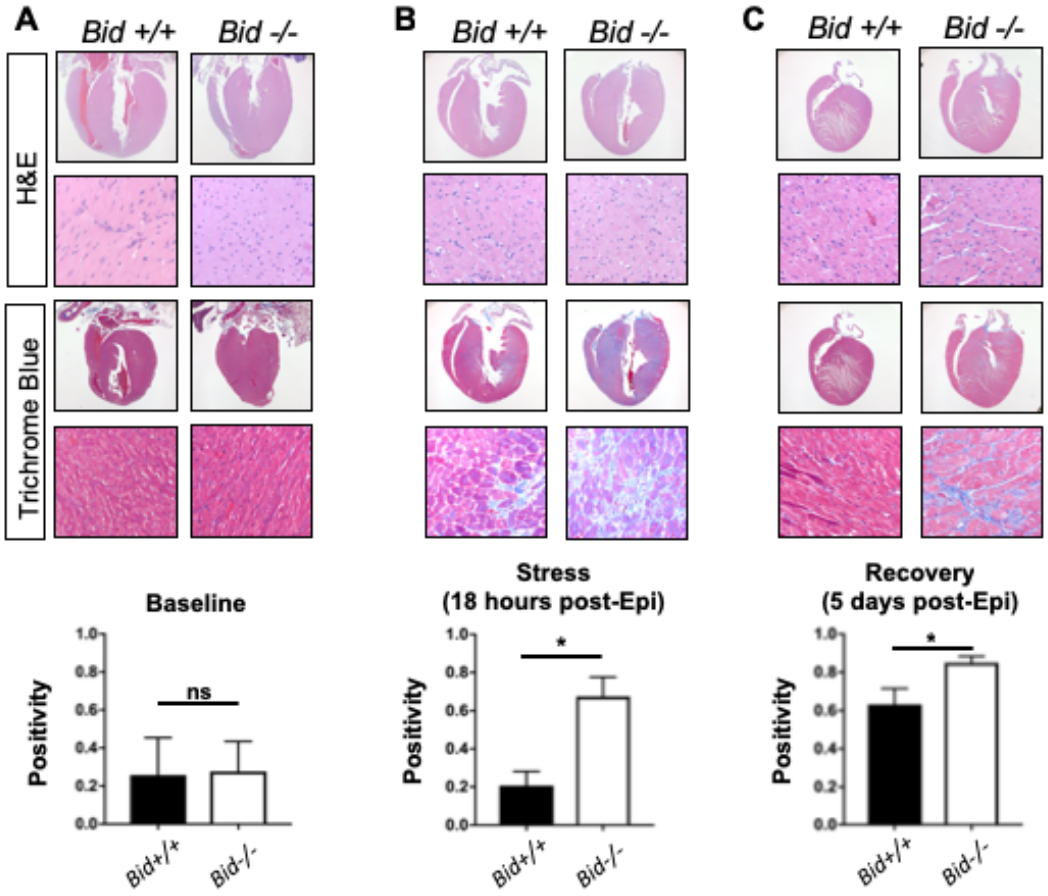

Figure 3-8. Epinephrine stress results in increased fibrotic damage in *Bid-/-* hearts. (A) Representative images of H and E staining of *Bid*+/+ and *Bid-/-* hearts (top) and Masson's Trichrome staining (bottom) without treatment. Quantitation of the Trichrome positivity (Total positive pixels/Total pixels), n = 3, 3 respectively. (B) H and E and Masson's Trichrome 18 hours after Epinephrine (0.5 mg/kg) with quantitation as in (A), n = 4, 3. (C) H and E and Masson's Trichrome 5 days after Epinephrine (0.5 mg/kg) with quantitation, n = 6,6. P-values were determined by unpaired Student's t-test. Error bars indicate ± SEM for all data. ns = not significant, *p<0.05. Contribution: All experiments shown performed by Salisbury-Ruf CT with staining assistance by TPSR (see Methods) and quantitation methodology assistance by Fortune NL.

Loss of Bid results in decreased respiratory complex subunits and ATP synthase dimer activity

The structural and functional defects observed in *Bid-/-* mitochondria suggested that defects in cristae were directly impacting the function of the electron transport chain (ETC). To determine if the loss of Bid specifically disrupted ETC complexes or proteins

involved in maintenance of cristae, such as ATP synthase, we took a proteomics approach. Using Multidimensional Protein Identification Technology (MudPIT) on equal concentrations of isolated mitochondrial protein from *Bid* +/+ and *Bid*-/- MPCs (Figure 3-9A). We identified a total of 3,258 proteins that mapped to unique Entrez gene identifiers. Cross referencing our hits to the Mouse MitoCarta 2.0 (237), we identified 54 significantly different mitochondrial proteins between the *Bid*+/+ and *Bid*-/- samples (Figure 3-8 B, C).

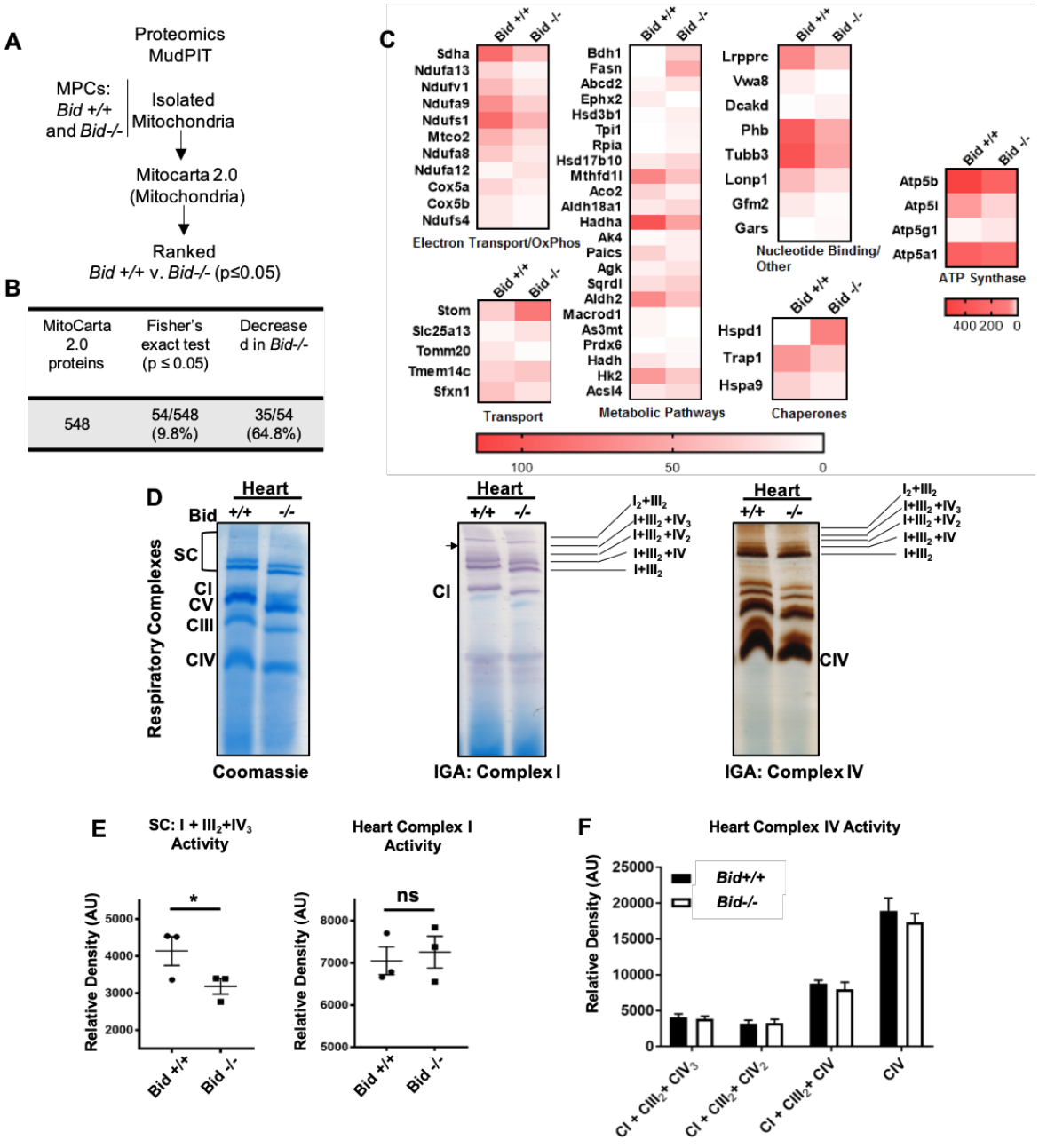

Figure 3-9. *Bid-/-* MPC mitochondria have a decreased CI proteins and decreased activity, but no difference in CIV activity.

(**A**) MudPIT analysis workflow on isolated MPC mitochondria. (**B**) Summary of results revealing 54 significantly different mitochondrial proteins different by Fisher's exact test ($p < 0.05$). (**C**) Heat map highlights spectral count differences between identified cristae-related proteins. Scale indicates no spectral counts (white) to high spectral counts (red). (**D**) Representative Coomassie stained gradient native gel of equivalent amounts of *Bid* +/+ and *Bid* -/- heart mitochondria protein (left), in-gel activity (IGA) assay for Complex I (middle, arrow denotes significantly different complex activity), and in-gel activity for

Figure 3-9 Continued.
Complex IV (right). CI=Complex I, CIII = Complex III, CIV= Complex IV, CV=Complex V, and SC=supercomplexes. (**E**) Quantitation of in-gel activity assay for CI respiratory complexes In *Bid*+/+ and *Bid-/-* hearts, arbitrary units, n=3 per gel (representative of 4 independent runs). **(F**) Quantitation of in-gel activity assay for all CIV respiratory complexes In *Bid*+/+ and *Bid-/-* hearts, arbitrary units, n=3 per gel. P-values were determined by unpaired Student's t-test for **E**. Error bars indicate +/- SEM for all data. ns=not significant, * p <0.05. Contribution: All experiments shown performed by Salisbury-Ruf CT with MudPIT assistance by Mass Spectrometry Research Center (MSRC).

Of our 54 mitochondrial hits, we found 11 subunits of respiratory chain components, including complex I, II, and IV, as well as 4 subunits of the ATP synthase complex, that were significantly decreased in *Bid-/-* MPCs. Furthermore, we also identified decreased mitochondrial transport proteins as well as some metabolic proteins (Figure 3-9 C). These findings suggest that loss of cristae structure impacts mitochondrial function on multiple levels and prompted us to further investigate the contribution of individual respiratory complexes to mitochondrial function.

To more closely interrogate the respiratory chain, we analyzed enzymatic activities of the specific respiratory complexes by isolating mitochondria from heart tissue of age matched *Bid* +/+ (WT) and *Bid-/-* mice. We then resolved digitonin-extracted complexes using gradient Native-PAGE, stained with Coomassie blue, and treated with complex-specific substrates to measure enzymatic activity. We observe a decrease in the activity of ATP synthase dimers from *Bid-/-* heart mitochondria ($p<0.05$) (Figure 3-10 A, B), consistent with the known association between dimerization of ATP synthase in cristae loop formation and stabilization of cristae structure (140, 271).

Enzymatic activity of additional respiratory complexes and supercomplexes were also evaluated including Complex I (CI) and complex I V (CIV). We observed a significant decrease in the activity of complex I within the SCs and a trend for decreased

activity of complex I V containing SCs (Figure 3-9 D-F). Overall, these results are consistent with a role for Bid in maintenance of cristae structure linked to respiratory chain function.

Bid -/- MPCs display decreased respiration

We next measured respiration directly from *Bid-/-* MPCs and LV fibers. Using an Oroboros Oxygraph, we found *Bid-/-* MPCs displayed significantly decreased oxygen consumption rates (OCR) compared to *Bid+/+* cells (p=0.008), consistent with a cristae defect. Respiration could be restored in *Bid-/-* MPCs by re-introduction of FHA-Bid^{BH3} and FHA-Bid^{D59A} but not FHA-Bid into *Bid-/-* MPCs (*Bid-/-* v. *Bid-/-* + *FHA-Bid^{BH3}*, p<0.0001 and *Bid-/-* v. *FHA-Bid^{D59A}*, p=0.0008) (Figure 3-10 C).

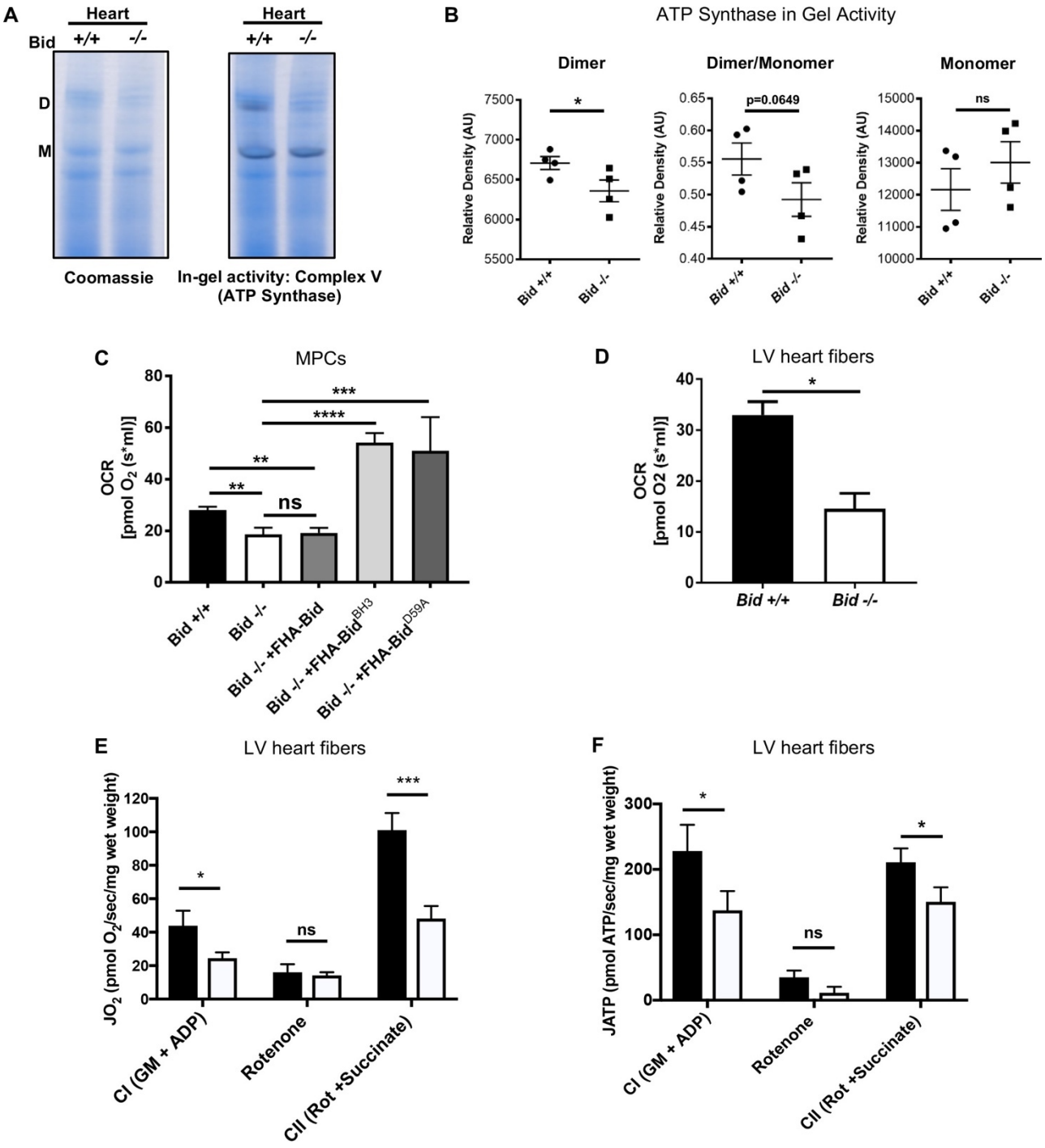

Figure 3-10. Loss of Bid results in decreased ATP-synthase activity and respiration. (A) Representative native gel (left) and in-gel activity (IGA) assay (right) for Complex V (ATP synthase) from isolated Bid +/+ and Bid-/- heart mitochondria, D = dimer and M = monomer of ATP synthase. (B) Quantitation of IGA assay for heart CV activity as measured by the relative density of indicated dimer and monomer bands (arbitrary units), (n = 4). (C) Oxygen consumption rate (OCR) was measured in an Oroboros Oxygraph in

Figure 3-10. Continued
complete IMDM media on equivalent numbers of indicated cells (2 x10^6) (n = 7,7,4,3,3 respectively). (D) State 3 respiration of saponin permeabilized left ventricle cardiac fibers from Bid +/+ and Bid-/- mouse hearts in MiRO5 respiration medium supplemented with glutamate, malate, and ADP (n = 3). (E) Oxygen consumption (JO_2) of permeabilized left ventricular cardiac fibers from Bid+/+ and Bid-/- mice in the presence of indicated metabolic substrates. G = glutamate, M = malate, CI = Complex I, CII = Complex II, Rot = Rotenone (n = 6,6 respectively). (F) Simultaneous ATP synthesis in presence of metabolic substrates as in (E). P-values determined by unpaired Student's t-test (B), (D), one-way ANOVA ($p<0.0001$) with unpaired Student's t-test (two-way) for (C), and two-way ANOVA ($p<0.01$) with unpaired Student's t-test for (E) and (F). Error bars indicate ±SEM for all data. ns = not significant, *$p<0.05$, **$p<0.01$, ***$p<0.001$, and ****$p<0.0001$. Contribution: All experiments shown performed by Salisbury-Ruf CT with contribution from Bertram CC (Panel C) and assistance with experimental design by Fessel J (Panel C-D) and Lark DS (Panel E-F).

Despite decreased oxygen consumption, one possible explanation for the observed mitochondrial defects in *Bid-/-* cells could be damage from the generation of reactive oxygen species (ROS). We assessed baseline mitochondrial and cellular superoxide with MitoSOX and DHE, respectively, and found no difference between *Bid-/-* and *Bid +/+* MPCs, however mitochondrial superoxide was increased in *Bid-/-* cells under conditions of nutrient withdrawal ($p<0.01$) (Figure 3-11 A, B and C).

Bid's phosphorylation sites S61 and S78 (Bid^{AA}) have also been shown to correspond with increased ROS and respiration in hematopoietic stem cells (93, 259). Additionally, it was shown that truncated Bid (tBid) residues 57–73 had strong binding to MTCH2 (92). To determine if these phosphorylation sites are involved in full-length Bid's regulation of cristae function, we made both S61A and S78A point mutations in BH3-mutated Bid followed by stable re-introduction into *Bid-/-* MPCs (*Bid-/- + FHA-*Bid^{BH3AA}). Interestingly, we find that even in the context of a BH3-mutant, these cells were highly unstable, which we attribute in part to the important role of these

phosphorylation sites in the DNA damage response (36, 100) as well as preventing cleavage of Bid and thus initiation of apoptosis (106).

We measured TMRE and MitoSOX by flow cytometry, gating on cells positive for human CD25 (co-expressed with FHA-Bid). We find that compared to Bid^{BH3}, FHA-Bid^{BH3AA} MPCs do not have altered membrane potential and show only a trend for increased ROS ($p=0.1956$) (Figure 3-11 D, E). Thus, our results in MPCs are most consistent with a role for these phosphorylation sites in overall cell viability, by preventing caspase-8 cleavage of Bid (106), rather than specifically in the regulation of mitochondrial membrane potential or ROS production.

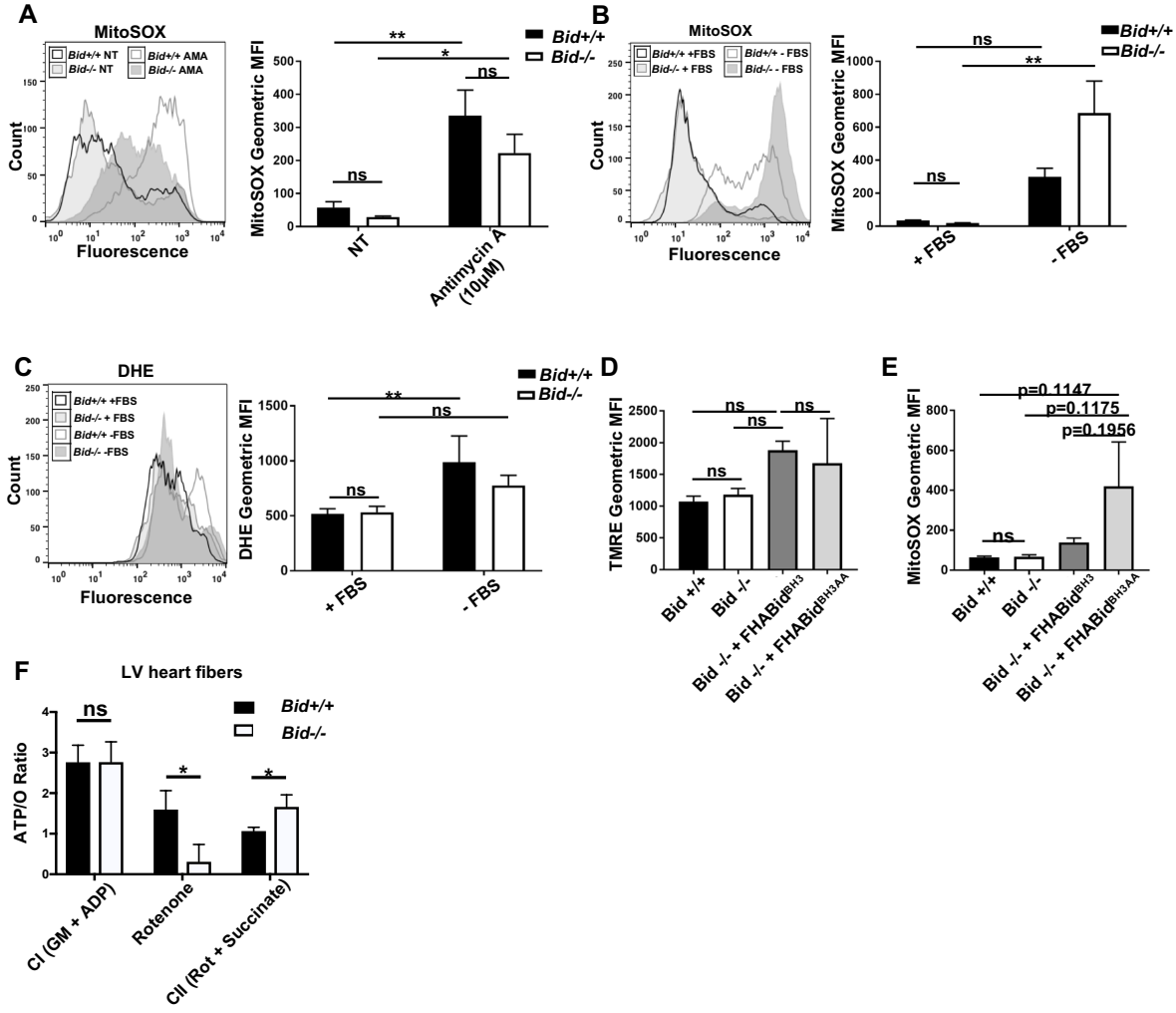

Figure 3-11. *Bid-/-* MPCs maintain their membrane potential and do not generate increased ROS

(A) *Bid*+/+ and *Bid-/-* MPCs were cultured for 24 hours in complete media (no treatment=NT) or treated with10 μM Antimycin A (AMA) as a positive control for the last two hours followed by staining with 2 μM MitoSOX for mitochondrial ROS. Data are represented as geometric mean fluorescence intensity (MFI). NT n=7,6 and AMA n= 6,6 for *Bid*+/+ and *Bid-/-*, respectively. (B) *Bid* +/+ and *Bid-/-* MPCs were subjected to serum withdrawal for 24 hours and stained with MitoSOX. n=4,4 for *Bid*+/+ and *Bid-/-* with and without FBS. (C) Treatment as in B followed by staining with 5μM of DHE for cellular ROS. n=11,10 with FBS and n=4,4 without FBS for *Bid*+/+ and *Bid-/-*, respectively. (D) Mitochondrial membrane potential assessed with 50nM TMRE in *Bid* +/+, *Bid-/-*, *Bid-/-* + *FHA-Bid*^{BH3} and *Bid-/-* + *FHA-Bid*^{BH3AA} MPCs , n=4,4,4,3 respectively. Cells overexpressing BH3- or BH3AA-mutanted Bid were gated on CD25 high expressing cells (i.e. only cells containing FHA-Bid). (E) Mitochondrial ROS of the indicated cell lines measured with MitoSOX as in D, n= 4,4,4,3 respectively. (F) ATP/O ratio determined from data shown in Figure 6E and F. P-values were determined by two-way ANOVA ($p<0.001$)

Figure 3-11 Continued.
with Tukey's post-test for A-C, one-way ANOVA (not significant) with Student's t-test D, E, and two-way ANOVA with unpaired Student's t-test for F. Error bars indicate +/- SEM for all data. ns=not significant, * $p < 0.05$, ** $p < 0.01$. Contribution: All experiments shown performed by Salisbury-Ruf CT (Panels A-E) including generation of *FHA-Bid*^{BH3AA} MPCs. Panel F as in Figure 3-10 E.

Permeabilized cardiac fibers from Bid-/- mice exhibit decreased respiration and ATP production

Next, to determine whether the decreased respiration is also observed in mouse cardiac fibers, we evaluated oxygen consumption in *Bid-/-* and *Bid+/+* heart tissue. Respiration of permeabilized left ventricular (LV) cardiac fiber bundles (PmFBs) was measured in the presence of the complex I (CI) substrates malate and glutamate, as well as ADP (state 3). *Bid-/-* LV fibers also displayed significantly decreased oxygen consumption compared to *Bid+/+* LV fibers ($p=0.0103$) (Figure 3-10 D).

To more thoroughly interrogate the mitochondrial defect from *Bid-/-* hearts, we used a customized instrument platform optimized for permeabilized muscle fibers (240) and simultaneously measured ATP production and O_2 consumption. We first analyzed PmFBs in the presence of complex I substrates (glutamate, malate and ADP). *Bid-/-* fibers had decreased respiratory function as well as decreased ATP production ($p<0.05$) (Figure 3-10 E, F) compared to *Bid +/+* fibers.

Rotenone, (complex I specific inhibitor) prevents electron flux through CI and we observe decreased O_2 consumption and ATP production as expected. Succinate directly contributes electrons to CII and was added in the presence of rotenone to interrogate CI-independent respiration. *Bid-/-* PmFBs had decreased respiration in the presence of rotenone and succinate ($p<0.001$), and decreased ATP production ($p<0.05$) (Figure 3-10

E, F), consistent with our finding that irregular cristae correspond with decreased ATP synthase activity.

Oxidative phosphorylation efficiency can be defined as the ratio of ATP to O. Interestingly, despite an overall decrease in respiration and ATP production, *Bid-/-* PmFBs have similar efficiency to *Bid* +/+ when using CI substrates. This is consistent with our finding that *Bid-/-* mitochondria do not have increased ROS or loss of membrane potential (Figure 3-11 A-D). However, in the presence of rotenone and succinate, *Bid-/-* PmFBs have an increased ATP/O ratio ($p<0.05$) (Figure 3-11 F). This suggests *Bid-/-* mitochondria may compensate by bypassing complex I in favor of respiratory complex II, which is not found in respiratory supercomplexes (272) and therefore would be less impacted by disorganized cristae.

PrediXcan analysis reveals decreased BID expression associates with myocardial infarction

Given the observed increased fibrosis in *Bid-/-* mice, phenotypically similar to post-MI damage in humans, we investigated the clinical relevance of our findings. We applied PrediXcan (228, 229) (Figure 3-12 A) to test the association of genetically determined BID expression in 29,366 patients in BioVU (224) with MI predisposition. Because of the substantial prior support from our studies observed for Bid's role in heart function and inducing fibrotic damage with acute stress, we evaluated the association with MI risk of BID expression and used Bonferroni adjustment for the

number of cardiac traits tested to assess statistical significance. Consistent with our findings in mice, we observed that decreased BID expression is significantly associated with MI (Figure 3-12 B).

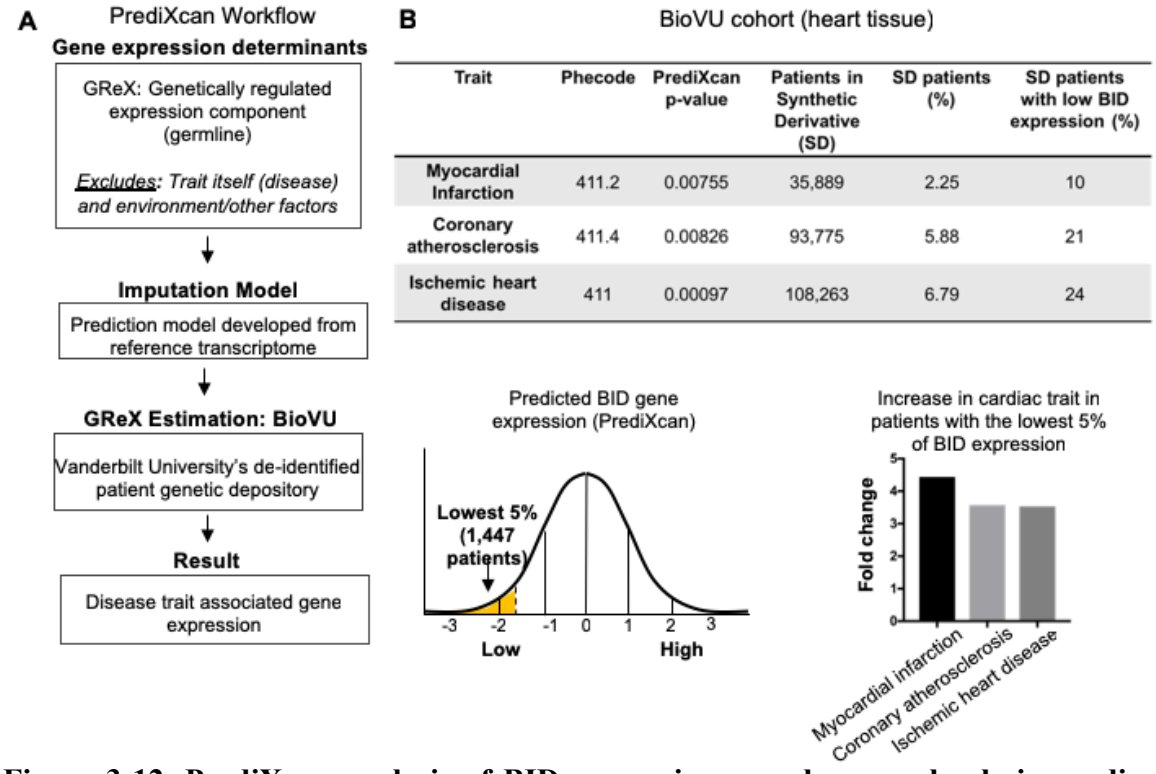

Trait	Phecode	PrediXcan p-value	Patients in Synthetic Derivative (SD)	SD patients (%)	SD patients with low BID expression (%)
Myocardial Infarction	411.2	0.00755	35,889	2.25	10
Coronary atherosclerosis	411.4	0.00826	93,775	5.88	21
Ischemic heart disease	411	0.00097	108,263	6.79	24

Figure 3-12. PrediXcan analysis of BID expression reveals a novel role in cardiac diseases. (A) Diagram of PrediXcan analysis workflow. PrediXcan estimates the genetically regulated component of gene expression (germline), excluding the impact of the disease itself and the environment on expression. (B) PrediXcan in a BioVU replication cohort of 29, 366 patients (in heart tissue). Patients were also binned by BID gene expression, with the lowest 5% analyzed for incidence of the cardiac traits discovered by PrediXcan. A total of 1447 patients encompassed the lowest 5% in BID expression. Myocardial infarction had the highest increased incidence, represented by graph for fold change in these patients compared to all Vanderbilt Synthetic Derivative (SD) patients (1,593,350 records). P-values were determined by logistic regression with disease status as response variable and imputed gene expression as predictor. Contribution: Experimental design by Salisbury-Ruf CT with PrediXcan analysis by Gamazon ER.

To quantify the extent of genetic control of BID expression, we performed SNP-based heritability analysis (273). Genotype-Tissue Expression (GTEx) project data, despite the breadth of tissues, are still generally underpowered for this analysis (because of sample size), and we therefore utilized a larger transcriptome panel DGN (n = 922) (274), which is, however, available only in whole blood. The BID heritability estimate was significant ($h^2 = 0.08$ with standard error [SE] of 0.026), providing support for genetic regulation (Figure 3-13 A, B).

A Genes for heritability and expression analysis

Primary analysis	Secondary analysis
BID	BAD
	PMAIP1 (NOXA)
	BNIP3
	BNIP3L
	BCL2L11 (BIM)
	BBC3 (PUMA)
	MTCH2
	BECN1

B

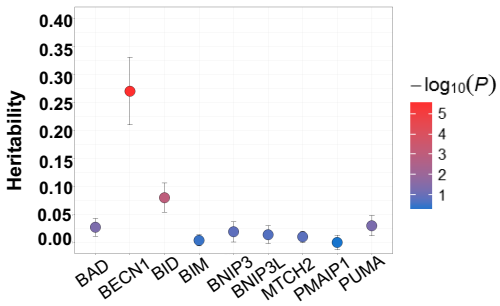

C

BID PrediXcan cardiac traits (BioVU validation cohort)	Effect Size	P-value	Tissue Type
Myocardial Infarction	-1.2823	0.0023	*Artery-Aorta*
Cardiac shunt/ heart septal defect	-1.4190	0.0029	Brain-Cortex
Paroxysmal supraventricular tachycardia	-4.4878	0.0032	Small Intestine – Terminal Illieum
Unstable angina (intermediate coronary syndrome)	-1.9810	0.0074	Spleen
Right bundle branch block	-2.8602	0.0348	*Artery-Aorta*
Heart failure with preserved EF (Diastolic heart failure)	-1.7073	0.0493	Spleen

D PrediXcan association with Myocardial Infarction

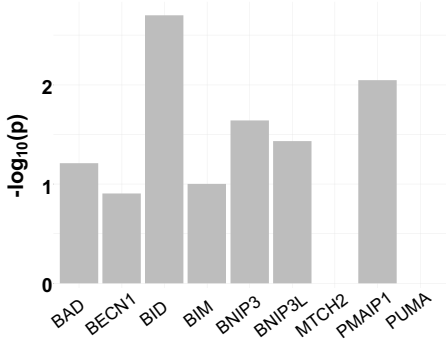

Figure 3-13. BID and BECN1 are significantly heritable and PrediXcan reveals significantly decreased BID expression for cardiac traits.
(A) Table of genes used for heritability and expression analysis. BID was analyzed in a primary analysis while all other genes encompassed a secondary analysis. (B) Heritability analysis for all indicated genes. Only BECN1 and BID were found to be significantly heritable. (C) Table of BID traits with associated p-values, effect size, and tissue type for all significant traits. Cardiac traits that appeared more than once were represented in the graph by the most significant p-value. (D) PrediXcan analysis results for gene expression and association with MI in BID and secondary analysis of all other genes. Contribution: PrediXcan methodology and hereditability analysis by Gamazon ER.

We determined the prevalence of MI, coronary atherosclerosis and ischemic heart disease in Vanderbilt University's Synthetic Derivative (SD), which contains over 2.8 million de-identified patient records linked to electronic health records (224). For comparison, we evaluated the prevalence of MI, coronary atherosclerosis, and ischemic heart disease in individuals with the lowest 5% of BID expression, thus approximating the *Bid-/-* condition of our mouse model. Within this group, we find a > 4 fold increase in the prevalence of myocardial infarction compared to the rest of the Synthetic Derivative. Decreased BID expression in heart tissue significantly associated with myocardial infarction ($p=7.55\text{x}10^{-3}$) as well as coronary atherosclerosis ($p=8.26\text{x}10^{-3}$), and ischemic heart disease ($p=9.7\text{x}10^{-4}$) (Figure 3-12 C). These results are notable, as they not only suggest the impact that loss of Bid would have in humans but also highlight the continuity of phenotypes observed in the *Bid-/-* mice with human patient data.

In order to more precisely characterize the effect of decreased genetically determined BID expression on cardiac phenotypes, we additionally analyzed the recently available GWAS of atrial fibrillation (N > 1 million individuals) (242). Notably, we find no significant association between BID genetically determined expression and atrial fibrillation in this dataset (p=0.63), consistent with the lack of significant association in BioVU. Thus, while we identify multiple cardiac traits associated with BID expression, BID's effect is specific to particular pathophysiologies

To determine whether our findings are unique to BID among other BH3-only and related genes, including BECN1 (a Bcl-2-interacting protein involved in autophagy) and MTCH2 (a Bid-interacting protein) (87, 91, 92), we performed a secondary PrediXcan analysis. The results revealed a unique role for BID among these genes in conferring MI risk (see Materials and methods and Figure 3-14 A-F).

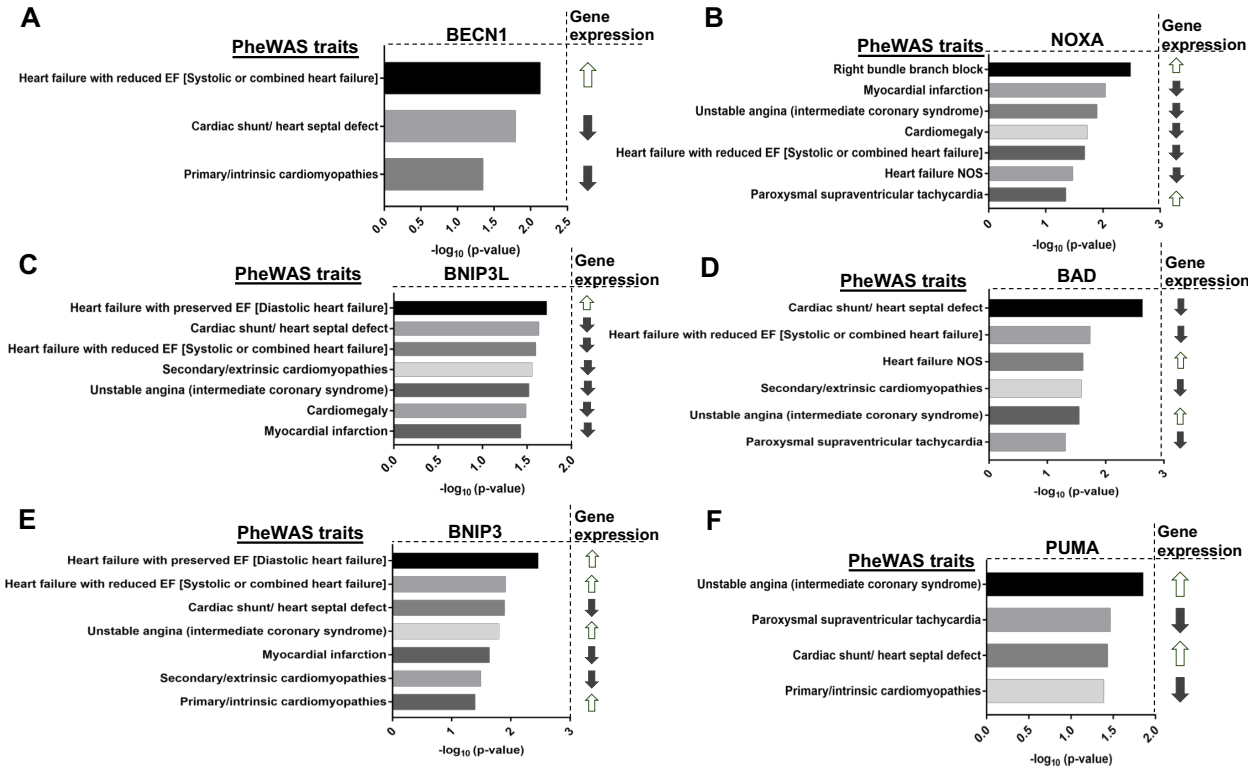

Figure 3-14. Secondary PrediXcan analysis of BH3-only Bcl-2 family genes shows discordant direction of effect with heart conditions.
(A-F) Graphs of significant cardiac traits in the BioVU validation cohort ranked by p-values ($-\log_{10}$) for BECN1, NOXA, BNIP3L, BAD, BNIP3, and PUMA and the corresponding direction of gene expression. For all genes, cardiac traits that appeared more than once were represented in the graph by the most significant p-value. P-values were determined by logistic regression with disease status as response variable and imputed gene expression as predictor. Contribution: Experimental design by Salisbury-Ruf CT and PrediXcan analysis by Gamazon ER.

Validation in BioVU and CARDIoGRAMplusC4D GWAS

In a separate BioVU sample set (see Materials and methods and Figure 3-15), we observed a significant correlation (p=0.002) between decreased genetically determined BID expression in the aorta and MI. We analyzed the publicly available CARDIoGRAMplusC4D GWAS datasets (156, 245). Consistent with the BioVU discovery and validation results, decreased genetically determined expression of BID in heart was associated (p=0.02, effect size = −0.06, SE = 0.026) with MI in CARDIoGRAMplusC4D.

Interestingly, several of the SNPs (in the locus) nominally associated with MI and CAD clustered within the adjacent BCL2L13 (Bcl2-rambo) gene, the most significant being rs2109659 (p=0.004). However, no association with MI in CARDIoGRAMplusC4D was observed with BCL2L13 (p=0.75) (Figure 3-15 A, B), consistent with the SNPs being regulatory for BID.

For completeness, we report the BID associations with cardiac traits using additional tissues (275). Interestingly, all nominally significant associations with other cardiac traits in these tissues in BioVU were consistent with decreased expression of BID (Figure 3-15 C).

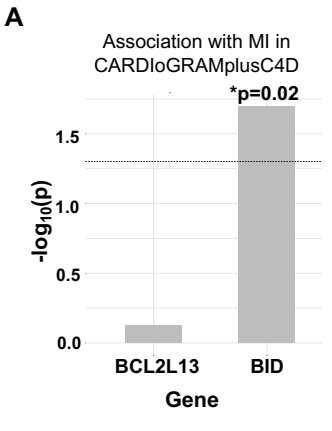

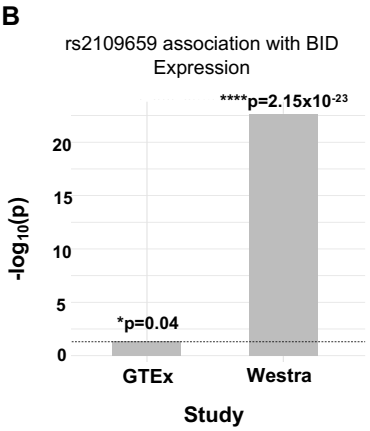

C

S-PrediXcan of UK Biobank BID association with MI

Z-score	P-value	Tissue Type
-2.37	0.018	Skin
-2.26	0.024	Nerve-Tibial
-2.01	0.045	Brain-cerebellum

Figure 3-15. Decreased BID expression is associated with MI in two additional independent cohorts.
(A) PrediXcan analysis in CARDIoGRAMplus C4D for association of BCL2L13 and BID with MI in. (p=0.02, effect size=-0.06, SE=0.026). (B) Association of SNP rs2109659 with BID gene expression in GTEx (n=114 lymphoblastoid cells, p=0.04, z-score=-2.05, effect allele=C) and Westra data sets (n=5,311 peripheral blood samples, $p=2.15x10^{-23}$, z-score=-9.97, effect allele=C). (C) S-PrediXcan analysis of a UK Biobank of greater than 430,000 people reveals significantly decreased BID gene expression associated with MI. P-values were determined by logistic regression with disease status as response variable and imputed gene expression as predictor. Contribution: Experimental design by Salisbury-Ruf CT with PrediXcan analysis by Gamazon ER.

Bid's alpha-helix 6 is important for its ability to regulate mitochondrial function

Here we show that site-directed mutagenesis informed by exome association analysis of BID revealed that Bid's alpha-helix-6 directs its role to regulate mitochondrial function. First, we evaluated whether there was an association between coding SNPs within BID and MI risk. Using BioVU, we developed a cohort of 23,195 self-reported Caucasian subjects (median age 63 years [IQR 43 to 57 years] and 52% female) who had previously undergone genotyping (Illumina Human Exome Bead- Chip v1) (see Supplementary Information), of whom 1507 were MI cases. In multivariable logistic regression, a significant association was observed between carrier status (i.e. presence of any mis- sense variant) and MI (p=0.013; OR 1.7 [95% CI 1.1–2.6]). Although this would not meet significance in an unbiased, exome-wide search, we are testing only a single

gene for which we have already observed substantial evidence for its role in conferring MI risk. This gene-level association was primarily driven by variants in the membrane binding domain (MBD), including E120D, R123Q and M148T (Figure 3-16A). Carrier status for MBD variants (i.e. presence of any missense variant in the MBD) was strongly associated with MI (p=0.002; OR 8.5 [95% CI 2.1–33.6]) (Figure 3-16 B, C). Notably, M148T was also associated with MI risk (p=0.029, OR = 1.47) in the recent meta-analysis of exome-chip studies involving 42,335 patients and 78,240 controls of European ancestry, consistent with the BioVU results (248).

We next evaluated whether any of these coding variants, particularly those that lie within the MBD, affect Bid's regulation of mitochondrial function. In particular, the conserved M148 residue lies within Bid's alpha-helix-6, which regulates mitochondrial association and cristae remodeling in the context of cBid during apoptosis (86, 87, 94).

We introduced the M148T mutation in conjunction with full-length BH3-mutated Bid, which can rescue mitochondrial function, into *Bid-/-* MPCs (Figure 3-16 D). To establish that introduction of the M148T mutant does not disrupt Bid's overall structure, we evaluated apoptotic function by assessing cell death with TNFα/Actinomycin D. As expected, *Bid-/-* MPCs were protected from death com- pared to *Bid* +/+ MPCs (p=0.0068). Importantly, *Bid-/-* + *FHA-Bid*$^{BH3/M148T}$ MPCs displayed similar death kinetics to *Bid-/-* + *FHA-Bid*^{BH3} MPCs which has been shown to have some sensitivity to TNFα/Actinomycin D stimulated death (78). This indicates that the M148T mutation has no effect on Bid's apoptotic function in the presence of a mutated BH3 domain (Figure 3-7 A, B).

We evaluated mitochondrial cristae number in *Bid* +/+, *Bid*-/- + *FHA-Bid*^{BH3} and *Bid*-/- + *FHA- Bid*^{BH3M148T} (double mutant) as in Figure 3-3, and found that the double mutant had significantly less cristae compared to *FHA-Bid*^{BH3} alone ($p<0.01$). Interestingly, we found that the double mutant had an increase in overall mitochondrial area density per cell, likely as a compensatory mechanism for decreased cristae function ($p<0.01$) (Figure 3-16 E-G). Respiratory efficiency of MPCs was then assessed using these mutants, directly comparing the BH3-mutant to the double mutant. Expression of the Bid$^{BH3/M148T}$ double mutant was insufficient to restore respiratory levels comparable to *Bid* +/+ or *Bid*-/- + *FHA-Bid*^{BH3} MPCs (Figure 3-16 H).

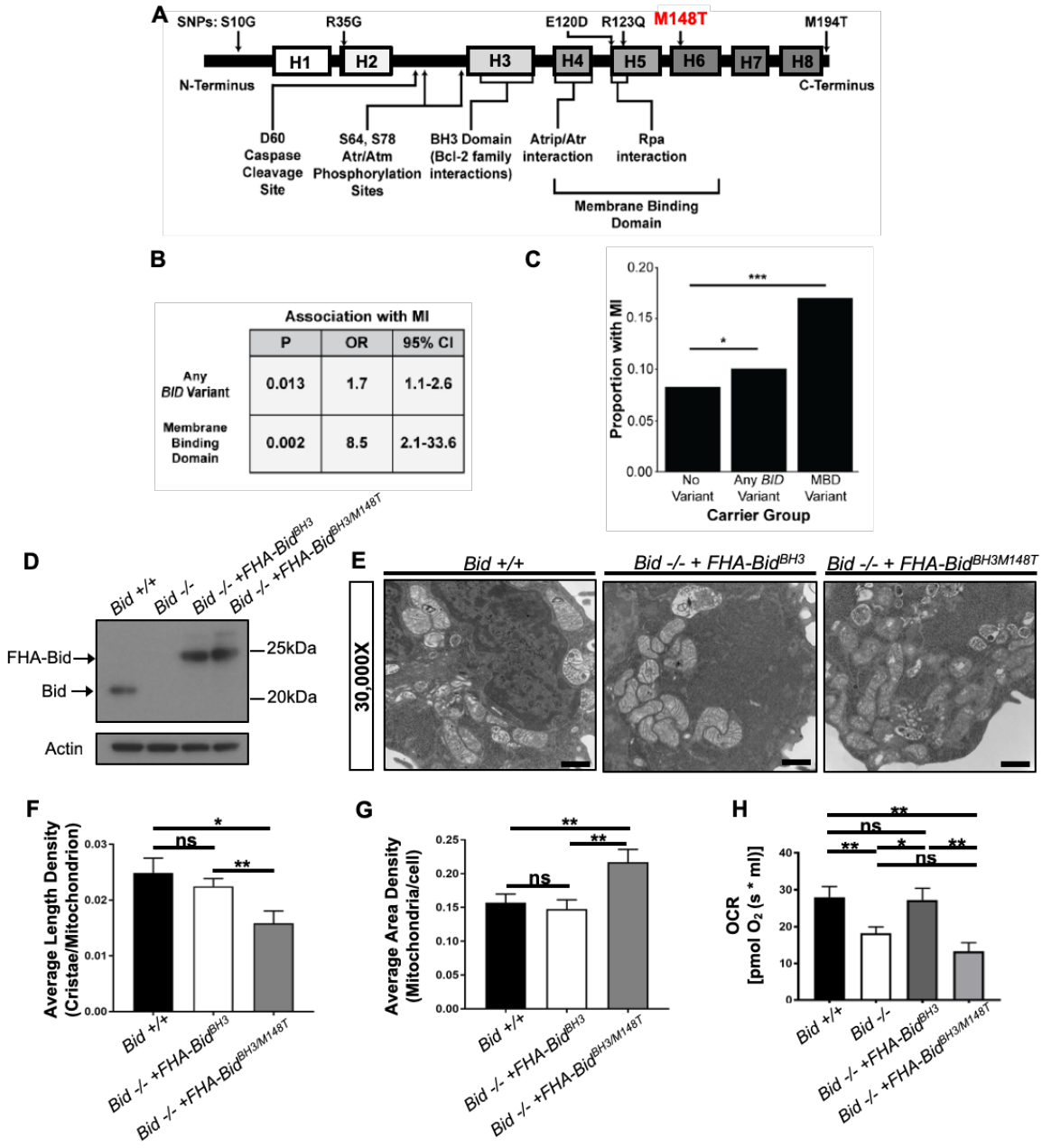

Figure 3-16. BID coding SNPs associate with myocardial Infarction (MI) in humans and reveal helix-6 SNP M148T is critical for Bid's regulation of mitochondrial function. (A) Linear representation of Bid protein structure and approximate SNP locations. Human BID SNPs and several key domains and regions of Bid are indicated. (B) Statistical values including p-value, odds ratio (OR), and 95% confidence interval (95% CI) for Bid SNP association with MI for overall carrier status of BID variants or with variants in the membrane binding domain. (C) Graphical representation of the proportion of patients with MI in carrier groups with no SNPs in BID (no variant), any BID variant, or MBD variant. (D) Western blot of expression levels of Bid for the indicated cell lines. (E) TEM of *Bid* +/+, *Bid-/-* + *FHABid*^{BH3}, and

Figure 3-16 Continued.
Bid-/- + *FHABid*$^{BH3/M148T}$ MPCs. Representative images at 30,000X (scale bar = 500 nm). (F) Quantitation of the number of cristae per mitochondria (average length density) and (G) the mitochondrial density per cell (average area density) of the MPC lines shown in (E). (n = 40,40,15 images per cell line respectively). (H) OCR of *Bid* +/+, *Bid-/-*, *Bid-/-* + *FHA-Bid*^{BH3}, and *Bid-/-* + *FHA-Bid*$^{BH3/M148T}$ MPCs for all cell lines (n = 6,12,6,5 respectively). P-values were determined by multivariable logistic regression with Bonferroni correction as described in methods for (B) and (C), one-way ANOVA with Student's t-test for (F) and G), and one-way ANOVA ($p<0.05$) with Student's t-test for (H). Error bars indicate ±SEM for all data. ns = not significant, *$p<0.05$, **$p<0.01$, and ***$p<0.001$. Contribution: Whole exome sequencing analysis by Wells QS (Panels A-C). All additional experiments shown performed by Salisbury-Ruf CT (Panels D-H) with TEM assistance by Williams J (Panel E). Generation of *FHA-Bid*$^{BH3/M148T}$ MPCs by Bertram CC with respiration assistance by Bertram CC and Heberling ML.

Interestingly, the two other SNPs identified in the membrane binding region of Bid also lie within a hydrophobic region of Bid as well as the region predicted to interact with MTCH2 (92). We made the corresponding mutations, E120D and R124Q in BH3-mutated Bid to determine if these would also result in altered mitochondrial function (Figure 3-17 C). Compared to BH3-mutated Bid, Bid$^{BH3/E120D}$ MPCs had equivalent respiration. While Bid$^{BH3/R124Q}$ MPCs had decreased respiration (Figure 3-17 D), it was not significantly different from WT MPCs. Neither Bid$^{BH3/E120D}$ nor Bid$^{BH3/R124Q}$ MPCs displayed altered sensitivity to TNFα/Actinomycin D stimulated cell death (Figure 3-17 E, F).

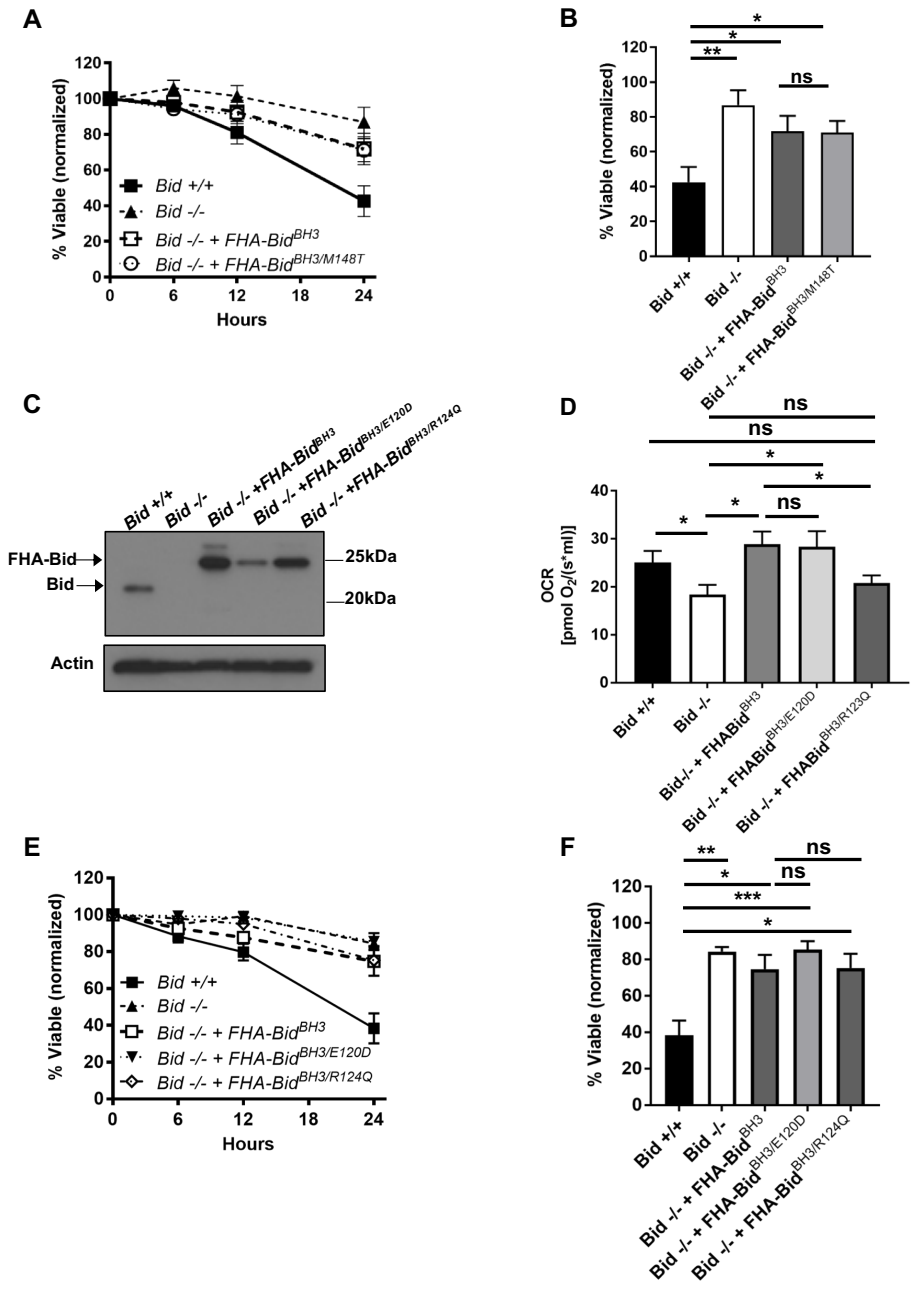

Figure 3-17. Mutations in Bid corresponding to Helix-5 SNPs show less impact on respiration than Helix-6 mutation M148T.

(A) Viability assay (AV/PI) for indicated cell lines corresponding to Figure 8 and (B) the 24 hour time-point (n=5). (C) Western blot of expression levels of Bid for the indicated genotypes. (D) OCR of *Bid -/-*, *Bid-/- + FHABid^{BH3}*, *Bid-/- + FHABid$^{BH3/E120D}$*, and *Bid-/- + FHABid$^{BH3/R124Q}$* MPCs for all cell lines (n=4,4,6,6 respectively). (E) Viability assay (AV/PI) of MPCs for indicated times following TNFα/Actinomycin D treatment and (F) 24-hour timepoint (n=3,3,3,6,6 respectively). The percent of viable cells was normalized to no treatment. P-values were determined by one-way ANOVA ($p<0.05$) with Student's t-test for B, D, and F. Error bars indicate +/-SEM for all data. ns=not significant, * $p<0.05$, ** $p<0.01$, ***$p<0.001$. Contribution: All experiments shown performed by Salisbury-

Figure 3-17 Continued.
Ruf CT, Bertram CC, and Heberling ML. Generation of *FHA-Bid$^{BH3/E120D}$* and *FHA-Bid$^{BH3/R124Q}$* MPCs by Bertram CC.

Bid binds the matrix form of Mcl-1, which can be altered with helix-6 mutant M148T

Our observation that Bid is found within the mitoplast (Figure 3-5 C, D) raised the possibility that it is interacting with mitochondrial matrix proteins known to regulate cristae structure. In particular, the anti-apoptotic Bcl-2 family member Mcl-1 has been shown to have a matrix isoform involved in respiratory chain maintenance and mitochondrial metabolism (125–128). It is known that the BH3-domain of cBid associates with Mcl-1, to inhibit apoptosis (276).

We tested whether full-length Bid associates with WT Mcl-1, an outer mitochondrial membrane form of Mcl-1^{OM} or the matrix form of Mcl-1, Mcl-1^{Matrix}. Using FlagHA-tagged Bid expressed in 293T cells, we were able to immunoprecipitate all three forms of Mcl-1 (Figure 3-18A). This is in contrast to the other BH3-only protein Bim, which did not associate with Mcl-1^{Matrix} (125). We then sought to determine the role of helix-6 in this association. We find that FHA-Bid^{M148T} dis- plays decreased association with Mcl-1^{Matrix} compared to both WT-Bid and our rescue mutant, FHA- Bid^{D59A}. Furthermore, FHA-Bid^{M148T} displays increased association with WT Mcl-1 relative to either WT Bid or FHA-Bid^{D59A} (Figure 3-18 B). The above results are consistent with a role for helix-6 in Bid's association with Mcl-1^{Matrix}, in the context of the mitochondrial cristae.

PrediXcan reveals decreased MCL-1 gene expression is associated with myocardial infarction

Informed by our observation of Bid's interaction with mitochondrial matrix proteins known to regulate cristae structure organization, we applied PrediXcan to evaluate potential contribution to MI susceptibility for these genes. Loss of Mcl-1 has previously been shown to result in cardiomyopathy and impaired autophagy leading to heart failure in mice (126, 127). We find that decreased genetically determined expression of MCL-1 is significantly associated with MI ($p=0.00903$) (Figure 3-18 C). In addition to MCL-1, we find that MTX1 (Metaxin1), a mitochondrial protein transporter that associates with the MICOS complex (262), has reduced genetically determined expression significantly associated with MI ($p=1.93\times10^{-5}$).

Furthermore, we utilized the Synthetic Derivative to gain additional insights into the cardiac traits known to result from loss of Mcl-1. Using ICD9-codes, we identified 20,834 patients diagnosed with an MI (among the nearly 2.8 million patients). Using this information, we constructed a contingency table, first looking at the relative risk for control phenotypes (headache and burn) as well as known risk factors for MI including hypertension, hypercholesteremia, and diabetes mellitus (277). Interestingly, we find that patients with a history of cardiomyopathy have a significantly increased relative risk for MI compared to the known risk factors, connecting these two phenotypes genetically (Figure 3-18 D).

Thus, we propose a model in which we have evidence from cell lines, mice, and multiple human genetics studies that converge on a role for Bid in the regulation of

mitochondrial cristae structure and predisposition to MI (Figure 3-18 E). We further find genetic evidence that decreased expression of two additional genes known to regulate cristae structure, MCL-1 and MTX1, is also associated with susceptibility to MI. In addition to its apoptotic function, we now add a homeostatic function for Bid at the mitochondria which is dependent on its full-length form in the matrix, and the helix-6 residue M148, uncovered directly from human exome data. Finally, we find an association between Bid and the matrix form of Mcl-1 mediated by the helix-6 residue M148, suggesting that Bid may perform its role at the mitochondrial matrix through interaction with Mcl-1.

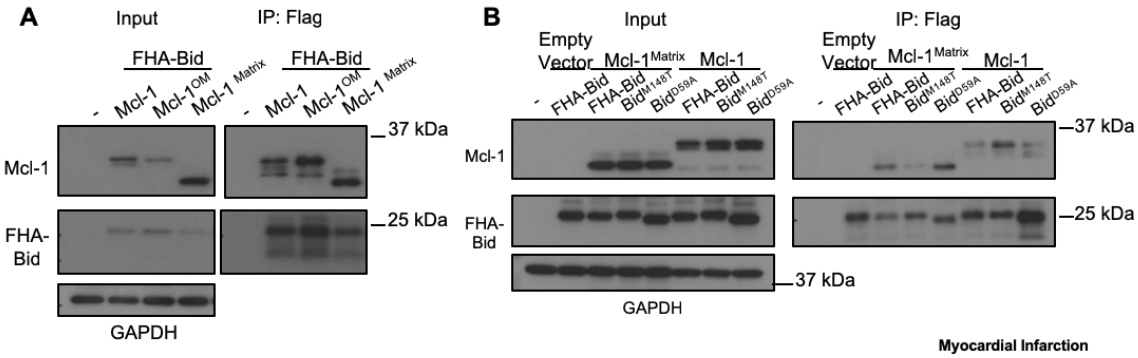

C

Cristae-associated genes	Trait	P-value	Gene expression	No. of Cases	No. of Controls
MCL-1	Myocardial Infarction (MI)	$9.03x10^{-03}$	Decreased	2512	13196
MTX1	Myocardial Infarction (MI)	$1.93 x10^{-05}$	Decreased	2512	13196
MTX1	Other forms of chronic heart disease	$1.39x10^{-04}$	Decreased	1757	13196

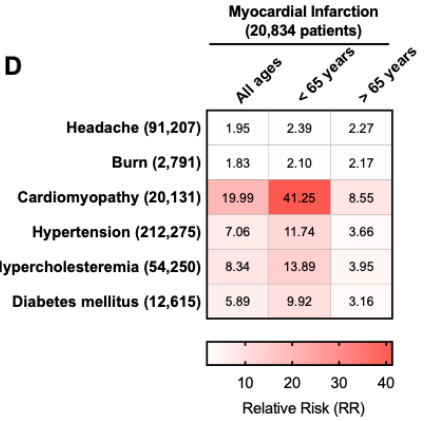

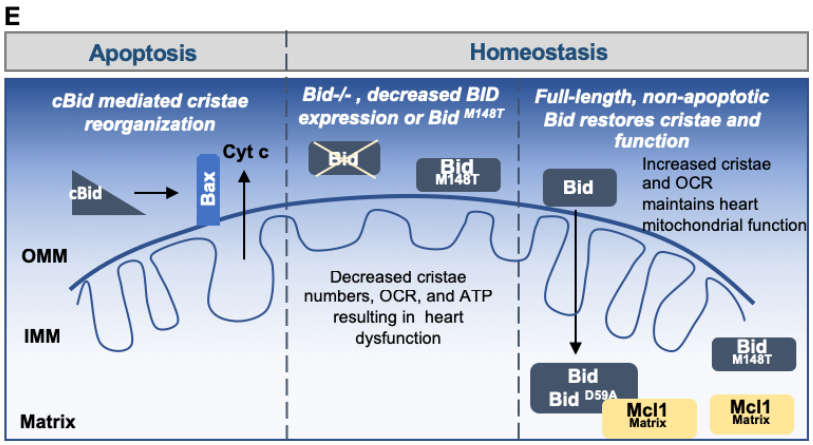

Figure 3-18. Full-length Bid interacts with Mcl-1^{Matrix}, which is diminished by M148T-mutated Bid.

(A) Immunoprecipitation of FlagHA-Bid with anti-Flag M2 agarose beads from 293T whole cell lysate overexpressing FHA-Bid and one of the indicated Mcl-1 constructs: Mcl-1 (WT), Mcl-1^{OM} (outer membrane), or Mcl-1^{Matrix}. (B) Immunoprecipitation as in A with the indicated Bid constructs overexpressed with either empty vector (MSCV), Mcl-1 (WT) or Mcl-1^{Matrix} in 293 T cells. Input represents approximately 1/70th of total protein used for immunoprecipitation. (C) PrediXcan analysis of proteins previously found to be involved in cristae stability. MTX1 = Metaxin1. (D) Contingency table of patients queried in the BioVU Synthetic Derivative for MI and the indicated diseases (left) identified by ICD9 code. Patient numbers are indicated in parenthesis and values in the heat map indicate the raw relative risk (RR) values. $p=3.944x10^{-16}$ for MI v burn or headache (control diseases) and $p<2.2x10^{-16}$ for MI v all other diseases. (E) Proposed model for a full-length Bid's

Figure 3-18 Continued.
homeostatic role in regulating mitochondrial cristae structure. Bid can localize to the matrix where its association with Mcl-1 (directly or indirectly) facilitates the stabilization of respiratory complexes and cristae structure. This interaction is diminished by M148T-mutated Bid. Contribution: All experiments shown performed by Salisbury-Ruf CT (Panels A, B, and D) and PrediXcan analysis on cristae-associated genes by Gamazon ER (Panel C). Diagram in Panel E by Salisbury-Ruf CT.

Discussion

Our results add to the body of literature implicating a role for the Bcl-2 family in mitochondrial mem- brane remodeling in the absence of apoptosis. While full-length Bid is observed at the mitochondria homeostatically (107, 259) (Figure 3-5), the purpose for this localization, especially given that cleaved Bid is potently apoptotic, was unclear. We find that Bid, like Bcl-X_L and Mcl-1 (122, 123, 125) is critical for the structural and functional maintenance of mitochondrial cristae and this occurs independently of caspase-8 cleavage. The significance of this finding is strengthened by our complementary approach, which integrates cell biology with human genetics data.

In both MPCs as well as LV tissue, loss of Bid results in absent or abnormal mitochondrial cristae structure. Acute cardiac stress not only exacerbates this cristae disorganization but leads to cardiac dysfunction in *Bid-/-* mice, including increased left ventricular diameter and reduced ejection fraction. While mice are able to recover functionally, this ultimately results in increased cardiomyocyte fibrosis, damage similar to that observed after an MI. We propose that the association between Bid and MI can be linked to mitochondrial function. Real-time analysis of permeabilized cardiac fibers revealed that loss of Bid results in decreased respiration and ATP production. Thus *Bid-/-* cells and tissue function at their maximum efficiency, yet produce less energy, consistent with disrupted respiratory chain formation (253). Under conditions of stress, *Bid-/-*

mitochondria are unable to meet increased energetic demand, thus decreasing the threshold to cardiac failure, and ultimately myocardial dysfunction.

To determine the human disease relevance of our findings, PrediXcan analysis (229) was applied to BioVU. The PrediXcan-derived association of BID with MI has important implications. Firstly, the association derives from common genetic variants, and there- fore has potential diagnostic implications in the general population. Secondly, use of germline genetic profile to estimate BID expression removes any potential confounding effect the environment or disease itself could have on gene expression.

Importantly, we also evaluated the individuals with the lowest BID expression, thus approximating the situation in *Bid-/-* mice in humans. Strikingly, the lowest 5% of individuals had a > 4 fold increase for incidence of MI. This remarkable result further connects our genetic findings to the cardiac phenotype observed in *Bid-/-* mice.

Lastly, we sought independent validation for BID's association with MI. We used the publicly avail- able CARDIoGRAMplusC4D GWAS datasets (156, 245), and an additional independent cohort of BioVU patients. This result was also unique to BID among other BH3-only proteins.

At the coding level, we have also identified SNPs within the membrane binding region of BID associated with MI. In particular, M148T in helix 6 was of interest as two additional downstream residues, K157 and K158, have been shown to be essential for cristae re-organization in the context of apoptosis (94). This SNP was also found to be significant in a meta-analysis of exome-chip studies of European ancestry (248). To determine the functional consequence of this SNP, we made the corresponding M148T point mutant in Bid and find it fails to fully restore cristae structure, and results in a loss

of respiratory function when combined with our rescue BH3-mutant Bid. In contrast, two SNPs in the putative Bid-MTCH2 binding domain (Bid^{E120D} and Bid^{R124Q}) did not alter mitochondrial function compared to WT MPCs.

Our results indicating the presence of Bid in the matrix prompted us to determine if the M148T mutant would also impact a possible protein-protein interaction. A strong candidate is the anti-apoptotic Bcl-2 family member Mcl-1, which was rigorously shown to have a mitochondrial matrix isoform that mediated mitochondrial cristae structure and lipid metabolism independent of Mcl-1's apoptotic function (125, 128). We find that this point mutant decreases the association between Bid with $Mcl\text{-}1^{Matrix}$ compared to WT and D59A-mutanted Bid (rescue mutant). Interestingly, we also observe that Bid^{M148T} associates with WT Mcl-1. We propose that Bid interacts with Mcl-1 in a manner that requires not only a BH3-domain, but also helix- 6. Based on the NMR structure of Bid (84, 85), Bid^{M148T}, as well as the previously implicated Bid^{K158} (94), lie in approximately the same plane of helix-6, in an orientation facing away from helix-3 (BH3-domain) in solution. EPR analysis of p15 Bid also places both of these residues in the headgroup region of a lipid bilayer when cBid is inserted into a membrane (86). It is possible that mutating these residues decreases the affinity of Mcl-1 to full-length Bid in solution by destabilizing the hydrophobic core of Bid adjacent to helix-3. Alternatively, these mutants might also be predicted to decrease Bid's association with a membrane. This may be more critical for Bid's interaction with $Mcl\text{-}1^{Matrix}$ in regulating membranes than for its interaction on the surface of mitochondria with WT Mcl-1 and may account for the difference in affinity found by immunoprecipitation.

In sum, we have identified a homeostatic role for Bid in the regulation of mitochondrial structure and function extending initial observations in tissue culture to an in vivo model that converges on a unique role for BID in human cardiac disease. We

propose that loss of Bid or decreased BID gene expression contributes to cardiac diseases, particularly MI. Furthermore, we provide evidence that this mitochondrial function for Bid is dependent at least in part upon Bid's alpha-helix-6, that mediates Bid's interaction with Mcl-1^{Matrix}, implicating a Bid-Mcl-1 interaction at the matrix in mitochondrial cristae organization. Finally, we find an association between decreased expression of MCL-1 and MTX-1 with susceptibility to MI, linking altered cristae structure with MI. Our integrated approach, combining multiple avenues of investigation, has identified previously unknown proteins involved in complex genetic diseases, and can be used to bridge the gap between basic biological findings and translational science.

Chapter IV

INCREASED RIPK1-MEDIATED BONE MARROW NECROPTOSIS LEADS TO MYELODYSPLASIA AND BONE MARROW FAILURE IN MICE

Data in this chapter is from:

Wagner PW, Shi Q, Salisbury-Ruf CT, Zou J, Savona MR, Fedoriw Y, and Zinkel SS. Increased Ripk1-mediated bone marrow necroptosis leads to myelodysplasia and bone marrow failure in mice. Blood 2019 Jan 10; 133(2):107-120.

Project Contribution: In this project, I directed the analysis of genetic rescue experiments for the TKO*Ripk1(+/-)* mice. This included flow cytometry analysis of progenitor cells, intracellular flow for Ripk1 levels, and cytokine analysis. I also acquired peripheral blood samples for complete blood count analysis and performed western blots assessing TKO*Ripk1(+/-)* bone marrow. I additionally contributed to western analysis of caspase-8, MLKL crosslinking, and whole bone marrow for necrotic proteins. Lastly, I wrote the sections of the manuscript related to these results. Note that all contributions to experiments shown in each figure are noted in the captions.

Introduction

Programmed cell death (PCD) is required to maintain homeo-stasis in dynamic systems such as hematopoiesis. The two main forms of PCD, apoptosis and necroptosis, result in markedly different outcomes with important implications for the cellular microenvironment. Whereas apoptosis is predominantly immune silent, necroptosis promotes inflammation through release of endogenous molecules such as DNA or membrane lipids, known as damage-associated molecular patterns (DAMPS) (60).

The process of necroptosis has the potential to amplify both cell death and inflammation within the bone marrow. Hematopoietic and stromal cells can respond to necroptosis-released DAMPS to produce cytokines such as tumor necrosis factor a (TNFα) that also act as death receptor ligands. In the bone marrow microenvironment,

cytokines such as TNFα provide cues to maintain homeostasis (56, 194, 278). In addition, TNFα as well as interferon can impair hematopoietic stem cell colony formation and the ability to sustain multilineage differentiation (66). The impact of necroptotic cell death on hematopoietic homeostasis is there-fore potentially substantial and not well understood.

Seminal results from genetic mouse models demonstrate that the upstream activators of apoptosis, Fas-associated protein with death domain (FADD) and caspase-8, act as key inhibitors of necroptotic cell death during embryonic development (70, 279–284).

Situated at this central decision point of cell death fate, the Bcl-2 (B-cell lymphoma) family functions downstream of death receptor signaling before activation of executioner caspases. In particular, the BH3-only family member Bid acts as a sensor and amplifier of death receptor signaling. Upon activation of death receptors (TNF receptor [TNFR] and Fas), Bid is cleaved by caspase-8 (80) and activates Bax/Bak to initiate the release of cytochrome c and the execution of apoptosis (285). The interaction of Bid with caspase-8 and Bid's role in early activation of apoptosis are therefore well established. Bid has been shown to function in a pro-survival role, independent of apoptosis, in certain contexts (36, 97) raising the possibility that Bid's pro-survival function may extend to necroptosis.

We have developed a series of mouse models in which we alter the mechanism of cell death in hematopoiesis. Bone marrow in wild-type (WT) mice undergoes predominantly apoptotic cell death. As necroptosis is known to occur in situations where apoptosis is inhibited (49) we constructed a mouse in which intrinsic apoptosis is blocked in hematopoiesis: germline deletion of *Bak* and conditional deletion of *Bax* within the

hematopoietic system with *VavCre* (DKO mice) completely blocks apoptotic cell death but is not sufficient to initiate necroptotic cell death. Further deletion of Bid (to create *BaxBakBid* triple-knockout [TKO] mice) leads to robust activation of necroptosis. While protection from programmed cell death leads to leukemia (double-knockout [DKO] mice), increased necroptotic cell death (TKO) leads to decreased survival due to bone marrow failure (BMF). Importantly, restoring WT levels of Ripk1 through genetic knockdown of 1 allele of Ripk1 fully restores peripheral blood counts and substantially increases progenitor cell percentages and proliferation as measured by 5-bromo-29-deoxyuridine (BrdU) incorporation, establishing that TKO BMF is driven by Ripk1.

As a consequence of necroptosis, TKO mice display increased bone marrow cytokine production. This cytokine production is significantly diminished by genetically restoring normal levels of Ripk1 in TKO mice. Furthermore, blocking TNFα in TKO mice with the decoy TNFR etanercept (Enbrel) partially restores TKO progenitor cells, anemia, and thrombocytopenia. Lastly, in samples from patients with the BMF disorder myelodysplastic syndrome (MDS), we observe prominent Ripk1 and phospho-mixed lineage kinase domain-like pseudokinase (pMLKL) immunofluorescence staining and necroptotic morphology by electron microscopy. Thus, we propose that uncontrolled necroptosis-mediated cell death leads to BMF that is in part due to inflammation and resembles MDS.

Results

VavCreBaxBakBid TKO mice die of BMF

To create a mouse model with increased bone marrow necroptosis, we first blocked intrinsic apoptotic execution in hematopoiesis by creating *VavCreBax*$^{F/F}$*Bak-/-* DKO mice (Figure 4-1) (286). We then crossed DKO mice with mice harboring germline

deletion of Bid (95) resulting in *VavCreBax*$^{F/F}$*BakBid* TKO mice. *VavCre* efficiently deletes *Bax* in the bone marrow and spleen of DKO and TKO mice (Figure 4-1 B-C).

DKO mice die predominantly of leukemia (89%) that can be transferred to recipient mice, with a median survival of 10 months, consistent with loss of mitochondrial-mediated death (Figure 1D-F) (101). In contrast, TKO mice develop significant cytopenias (Figure 1G); 66% die of BMF, and 22% die of leukemia (Figure 1D-E), with a median survival of 5.5 months. Morphologically, TKO marrow harbors dysplastic myeloid cells, including neutrophil hypersegmentation, megakaryocyte hypo-lobulation, and erythroid precursor binucleation and intra-chromosomal bridging (Figure 1H) (287). Thus, hematopoietic loss of Bax and Bak prevents apoptosis and promotes leukemia. Further loss of Bid results in BMF.

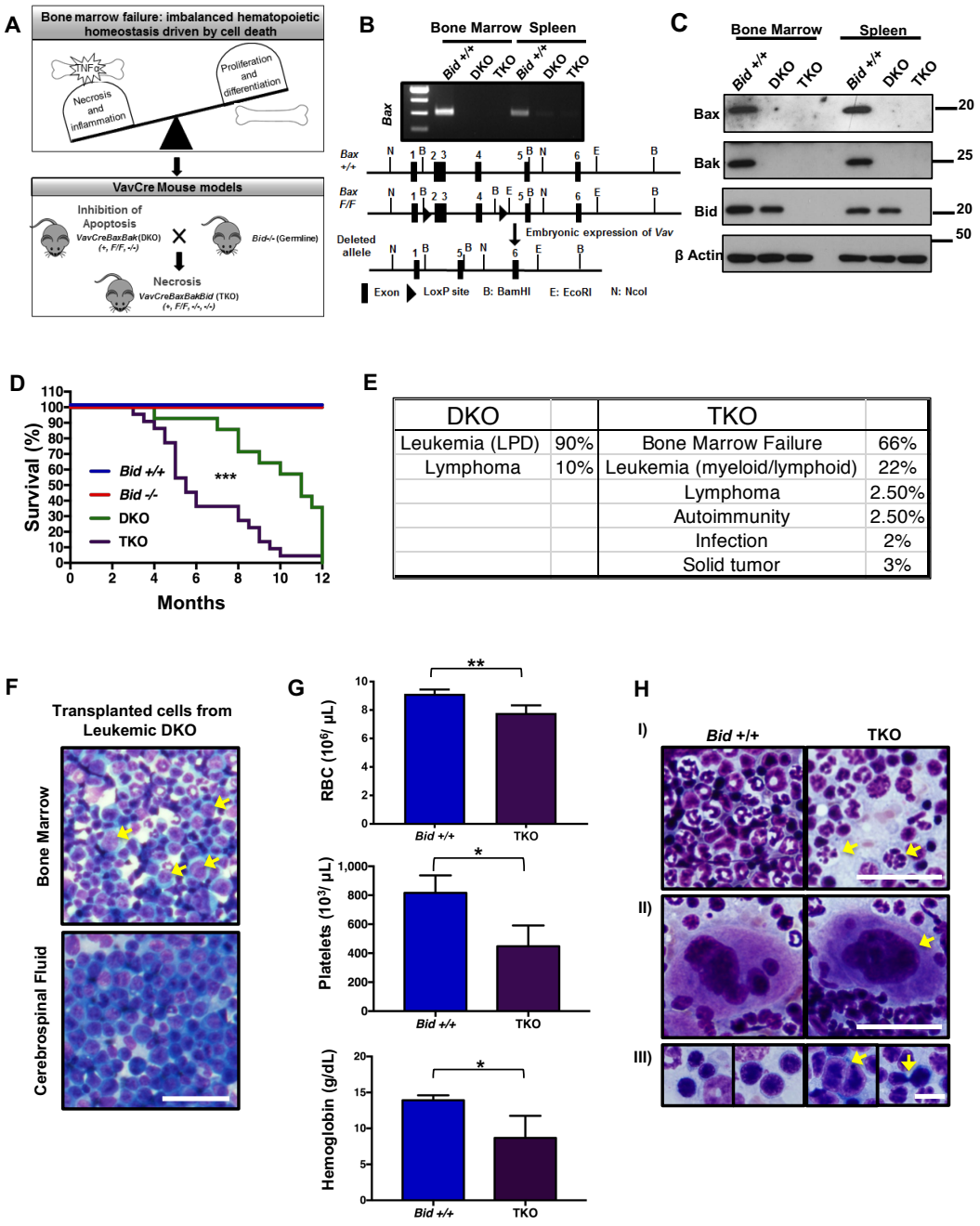

DKO		TKO	
Leukemia (LPD)	90%	Bone Marrow Failure	66%
Lymphoma	10%	Leukemia (myeloid/lymphoid)	22%
		Lymphoma	2.50%
		Autoimmunity	2.50%
		Infection	2%
		Solid tumor	3%

Figure 4-1. *VavCreBaxBakBid* TKO mice die of bone marrow failure (BMF).
(A) Schematic of hematopoietic homeostasis and bone marrow failure (BMF) and development of *VavCre* transgenic mouse models to study the role of cell death. (B) Deletion of *Bax* in bone marrow and spleen determined by RT-PCR (top) and diagram of highlighting Cre Lox recombination with LoxP sites flanking exons 2-4 of *Bax* gene (bottom). (C) Immunoblot examining expression of Bax, Bak, and Bid in WT (*Bid*+/+), *VavCreBaxBak* (DKO), and *VavCreBaxBakBid* (TKO) mice. (D) Survival curves of *Bid* +/+, *Bid* -/-, DKO,

Figure 4-1 Continued.
and TKO mice. Statistics demonstrate differences between DKO and TKO animals. *Bid*+/+ n=4, *Bid*-/- n=4, DKO n=14, TKO n=22. (E) Cause of death in DKO and TKO mice determined at time of necropsy. (F) Bone marrow and cerebrospinal fluid from *Bid* +/+ mice transplanted with leukemic DKO bone marrow post sub-lethal irradiation. Arrows indicate leukemic blasts. Scale bar denotes 50 microns. (G) From top to bottom complete blood counts (CBCs) including: RBCs (10^6/µl), platelet counts (10^6/µl), and hemoglobin (g/dL), n=3,4 *Bid*+/+ and TKO mice, respectively. (H) Cytospins from bone marrow *Bid* +/+ and TKO mouse bone marrow mice denoting I) neutrophils, II) megakaryocytes, and III) erythroid precursors. Arrows indicate I) hyper-segmentation, II) hypo-lobulation, and III) binucleation and intra-chromosomal bridging. Scale bars=10 microns. *p< 0.05, ***p< 0.001. Data are representative of mean +/- SEM. Contribution: PCR and Western blot analysis by Wagner PN and Shi Q (Panels B and C). All other experiments by Wagner PN with pathology assistance by Claudio Mosse (Panels D-H).

TKO bone marrow displays necrotic morphology and increased Rip1 kinase

We examined cellular morphology, a defining feature of both apoptosis (eg, pyknotic nuclei, cell membrane and organelle shrinkage) and necroptosis (eg, membrane integrity loss, cell membrane and organelle swelling) by transmission electron microscopy (TEM). TKO bone marrow cells displayed significantly increased necrotic morphology compared with *Bid*-/- bone marrow cells (25% vs 7% [of 100 cells], respectively) (Figure 4-2 A, B). Furthermore, cells undergoing necrotic death have recently been reported to display bubbles at the membrane by TEM as a consequence of phospho-MLKL (pMLKL) activation and translocation (288). We observe an increase in the number of these bubbles in TKO bone marrow compared with *Bid*-/- marrow (Figure 4-2 C, D), consistent with activated pMLKL.

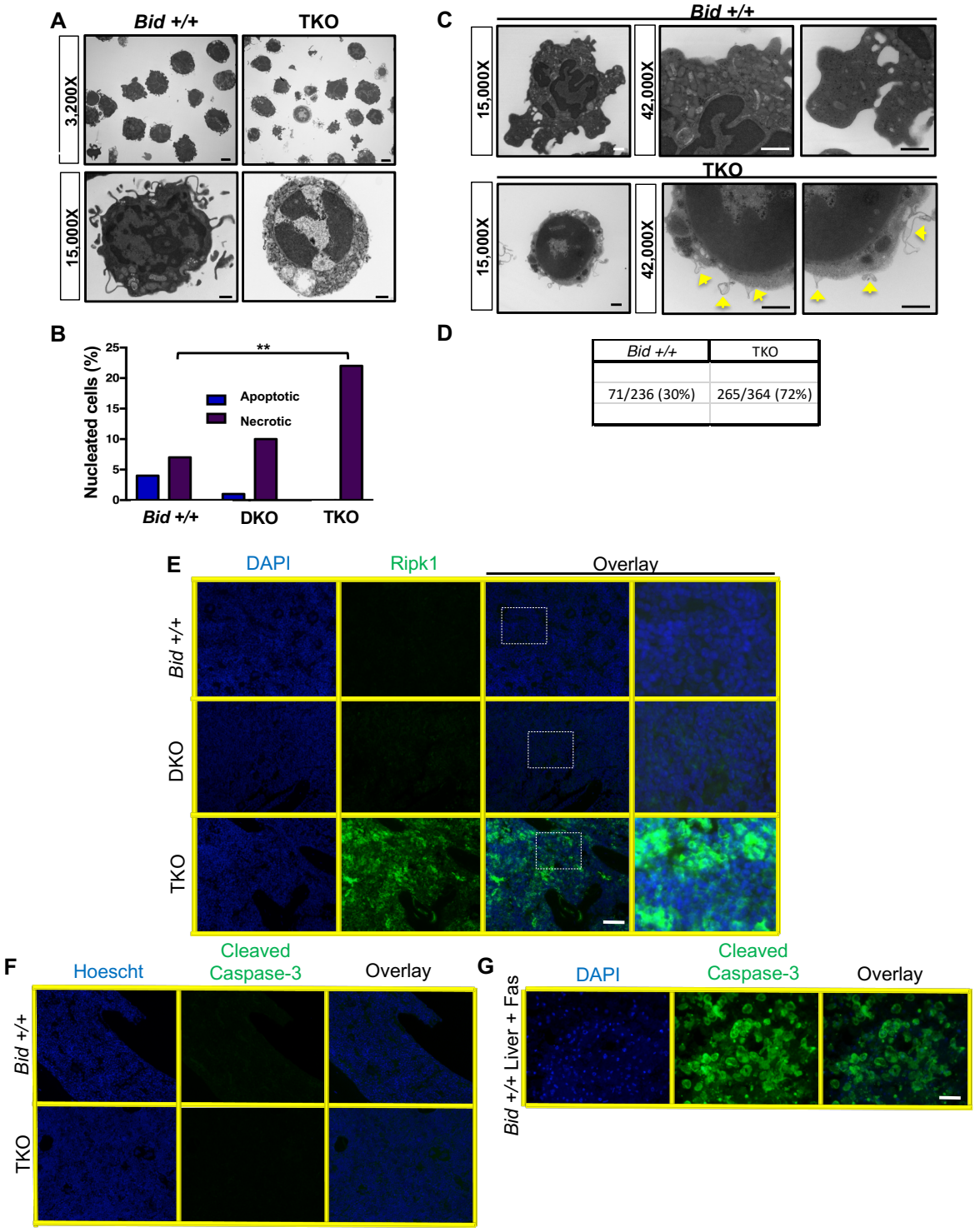

Figure 4-2. TKO bone marrow dies by necrosis.
(A) Representative transmission electron microscopy (TEM) images from *Bid* +/+ and TKO mice. Upper image (3,200X magnification), scale bar=2 microns and lower image (15,000X magnification), scale bar= 500 nanometers. (B) Quantitation of apoptotic and necrotic cells from *Bid*+/+, DKO, and TKO TEM. 100 cells with a nucleus from lower magnification images were scored based on cell and organelle morphology (See

Figure 4-2 Continued.
supplemental methods for quantitation details). (C) TEM images of bone marrow from *Bid*+/+ and TKO mice analyzed for membrane bubble. Images of the whole cell are 15,000X magnification and zoomed images of the cell membrane are 42,000X, scale bar = 500 nanometers for both. (D) Quantitation of the number of bubbles show in C. (E) Ripk1 fluorescent immunohistochemistry as a marker for necrotic cell death on paraffin-embedded bone marrow sections from *Bid* +/+, DKO, and TKO mice. Staining was performed three independent times, scale bar= 50 microns. Zoomed in images (250%) are of indicated boxed area. (F) Fluorescent immunohistochemistry for cleaved caspase-3 as a marker of apoptotic cell death on *Bid*+/+ and TKO bone marrow sections as in (C). (G) Fluorescent immunohistochemistry for *Bid* +/+ liver post-tail vein injection with Fas ligand as a positive control for cleaved caspase-3 staining. **p< 0.01. Data are representative of mean +/- SEM. Contribution: Electron microscopy and analysis by Wagner PN (Panels A, B). Analysis of membrane bubbles by Mary Dawes, Zinkel SS, and Salisbury-Ruf CT (Panels C and D). Immunofluorescence by Shi Q (Panels E-G).

Consistent with the observed cellular morphology, Ripk1 levels are increased in TKO bone marrow, but not *Bid*+/+, *Bid-/-*, or DKO bone marrow (Figure 4-2 E). Minimal cleaved caspase-3 was observed in *Bid*+/+, TKO (Figure 4-2 F), *Bid-/-*, and DKO bone marrow (Figure 4-3 A). A strong cleaved caspase-3 signal was observed in *Bid-/-* Fas-treated livers, validating our antibody and staining technique (Figure 4-2 G). Ripk1 staining of WT cells, but not *Ripk1-/-* 3T3 cells, validated specificity of Ripk1 staining (Figure 4-3 B, C). Only in the context of transformation from BMF to leukemia do we observe decreased Ripk1 (Figure 4-3 D). Overall, these results are consistent with abrogation of apoptosis in DKO bone marrow and increased necroptosis upon additional loss of Bid in TKO bone marrow under homeostatic conditions.

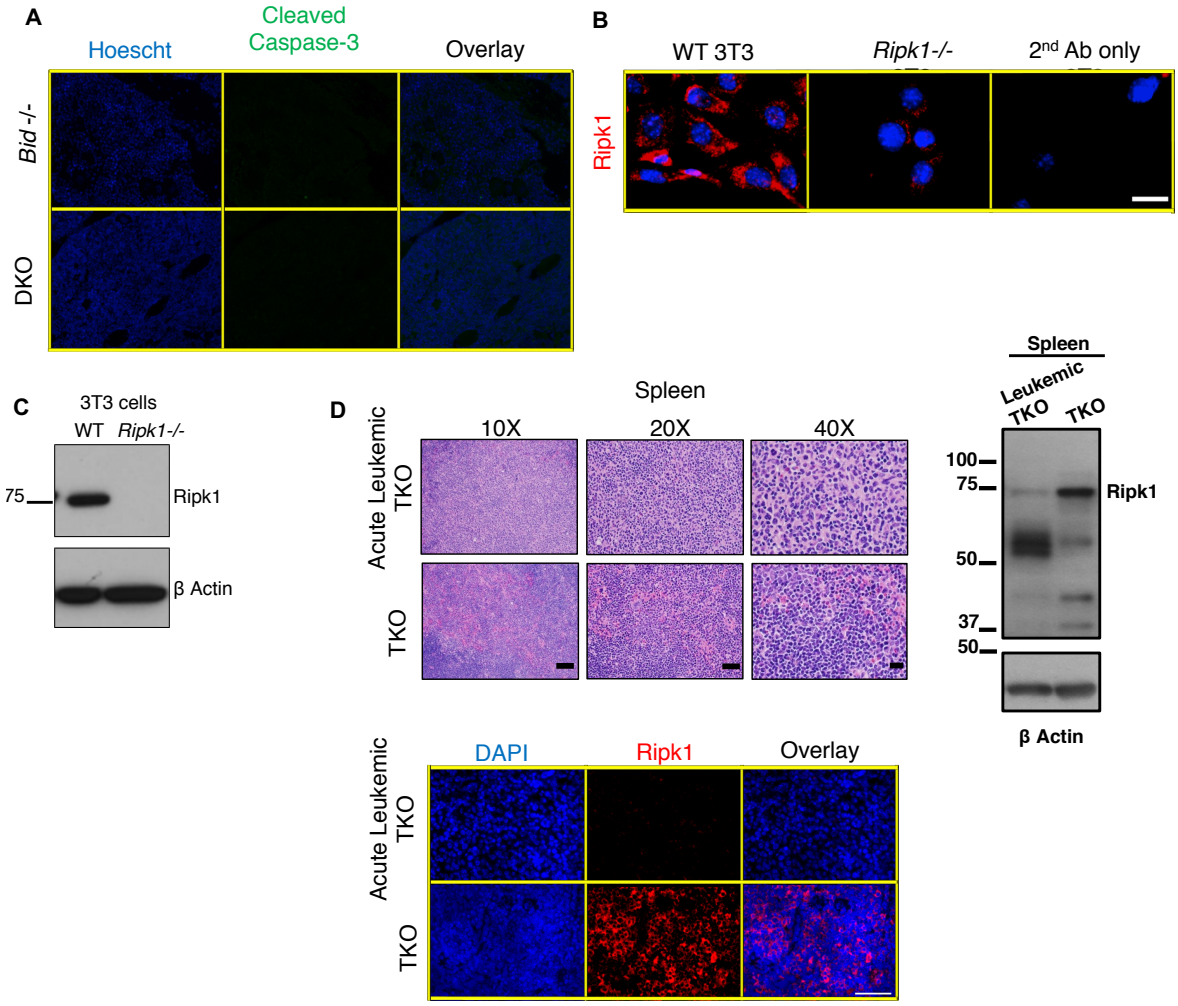

Figure 4-3. TKO mice have decreased Ripk1 upon transformation to leukemia.
(A) Fluorescent immunohistochemistry for cleaved caspase-3 on paraffin-embedded bone marrow sections from *Bid-/-* and DKO mice. Staining was performed three independent times, scale bar=50 microns. (B) Immunofluorescence for Rip1 in wild-type (WT) and *Ripk1-/-* 3T3 cells. (C) Western blot for Ripk1 from WT and *Ripk1-/-* 3T3 cells. ns=not significant. (D) Comparison of a non-leukemic and acute leukemic TKO mouse including H&E and immunofluorescence (IF) for Ripk1, and Western blot of Ripk1 of splenic tissue. H&E scale bars: 10X = 100 microns, 20x = 50 microns, and 40X = 20 microns. IF scale bar = 50 microns. Contribution: Immunofluorescence by Shi Q (Panel A). All other experiments by Salisbury-Ruf CT.

TKO myeloid progenitors die by necrosis

We next generated Hox11 immortalized myeloid progenitor cells (MPCs) from the bone marrow of *Bid*+/+, DKO, and TKO mice (36). We treated these MPCs with TNFα plus actinomycin D (ActD) to activate TNFR cell death signaling. As expected, $Bid^{-/-}$and DKO cells exhibited less death (by Annexin V^+/propidium $iodide^+$) in response to TNFα/ActD (289). TKO and *Bid*+/+ cells display similar death kinetics (Figure 4-4 A); however, *Bid*+/+, but not TKO MPCs, displayed increased cleaved caspase-3 (Figure 4-5A). TEM of untreated MPCs reveals minimal cell death (Figure 4-5B). TEM of TNFα/ActD-treated MPCs reveals predominantly apoptotic morphology in *Bid*+/+ cells and predominantly necrotic cell morphology in TKO cells (Figure 4-4 B). Canonical death receptor signaling is thus preserved in our MPCs. *Bid*+/+ MPCs undergo apoptosis in response to TNFα/ActD, and removal of *Bax* and *Bak* prevents cell death. Importantly, removal of *Bid* in addition to *Bax* and *Bak* results in necroptotic cell death, consistent with a novel role for Bid to restrain necroptosis.

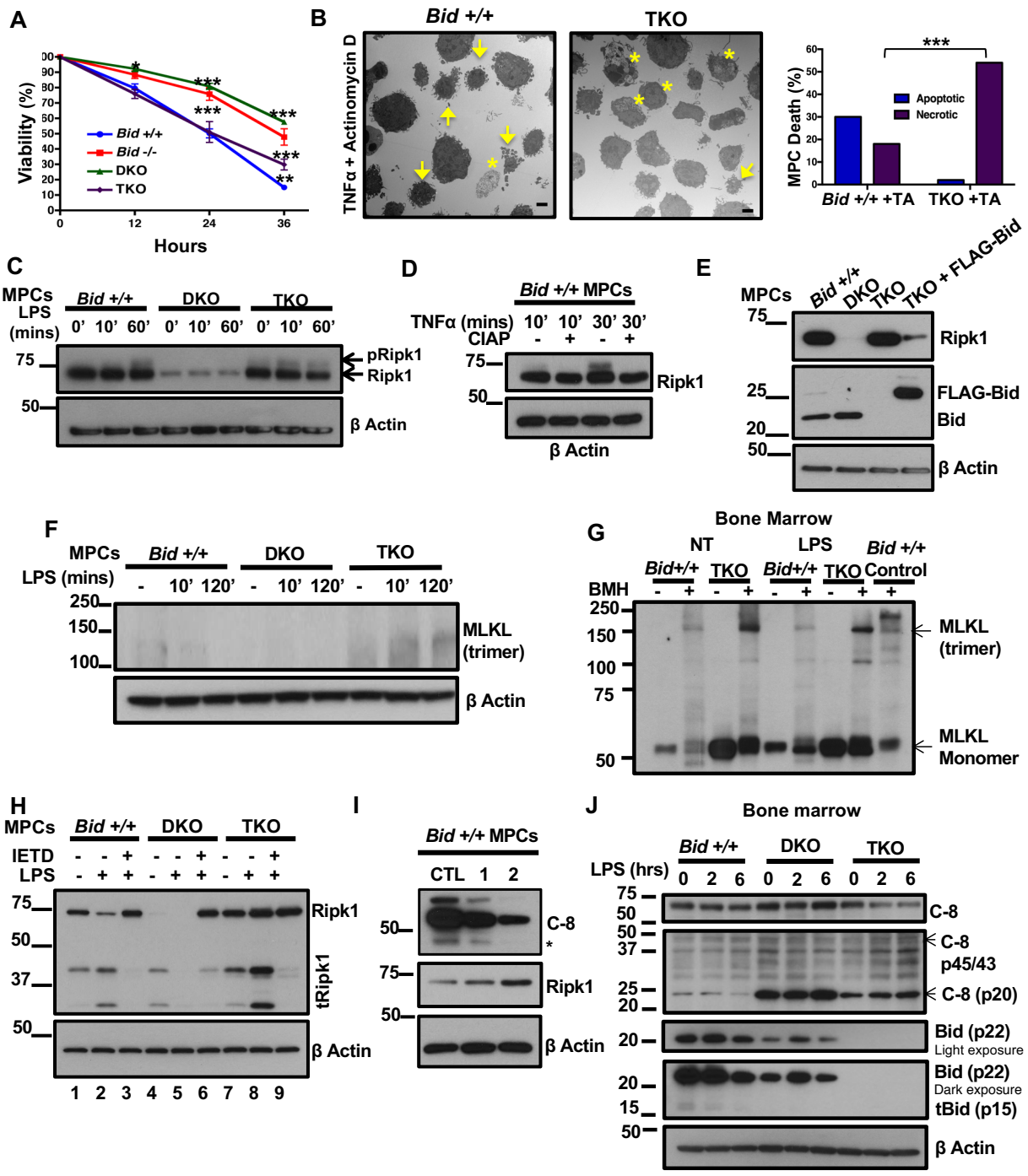

Figure 4-4. Bid modulates Ripk1 signaling in MPCs in a caspase 8-dependent manner. (A) Examination of death in myeloid progenitor cells (MPCs). MPCs were treated with 25 ng/mL TNFα + 50 ng/mL Actinomycin D (ActD). Viability was determined by Annexin V/ PI staining. Experiment was performed three independent times. Statistics indicate differences between *Bid* +/+ versus *Bid* -/-, DKO, and TKO. (B) *Bid* +/+ and TKO

Figure 4-4 Continued.
MPCs treated with TNFα/ActD were examined by transmission electron microscopy (TEM). 50 cells with a nucleus were examined and characterized as being apoptotic or necrotic. Arrows indicate apoptotic cells, and asterisks indicate necrotic cells, scale bar=2 microns. Quantitation of cells to the right of images. (C) MPCs unstimulated or stimulated with 250 ng/mL LPS for 10 minutes and 1 hour followed by immunoblot for Ripk1. pRipk1 indicates Ripk1 phosphorylation. Experiment was performed four times. (D) Immunoblot of *Bid*+/+ MPCs treated with or without TNFα in the presence or absence of CIAP. pRipk1 is lost in the presence of CIAP. (E) Immunoblot of Ripk1 in *Bid*+/+, DKO, TKO and TKO+ FLAG-Bid MPCs following LPS stimulation. Experiment performed two independent times. (F) Immunoblot of MLKL trimerization in *Bid* +/+, DKO, and TKO MPCs following stimulation with LPS. MLKL trimer is approximately 150 kDa. Experiment was performed three times. (G) Bone marrow from *Bid*+/+ and TKO mice treated with or without LPS (250 ng/mL) for 4 hours followed by BMH crosslinking and probed for MLKL. Control lane indicates *Bid* +/+ bone marrow pre-treated with zVAD (25 μM) followed by Smac mimetic (Birinapant, 100 nM) and TNFα (25 ng/ml) for 4 hours as a positive control. Experiment was performed 2 independent times. (H) Immunoblot of Ripk1 in *Bid*+/+, DKO, and TKO MPCs following stimulation with 250 ng/mL LPS and pre-treatment with 20μM Z-IETD-FMK (inhibitor of Caspase-8). Experiment was performed three independent times. (I) Ripk1 levels by immunoblot after knock-down of Caspase-8 utilizing the CRISPR-Cas9 system in *Bid* +/+ MPCs. Experiment was performed two times. (J) Immunoblot of bone marrow from *Bid*+/+, DKO, and TKO mice treated with LPS for the indicated times. **p<0.01, ***p< 0.001. Data are representative of mean +/- SEM. Contribution: Analysis of MPC cell death by Wagner PN (Panels A and B). Western analysis by Shi Q (Panels C-F, H and I) and Salisbury-Ruf CT (Panels G and J).

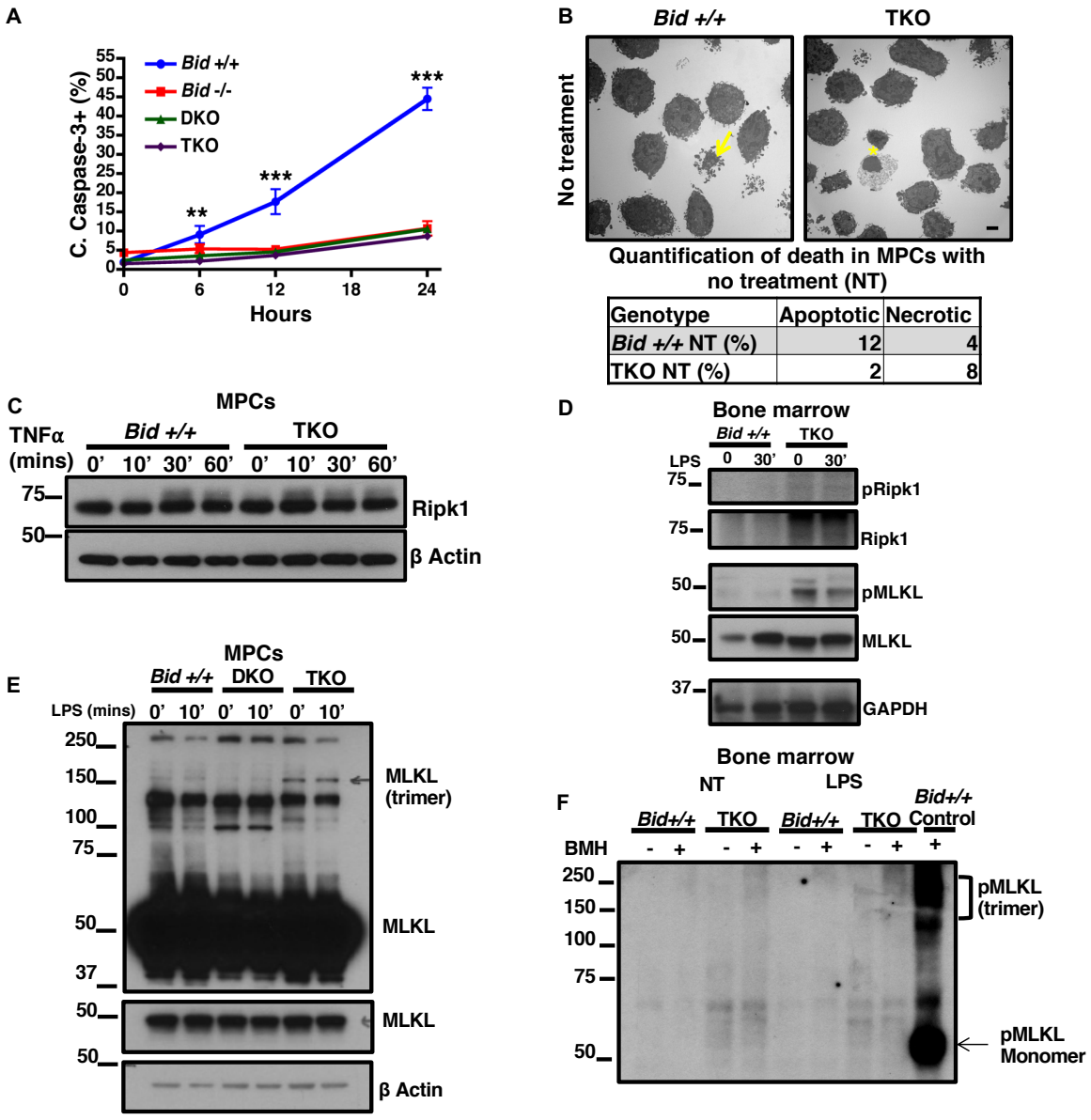

Figure 4-5. TKO MPCs and bone marrow have increased pRipk1 and pMLKL with and without TNFα or LPS stimulation.

(A) MPCs treated with TNFα/ActD (as in Fig. 3A) for cleaved Caspase-3 (C. Caspase-3+) by intracellular flow cytometry. Statistics indicate *Bid*+/+ versus all other cell lines. (B) TEM of *Bid* +/+ and TKO MPCs without stimulation and quantification in the table below. 50 cells with a nucleus were scored as being live, apoptotic, or necroptotic. Scale bar indicates 2 microns. (C) Examination of Ripk1 phosphorylation by immunoblot following stimulation of *Bid* +/+ *a*nd TKO MPCs with TNFα. Experiment was performed two independent times. (D) Bone marrow treated with or without LPS (250 ng/ml) for 30 minutes from *Bid*+/+ and TKO mice and probed for MLKL, phospho-MLKL (pMLKL), Ripk1, and phospho-Ripk1 (pRipk1). (E) MLKL immunoblot from *Bid*+/+, DKO, and

Figure 4-5 Continued.
TKO MPCs demonstrating MLKL trimer and monomer together. Second MLKL blot is a lower exposure of the monomer. Representative of 2 independent experiments. (F) Bone marrow from *Bid*+/+ and TKO mice treated with or without LPS (250 ng/ml) for 4 hours followed by BMH crosslinking and probed for phospho-MLKL. Control lane indicates *Bid*+/+ bone marrow treated with BMH as described in Fig. 3D. **p<0.01, ***p<0.001. Data are representative of mean +/- SEM. Contribution: MPC experiments performed by Wagner PN with electron microscopy by Janice Williams (Panels A and B). Western blot analysis by Shi Q (Panels C and D) and D and Salisbury-Ruf CT (Panels D and F).

TKO MPCs and bone marrow display increased necroptotic signaling

Phosphorylation of Ripk1 has been shown to stabilize its association with a pro-necroptotic complex and activate necroptotic kinase activity (290) TKO MPCs, but not *Bid*+/+, *Bid*-/-, or DKO MPCs, displayed constitutive and increased kinetics of Ripk1 phosphorylation manifested by a phosphatase-sensitive shifted band upon treatment with lipopolysaccharide (LPS) (291) or TNFα (Figure 4-4 C, D; Figure 4-5 C, D). Furthermore, TKO bone marrow exhibits more total Ripk1 and phospho-Ripk1 (Figure 4-5 D). Importantly, reintroduction of FLAG-tagged Bid into TKO MPCs by retroviral transduction results in decreased Ripk1 levels (Figure 4-4 E), demonstrating that decreased Ripk1 observed in DKO MPCs is due to the presence of Bid.

In addition, TKO MPCs, but not *Bid*+/+ or DKO MPCs, display increased MLKL trimerization with or without LPS stimulation (Figure 4-4 F; Figure 4-5 E) (53). Importantly, TKO bone marrow with and without LPS stimulation, displays increased MLKL monomers, trimers, and phospho-MLKL relative to *Bid*+/+ bone marrow (Figure 4-4 G; Figure 4-5). These results suggest that loss of Bid in addition to Bax and Bak is sufficient to stimulate Ripk1 phosphorylation and MLKL trimerization, consistent with increased necroptotic signaling.

Bid regulates Ripk1 stability by modulating caspase-8 activity

The above studies reveal that Ripk1 levels vary markedly between genotypes, with decreased Ripk1 observed in DKO MPCs compared with both *Bid*+/+ and TKO cells (Figure 4-4 C).

Ripk1 can be cleaved by proteases such as caspase-828 and cathepsins29 to generate truncated Ripk1 (tRipk1). Treatment with the caspase-8–specific inhibitor Z-IETD-FMK, but not MG132 (proteasome inhibitor) or Z-VAD-FMK (pan-caspase inhibitor), following LPS (Figure 4-4 H; Figure 4-6 A) completely recovered full-length Ripk1 in DKO MPCs and decreased tRipk1 in *Bid*+/+ and TKO MPCs, indicating that a Z-IETD-FMK–inhibitable enzyme cleaves Ripk1. Similar recovery of a caspase-8 substrate, cylindromatosis, was also observed (Figure 4-6 B). Furthermore, deletion of caspase-8 using CRISPR-Cas9 with 2 independent guide RNAs increased Ripk1 levels in *Bid*+/+ MPCs proportional to the degree of caspase-8 knockdown (Figure 4-4 I).

Treatment of *Bid*+/+, DKO, and TKO bone marrow with LPS also revealed striking differences in caspase-8 levels. Both the p43/45 and p20 forms of active caspase-8 are elevated in DKO bone marrow. Despite this, only minimal cleaved Bid (tBid) can be observed in *Bid*+/+, but not DKO, marrow (Figure 4-4 J). This suggests that in the absence of Bax and Bak, caspase-8 preferentially cleaves Ripk1 over Bid. The above results are consistent with a role for caspase-8 in mediating Ripk1 levels.

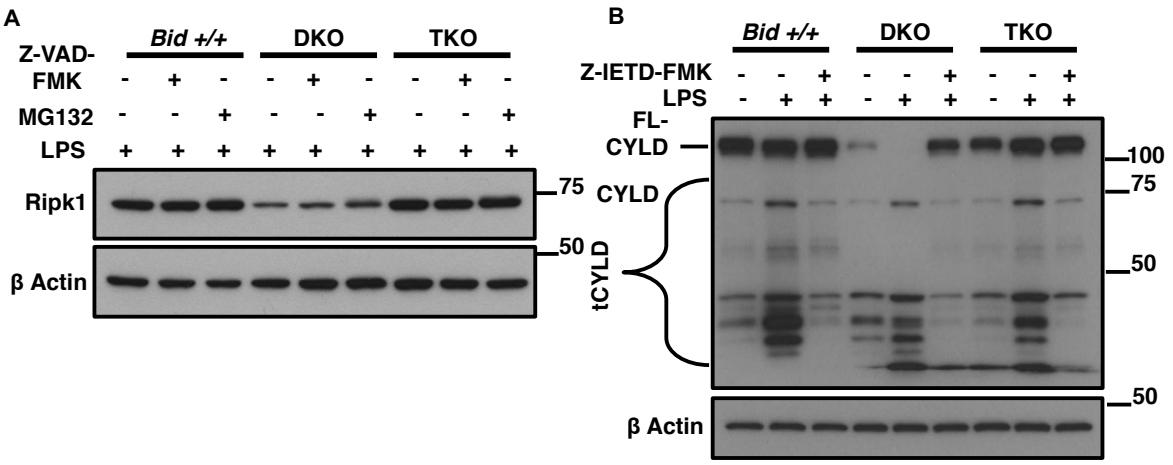

Figure 4-6. Proteasome inhibitor does not restore Ripk1 levels in DKO MPCs and caspase-8 inhibition prevents CYLD cleavage.
(A) Examination of Ripk1 following treatment of MPCs with LPS, MG132, and Z-VAD-FMK. Experiment was performed three independent times. (B) Examination of CYLD in *Bid*+/+, DKO, and TKO MPCs by immunoblot following stimulation with LPS (for 10 minutes) and pre-treatment with 20μM Z-IETD-FMK (inhibitor of Caspase-8/ Granzyme B). Experiment was performed two independent times. FL-CYLD=full-length, tCYLD=truncated. Contribution: All experiments performed by Shi Q.

Unrestrained bone marrow necroptosis disrupts hematopoietic homeostasis

To determine whether bone marrow necroptosis may impair hematopoietic homeostasis, we evaluated hematopoietic stem and progenitor cell (HSPC) populations. Immunophenotyping of HSPCs reveals that LSK (Lin^- $Sca1^-$c-Kit^+) cell populations are expanded in TKO mice, but not *Bid*+/+, *Bid*-/- or DKO mice (Figure 4-7 A). The signaling lymphocyte activating molecule hematopoietic stem cell (SLAM-HSC; LSK $Flt3^{Lo}CD48^-CD150^+$) population30 continues to expand in TKO mice with age, whereas SLAM-HSC populations decline in aged DKO mice. Accordingly, TKO, but not DKO, SLAM-HSCs displayed in-creased numbers (Figure 4-7 B; Figure 4-8 A) as well as proliferation assessed by in vivo BrdU analysis (Figure 4-7 C), consistent with an appropriate response to bone marrow stress. Long-term hematopoietic stem cell (Lin^-

$Sca1^{+}$c-$Kit^{+}CD135^{Lo}$) populations were not significantly changed between genotypes (Figure 4-8 B).

Given the apparent bone marrow stress observed in TKO SLAM-HSCs, we anticipated similar progenitor expansion. In contrast, we observed decreased TKO myeloid progenitor (Lin^{-} $Sca1^{-}$c-Kit^{+}) populations (Figure 4-7 D) with decreased BrdU incorporation as compared with *Bid*+/+ mice (Figure 4-7 E), consistent with increased progenitor cell death with compensatory hematopoietic stem cell proliferation. Despite a similarly decreased progenitor cell population, DKO mice do not display increased SLAM-HSC proliferation (Figure 4-7 B-C), suggesting a distinct defect in hematopoietic homeostasis in the setting of impaired apoptosis (DKO) vs increased necroptosis (TKO).

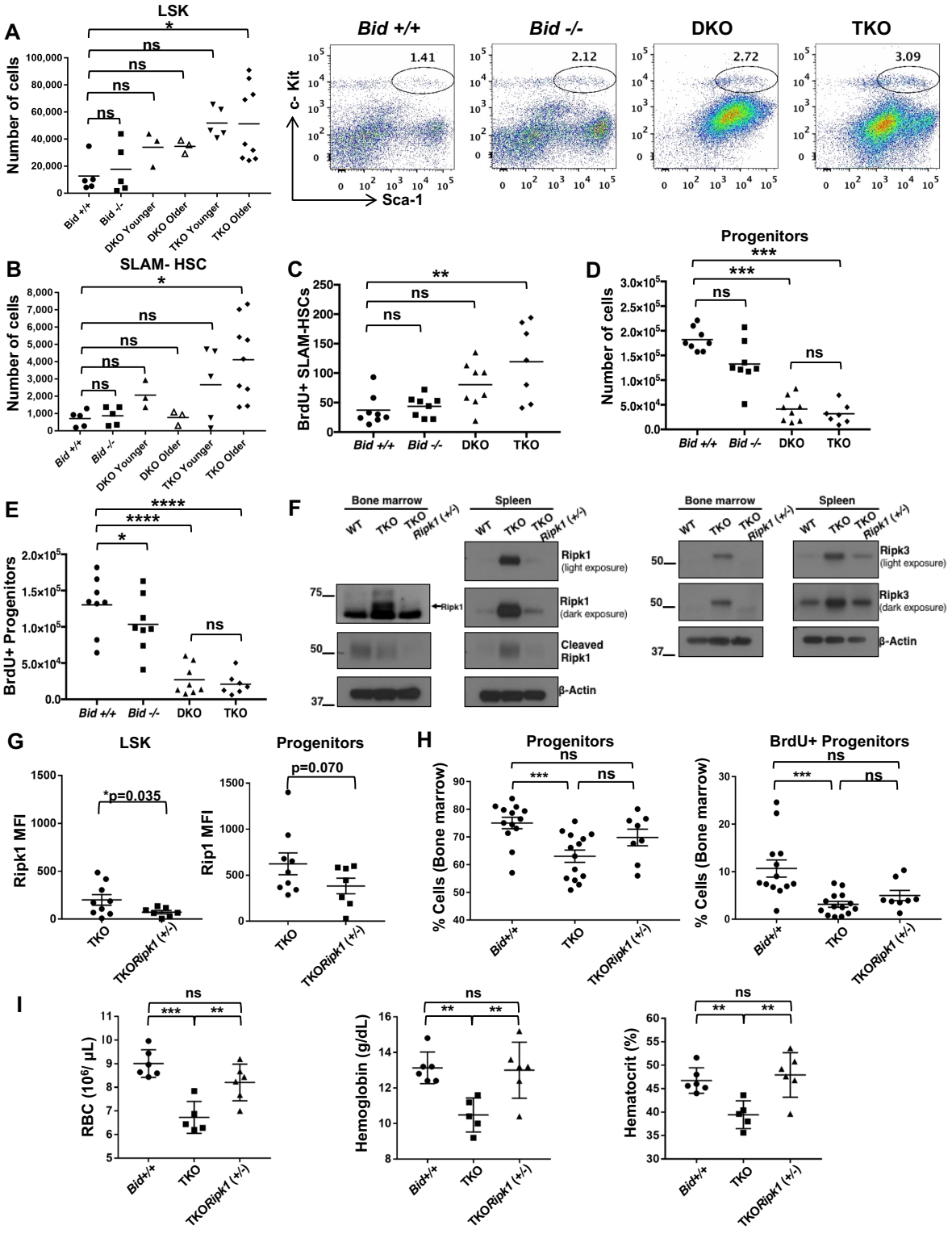
A
LSK
Number of cells
Bid +/+
Bid -/-
DKO Younger
DKO Older
TKO Younger
TKO Older
Bid +/+
Bid -/-
DKO
TKO
1.41
2.12
2.72
3.09
c- Kit
Sca-1
B
SLAM- HSC
C
BrdU+ SLAM-HSCs
D
Progenitors
E
BrdU+ Progenitors
F
Bone marrow
Spleen
WT
TKO
Ripk1 (+/-)
Ripk1
(light exposure)
(dark exposure)
Cleaved Ripk1
β-Actin
Ripk3
G
LSK
Progenitors
Ripk1 MFI
Rip1 MFI
*p=0.035
p=0.070
TKORipk1 (+/-)
H
Progenitors
BrdU+ Progenitors
% Cells (Bone marrow)
I
RBC (10⁶/ µL)
Hemoglobin (g/dL)
Hematocrit (%)

Figure 4-7. TKO mice have fewer myeloid progenitor cells and more hematopoietic stem cells (HSCs), which can be rescued with a genetic cross to *Ripk1* (+/-) heterozygous mice.
(A) Flow cytometry analysis of bone marrow to examine LSK (Lineage$^-$, Sca-1$^+$, c-Kit$^+$) and (B) SLAM-HSC (Signaling lymphocyte activating molecule- hematopoietic stem cell) populations. Mice were examined before onset of sickness. Younger mice were 11-15 weeks old and older mice were 15-20 weeks of age. *Bid* +/+ n=5, *Bid* -/- n=5, DKO n=6, TKO younger n=5, and TKO older n=9 (C) Examination of the number of BrdU+ SLAM-HSCs in bone marrow. Mice were injected with a total of 4mg of BrdU in three doses over 36 hours. Bone marrow was harvested, depleted for terminal lineages, and stained for flow cytometry. Mice were 18-20 weeks of age. (D) Numbers of myeloid progenitors (Lineage$^-$, Sca-1$^-$, c-Kit$^+$) as in (A). Mice were 18-20 weeks of age. (E) Number of BrdU+ myeloid progenitors. Numbers of mice for (C), (D), and (E) are as follows: *Bid*+/+ n=8, *Bid* -/- n=7, DKO n=8, TKO n=7. (F) Western blot of Ripk1, cleaved Ripk1, and Ripk3 expression in *Bid*+/+, TKO and TKO*Ripk1* (+/-) mouse bone marrow and spleen. (G) Intracellular flow cytometry analysis of LSK (left) and Progenitor cell populations (right). TKO n=9 and TKO*Ripk1* (+/-) n=6. (H) Myeloid progenitor cells (%) from lineage depleted mice. *Bid*+/+ n=12, TKO n=14, and TKO*Ripk1*(+/-) n=8. (I) BrdU+ myeloid progenitors (%) from mice. *Bid*+/+ n=13, TKO n=15, and TKO*Ripk1* (+/-) n=8. (I) RBCs (10^6/µl), Hemoglobin (g/dL), and Hematocrit (%) were measured in mice. *Bid*+/+ n=6, TKO n=6, and TKO*Ripk1* (+/-) n=6. ns= not significant, *p<0.05 **p<0.01, ***p<0.001, and ****p<0.0001. Data are representative of mean +/- SEM. Contribution: All experiments performed Wagner PN (Panels A-E) and Salisbury-Ruf CT (Panels F-I).

Consistent with the increased programmed cell death noted in myeloid cell lines, TKO mice, but not *Bid*+/+, *Bid*-/-, or DKO mice, display splenomegaly with increased Ter119 cells (erythroid), indicative of extramedullary hematopoiesis that is progressive with age (Figure 4-8 C-D). Notably, B-cell and monocyte populations are not different between genotypes at necropsy, but DKO and TKO T-cell populations are expanded (Figure 4-8 E).

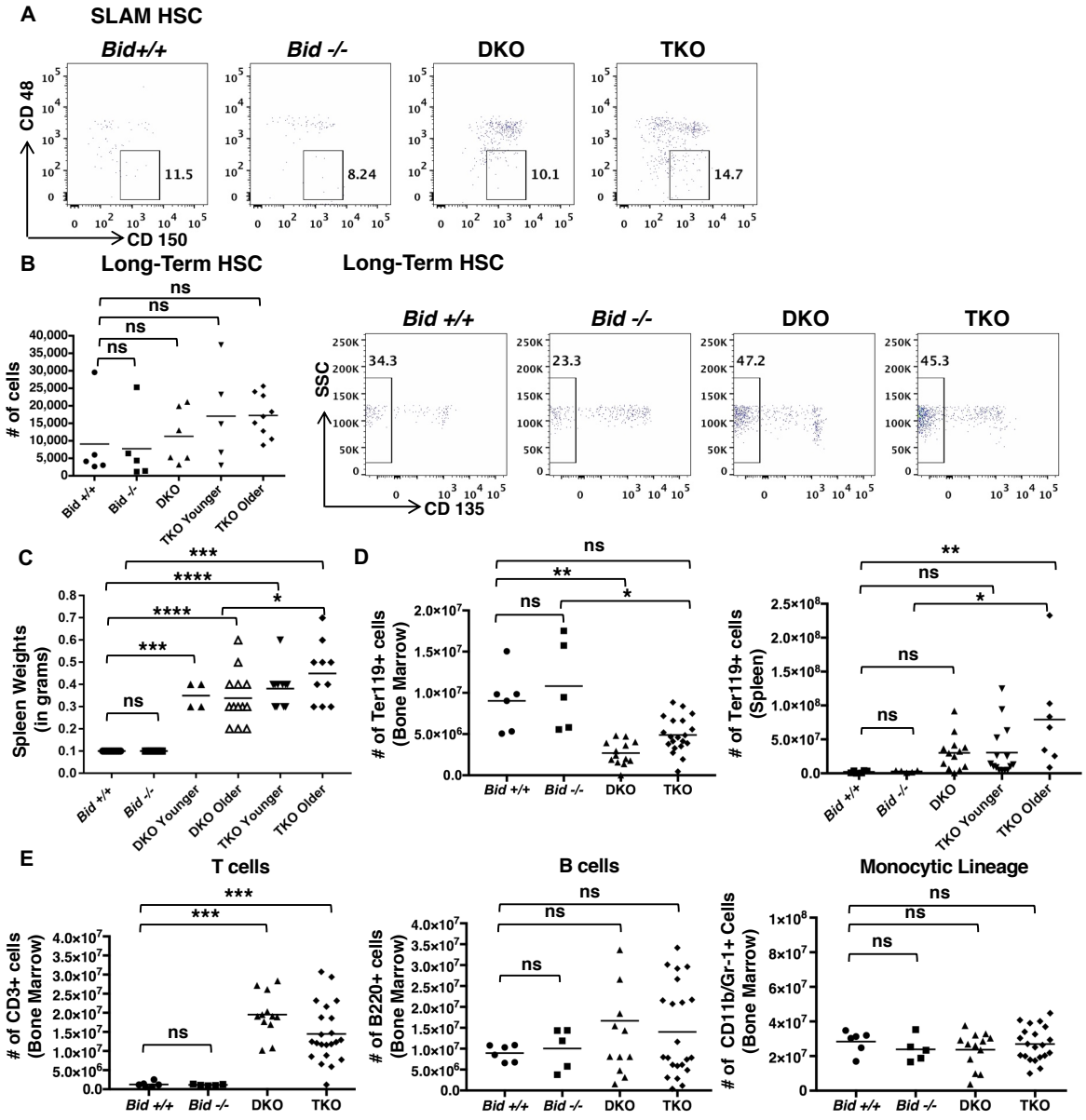

Figure 4-8. TKO mice have increased SLAM-HSCs and splenic hematopoiesis and expansion of CD3+ T-cells.

(A) Examination of SLAM-HSC population in *Bid* +/+, *Bid* -/-, DKO and TKO mice before sickness (11-20 weeks old). (B) Examination of the LT-HSC population in *Bid* +/+, *Bid* -/-, DKO and TKO mice before sickness (11-20 weeks old). Younger TKO mice are aged 11-15 weeks, and Older TKO mice are 15-20 weeks old. *Bid*+/+ n=5, *Bid*-/- n=5 DKO n= 6 TKO Younger n=5, TKO Older n=10 (C) Spleen weights of *Bid* +/+, *Bid* -/-, DKO and TKO mice before sickness as in (A) *Bid*+/+ n=11, *Bid*-/- n=9 DKO n= 15 TKO Younger n=10, TKO Older n=10. (D) Examination of Ter119+ cells in the bone marrow and spleen of mice at death (time of phenotype manifestation). TKO younger mice are 12 months old or younger, and TKO older mice are 12 months or older in age. *Bid*+/+ n=6, *Bid*-/- n=5 DKO n= 13 TKO n=22 (E) Examination of T, B, and myeloid cells in the bone

Figure 4-8 Continued.
marrow of mice at death (time of phenotype manifestation). Populations examined by flow cytometry for CD3 (T cells), B220 (B cells), and CD11b and Gr-1 double positivity (Myeloid cells). *Bid*+/+ n=6, *Bid*-/- n=5 DKO n= 13 TKO n=22. ns= not significant, *p<0.05 **p<0.01, ***p<0.001, and ****p<0.0001. Contribution: All experiments performed by Wagner PN.

Restoring normal Ripk1 levels rescues TKO red blood cells (RBCs) and bone marrow progenitors

To definitively establish whether the altered hematopoiesis observed in TKO mice was due to unrestrained necroptosis, we crossed *VavCre*TKO mice to mice in which exon 3 within the endogenous *Ripk1* gene locus is flanked by 2 loxP sites (197) to generate mice in which one allele of *Ripk1* was knocked out in hematopoietic tissues TKO*Ripk1(+/-)* (Figure 4-9 A, B). Deletion of one allele of Ripk1 resulted in decreased Ripk1 and Ripk3 levels in TKO bone marrow and spleen, comparable to Ripk1and Ripk3 levels in *Bid*+/+ mice (Figure 4-7 F). Intracellular Ripk1 staining revealed increased Ripk1 expression at baseline in progenitor compared with LSK cells in TKO*Ripk1(+/-)* mice. Importantly, Ripk1 levels were decreased in TKO*Ripk1(+/-)* LSK and progenitor populations (Figure 4-7 G; Figure 4-9 C). Compared with TKO mice, TKO*Ripk1(+/-)* mice have a trend for increased total cell number in the marrow (Figure 4-9 D), as well as increased progenitor cells and proliferation (Figure 4-7 H). Strikingly, loss of one allele of *Ripk1* is sufficient to restore red cell peripheral counts, as indicated by the number of red blood cells, hemoglobin, and hematocrit (Figure 4-7 I). Thus, we establish that increased Ripk1-mediated necroptosis drives the altered hematopoiesis observed in TKO mice.

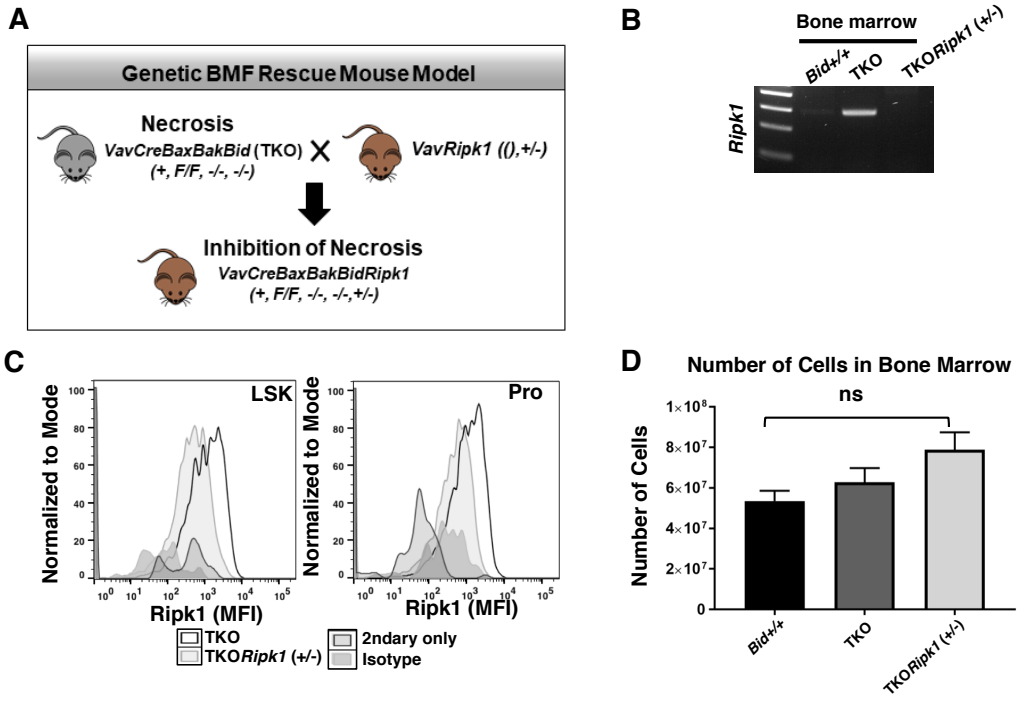

Figure 4-9. TKO*Ripk1(+/-)* mice have decreased Ripk1 in LSK and progenitor cells and no change in bone marrow cellularity.

Schematic of mouse model generated to rescue TKO mediated necrosis. (B) RT-PCR of *Ripk1* from *Bid*+/+, TKO, TKO*Ripk1* (+/-) mice. (C) Representative histograms of flow cytometry for intracellular Ripk1 mean fluorescence intensity (MFI) in TKO and TKO*Ripk1* (+/-) LKS and Progenitor (Pro) populations. (D) Number of cells from the bone marrow of *Bid*+/+, TKO, and TKO*Ripk1* (+/-) counted from all leg bones (2 tibias and 2 femurs). Contribution: All experiments performed by Salisbury-Ruf CT.

TKO cells outcompete Bid$^{+/+}$ cells but fail to maintain hematopoiesis in competitive repopulation experiments

To evaluate TKO HSPC function, we performed a competitive repopulation of lethally irradiated congenic mice. Accordingly, we injected a 1:1 ratio of TKO (Ly45.2^{+}) to *Bid*+/+ (Ly45.1^{+}) bone marrow into lethally irradiated *Bid*+/+ (Ly45.1^{+}) mice and evaluated peripheral blood for Ly45.2^{+} and Ly45.1^{+}mononuclear cells. Two additional cohorts of mice were examined in which a 1:1 ratio of *Bid*+/+ (Ly45.2^{+}) or DKO

(Ly45.2^{+}) to *Bid*+/+ (Ly45.1^{+}) marrow was similarly transplanted. Both DKO and TKO bone marrow displayed increased repopulating ability relative to *Bid*+/+ marrow (Figure 4-10 A). However, peripheral blood counts reflected bone marrow stress in TKO mice, with decreased RBC counts (anemia) and platelets (thrombocytopenia) and increasing platelet size (Mean platelet volume) over time (Figure 4-10 B-D; Figure 4-11 A, B), consistent with BMF. Despite the presence of WT bone marrow, hematopoiesis was not maintained, suggesting a cell-extrinsic effect of TKO bone marrow on WT HSPCs.

Hematopoietic stem and progenitor compartments reflect a distinct phenotype of DKO and TKO HSPCs

To further explore how altered cell death mechanism impacts non–cell-autonomous interactions in the HSPC and progenitor compartment, we evaluated progenitor, LSK, and SLAM-HSC populations after 20 weeks in primary competitive repopulation experiments. Progenitor cell numbers were similar between DKO and TKO transplanted mice and untransplanted mice (Figure 4-10 E; Figure 4-11 C) and markedly decreased relative to *Bid*+/+ transplanted mice. Interestingly, *Bid*+/+ pro-genitors in TKO transplanted mice were decreased relative to *Bid*+/+ progenitors in DKO transplanted mice, suggesting the possibility that the presence of dying TKO progenitors may impair co-transplanted *Bid*+/+ progenitors. Strikingly, whereas DKO and *Bid*+/+ LSK cell numbers are similar, TKO bone marrow displays a substantial increase in LSK cells (approximately sevenfold), with a highly significant difference between DKO and TKO LSK cell numbers (Figure 4-10 E, F). There was a trend to increased TKO SLAM-HSC (approximately twofold) numbers and a relative decrease in TKO progenitor cells

(Figure 4-11 C). In contrast, DKO HSPCs displayed a trend to an approximately twofold decrease relative to *Bid*+/+ HSPCs, consistent with bone marrow crowding due to increased mature cells (Figure 4-11 C).

To further evaluate HSPC function and compare DKO and TKO bone marrow reserve, we performed a secondary transplant. DKO bone marrow continues to outcompete *Bid*+/+ marrow even in secondary transplant conditions, indicating continued HSPC self-renewal capacity (Figure 4-10 G). In contrast, TKO bone marrow displays strikingly decreased competitive repopulating ability, consistent with decreased HSPC self-renewal capacity (exhaustion) in secondary transplant conditions (Figure 4-10 G). We thus demonstrate that increased necroptosis impairs long-term HSPC function, resulting in HSPC exhaustion.

To further explore the impact of TKO bone marrow on WT hematopoietic progenitor cell function, we isolated CD45.11 and CD45.21 cells from competitively repopulated mice by FACS sorting, cultured these cells in methylcellulose, and evaluated colony numbers 10 days after plating. Transplanted TKO cells display decreased colony-forming ability (Figure 4-10 H) relative to transplanted *Bid*+/+ cells. Strikingly, *Bid*+/+ cells transplanted in the presence of TKO cells also displayed decreased colony-forming ability as measured by the ratio of CD45.11 cells transplanted with *Bid*+/+ cells to CD45.11 cells transplanted with TKO cells (Figure 4-10 I).

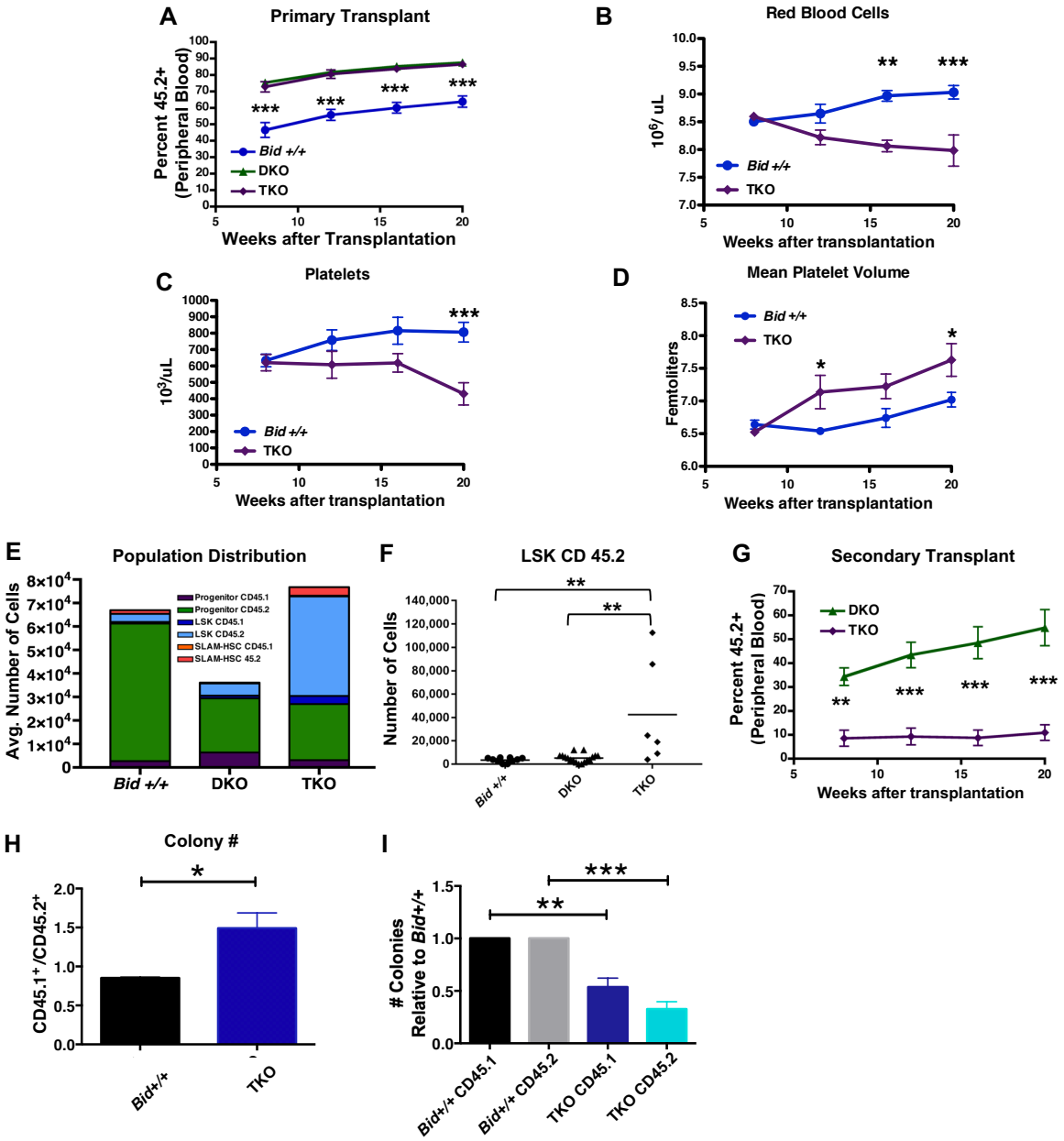

Figure 4-10. TKO bone marrow can reconstitute and outcompete *Bid* +/+ bone marrow but is unable to maintain long-term hematopoiesis.

Percent CD45.2+ cells in *Bid* +/+, DKO, and TKO transplant mice at 8,12,16, and 20 weeks after transplantation. Mice were transplanted with experimental and control bone marrow at a 1:1 ratio. *Bid* +/+ n=7, DKO n=7, TKO n=6. Statistics demonstrate differences between *Bid* +/+ and TKO animals. (B) RBCs (10^6/µl), (C) Platelet counts (10^3/µl), and (D) Mean platelet volume (FL) in transplanted *Bid* +/+ and TKO mice at 8, 12, 16, and 20 weeks after transplantation. *Bid* +/+ n=5, TKO n=8. Statistics demonstrate differences between *Bid* +/+ and TKO animals. € Distribution of myeloid progenitor, LSK, and SLAM-HSC populations in *Bid* +/+, DKO, and TKO transplanted mice. *Bid* +/+ n=5, DKO n=7, TKO n=6. (F) CD45.2 positive LSK cells in transplanted mice. (G) Secondary transplantation of DKO and TKO bone marrow (primary transplant in a 1:1 ratio with *Bid* +/+) to rigorously

Figure 4-10 Continued.
test HSC function. DKO n=8 and TKO n=7. (H) Ratio of the colony-forming ability of CD45.1$^+$ to CD45.2$^+$ cells isolated from primary transplants. *Bid*+/+ or TKO CD45.2$^+$ cells are transplanted in a 1:1 ratio with congenic CD45.1$^+$ *Bid*+/+ cells. CD45.1$^+$ and CD45.2$^+$ bone marrow cells were sorted and cultured in methylcellulose in the presence of IL3, IL6, SCF, EPO. Colonies were counted at 10 days. The data are from 3 independent experiments. (I) Number of colonies for indicated bone marrow cells relative to *Bid*+/+ colonies. *Bid*+/+ CD45.1 denotes WT CD45.1 cells transplanted with *Bid*+/+ CD45.2 cells. TKO CD45.1 denotes WT CD45.1 cells transplanted with TKO CD45.2 cells. ns = not significant, *p<0.05 **p<0.01, ***p<0.001, and ****p<0.0001. Data are representative of mean +/- SEM. Contribution: All experiments performed by Wagner PN and Zinkel SS.

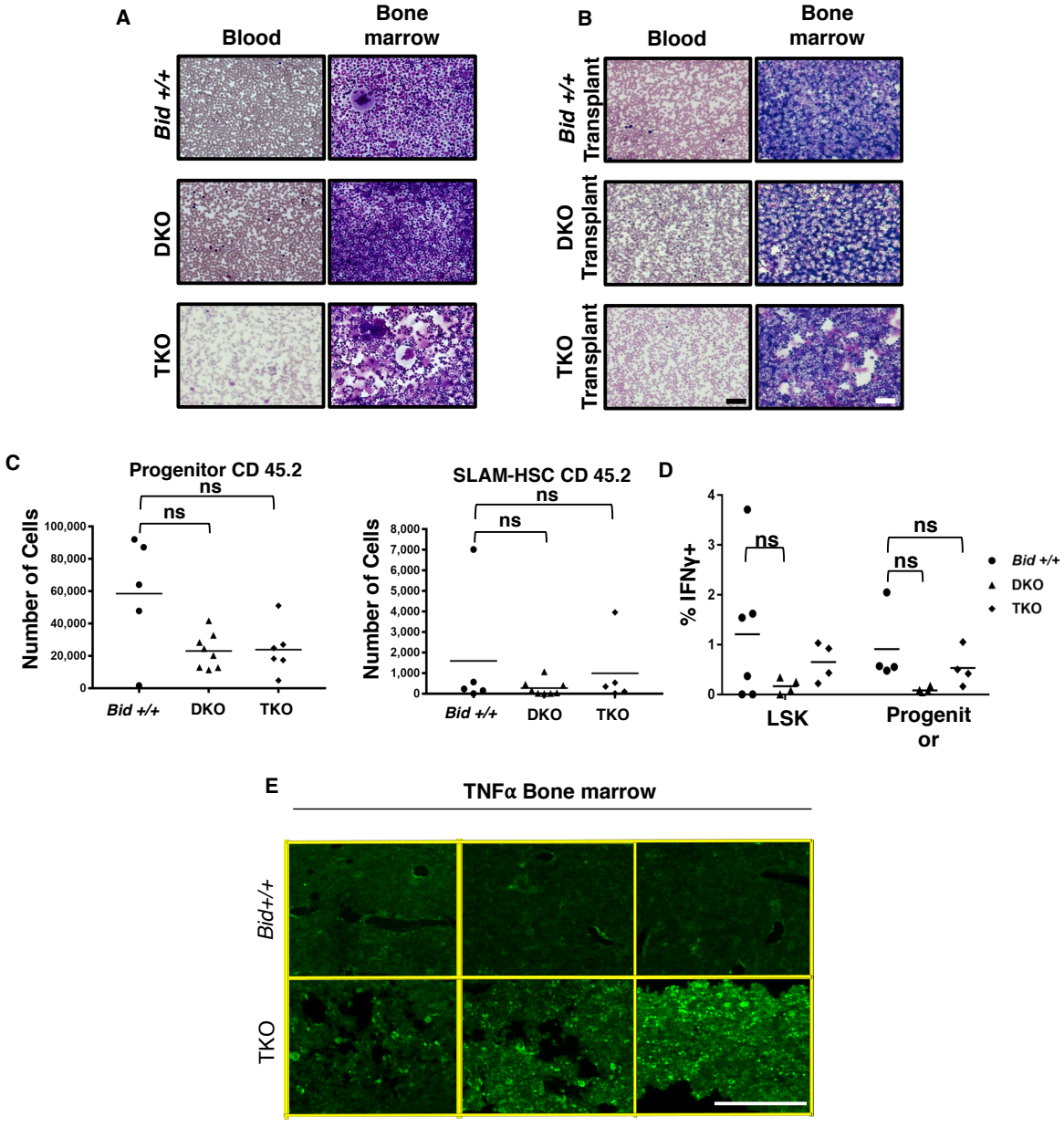

Figure 4-11. TKO bone marrow is cytopenic and displays increased TNFα.
(A) Blood and bone marrow smears from *Bid* +/+, DKO, and TKO mice. (B) Blood and bone marrow smears from *Bid* +/+, DKO, and TKO transplant mice. Scale bar indicates 50 microns. (C) Myeloid progenitor and SLAM-HSC CD45.2 positive populations in transplanted mice. (D) Examination of IFNγ positivity in LSK and myeloid progenitor populations in *Bid* +/+, DKO, and TKO mice. *Bid* +/+ n=6, DKO n= 4, TKO n=4. ns= not significant. (E) Bone marrow of *Bid*+/+ and TKO mice stained for TNFα as in E. n=3. 5x magnification. Scale bar=50 microns. Contribution: All experiments by Wagner PN (Panels A-D) and immunofluorescent staining by Shi Q (Panel E).

TKO bone marrow displays increased TNFα and IL-1β production

TKO bone marrow displayed elevated TNFα staining without treatment (Figure 4-11 E). Examination of HSPCs revealed significantly increased TNFα and interleukin-6 (IL-6) in LSK cells and IL-1β in both LSK and progenitors in TKO marrow compared with *Bid*+/+ marrow, but not interferon-γ. (Figure 4-12 A-C; Figure 4-11 D). Bone marrow from TKO*Ripk1(+/-)* mice has significantly decreased TNFα and IL-1β cytokine production (Figure 4-12 D, E) relative to bone marrow from TKO mice. The above results are consistent with inflammation induced by necroptotic TKO cells.

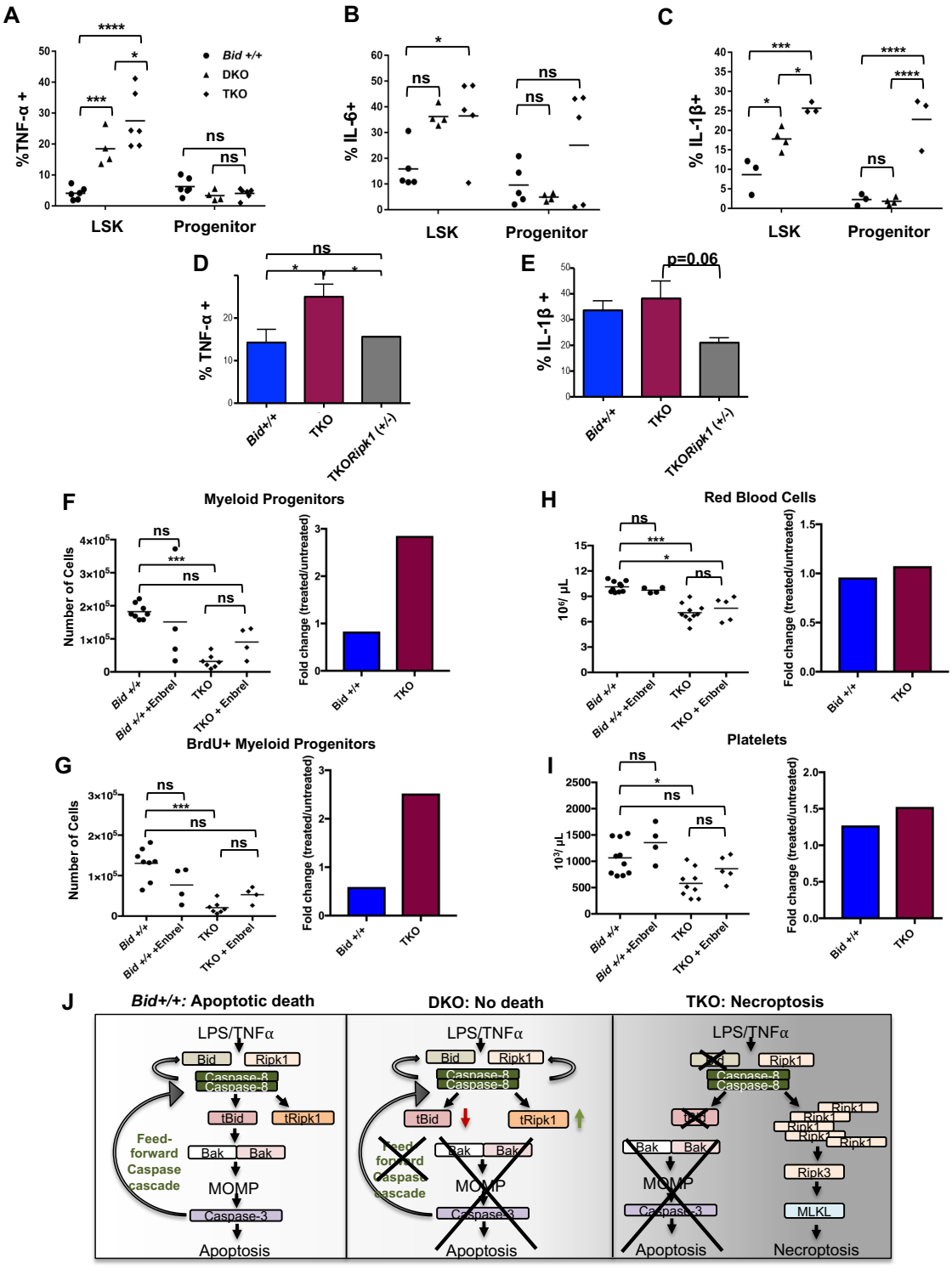
A
%TNF-α +
Bid +/+
DKO
TKO
LSK
Progenitor
B
% IL-6+
C
% IL-1β+
D
% TNF-α +
Bid+/+
TKO
TKORipk1 (+/-)
E
% IL-1β +
p=0.06
F
Myeloid Progenitors
Number of Cells
Fold change (treated/untreated)
H
Red Blood Cells
10⁶/ μL
G
BrdU+ Myeloid Progenitors
I
Platelets
10³/ μL
Bid +/+ +Enbrel
TKO + Enbrel
J
Bid+/+: Apoptotic death
DKO: No death
TKO: Necroptosis
LPS/TNFα
Bid
Ripk1
Caspase-8
tBid
tRipk1
Bak
MOMP
Caspase-3
Feed-forward Caspase cascade
Apoptosis
Ripk3
MLKL
Necroptosis

Figure 4-12. TKO mice display increased TNFα which can be rescued by a genetic cross with *Ripk1* (+/-) mice or the anti-inflammatory drug Enbrel.
(A) TNFα (B) IL-6, and (C) IL-1β positivity in myeloid progenitor and LSK populations in *Bid*+/+, DKO, and TKO. (D) Intracellular cytokine staining for TNFα and (E) IL-1β from *Bid*+/+, TKO, and TKO*Ripk1* (+/-) mouse bone marrow following 5 hours of LPS stimulation (200 ng/mL) + Golgi Plug. *Bid*+/+ n=5, TKO n=7, and TKO*Ripk1* (+/-) n=5. (F) Myeloid progenitor populations and corresponding fold change for *Bid* +/+ and TKO mice before and after treatment with Enbrel (TNF decoy receptor). (G) Number of BrdU+ myeloid progenitors and fold change as in (F). (H) RBCs (10^6/μl) (left) and (I) platelet counts (10^3/μl) (right) in *Bid* +/+ and TKO mice with and without Enbrel and corresponding fold change. (J) Model diagram for cell death pathways in *Bid*+/+, DKO, and TKO mice. In a TKO mouse, the absence of Bax and Bak inhibits the feed-forward caspase amplification while further loss of Bid results in necrotic cell death. *Bid* +/+ n=4 TKO n=4. ns= not significant, *p<0.05, ***p<0.001, and ****p<0.0001. Data are representative of mean +/- SEM. Contribution: Cytokine analysis performed by Wagner PN (Panels A-C). Salisbury-Ruf CT and Zinkel SS performed cytokine analysis in Panels D and E. Wagner PN performed Enbrel experiments with additional data analysis by Salisbury-Ruf CT (Panels F-I). Schematic by Salisbury-Ruf CT.

Treatment with the TNF decoy receptor Enbrel restores MPCs and improves cytopenia in TKO mice

We next sought to determine whether inhibiting TNFα could improve TKO cytopenia. We treated a cohort of *Bid*+/+, DKO, and TKO mice with the TNFR decoy Enbrel. Enbrel treatment increased the number of TKO myeloid progenitor cells and $BrdU^+$ myeloid progenitor cells so that they were not significantly different from the corresponding *Bid*+/+ cell numbers (Figure 4-12 F-G). Enbrel treatment also improved RBC and platelet counts in TKO mice (Figure 4-12 H-I), consistent with a role of necroptosis-induced TNFα in TKO BMF.

We propose that our results suggest a model (Figure 4-12 J) in which loss of Bax and Bak removes a feed-forward amplification of caspase activation and intrinsic apoptotic cell death. In a TKO mouse, further loss of Bid results in a change in caspase-8

activation, resulting in decreased cleaved Ripk1 and increased necroptosis, consequently creating a highly inflammatory microenvironment in the marrow, leading to failure.

MDS demonstrates increased Ripk1 and pMLKL expression, suggesting increased necroptotic signaling

We have demonstrated that increased necroptosis in mouse bone marrow results in BMF with hypercellular marrow, prominent dysplasia, and a small frequency of transformation to leukemia, phenocopying the human BMF disorder MDS. Increased cell death in MDS bone marrow has been attributed to apoptosis based on techniques to measure cell death that do not distinguish between apoptotic and necroptotic cells,31 including in situ end labeling, terminal deoxynucleotidyl transferase-mediated dUTP nick end labeling staining, or DNA laddering on gels (292). Increased caspase-3 activity was seen in cultured MDS bone marrow (293) but only in 10% of MDS samples measured directly ex vivo (294).

To determine whether necroptotic cell death may play a role in MDS, we investigated necroptosis and apoptosis in MDS patient bone marrow samples. Immunofluorescence for Ripk1 (Figure 4-13 A) and pMLKL (Figure 4-13 B) revealed increased expression of these markers in all samples of refractory cytopenia with multilineage dysplasia and 50% of RAEB-1 and RAEB-2 subtypes of MDS in our 22-patient cohort (Figure 4-13 C). Staining for cleaved caspase-3 reveals modest staining in only a few samples, including controls (Figure 4-13 D). These findings are consistent with increased necroptosis signaling in MDS bone marrow. We also observed an inverse correlation between Ripk1 and Bid expression in several MDS, but not control, patient samples (Figure 4-14A).

We further obtained bone marrow from 3 patients with normal bone marrow, early MDS, and RAEB at the time of biopsy for TEM to minimize cell death artifacts. Early MDS cells show marked necrosis morphology relative to RAEB or control bone marrow (Figure 4-13 E). While this study does not rule out a role for apoptosis in a subset of MDS patients, our study clearly implicates necroptosis signaling in MDS bone marrow cell death.

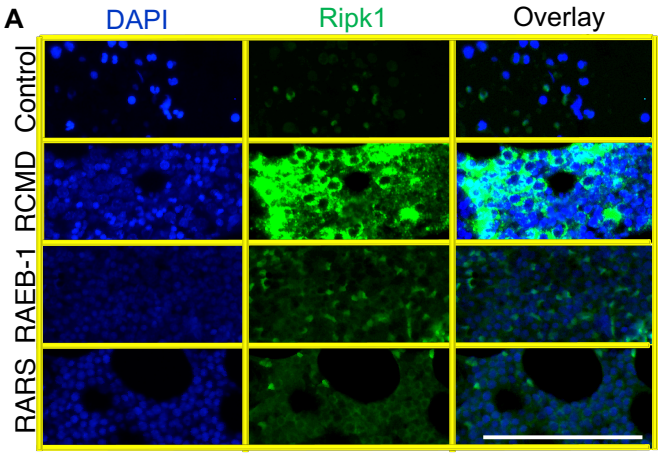

C % Positivity/Total Samples

Marker	Control	RCMD	RAEB-1/2	RARS
Ripk1	1/4	6/6	3/7	1/1
pMLKL	1/4	5/5	5/7	1/1

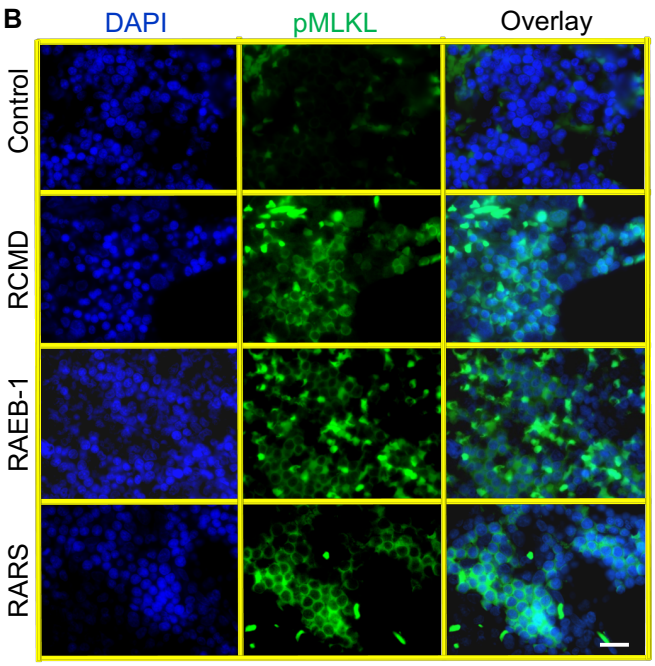

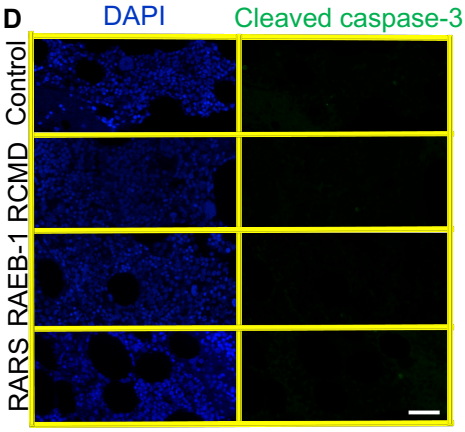

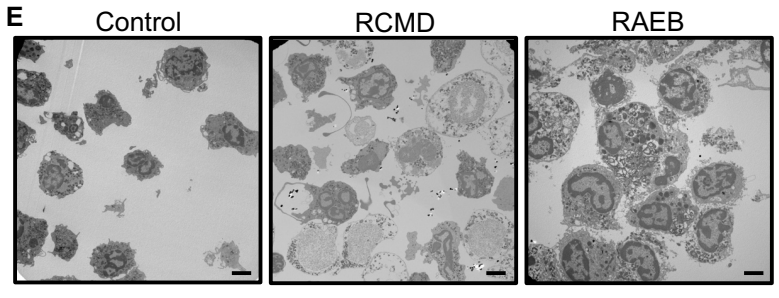

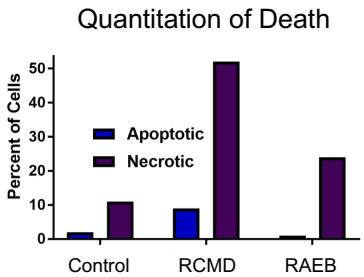

Figure 4-13. Bone marrow from patients with MDS displays increased Ripk1 and pMLKL and necrotic morphology on electron microscopy.
(A) Ripk1 staining on paraffin-embedded human bone marrow aspirate for DAPI and Ripk1. MDS subtypes include (from top to bottom): Refractory cytopenia with multilineage dysplasia (RCMD), Refractory anemia with excess blasts (RAEB-1), and Refractory anemia with ring sideroblasts (RARS). Scale bar=100 microns. Experiment was performed three independent times. (B) Phospho-MLKL staining on paraffin-embedded human bone marrow aspirate. Experiment was performed two independent times. Scale bar=50 microns. (C) Table demonstrating positivity of human samples for Ripk1 and phospho-MLKL by subtype. (D) Cleaved caspase-3 staining on paraffin-embedded human bone marrow aspirate. Experiment was performed three independent times. Scale bar=50 microns. (E) Transmission electron microscopy (TEM) of human bone marrow aspirate following RBC lysis from a normal control donor, an early MDS and RAEB patient. Scale bar =2 microns, 4,400X magnification. Quantitation of apoptotic or necroptotic cell death for each patient represented in graph (right). Contribution: Immunofluorescent staining performed by Shi Q and quantified by Wagner PN (Panels A-C). Electron microscopy performed by Janice Williams and quantified by Zou J and Wagner PN (Panel E).

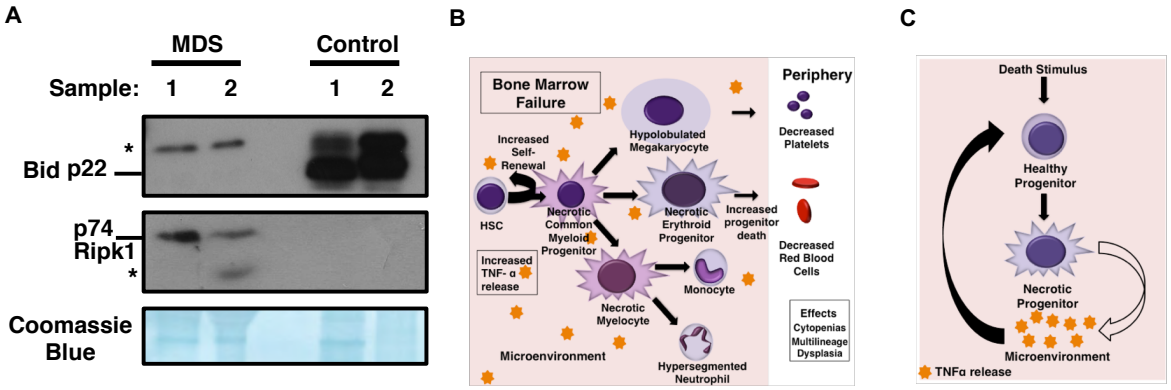

Figure 4-14. MDS patient marrow has increased Ripk1 signaling, which contributes to an inflammatory microenvironment by feed-forward activation of TNFα.
(A) Lysate from control and MDS patient bone marrow examining Ripk1 and Bid levels by immunoblot. Demonstrates increased Ripk1 expression and decreased Bid expression in MDS samples as seen in TKO myeloid progenitor cell lines. (B) Schematic of hematopoiesis under conditions of bone marrow failure in which necroptotic death of progenitor cells incites inflammatory cytokine production that impairs HSC function, leading to bone marrow failure. (C) Model of feed-forward TNFα signaling promoting increased necroptosis in bone marrow. Contribution: Western analysis performed by Zinkel SS (Panel A) and models illustrated by Wagner PN.

Discussion

The role of necroptosis in dynamic systems such as hematopoiesis and the impact on the microenvironment is not well understood. We have developed a novel set of mouse models tuned to undergo apoptosis (WT) or necroptosis (TKO) to explore the impact of necroptotic PCD on hematopoiesis. Using these models, we demonstrate that increased necroptotic cell death in the bone marrow leads to loss of the progenitor cell populations with compensatory expansion and proliferation of SLAM-HSCs (Figure 4-7), leading to an initial increase in repopulating ability in primary competitive repopulation studies; ultimately, this leads to stem cell exhaustion and BMF in secondary competitive repopulating experiments.

We further demonstrate in competitive repopulation experiments that necroptotic cells can cause cytopenias. This suggests that necroptotic cell death results in a cell extrinsic impairment of normal hematopoietic stem cells, mediated by the release of DAMPS, that promote release of inflammatory cytokines such as TNFα that amplify cell death in a feed-forward manner (Figure 4-14 B, C). Accordingly, while treatment of TKO mice with Enbrel partially restores TKO progenitor cells and peripheral cytopenias (Figure 4-12), loss of one allele of Rip1 kinase restores peripheral red cell counts and significantly improves progenitor numbers and proliferation. TKO*Ripk1*(+/-) marrow also exhibits reduced cytokine production compared to TKO marrow. Our data demonstrate that the mechanism by which cells die can have a marked impact on bone marrow homeostasis. Skewing death to necroptosis results in BMF driven at least in part by necroptosis-induced TNFα production.

Multiple lines of evidence have identified caspase-8 and the Rip kinases as central to the early signaling events that commit a cell to a given cell death fate. Leveraging cell

lines from our mouse models and bone marrow and splenocytes taken directly from the mouse, we demonstrate that Bid restrains hematopoietic necroptosis. Compared to WT cells and bone marrow, TKO cells exhibit constitutively phosphorylated Ripk1 as well as MLKL trimer and monomer formation, even in the absence of an inflammatory stimulus. DKO mice, which have Bid, exhibit increased caspase-8 and Ripk1 cleavage, but not increased Bid cleavage. TKO mice on the other hand, which additionally lack Bid, have increased full-length Ripk1 (Figure 4-4). This suggests that regulation of necrosis depends on a Bid/caspase-8 axis. These findings are consistent with a previous finding that Ripk3 activates an apoptotic cell death pathway in settings where Ripk1 is blocked and also highlights a new, central role for Bid in the restraint of necroptosis (70).

Two recent studies demonstrate hematopoietic stem cell dysfunction in mice harboring genetic loss of Ripk1 in hematopoietic cells. Roderick et al demonstrated that a hematopoietic specific deletion of *Ripk1* (*Vav-iCre-Ripk1*$^{F/F}$) resulted in BMF as a result of HSPC loss that is partially restored by loss of Ripk1 (198). Rickard et al demonstrated impaired engraftment of fetal liver cells from *Ripk1-/-* embryos that could be partially restored with a TNF blocking antibody (295). These studies are both consistent with a requirement for signaling through Rip1 kinase to support proper HSC function. Our study, designed to interrogate increased necroptosis signaling, demonstrates an expanded HSC population with increased repopulating ability, in agreement with a role for Ripk1 kinase signaling to support hematopoietic stem cell function. We further provide evidence that the level of Rip1 kinase signaling is critical, as restoring normal Ripk1 levels in hematopoietic cells can restore normal peripheral blood counts.

Significantly, the hematopoietic phenotype of our TKO mice phenocopies the human BMF disorder MDS. Substantial data have established the presence of increased

cell death and increased inflammation in MDS, and we now demonstrate increased necroptosis in MDS patient bone marrow. These findings are of particular interest as low-grade MDS which presents with pan cytopenia and particularly anemia, is very difficult to treat. In a complimentary study (*In revision*) (296) our lab has shown in a larger cohort of MDS cases increased Ripk1 is present in low-grade but not high-grade MDS. These patients also present with increased Ripk1 in the red cell compartment.

Given the results presented here, this suggests that Ripk1 mediated bone marrow failure and consequently inflammation is likely a critical driver of MDS. Genetic loss of one allele of *Ripk1* is sufficient to restore RBC peripheral counts and ameliorate excess cytokine production, highlighting the need for additional investigation into the role of necrosis and inflammation specifically in erythropoiesis. Additional studies will help determine whether inhibition of both necroptosis and cytokines will provide added benefit.

Chapter V

RIPK1-MEDIATED NECROSIS IS ASSOCIATED WITH STRESS ERYTHROPOIESIS IN MOUSE MODELS OF BONE MARROW FAILURE AND HUMAN GENETIC STUDIES

Introduction

Myelodysplastic syndromes (MDS) are chronic, multi-lineage myeloid disorders in which ineffective hematopoiesis results in cytopenia, particularly anemia. Treatment of anemia with erythropoiesis stimulating hormones such EPO (erythropoietin) and GM-CSF (granulocyte-macrophage-colony stimulating factor), EPO synthetic drugs, or transfusions are temporary and do not address the underlying cause of the anemia itself (297). We have shown in a mouse model that necrotic cell death in the marrow leads to failure, anemia, and increased inflammatory cytokine production in a Ripk1-dependent manner. MDS patient bone marrow also presents with hallmark features of necrotic cell death, rather than apoptosis as previously described (298, 296). This is consistent with known association between inflammation and MDS, and suggests that necrotic cell death can directly contribute to this inflammation and anemia (299).

Necrosis has been shown to promote inflammation and autoimmunity in multiple diseases models including systemic inflammatory response syndrome (SIRS), atherosclerosis, and multiple sclerosis (MS) (300). These diseases are associated with the release of cytokines due immune sensing of damage associated molecular patterns (DAMPs), resulting in further inflammation which can be alleviated by inhibiting Rip-kinases. Specifically, it has been shown that inhibition of Ripk1's kinase domain in dendritic cells can prevent auto-immunity. This suggests that the role for Ripk1 in role in driving necrotic death is critical for promoting inflammation (301).

Erythropoiesis is particularly sensitive to inflammation, as highlighted by anemia of inflammation or chronic disease (ACD). Inflammation has several direct consequences on red cells (302). These effects include defects in iron homeostasis and proliferation of early red blood cell (RBC) precursors, particularly BFU-E and CFU-E units. TNFα has been directly shown to inhibit colony formation and EPO, required for early red cell progenitor growth. LPS injected mice have also been shown to have decreased EPO gene expression through TNFα suppression of EPO (302–304).

Interestingly it has been reported that red cells can also contribute to inflammation. For instance, RBCs have been proposed to have a protective, chemokine scavenging function. Through TLR9 it was found that RBCs bind cell free DNA. Compared to RBCs from Ripk3 knock-out mice, WT RBCs had a higher burden of bound DNA, indicating necrotic cell death directly contributes to inflammation and subsequently impacting red cells (305). Importantly, red cells also contain high concentrations of pro-inflammation cytokines, and it has been proposed that they play an important role cytokine signaling (306, 307). In MDS, damage to the red cells membrane integrity from underlying inflammation would undoubtedly worsen disease progression.

Lastly, several of the genetic mutations identified both in MDS and in individuals with clonal hematopoiesis of indeterminant potential (CHIP) patients are associated with dysfunctional erythropoiesis and inflammation. These include ASXL1 (308–310) and TET2 (249, 311–313). In particular, TET2 has also been shown to play a role in restraining inflammation through its ability to regulate gene transcription (217). While it is currently unknown what factors drive a small percentage of CHIP patients to progress to

bone marrow failure, inflammation and consequently defective erythropoiesis are likely involved.

To better understand the impact of underlying of necrosis and inflammation on erythropoiesis, we take an approach that combines human genetic studies, including phenotypic and gene expression analysis, with mouse models of bone marrow failure (Figure 5-1A). Phenotypic analysis reveals association between inflammatory conditions and infection with anemia and MDS risk. We further show that anemia is associated with increased RIPK1 and MLKL gene expression, and autoimmune conditions associate with increased RIPK1 expression in three independent cohorts.

VavCre^{+}*Bax* $^{F/F}$*Bak* $^{-/-}$*Bid* $^{-/-}$ (TKO), mice previously shown to have bone marrow failure (298) have significantly decreased mature red cells and increased extramedullary hematopoiesis. This is due in part to increased inflammation within the bone marrow, which can be modulated by both impacting overall levels of, TKO*Ripk1(+/-)* mice and specifically its kinase function, TKO *Ripk1*$^{D138N/D138N\ (D/D)}$ (197). We also evaluate the role of necrosis in *VavCre*$^{+}$*Tet2*$^{F/F}$ (*VavTet2*$^{-/-}$*)* mice and find we can restore normal CFU-E colonies by crossing to *Ripk1*$^{D138N/D138N\ (D/D)}$ mice. To mimic conditions of underlying inflammation, *VavTet2*$^{-/-}$ mice injected with LPS have increased necrotic cell death as well as TNFα expression in the marrow. LPS-injected mice specifically have decreased numbers of RBCs due to increased death in Ter119+/CD71+ populations.

Lastly, to evaluate modulation of inflammation in people and risk for MDS, we performed phenotypic analysis on electronic health records (EHRs). We find that clinical intervention with the anti-TNFα biologics Humira or Enbrel reduced overall MDS risk.

These data suggest that alleviating inflammation due to necrosis may directly impact red cell homeostasis and consequently progression of MDS.

Results

Phenotypic analysis of 2.8 million electron health records reveals elevated risk between inflammatory diseases and infection with anemia and MDS

We first performed phenotypic analysis of using Vanderbilt University's Synthetic Derivative (SD), which contains 2.8 million de-identified electron heath records (EHRs). EHRs were mined to determine the strength of association between anemias and MDS (Figure 5-1 B). Aplastic anemia as well as aplasia have been shown to evolve to MDS (314). This is reflected by reflected by high odds ratios (OR) and serve as a positive control. Interestingly, we find that other genetically driven anemias such as hereditary hemolytic anemias (HHA) (encompassing Thalassemia and sickle cell disease), as well as deficiency anemias (vitamin-driven rather than iron), have comparatively smaller ORs, accurately corresponding with no-known predisposition for these anemias with MDS. This suggest our phenotypic analysis can be accurately used to evaluate phenotypic associations (Figure 5-1 C). Our method is further validated by MDS high odds ratios for AML and myelofibrosis (Figure 5-1 D). It is important to note that with the strategy used here, we are unable to distinguish between secondary AML (sAML) and primary AML, which would likely further strength our results. Importantly, we find no association between numbers of patients evaluated and OR values suggesting these result are not driven by sample size.

We next wanted to use this data to determine if there was an association between anemias or MDS and inflammation. We created a "super-inflammatory" phenotype characterized by patients with autoimmune diseases with inflammatory etiologies (Figure

5-1 E). Grouping these disease is beneficial in that it gives us larger patient numbers, and thus power to find risk associations. We find that compared to our control phenotypes, there are strong ORs between all anemias and MDS with “super-inflammatory” diseases, with the exception of HHA which is driven by genetic changes in red cell membrane integrity (Figure 5-1 F). Lastly, we analyzed a number of common bacterial and viral infections and find that sepsis in particular highly associates with MDS risk (Figure 5-1 H). In sum, these results suggest indeed there is an association between inflammation and MDS.

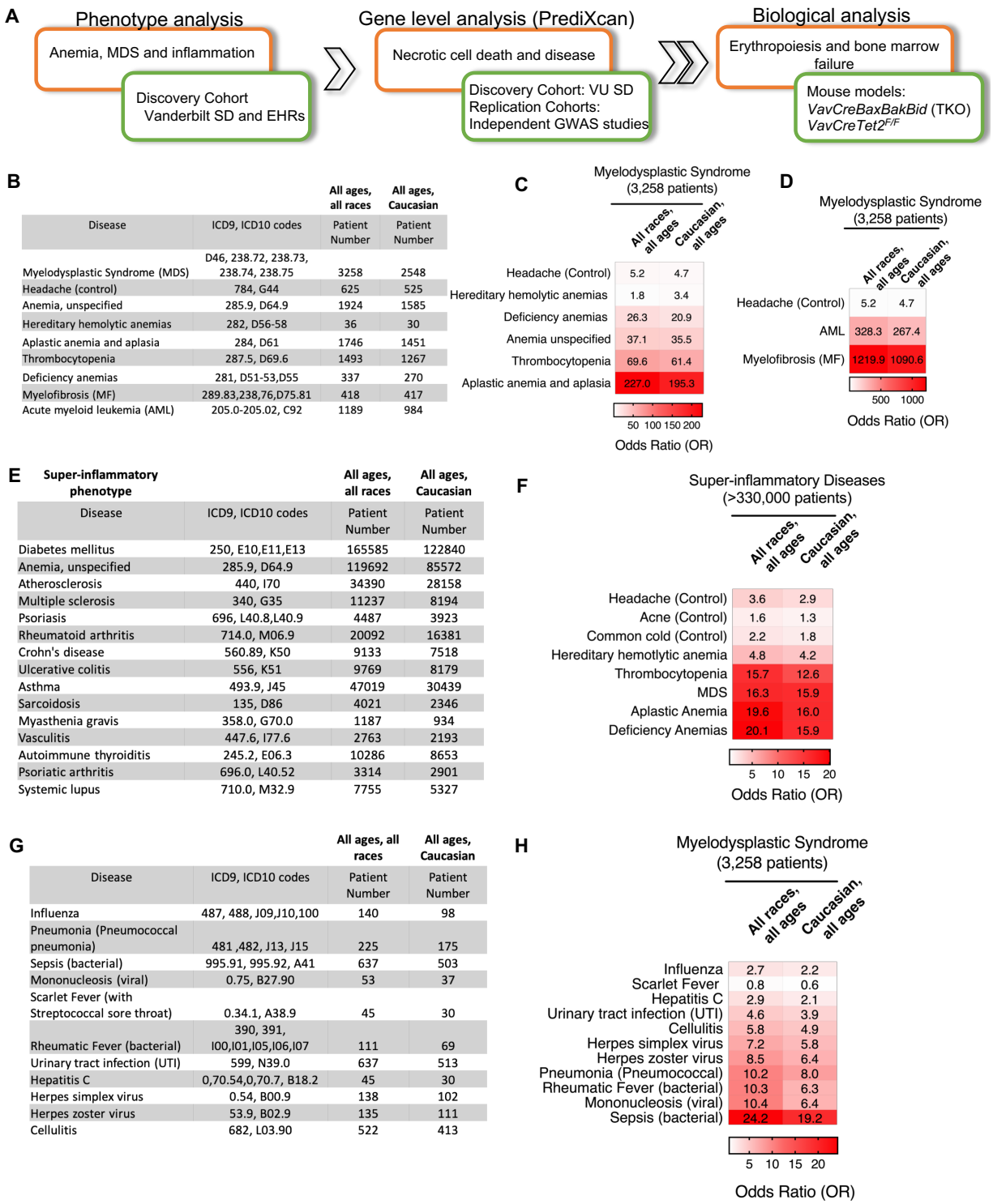

B

Disease	ICD9, ICD10 codes	All ages, all races Patient Number	All ages, Caucasian Patient Number
Myelodysplastic Syndrome (MDS)	D46, 238.72, 238.73, 238.74, 238.75	3258	2548
Headache (control)	784, G44	625	525
Anemia, unspecified	285.9, D64.9	1924	1585
Hereditary hemolytic anemias	282, D56-58	36	30
Aplastic anemia and aplasia	284, D61	1746	1451
Thrombocytopenia	287.5, D69.6	1493	1267
Deficiency anemias	281, D51-53,D55	337	270
Myelofibrosis (MF)	289.83,238,76,D75.81	418	417
Acute myeloid leukemia (AML)	205.0-205.02, C92	1189	984

E

Super-inflammatory phenotype		All ages, all races	All ages, Caucasian
Disease	ICD9, ICD10 codes	Patient Number	Patient Number
Diabetes mellitus	250, E10,E11,E13	165585	122840
Anemia, unspecified	285.9, D64.9	119692	85572
Atherosclerosis	440, I70	34390	28158
Multiple sclerosis	340, G35	11237	8194
Psoriasis	696, L40.8,L40.9	4487	3923
Rheumatoid arthritis	714.0, M06.9	20092	16381
Crohn's disease	560.89, K50	9133	7518
Ulcerative colitis	556, K51	9769	8179
Asthma	493.9, J45	47019	30439
Sarcoidosis	135, D86	4021	2346
Myasthenia gravis	358.0, G70.0	1187	934
Vasculitis	447.6, I77.6	2763	2193
Autoimmune thyroiditis	245.2, E06.3	10286	8653
Psoriatic arthritis	696.0, L40.52	3314	2901
Systemic lupus	710.0, M32.9	7755	5327

G

Disease	ICD9, ICD10 codes	All ages, all races Patient Number	All ages, Caucasian Patient Number
Influenza	487, 488, J09,J10,100	140	98
Pneumonia (Pneumococcal pneumonia)	481 ,482, J13, J15	225	175
Sepsis (bacterial)	995.91, 995.92, A41	637	503
Mononucleosis (viral)	0.75, B27.90	53	37
Scarlet Fever (with Streptococcal sore throat)	0.34.1, A38.9	45	30
Rheumatic Fever (bacterial)	390, 391, I00,I01,I05,I06,I07	111	69
Urinary tract infection (UTI)	599, N39.0	637	513
Hepatitis C	0,70.54,0,70.7, B18.2	45	30
Herpes simplex virus	0.54, B00.9	138	102
Herpes zoster virus	53.9, B02.9	135	111
Cellulitis	682, L03.90	522	413

Figure 5-1. Phenotype analysis using EHRs reveals increased odds ratios for MDS and inflammatory diseases and sepsis. (A) Schematic of experimental approach, combining evidence from electronic health record (EHR) phenotyping, genotyping analysis using

Figure 5-1 Continued.
PrediXcan, and evidence from mouse studies. (B) Table of hematopoietic diseases assessed including ICD9 and 10 codes used to mine EHRs as well as number of patients in each disease category with MDS. Comorbidity analysis results from contingency tables looking at the association between MDS and (C) anemias and (D) control diseases. (E) Table as in (B) for super-inflammatory disease phenotype assessed for risk with hematopoietic diseases. (F) Comorbidity analysis as in (C, D). (G) Table for infectious diseases and (H) Comorbidity analysis for risk between infectious diseases and MDS. Contribution: All experiments shown performed by Salisbury-Ruf CT.

PrediXcan analysis reveals increased RIPK1 expression associated with anemia and autoimmunity in 3 independent cohorts

Given the association between necrosis and inflammation, we were interested to know if genetic predisposition for anemia or autoimmune disorders corresponded with necrotic pathway genes. We first performed gene level analysis using PrediXcan (229) on a group of anemic patients identified in BioVU. PrediXcan allows us to determine the genetically regulated component of gene expression based on the Genotype-Tissue Expression (GTEx) project reference transcriptome, excluding confounding factors, such as environmental influences and disease, on genetic predisposition (Figure 5-2 A). Testing a BioVU cohort of patients with hereditary anemia, we assessed genes involved in the regulation of both apoptosis and necrosis. We find a significant increase in necrosis genes, including RIPK1 and MLKL in anemia and a decrease in all apoptotic genes, with the exception of caspase-3 (Figure 5-2 B). These findings suggest that indeed genetically driven necrosis may be predisposing for anemia.

We also extended our analysis to autoimmune disorders given the odds ratios with anemia and MDS in our super-inflammatory phenotypic analysis. In a separate BioVU cohort we find that increased Ripk1 expression is associated with several inflammatory autoimmune diseases (Figure 5-2 C). In particular, we find hypothyroidism which had been previously been linked to MDS and is associated with worse outcome (315). Lastly, we

also performed PrediXcan analysis on two-independent GWAS studies consisting of 1,963 patients with inflammatory bowel disease (IBD) (316) and a European cohort of 86,640 patients with IBD or ulcerative colitis (UC) (317). We find nominally significant association with increased RIPK1 in both cohorts (Figure 5-2 D).

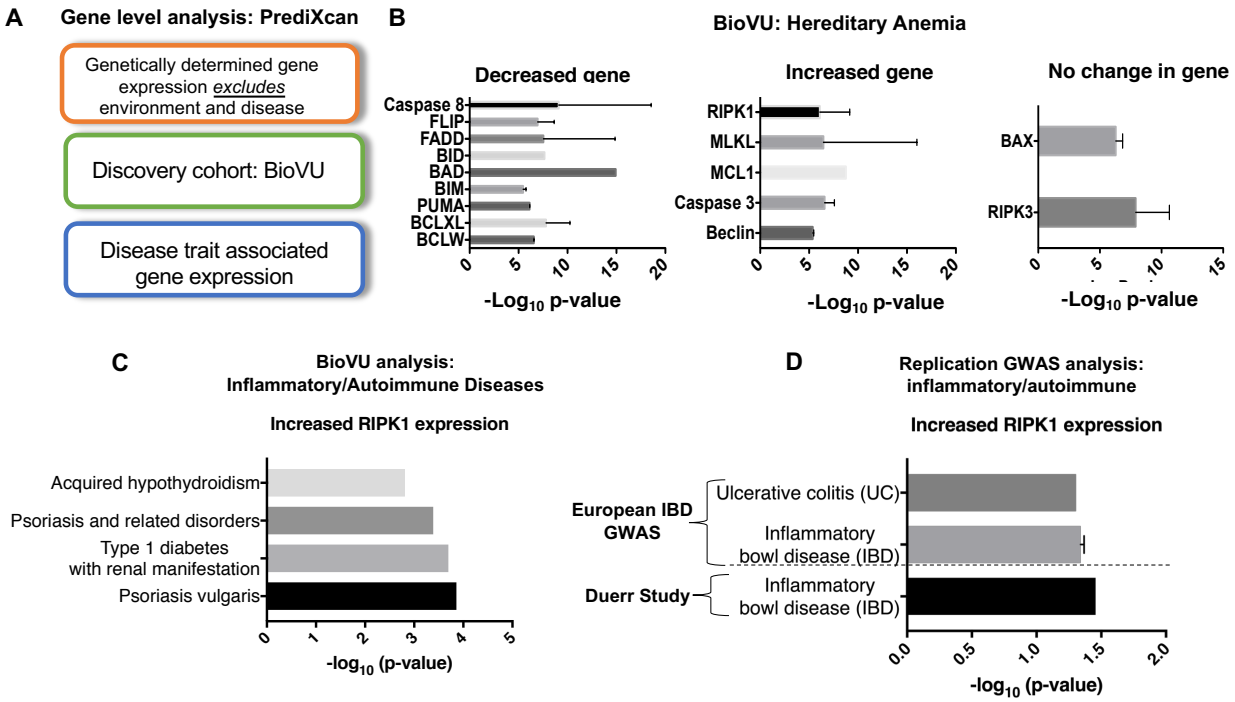

Figure 5-2. Genetic analysis using PrediXcan reveals increased RIPK1 expression associated with anemia and autoimmune disease.
(A) General outline of PrediXcan analysis methodology. (B) PrediXcan analysis results for a cohort of patients with hereditary anemia assessed for gene expression of 16 genes involved in necrotic and apoptotic cell death. Genes are organized by predicted changes in gene expression as indicated and plotted against -log10 p-value (all results are significant). (C) BioVU discovery cohort PrediXcan analysis of autoimmune diseases associated with significantly increased RIPK1 gene expression. (D) Independent PrediXcan analysis of two independent GWAS studies for autoimmune inflammatory bowel diseases reveals significantly increased RIPK1 gene expression. Contribution: All experiments shown performed by Gamazon ER.

TKO mice have increased extramedullary hematopoiesis and decreased mature red cells that can be rescued with a genetic cross to Ripk1+/- or Ripk1$^{D138N/D138N\ (D/D)}$ mice

In order to more precisely understand how inflammation impacts anemia and MDS, we evaluated erythropoiesis in our TKO mice, as well as mice crossed to haploinsufficient *Ripk1* (TKO*Ripk1*+/-) as this was shown to decrease Ripk1 to WT levels (Wagner et al. 2019 Blood). Additionally, we also crossed TKO mice to Rip1-kinase dead mice, *Ripk1*$^{D138N/D138N\ (D/D)}$ (196). The mice are mutated in proton acceptor region of the catalytic site and thus are unable to carry out kinase activity necessary for necrotic signaling.

We found that overall, TKO mice have significantly decreased cellularity in the bone marrow and increased splenic weights, indicative of extramedullary hematopoiesis. Both cellularity and spleen weights could be restored by crossing TKO mice to either *Ripk1*+/- or *Ripk1*$^{D138N/D138N\ (D/D)}$ mice (Figure 5-3A). It is important to note the decreased cellularity observed here, but not by Wagner et al. (298) is due to the fact that these numbers reflect marrow that has not had red cells removed by lysis. This suggests on of the major compartments decreased in these mice is indeed the erythrocytes.

We then evaluated erythropoiesis by flow cytometry in both in the bone marrow and spleen of WT, TKO, TKO*Ripk1*+/-, and TKO*Ripk1*$^{(D/D)}$ mice. We find that TKO mice have significantly decreased numbers of cells positive for the RBC lineage marker Ter119+ compared to WT mice. Both TKO*Ripk1*+/- and TKO*Ripk1*$^{(D/D)}$ can increase these populations. Interestingly, we also observe a compensatory increase in extramedullary Ter119+ cells in the spleen, however this is not significantly reduced in either TKO*Ripk1*+/- and TKO*Ripk1*$^{(D/D)}$ mice (Figure 5-3 B).

We next used Ter119+CD44+ and FSC to determine the number of mature red cells as well as red cell precursors in the marrow (Figure 5-3 C). We find a significantly decreased red blood cells (RBCs) and reticulocytes (Figure 5-3 D, E) as well as erythroid precursors including Proerythroblasts (ProE), basophilic erythroblasts (EryA), poly erythroblasts (EryB) and orthro erythroblasts (EryC) (Figure 5-3 F-I) in TKO mice. This suggests that there is not a defect in red cell maturation at any one step, but rather a broader impact on necrosis on the whole bone marrow microenvironment. Both TKO*Ripk1*+/- and TKO*Ripk1*$^{(D/D)}$ can significantly increase RBCs and reticulocytes compared to TKO mice however, fail to rescue precursors with the exception of basophilic erythroblasts (Figure 5-3 D, E and G). Furthermore, CFU assay revealed that while TKO mice also have decreased BFU-E and CFU-E colonies, neither TKO*Ripk1*+/- and TKO*Ripk1* $^{(D/D)}$ can restore these populations.

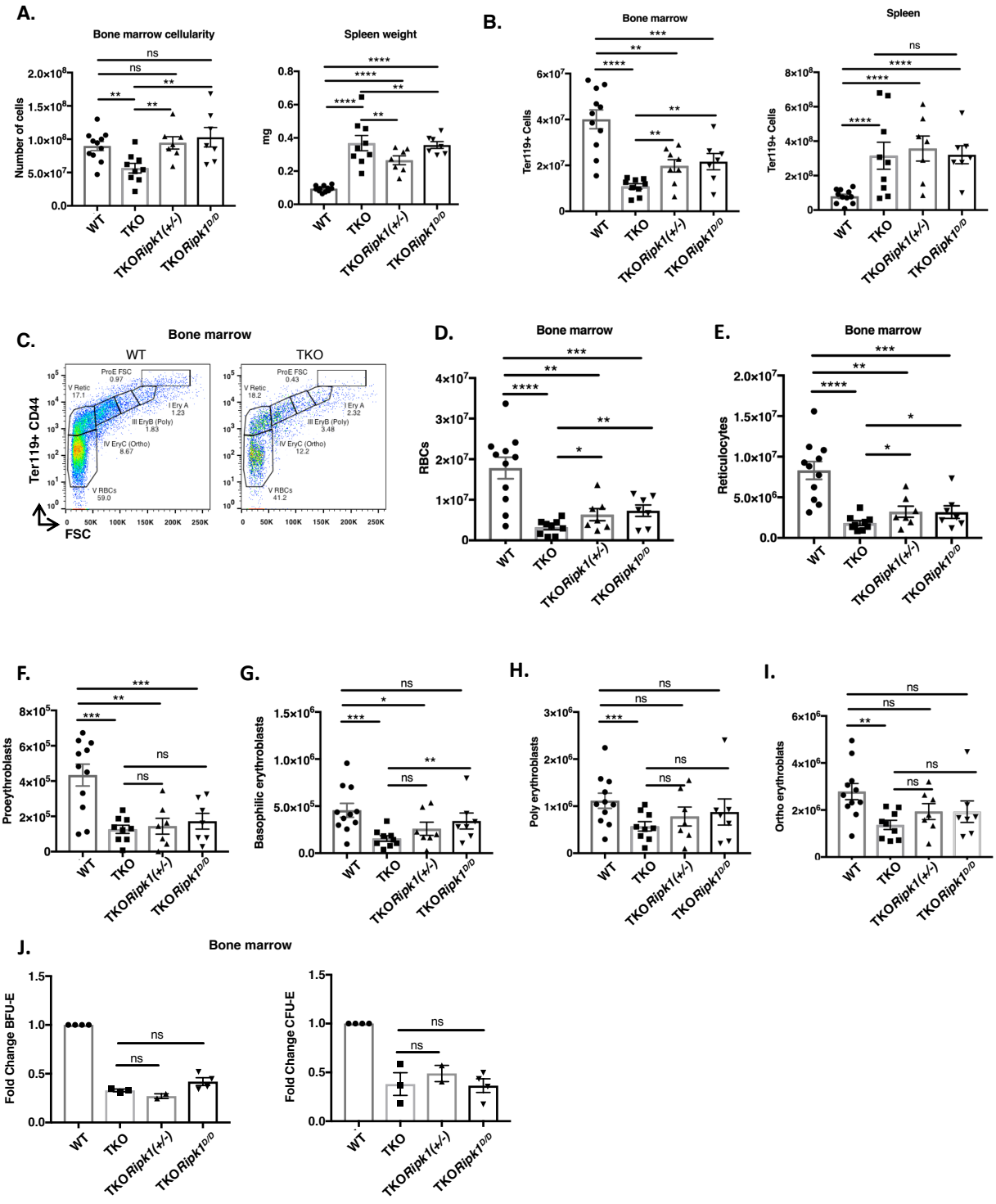

Figure 5-3. TKO mice have decreased bone marrow cellularity due in part to loss of mature Ter119+ cells. (A) Bone marrow cellularity (left) and splenic weights (right) for indicated genotypes. Note that RBC lysis was not done on samples to determine total marrow cellularity. (B) Flow cytometry data for all live cells (PI negative) followed by gating for Ter119+ positivity of the indicated genotypes. (C) Schematic of gating scheme for PI-

Figure 5-3. Continued.
erythroid cell precursors stained with Ter119 and CD44 versus forward scatter (FSC). Total numbers of bone marrow Ter119+ RBCs (D) and reticulocytes (E) are shown for indicated genotypes. (F-I) Flow cytometry analysis of bone marrow red cell precursors from ProE to Ery C populations as indicated in (C). ProE=proerythroblasts, EryA= Basophilic erythroblasts, Ery B= Poly erythroblasts, Ery C=Orthro erythroblasts. For panels A-I: WT n=11, TKO n=9, TKO*Ripk1*+/- n=7, and TKO*Ripk1* $^{(D/D)}$ n=7. (J) Fold change over WT for BFU-E and CFU-E colonies from bone marrow and spleen counted on day 10 and 48-72 hours after plating in methylcellulose for the indicated genotypes. WT n=2, TKO n=3, TKO*Ripk1*+/- n=2, and TKO*Ripk1* $^{(D/D)}$ n=4. P-values were determined by with unpaired Student's t-test, ns=not significant, *p<0.05, **p<0.01, ***p<0.001. Data are representative of mean +/- SEM. Contribution: All experiments shown performed by Salisbury-Ruf CT.

TKO mice have increased expression of Ripk1 and TNFα in their bone marrow that is reduced in TKORipk1+/- mice

To better understand why we observe overall decreased red cell populations in TKO mice, we evaluated the extent and potential impact of increased necrosis on bone marrow microenvironment morphology. We evaluated Ripk1, Ter119 and TNFα in sternums from of WT, TKO and TKO*Ripk1*+/- mice. Our preliminary results indicate that TKO mice have both increased Ripk1 and TNFα compared to WT mice. Interestingly, for Ripk1, the staining in TKO mice is clustered, showing areas of focal positivity generally adjacent to red cells (Figure 5-4 A). TNFα staining however is more diffuse, consistent with our hypothesis that necrosis impacts the inflammation throughout the marrow rather than in areas surrounding necrotic cells (Figure 5-4 B). Examination of TKO*Ripk1*+/- mice reveal generally both decreased Ripk1 and TNFα staining compared to TKO mice consistent with improved erythropoiesis in these mice (Figure 5-4 A, B). Further quantitative analysis will be done to determine if there is any co-localization of Ripk1 and TNFα with Ter119+ erythroid progenitors as well evaluate addition mice to quantify the amount of positivity for each marker, including in TKO*Ripk1* $^{(D/D)}$.

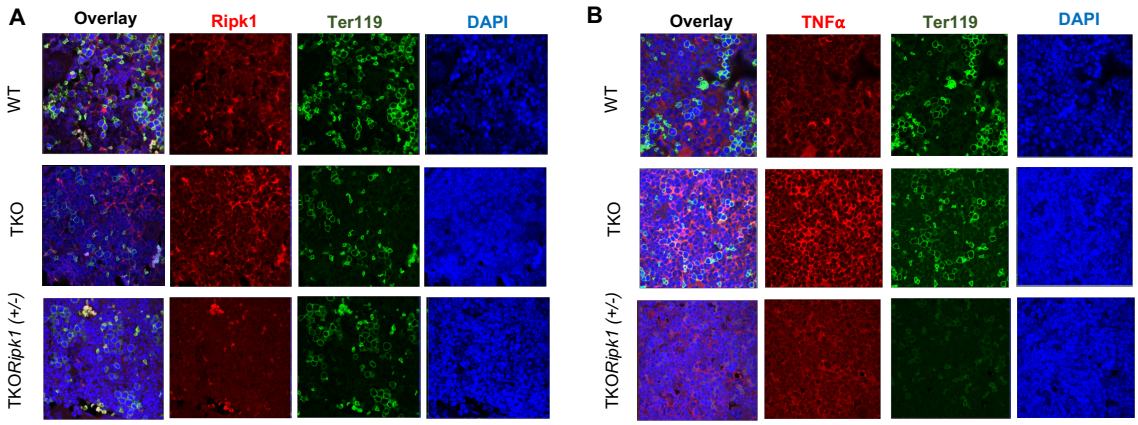

Figure 5-4. TKO mice have increased Ripk1 and TNFα staining in the bone marrow. Mouse sternums stained for (A) Ripk1 (Cy5), or (B) TNFα (Cy5) in conjunction with Ter119 (Alexa488) and DAPI. Imaging was done on an LSM 710 inverted confocal microscope. 63X magnification. WT n=2, TKO n=3, TKO*Ripk1*+/- n=3, TKO$Ripk1^{D/D}$ n=3. Contribution: All experiments shown performed by Salisbury-Ruf CT and Teresa Dugger.

Stress erythropoiesis in VavTet2$^{-/-}$ mice is exacerbating by acute LPS resulting in necrotic cell death

As the mechanistic role for CHIP genes, including TET2, in MDS remains to be determined, we were interested in also evaluating erythropoiesis in *VavTet2*$^{-/-}$ mice. Previous *in vitro* studies demonstrated delayed erythroid development with increased compensatory CFU-E colonies, as well as inflammation in *Tet2* deficient cells (311). As with TKO mice, we evaluated erythropoiesis by flow cytometry and methylcellulose assay and compared this to both *Tet2*$^{-/-}$*Ripk*$^{D/+}$ and *Tet2*$^{-/-}$*Ripk*$^{D/D}$ mice. Preliminary studies reveal increased CFU-E colonies in *VavTet2*$^{-/-}$ bone marrow which we are able to return to WT levels upon crossing to Ripk1$^{D/D}$. Analysis of the bone marrow revealed decreased early basophilic erythroblasts but not overall differences in Ter119+ cells. Interesting *VavTet2*$^{-/-}$ mice had a significant increase in extramedullary hematopoiesis compared to WT mice (Figure 5-5 B, C). This data suggests that loss of *Tet2* results in stress on erythropoiesis an

increased compensation of immature populations both in the marrow and in the spleen. Unlike TKO mice, this compensation is sufficient to maintain overall RBCs levels as we and others do not observe anemia in these animals.

We were next interested to know if erythropoiesis would be further impacted by the presence of increased inflammation. Using LPS to stimulate an acute infection, mice were IP-injected with a single dose (1.5 mg/kg) and marrow was harvested for analysis the following day. We find significantly decreased Ter119+ cells as well as RBCs and reticulocytes in *VavTet2*$^{-/-}$ mice compared to WT, which can be improved by crossing to *Ripk*$^{D/+}$ mice (Figure 5-5 D). To determine the cause of this significant decrease in red cells, we looked at overall cell viability and observe that *VavTet2*$^{-/-}$ mice had significantly increased death in the bone marrow, which was attributed almost entirely to loss of Ter119+/CD71+ erythroid progenitors (Figure 5-5 E). Examination of the marrow by Western blot revealed that LPS-injected *VavTet2*$^{-/-}$ mice indeed had increased levels of Ripk1, TNFα, and the anti-oxidants glutathione peroxidase-4 (GPXIV) and peroxiredoxin-II (PRXII) which were reduced in *VavTet2*$^{-/-}$*Ripk*$^{D/+}$ mice (Figure 5-5 F). Importantly, we did not observe an increase in TNFα in the spleen of these mice, pointing to the feed-forward activation of inflammation that can occur in the microenvironment of the marrow. These results suggest that in a setting of erythropoietic stress, red cells are highly susceptible to damage and death from inflammation *VavTet2*$^{-/-}$ confers increased sensitivity.

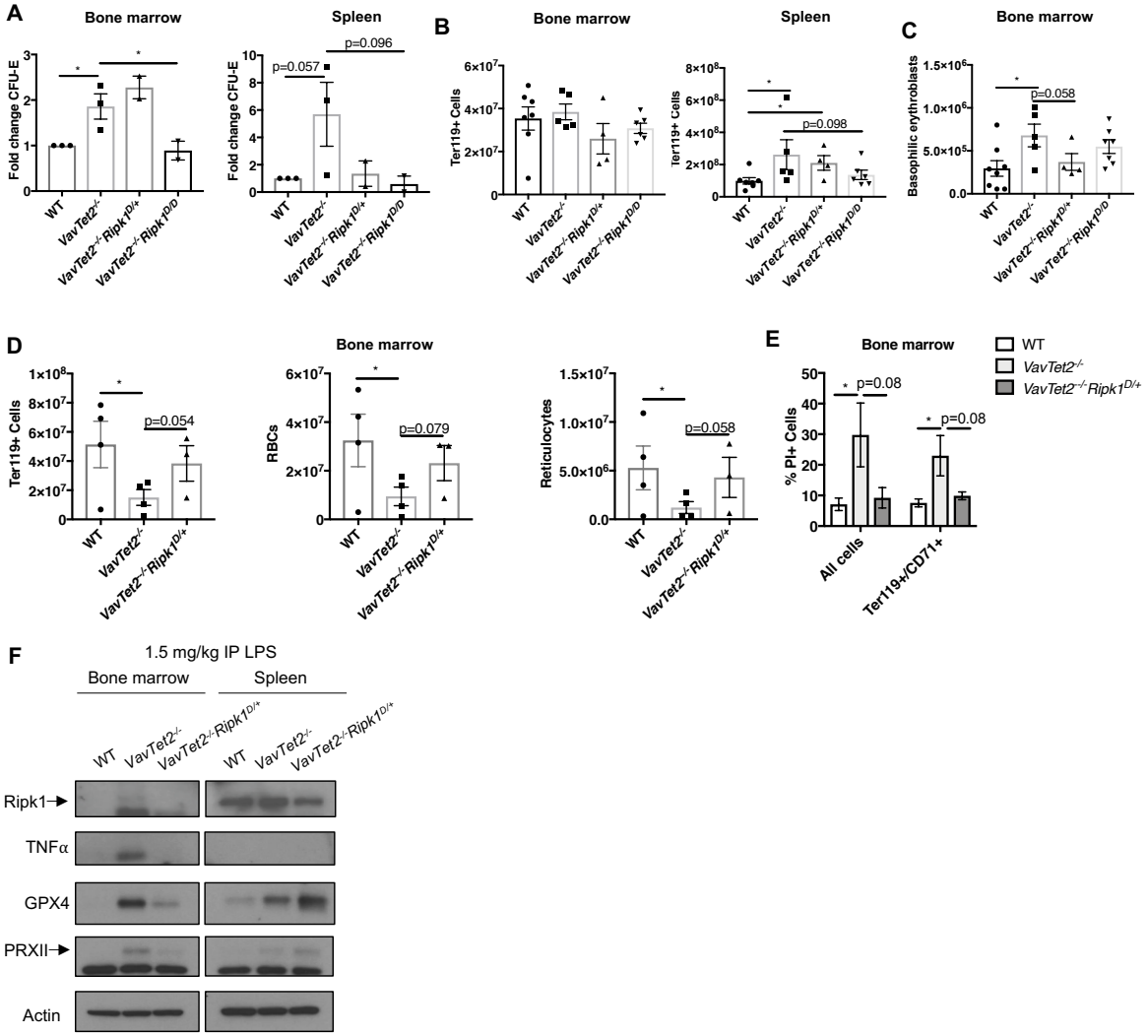

Figure 5-5. *VavTet2*$^{-/-}$ mice have enhanced sensitivity to LPS injection due to increase stress in the bone marrow. (A) Fold change over WT for CFU-E colonies from bone marrow and spleen counted for the indicated genotypes 48-72 hours after plating in methylcellulose. WT n=3, *VavTet2*$^{-/-}$ n=3, *VavTet2*$^{-/-}$*Ripk*$^{D/+}$ n=2, and *VavTet2*$^{-/-}$*Ripk*$^{D/D}$ n=2. (B) Flow cytometry analysis of bone marrow and spleen indicating for erythroid precursors. (C) Basophilic erythroblasts in the bone marrow are significantly increased in *VavTet2*$^{-/-}$ mice compared to WT mice consistent with increased stress in early red cell precursors. WT n=8, *VavTet2*$^{-/-}$ n=5, *VavTet2*$^{-/-}$*Ripk*$^{D/+}$ n=4, and *VavTet2*$^{-/-}$*Ripk*$^{D/D}$ n=6. (D) Mice were IP-injected with 1.5 mg/kg LPS and marrow was harvested 18 hours later. Flow cytometry on whole bone marrow for Ter119+ cells, mature RBCs, and reticulocytes shows decreased red cell populations in *VavTet2*$^{-/-}$ mice. (E) Flow cytometry analysis of dead cells indicated by percent propidium iodide (PI) positive for all cells acquired and for Ter119+CD71+ progenitors. For LPS experiments: WT n=4, *VavTet2*$^{-/-}$ n=4, *VavTet2*$^{-/-}$*Ripk*$^{D/+}$ n=3. (F) Western analysis of whole bone marrow and spleen from the indicated genotypes 18 hours after IP-injection at 1.5 mg/kg per mouse. P-values were determined by with unpaired Student's t-test *p<0.05. Data are representative of mean +/- SEM. Contribution: All experiments shown performed by Salisbury-Ruf CT.

Phenotypic analysis reveals that targeted TNFα biologics reduce MDS risk in approved use patient groups

Lastly, these data suggest that modulating inflammation may be beneficial to anemia and MDS. To test this idea in humans, we performed phenotype analysis using the Vanderbilt University SD, creating disease groups to test approved-use drugs including the targeted TNFα biologics Enbrel and Humira. We compared this to other common non-steroidal anti-inflammatory drugs (NSAID) used for inflammation and autoimmunity (Figure 5-6 A). We find decreased MDS risk for patients taking either Enbrel and Humira as compared to all patients in a disease group (not categorized by medication). We find no benefit for common NSAIDs including ibuprofen, Celebrex, and naproxen, nor do we see a benefit from acetaminophen, used primarily as an analgesic (Figure 5-6 B). This data suggests that targeted anti-inflammatories may be beneficial for MDS patients.

A

Inflammatory phenotypes			All ages, all races	All ages, Caucasian
Group	Diseases	Drugs	Patient Number (Patient number with drug)	Patient Number (Patient number with drug)
1	Rheumatoid Arthritis (RA), Plaque Psoriasis, Psoriatic Arthritis, Ankylosing Spondylitis (AS)	Enbrel (Etanercept)	27936 (135)	23081 (112)
2	Psoriatic Arthritis, Rheumatoid Arthritis, Crohn's, Ulcerative Colitis, Psoriatic arthritis, Ankylosing Spondylitis, Hidradenitis Suppurativa, Non-infectious Uveitis	Humira (Adalimumab)	4079 (15)	3550 (15)
3	Osteoarthritis, Rheumatoid Arthritis, Ankylosing Spondylitis	Celebrex (Celecoxib)	38262 (194)	31135 (151)
4	Rheumatoid Arthritis, Systemic lupus erythematosus, Psoriasis, Psoriatic arthritis, Multiple Sclerosis, Crohn's, vasculitis, sarcoidosis, Asthma, Myasthenia Gravis, autoimmune thyroiditis, Ulcerative colitis	Prednisone Ibuprofen Acetaminophen Naproxen	125130 (440, 338, 208, 424, 115)	92037 (348, 270, 162, 333, 85)

B

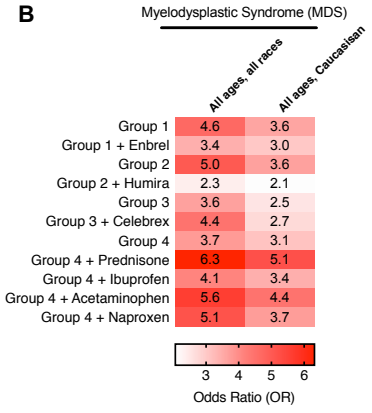

Figure 5-6. Phenotypic analysis reveals TNFα targeted biologics decrease association between inflammatory autoimmune diseases and MDS risk.
(A) Disease groups categorized by approve use drugs including the total number of patients in each group as well as in parenthesis the number of patients in that group taking the indicated drug with MDS. (B) Odds ratios for comorbidity analysis comparing MDS to the indicated group with or without drug criteria. Odds ratios were not correlated with patient numbers. Contribution: All experiments shown performed by Salisbury-Ruf CT.

Discussion

MDS is estimated to impact between 75-162 individuals per 100,000 greater than 65 years of age, and also highly impacts military veterans, especially those exposed to toxins such as Agent Orange (318). While treatments with EPO can alleviate symptoms of anemia in early MDS patients, the effect is temporary. Therefore, a more detailed understanding of erythropoiesis in the setting of inflammation is necessary to have any significant impact on disease response to treatment and overall progression.

We propose that anemia and MDS are influenced by a combination of underlying genetic predisposition, such as loss of Tet2 function or increased Ripk1 expression, and an inflammatory event such as infection or autoimmune dysfunction. Indeed, it has been shown that autoimmune and inflammatory syndromes tend to associate with MDS, such as hypothyroidism, vasculitis and rheumatoid arthritis (RA) (319). Our phenotypic analysis of disease associations based on EHRs records supports this association. We observe increased risk between inflammatory phenotypes and anemia and MDS compared to control diseases. The limitation of this analysis is determination of directionality, we have no information regarding the presence of these disorders before and after MDS diagnosis precluding understanding their role in disease pathogenesis. Genetically determined gene expression (PrediXcan analysis), which is based on the germline variation rather than environmental factors, can be leveraged to help determine predisposition. Our results

reveal that significantly increased expression of necrotic genes, particularly RIPK1, significantly associates with anemia as well as autoimmune diseases. This suggest that indeed underlying predisposition for necrosis is a risk factor for inflammation and anemia in both in the bone marrow as well as systemically.

To better understand the role of necrosis in erythropoiesis, we evaluated TKO mice, which have been previously shown to have bone marrow failure (298). Compared to TKO mice, TKO*Ripk1 (+/-)* mice have overall increased bone marrow cellularity due in part to restoration of mature RBCs but not early red cell precursors. We also observe increased Ripk1 and TNFα in the bone marrow of TKO mice that is reduced in TKO*Ripk1 (+/-)* mice. Importantly, immunofluorescence of formalin-fixed paraffin embedded sternums has the advantage over cell based assays in that the structure of the microenvironment is maintained, allowing characterization of extent and distribution of the inflammation and its impact on the architecture of the marrow. Further quantitative analysis of these samples will be necessary to determine the magnitude of the difference between TKO and TKO*Ripk1 (+/-)* mice. *VavTet2*$^{-/-}$ analysis is in progress.

There is currently a great deal of interest in defining the mechanisms for CHIP genes. While very few CHIP patients actually progress to MDS, the majority of MDS patients present with mutations in one or more of these genes. TET2 is of particular interest given its role in erythropoiesis, inflammation, and more recently its association with atherosclerotic cardiovascular diseases (209). We find that compensatory expansion of CFU-E colonies in *VavTet2*$^{-/-}$ mice can be decreased by crossing to *Ripk1*$^{D/D}$ mice, suggesting that decreasing necrotic cell death in the marrow alleviates stress erythropoiesis.

We find that *VavTet2*$^{-/-}$ mice are also highly sensitive to LPS injection, particularly resulting in erythroid precursor death and increased Ripk1 and TNFα. This sensitivity to LPS is decreased upon crossing to *Ripk1*$^{D/+}$ mice. We propose that this sensitivity in part may be due to underlying inflammation or necrosis in these mice thus priming them for hyper-responsiveness to additional inflammatory insults. This result is especially important in light of a recent study that suggests that in the setting of bone marrow transplant, as *Tet2-/-* transplanted marrow treated with LPS had increased capacity for clonal expansion, which could be partially reduced with inhibitors targeting inflammatory pathways (219).

Lastly, our comorbidity analysis in humans reveals that indeed modulating inflammation can impact risk for MDS. Importantly, while TNFα targeted therapies decrease MDS risk, prednisone, a commonly use anti-inflammatory, increases risk. This result may potentially be due to lymphopenia caused by corticosteroid drugs, and thus increased risk of infection in these patients (Figure 5-6 B). Overall, this data suggests an approach using targeted anti-inflammatory drugs could be highly effective treating in low-risk MDS patients. This regime may be especially effective when used in combination with EPO, as the negative impact of TNFα on EPO may be lessened, resulting in better overall response to therapy.

Chapter VI

SUMMARY AND FUTURE DIRECTIONS

Bid and Mitochondrial Homeostasis

Summary of Findings

Bid was initially characterized as a cytochrome c releasing factor, a finding that dictated the early studies of its function. (79–81, 83, 106). Investigation into Bid's affinity with membranes however revealed pools of full-length Bid at the mitochondria in the absence of cell death, an association dependent in part on its interaction with cardiolipin but independent of its BH3-domain (88, 90). Targeting of Bid to mitochondria was proposed to require a minimal binding domain of amino acids 148-180 on helix 6 and 7 (89, 90, 320, 321) (although the role of helix 7 has been disputed (90)). These finding suggested that Bcl-2 interactions were not required for Bid's localization to mitochondria, and it could reside there, perhaps transiently, without killing the cell.

Our initial indication of a mitochondrial role for Bid came from immortalized *Bid-/-* myeloid progenitors (MPCs), which were unexpectedly less viable than WT cells, even in the absence of stress. Electron microscopy studies on MPCs as well as primary heart tissue from *Bid-/-* mice revealed clear structural abnormalities and decreased numbers of mitochondrial cristae. This could be rescued in cells with non-apoptotic Bid mutants: non-caspase cleavable Bid (Bid^{D59A}) and BH3-mutant Bid (Bid^{BH3}). Metabolic assessment of mitochondria from *Bid-/-* MPCs and heart tissue revealed respiratory and functional defects, which were particularly pronounced in the heart under conditions of acute stress. This corresponded with decreased ATP production in the heart as well as increased cardiac remodeling indicated by fibrosis.

These results however also posed an obvious question: how does an outer mitochondrial protein alter inner membrane structure? Furthermore, Bid does not fully-span membranes, rather partially integrating. To address this question, I took a biochemical approach and sub-fractionated isolated liver mitochondria. Both an osmotic shrink-swell method as well as Proteinase K treatment of isolated mitochondria revealed Bid in an inner membrane/matrix fraction called the mitoplast. This result provides an initial explanation as how Bid could alter cristae by placing it at the scene of the action.

The known role for apoptotic remodeling of cristae by Bid had previously been linked to helix-6 sites K157 and K158, but not the BH3-domain (20, 94). This suggests that the cristae remodeling function of Bid may also be independent of apoptosis. Whole exome level analysis of rare variants in BID identified several mutations in the membrane binding region, and in particular the helix-6 point mutation, M148T, which associated with patients who had a myocardial infarction (MI).

Given that the predicted mitochondrial binding domain for Bid included this amino acid, as well as its proximity to helix-6 residues K157 and K158, we created double $Bid^{M148T/BH3}$ mutant MPCs. We assessed mitochondrial structure and respiratory function and found that this double mutant failed to restore either compared to our rescue Bid^{BH3} mutant.

Two other Bcl-2 family proteins, Mcl-1 and Bcl-XL, have also been shown to localize to the mitochondrial the matrix. Moreover, mitochondria lacking Mcl-1 look similar to *Bid-/-* mitochondria. Thus, we hypothesized that Bid interacts with Mcl-1 to maintain cristae. Over-expression of 3 Mcl-1 constructs including $Mcl\text{-}1^{WT}$, $Mcl\text{-}1^{OM}$ (outer membrane), $Mcl\text{-}1^{Matrix}$ (matrix-localizing isoform) (125), co-immunoprecipitated

with Bid but to a much lesser degree with M148T mutated Bid. Of note, Mcl-1^{Matrix} was previously shown to fail to interact with the BH3-only protein Bim, suggesting indeed this interaction with Bid is unique.

Lastly, these findings were further supported by additional human genetics studies. which revealed that individuals with genetically predicted decreased expression of BID had an increased association with myocardial infarction (MI). This is critical as PrediXcan analysis is directional, suggesting BID can contribute to MI, rather than an MI reducing the expression of BID.

Overall this work reveals several novel findings including: a new homeostatic role for Bid in cristae organization, likely involving its localization to the mitochondrial matrix, a novel mitochondrial association with Mcl-1 mediated in part by helix-6, and lastly genetic implications for Bid-mediated mitochondrial structure in MI risk. A detailed discussion of these points as well as proposed future studies are described.

Discussion and Future Directions

Why would Bid have alternative mitochondrial functions?

Although Bid is described as BH3-only protein, it is unlike all other proteins in this category. From an evolutionary stand-point, it can be grouped in its own clade. This classification is defined by its unique sequence as well as its structural similarity to other Bcl-2 proteins, which is not shared by other pro-apoptotics such as Bad or Bim (84, 85). Its classification as a BH3-only protein was based on initial biochemical functions, however there is an enormous amount of diversity in proteins with a BH3-sequence, and in fact some debate as to how to actually define family members. Thus, BH3 motifs, which likely

arose from both divergent and convergent evolution, do not accurately categorize the structure and function of their family members (322).

Interestingly, given the microbial origins of mitochondria, it is worth noting the structural similarities between the Bcl-2 family and bacterial proteins. For example, when the NMR structure of Bcl-XL was determined, it was observed that its membrane insertion domain, particularly two central alpha helices, highly resembled the transmembrane domain of diphtheria toxin (323). The pore forming motif of Bcl-XL was also be structurally similar to the Prgl protein from Salmonella typhimurium (324). Regardless of how this structure evolved, perhaps simply from positive selection, it highlights the role the Bcl-2 family and Bid, given its shared structural motifs with Bcl-XL, have in functioning on or in membranes (325).

These observations however leave many open-ended questions. In particular, if cleavage of Bid can facilitate cytochrome c release, then why could it reside at the mitochondria in the absence of a death signal. How is Bid's role in cristae maintenance functionally separated from executing apoptotic cell death?

From a homeostatic perspective, Bid can be considered a sensor of overall cell health. This was first revealed when its BH3-indpendent functions were found to be essential for the DNA damage response (98–100). Mitochondria also rely on sensors and communication from other cellular compartments can result in altered metabolic output, changes in subcellular localization, fission-fusion, or turn over via mitophagy. Some of the pathways that mediate these processes are metabolic by-products of the mitochondria themselves, such as ROS and Ca^{2+} and nuclear transcription factors such as PGC1α can sense changes in ATP, NADH, or Acetyl-CoA. Mitochondrial damage, such as loss of

membrane potential is sensed by the PINK1 kinase which phosphorylates and activates of the E3 ligase Parkin (326).

Given this highly tuned sensing system, it follows that intrinsic apoptosis would be tightly regulated by sensors, especially given that this is a terminal process. Bid's residence at the mitochondria particularly in the matrix, puts it directly at the site of regulation of cristae structure, and thus the regulation of both metabolic output and cytochrome c sequestration. As with post-translational modifications that regulate mitophagy, Bid's apoptotic function is activated by its proteolytic cleavage. This process, removing alpha-helices 1 and 2, exposes its BH3-domain both in both solution and membrane bound orientations. Thus, retaining a pool of Bid within the mitochondrial matrix physically separates it from caspases, precluding this process under normal conditions.

I propose that these findings could also explain in part the rapid kinetics of MOMP, highlighted by the fact that upon Bax-pore formation, cytochrome c release occurs rapidly (327). An "inside-out" model, in which matrix localized Bid can react to an apoptotic signal, dissociating from Mcl-1, or other cristae stabilizing proteins, would result immediately in the widening of cristae, mobilizing cytochrome in the IMS. Bid itself could then translocate to the mitochondrial surface to be cleaved, or a separate cytosolic pool of Bid could activate Bax/Bak to promote pore formation and MOMP.

Loss of mitochondrial function in Bid-/- mice and the connection to Mcl-1

While it is clear that loss of Bid results in mitochondrial dysfunction, it still remains to be determined how Bid mediates this function. Specifically, how does Bid interact with Mcl-1 in the matrix or on the IMM. Secondly, how does Bid, with or without Mcl-1, carry

out its role in regulating cristae? Based on the results presented here, I will propose several possibilities and experimental strategies that could be used to answer these questions.

First, the structure of Bid can be used to make several predictions. Helix-6 has previously been implicated in regulating cristae, however in solution, this helix is buried within the hydrophobic core of Bid (84, 85). Thus, for this helix to be accessible to interact with Mcl-1, it is likely that Bid is associated with the IMM (as illustrated in Figure 1-4). As discussed, two conserved helix-6 amino acids K157 and K158 were found to be necessary for tBid mediated cristae remodeling, cytochrome c release, and apoptosis (94). EPR structure of membrane bound tBid provides important clues about where these residues, as well as M148, lie in relation to the membrane (86). Specially, when helix-6 partially integrates into the membrane, it maintains its helical structure, inserting downward at a 25° angle. Interestingly it only reaches a predicted depth of approximately 7.9 Angstroms (Å) (lipid bilayers are approximately 45Å wide). In this orientation, M148, K157 and K158 are predicted to be within the headgroup region. Other residues that lie in the headgroup region include A147, V150, L154, and S161. Of these S161 and L154 are conserved in both mouse and human.

I propose that these residues may have several critical functions. First, it is possible that they are necessary for stabilizing Bid within the membrane itself, and mutations in one or more of these hydrophobic regions may impede Bid from inserting into the membrane altogether. Secondly, they could disrupt a protein-protein interaction. Mcl-1 has not been shown to integrate into membranes itself. A non-canonical interaction site with Bid has also not yet been identified. This region of Bid however, and potentially flanking regions in helix-5 and 7, could help to stabilize its interaction with Mcl-1, anchoring it in closer

proximity to the inner membrane for its function. Immunogold-EM of Mcl-1 supports the idea that close proximity to the cristae is necessary for its function (125). These two possibilities, however are not mutually exclusive, and it is likely that if Bid cannot interact with a membrane, and thus achieving the proper orientation, then it may not interact non-canonically with Mcl-1.

To determine if this is true, the minimal binding region of Bid and Mcl-1 could be mapped. One approach would be to create a series of purified Bid protein mutants to determine the minimal binding helices required for its interaction with Mcl-1^{Matrix} *in vitro*. Helix-6 point mutants, particularly M148T alone, as well as in combination with K157/158 and other hydrophobic residues would also be important to test. In vitro interactions could be done in the both in the presence and absence of an isolated membrane platforms such as liposomes, which is common strategy used to stabilize Bcl-2 protein interactions (328). Importantly these liposomes can be constructed to contain cardiolipin, an essential component of the IMM. Cross-linking these complexes, followed by immunoblot would then provide critical information about the nature of this interaction. This approach is also useful as it removes the need to isolate purified mitochondrial from cells or liver tissue.

In respect to how Bid and Mcl-1 interact to facilitate cristae, I propose 3 possibilities: 1.) The association between Bid and Mcl-1 is required for their ability to regulate cristae, and thus loss of one of these proteins would look phenotypically similar to the loss of both. 2.) Bid and Mcl-1 act independently of each other to regulate cristae, and loss of both proteins may cause increased cristae abnormalities due to disruption of two separate cristae regulatory pathways. 3.) Bid and Mcl-1 both interact with an unknown protein which destabilizes cristae. For example, Bid may in a negative manner, inhibit a

protease that destabilizes cristae. Mcl-1 conversely may act on the same protease to promote its function. In this scenario, loss of both proteins would in fact rescue cristae function. These possibilities are illustrated in Figure 6-1 are easily testable by knocking down both Bid and Mcl-1 in the same cell line, as was previously done for Mcl-1 in MEFs.

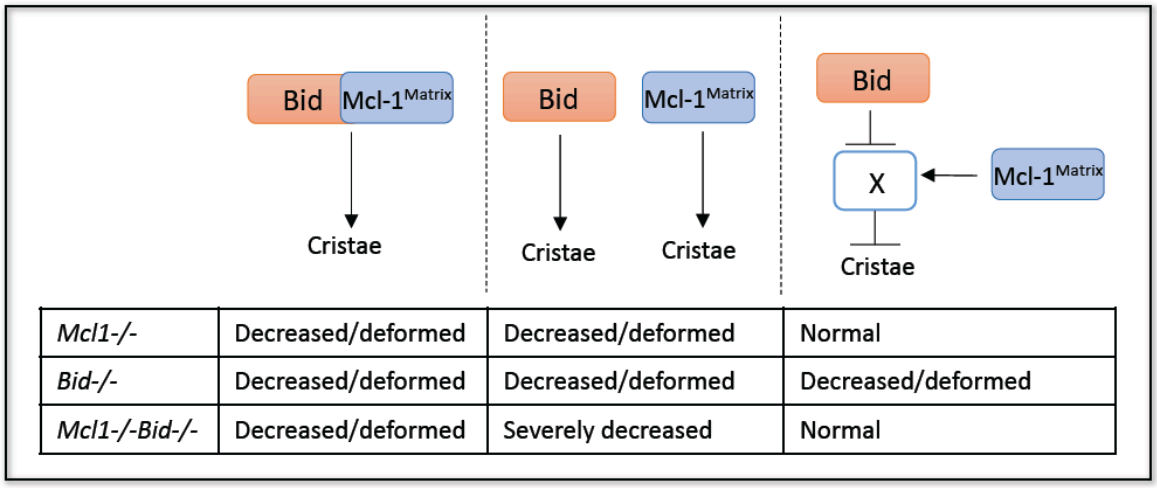

Mcl1-/-	Decreased/deformed	Decreased/deformed	Normal
Bid-/-	Decreased/deformed	Decreased/deformed	Decreased/deformed
Mcl1-/-Bid-/-	Decreased/deformed	Severely decreased	Normal

Figure 6-1. Models for Bid and Mcl-1^{Matrix} mediated cristae organization.
Results presented here suggests that Bid and Mcl-1^{Matrix} interact to maintain cristae structure (left). It is possible however that Bid and Mcl-1 are acting on cristae independently (middle), or through a yet unknown protein or protein complex (right). Expected cristae morphology for each of the proposed knockout cell lines is described.

The more challenging question that remains is how Bid, with or without Mcl-1 regulates cristae structure. I suggest two possibilities based on the findings presented here as well what is already known about cristae regulation. One model is that Bid regulates ATP synthase dimerization, which creates bends in the IMM. Secondly, Bid's role is linked to its function as a sensor and could relay signals between the mitochondrial contact sites and large tethering complexes.

The role of ATP synthase dimerization in maintaining cristae structure is well established, highlighted by structural observations made by tomography (141, 329) and

loss of cristae structure upon deletion of ATP synthase subunits (142). In yeast, which have a similar ATP synthase structure to mammals, it has been shown that dimerization of the membrane embedded Fo subunits results in an almost 90° curvature of the lipid membrane.

Upon Mcl-1 deletion in MEFs, respiratory chain defects were observed. BN-PAGE analysis revealed decreased ATP synthase oligomers and increased monomers (125). Likewise, BN-PAGE of *Bid-/-* heart mitochondria revealed decreased ATP synthase dimer activity. Furthermore, proteomic analysis of isolated mitochondria from *Bid-/-* MPCs also revealed a decrease in 4 ATP synthase subunits, specifically Atp5a1 (231). Interestingly, the Fo subunit a (along with i/j, which is not present in mammalian cells) is predicted to be the interacting interface between ATP synthase monomers (330).

In further support of this hypothesis, it has previously been shown that Bcl-XL associates with the F1 subunit β, improving ATP synthase efficiency (122–124). It is possible that Bid, with its Bcl-XL like structure, performs a similar function, which may also be true for Mcl-1. Given our results for decreased mitochondrial function with $Bid^{BH3/M148T}$ and decreased Bid^{M148T} interactions with Mcl-1, it is reasonable to propose that these two proteins are working together to stabilize ATP synthase dimers. This is supported by the idea that ATP synthase dimerization may require additional protein interactions, as it is thought this association in mammals is weaker due to missing i/j subunits.

One of the other critical regions necessary for maintaining cristae function are the cristae junctions, also referred to as mitochondrial contact sites. This region of the mitochondria is enriched for translocases for protein transport, the MICOS complex, and in the IMS protein, Opa-1. During apoptosis, tBid can be found at these contact sites on the

OMM, a process shown to be dependent on its binding to cardiolipin and independent of its BH3-domain (320).

At these contact sites, it is possible that Bid acts as a sensor. Bid's integration into the membrane is so peripheral, that it is possible it is reversible. This has shown to be true for Bax at the OMM (260). One hypothesis is that under stable metabolic conditions, Bid remains peripherally integrated into the membrane, associating with Mcl-1 and/or one or more MICOS subunits, stabilizing cristae. During conditions that require cristae remodeling, including apoptosis, Bid's dissociation from the membrane could disrupt these cristae stabilizing complexes. Given that Bid is neither a kinase nor ubiquitinase itself, this could be one way it relays messages.

This idea is particularly intriguing given our human genetics findings. We queried all known genes involved in cristae regulation for an association with any cardiac issues and found two hits: Mcl-1 and the OMM protein Metaxin-1. Metaxin-1 (MTX1), along with Metaxin-2 associate with the MICOS complex through SAMM50, forming what is known in humans as the mitochondrial intermembrane space bridge (MIB) (as shown in Figure 1-6) (331).

In sum, these potential mechanisms of cristae stabilization for Bid and Mcl-1 are intriguing but will require a substantial amount of additional work to determine the precise roles for these proteins. The results presented in this work however lay the groundwork, particularly establishing the novel matrix localization for Bid, as well as its association with Mcl-1^{Matrix}, mediated in part by helix-6.

BID, human genetics and clinical implications for MI

The severe mitochondrial abnormalities observed in *Bid-/-* cells and tissue implored further inquiry into whether or not these findings had an any association with human

mitochondrial diseases. In *Bid-/-* mice, we focused our physiological analysis on the heart, given both its high mitochondrial burden and the fact that most mitochondrial disease presents with cardiac dysfunction. Our findings from echocardiograms performed on *Bid-/-* mice suggested that in conditions of stress, they were particularly susceptible to dysfunction, mimicking stress observed during an MI.

To determine if these findings were translatable, we took advantage of Vanderbilt's de-identified EHR database, BioVU and approached this question by looking both at BID gene expression as well as clusters of rare variants in the BID gene. Consistent with our *Bid-/-* mouse model, "BID-/-" people (lowest 5% of individuals for BID expression) had a significantly increased risk of MI. The approach here is important to re-emphasize. PrediXcan measures germline predisposition, rather than the effect a prior MI (or any disease), and also excludes environmental factors that could impact gene expression. This gives us the power to determine directionality, and thus predisposition. Furthermore, our combined rare variant analysis also revealed M148T, informing the results described above.

The merging of these two approaches, biological and human genetics, is extremely powerful. Our findings in mice informed our genetic approach, and our findings in human genetics, especially the SNP M148T, directly translated back to the bench. While each approach alone is interesting, together they both validate and strengthen one another. Given that NIH funded genetics research must be made available to the scientific community (described by the Genomic Data Sharing Policy), a wealth of information is accessible for research. Large-scale GWAS and WES studies, as well as BioVU available at Vanderbilt, can be a tremendous research tool.

Our finding that decreased BID is a predisposing factor for MI is especially intriguing given the known connections between mitochondrial fitness in resistance to

aging, atherosclerosis, and ischemic/reperfusion damage. We propose that mitochondrial dysfunction due to genetically inherited changes in BID expression, could be an interesting biomarker of increased susceptibility to MI. While this is far from becoming clinically useful until further mechanistic and genetic studies are performed, we propose this approach could uncover additional risk factors with important clinical implications.

Cell death, inflammation and bone marrow failure

Summary of Findings

Hematopoietic cells in the bone marrow are sensitive to changes in oxygen, ROS, cytokines and chemokines, as well as their proximity to vasculature, nerves, and bone. Inflammation within the microenvironment due to systemic infection, normal aging, or therapies such as chemo and radiation can profoundly impact normal hematopoiesis. Necroptosis is a source of this inflammation and can be distinguished from other forms of death morphologically and by Rip-kinase signaling. Cell death in marrow has largely been characterized by flow cytometry techniques using propidium iodide and Annexin V, however these markers are shared by all dying cells, regardless of how they are dying. To determine precisely how necrosis impacts normal hematopoiesis, we created a mouse model genetically poised to undergo necrotic cell death. I will briefly summarize these findings and then more broadly expand on the importance of necrosis in the pathogenesis and treatment of bone marrow failure disorders.

To establish a model of baseline necrosis in the marrow, we took advantage of the hematopoietic Vav-Cre. Using this Cre, we removed the pro-apoptotic protein Bax, and crossed these mice to either germline deleted *Bak* (DKO mice) or double knock-out *Bak and Bid* mice (TKO mice). Of note we used a Cre-Lox system due to the fact male germline *Bax-/-* mice are infertile, and *Bax/Bak* double knockouts are rarely born, or

survive to adulthood (332). Importantly, loss of apoptotic Bax and Bak alone is not sufficient to promote necrosis. Additional loss of Bid however resulted in baseline necrotic death, again revealing a pro-survival function for Bid.

We found that compared to both WT and DKO mice, TKO mice had decreased overall survival due to bone marrow failure, presenting with anemia and dysplasia. Characterization of the bone marrow revealed necrotic features, including Ripk1 positivity (but not cleaved caspase-3), as well as MLKL bubbling of the cell membrane. Detailed flow cytometry analysis revealed TKO mice had expanded stem cells both in the LSK and SLAM-HSC compartments, and decreased progenitors. This suggested a compensatory mechanism, however when we evaluated HSPC function with competitive BMT, TKO marrow failed to reconstitute in a secondary transplant as a consequence of stem cell exhaustion. As a consequence of necrosis, TKO mice also had increased pro-inflammatory cytokines, particularly TNFα , IL-6, and IL-1β in the LSK compartment.

To determine if these findings were indeed mediated by Ripk1, we crossed TKO mice to *Ripk1* haploinsufficient mice. We found TKO*Ripk1*+/- mice had improved total numbers of progenitor cells, as well as peripheral red blood cell counts. This rescue could be explained in part by decreased TNFα and IL-1β in these mice. This data was also consistent with increased progenitor and peripheral erythroid populations when TKO animals were treated with TNFα decoy receptor Enbrel, used for rheumatoid arthritis (Figure 4-12).

Given the phenotypic similarities between these mice and bone marrow failure disorders, we obtained human bone marrow samples from MDS patients. As in TKO mice, we observed increased Ripk1 staining, as well as pMLKL, and necrotic morphology by EM immediately after patient biopsy. This finding was also replicated in a larger cohort of

MDS patient bone marrow biopsies, and when stratified for risk and grade, lower risk patients had increased Ripk1 positivity (298). These results strongly point to the pro-inflammatory consequences necrotic cell death has on the bone marrow, as well as the significance of necrosis in bone marrow failure, previously attributed to apoptotic death.

Going forward, we have started to extend our findings to a more detailed analysis of the erythropoietic compartment. Patients with BMF, especially MDS, present with refractory anemia requiring treatment with EPO or transfusions. As described below, these treatments only provide temporary management of symptoms. As a genetic model of necrosis-driven anemia, TKO mice, as well as the CHIP mice, can be used for a more detailed analysis of the erythropoietic compartment, specifically revealing the role of necrosis, inflammation, and acute infection in anemia.

Our hypothesis that inflammation and anemia contribute to bone marrow failure was first tested using phenotypic analysis. Comorbidity evaluation of SD EHRs revealed that aplastic anemia (AA), compared to other anemias, corresponded with a odds ratios (ORs), and thus increased association, with MDS, validating the approach. We next created a super-inflammatory phenotype consisting of a group of local or systemic inflammatory diseases. We then compared these patients to those with anemia and MDS. We found a high association particularly between MDS and AA and these inflammatory diseases compared to control phenotypes. Lastly, we performed a preliminary PrediXcan analysis of anemia patients for programmed cell death genes, including key regulators of apoptotic and necrotic death. We find increased expression of RIPK1 and MLKL in anemia patients and decreased expression of almost all the Bcl-2 family genes and caspases, suggesting a role for necrosis in predisposition to anemia.

To better characterize how inflammation impacts erythropoiesis, we evaluated both TKO and *VavCreTet2*$^{F/F}$ mice crossed to either *Ripk1*+/- mice, or kinase-mutated *Ripk1*

$^{D138/D138N}$, which specifically targets Ripk1 mediated necrosis. In TKO mice, we observed prominent extramedullary hematopoiesis corresponding to decreased bone marrow cellularity. TKO mice have decreased erythrocytes overall, from immature BFU-Es identified by CFU-assay, to more mature reticulocytes and RBCs identified by flow. Interestingly, TKO*Ripk1-/+* and TKO*Ripk1* $^{D138/D138N}$ could rescue these mature populations, but not extramedullary hematopoiesis.

One explanation for this finding may be the dual functionality of *Ripk1*, as it can promote inflammatory cytokine production via NFκB and necrotic death. Immunofluorescence staining of TKO sternums showed increased Ripk1 and TNFα compared to TKO*Ripk1-/+* and TKO*Ripk1* $^{D138/D138N}$ but still more than WT. Thus highlighting the sensitivity of the marrow, and especially the erythroid compartment to TNFα, previously shown to dysregulate RBC production (302, 333).

VavCreTet2$^{F/F}$ mice have been previously shown to have increased extramedullary hematopoiesis, and transient knockdown of *Tet2* results in a delay in maturation (249). These mice have also been shown to have increased inflammatory cytokines, especially IL-6, however it is unknown if this inflammation contributes to erythroid dysfunction (217). We find that *Tet2*$^{F/F}$ mice have increased CFU-E bone marrow colonies, and this can be rescued by crossing to either *Ripk1-/+ or Ripk1* $^{D138/D138N}$ mice. While *Tet2*$^{F/F}$ mice also have increased extramedullary hematopoiesis, they have increased rather than decreased red cell progenitor populations in the marrow, which is likely compensatory. Interestingly, both *Ripk1-/+ or Ripk1* $^{D138/D138N}$ can decrease these populations, suggesting that while overwhelming inflammation results in increased death, a more chronic level of necrosis results in stress.

To test this idea, we injected *Tet2*$^{F/F}$ mice with LPS. Previously it was shown that stimulation of *Tet2*$^{F/F}$ cells with LPS *in vitro* showed an acute increase in inflammatory cytokines and bacterial infection has been shown to promote BMF (218, 334). Strikingly, we observe decreased erythroid cells in *Tet2*$^{F/F}$ mice attributed to increased cell death and ROS, which can be rescued upon crossing to *Ripk1* $^{D138/D138N}$. This suggests that *Tet2*$^{F/F}$, and more broadly individuals with CHIP mutations, may be more sensitive anemia in the setting to infection.

To evaluate the role of infection and MDS in human patients, we performed further phenotypic analysis comparing infectious diseases with risk for MDS. Although in this case, we cannot imply directionality, the OR between MDS and sepsis is very high, followed by other bacterial infections including pneumococcal pneumonia, rheumatic fever, as well as viral infections such as mononucleosis. Importantly, we do not see this association with influenza, suggesting the type of infection is likely important. Lastly, we were interested to know if targeted, biological anti-inflammatory drugs, especially TNFα inhibitors, make a difference in risk for MDS. We find that patients taking Humira or Enbrel have decreased ORs for MDS compared to all patients with approved-use diseases. We propose that this evidence, in conjunction with our mouse models, suggest an

important association between infection and BMF, mediated in part by erythropoietic dysfunction (Figure 6-2).

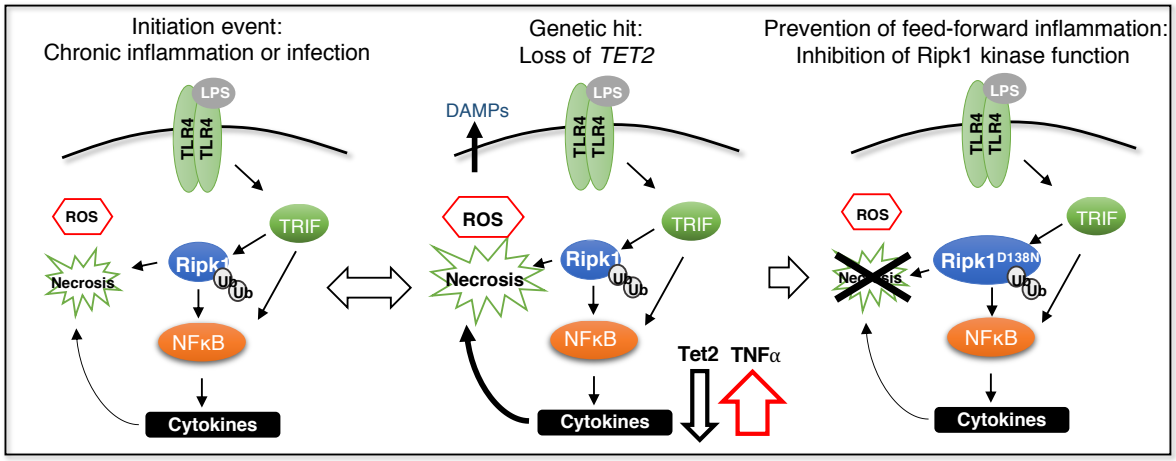

Figure 6-2. A model for inflammation in bone marrow failure.
Signaling through Ripk1 can promote both necrosis and NFκB cytokine stimulation. Under conditions of prolonged infection or as a consequence of underlying autoimmune disease such as Rheumatoid arthritis, Ripk1 can promote increased production of cytokines through its scaffolding function (described in Figure 1-3). An additional genetic hit, such as loss of TET2 function, could exacerbate this underlying inflammation through additional inflammatory cytokines production such as IL-6 or TNFα. This in turn could result in activation of necrotic cell death. Targeted inhibition of Ripk1-kinase function (genetically modeled by Ripk1$^{D138N/D138N}$) can alleviate inflammation in the bone marrow microenvironment by preventing the feed-forward amplification of necrosis. This in turn helps to partially alleviate dysfunctional erythropoiesis.

Discussion and Future Directions

Revisiting BMF and mouse models: A closer look at MDS

MDS is a particularly difficult disease to study for several reasons. Although it can be clonal, primary cell lines are not stable (204). Available immortalized cells are limited, and most have been shown to be either cross-contaminated with leukemia or established in the leukemic phase of disease (335). The use of patient derived xenograph (PDX) mouse models has also been challenging. Engraftment of human MDS into immunocompromised NOD/SCID mice was unsuccessful, partly due to the small percentage of normal marrow from the MDS patient outcompeting diseased marrow (336). NSG-S mice (NOD-SCID-IL-

2RcNull with transgenic expression of human growth factors SCF, IL-3 and GM-CSF), did not improve MDS patient derived PDX engraftment (337), however co-transplantation of human MDS with mesenchymal cells does somewhat improve engraftment (338). More recently, the MISTR mouse ($Rag^{-/-}$, $IL2R\gamma^{-/-}$ mice expressing humanized M-CSF, IL3/GM-CSF, SIRP-α and Thrombopoietin) has shown some success with low-risk MDS PDXs, which have been particularly challenging (339). Due to patent constraints, these mice are not yet available to the scientific community.

While PDX models are improving, none have directly addressed the role of inflammation on the progression of MDS within the bone marrow microenvironment. It has previously been shown human MDS bone marrow has increased inflammatory cytokines, and more recently IL-6 and IL-1β are elevated in the absence of the CHIP gene TET2 (205, 214, 219). Our work in TKO and subsequently *Tet2*$^{F/F}$ mice highlights the essential role inflammation, particularly geneticly determined inflammation, in BMF. The particular advantage of our TKO is the inflammation we observe is genetically driven and low us to better understand how CHIP may evolve overtime. Using Vav-Cre also has an advantage over the commonly used hematopoietic Mx1-Cre, which requires interferon activated by injection of the synthetic dsRNA Poly(I:C). Poly(I:C) is itself highly inflammatory. This likely confounds mouse experiments attempting to discern the impact of individual genes on MDS progression such as *Asxl-1*. Of note, *Ifngr1* was one of the genes upregulated in *Mx1-Cre Asxl1*$^{F/F}$ mice (310).

Going forward, I propose several experiments and strategies that can be used to better understand 1.) the role of inflammation in the progression of BMF and MDS and 2.) how the erythroid compartment may contribute to disease progression and 3.) evaluate predisposing genetic factors that may be useful for risk assessment in patients.

Our characterization in TKO mice revealed necrosis throughout the marrow, impacting the entire microenvironment rather than any one specific cell type. This suggests a critical role for the stroma in MDS progression, which is also supported by the mouse models described above. To further evaluate the microenvironment, two key strategies could be used. Firstly, we propose to perform competitive bone marrow transplant of WT marrow into TKO mice. This could be done with WT: WT marrow, or WT: *Asxl1-/-*, *Tet2-/-* or *SRSF2-/-* marrow. This would allow us to determine how genetically driven inflammation affects normal HSPCs function as well as the contribution of CHIP genes. After reconstitution, recipient mice could then be treated with either anti-inflammatory drugs (such as Enbrel) or necrosis pathway inhibitors such as Nec-1 to determine if either treatment improves either peripheral blood counts for engraftment and overall anemia as well as cytokines present in the serum. After sacrifice, marrow would be harvested for flow cytometry including erythroid evaluation, cell death protein analysis, or transcription level analysis of cytokines by qPCR or transcriptome analysis by RNA-Seq. Secondly, while flow cytometry is a tremendous tool, it eliminates the architectural information of the bone marrow. Fixed tissue could be evaluated for a structural, immune, or inflammatory markers using cyclic or multiplex immunofluorescence (340). This would help to shed light on how inflammation impacts overall bone marrow architecture, and importantly it is a technique can also be extended to fixed-MDS patient samples.

As described, one of the greatest risk factors for MDS is age. Mouse models of aged marrow have increased inflammatory cytokines (341), and in TKO mice we observe increased LSK and SLAM-HSC numbers, compensating for dying progenitors (298). Age also decreases immune function (342), with a myeloid skewing of the marrow and decreased T and B cell function, as well as sensitivity to infections. Although it is known that individuals with MDS have increased risk of infection due to neutropenia, it is

unknown if prior infections contribute overall disease risk. Some hints from the literature, particularly for *Tet2-/-* mice suggest that dysfunction of the intestinal barrier resulting in increased bacterial burden indeed promotes bone marrow failure (334). We can also test this possibility in our CHIP mouse models chronically stimulating with lower doses of LPS, TNFα, or Poly I:C. Overtime we can determine if these treatments accelerate bone marrow failure, particularly red cell development, and if intervention with anti-inflammatories or cell death inhibitors alters disease course.

Given that erythroid cells are particularly sensitive to TNFα inflammation, it would be interesting to further evaluate red cells for damage and oxidative stress in these models. Red cell membranes are particularly prone to oxidative stress, resulting in deformities, increased hemolysis, and decreased oxygen handling abilities (343). Oxidative stress has specifically been shown to contribute to hemolytic anemia (344). Furthermore, red cells themselves have been recently shown to harbor a multitude of cytokines, including IFN-γ and TNFα (306). This suggests that anemia and red cell stress could directly contribute to disease progression in a feed-forward manner. It would be interesting to know if *Tet2-/-* crossed to mice with decreased ROS handling abilities, such *Nfr2-/-* or *PRX2 -/-*, would exacerbate this phenotype (345).

Lastly, in an approach similar to the one presented in Chapter 3, human genetics can be used to compliment mouse studies, particularly helping to improve our understanding of genetic predisposition to BMF disorders. As described, GWAS studies and BioVU can be evaluated using PrediXcan for inflammatory, CHIP and necrotic genes of interest. This will help to determine how germline changes (rather than environmental) increase or decrease associations with bone marrow failure. This will particularly important for CHIP genes, as it is currently unknown why some individuals with these mutations

progress while others do not. We can also use this information to look at genes in combination or at individuals who fall at extreme ends of genetically determined expression. These genetic studies are only limited by patient numbers, which can be increased by sequencing BMF patients at Vanderbilt already in the SD. Thus, genetic tools in combination with the mouse experiments proposed above can begin to unravel pending questions concerning causes and progression of this disease.

Important considerations for current therapies for MDS

There has been long-standing interest in inhibiting anti-apoptotic proteins in blood cancers. Bcl-2 is highly overexpressed in follicular lymphoma, chronic lymphocytic leukemia (CLL), and mantle cell lymphoma (MCL), while also contributing to acute lymphoblastic leukemia (ALL), and acute and chronic myeloid leukemias (AML and CML). One of the first successful drugs used in the clinic has been Navitoclax (ABT-263), which targets Bcl-2, Bcl-XL, and Bcl-w. It has shown promising results in patients with CLL and is currently still in clinical trials for leukemias and solid tumors. Navitoclax however can only be used in limited does due to severe thrombocytopenia caused by inhibiting Bcl-XL (346, 347). Venetoclax, which specifically targets Bcl-2 is better tolerated, and was approved in 2016 for therapeutic use for CLL and in 2018 in combination with Rituxan for refractory CLL (348). Currently, it has been granted accelerated FDA approval for AML (patients ineligible for induction chemotherapy).

The anti-apoptotic protein Mcl-1 is also overexpressed in numerous blood cancers and solid tumors. Currently, Phase I clinical trials using multiple Mcl-1 inhibitors such as AZD5991 (AstraZeneca), MIK665/S64315 (Novaritis), and AMG176/AMG 397 (Amgen) are recruiting patients with multiple relapsed or refractory malignancies including multiple

myeloma and lymphoma. Several Phase I trials are also recruiting to test Mcl-1 inhibitors (MIK665/S6431) in patients with AML and MDS.

Despite the presence of clones or blasts in MDS, it is not leukemia, and therefore several considerations should be made when using these inhibitors. Firstly, from a biological perspective, targeting Mcl-1 will only be effective if a dose can be achieved that is not toxic to normal stem cells (349). Particularly in MDS, where there may not be excessive blasts, Mcl-1 has the potential to exacerbate disease progression. Secondly, it has been shown that expression levels of MCL-1 are not different between healthy human marrow and MDS marrow, nor is it different between MDS risk groups (350). Bcl-2 family proteins however have been shown to be increased in high-risk MDS, but not low-risk (351), consistent with our findings that necrosis and inflammation, rather than apoptosis, may be important drivers in early disease. Currently, Phase I clinical trials recruiting for the use of Venetoclax in high-risk MDS may be promising.

Our results suggest that therapeutic intervention with anti-inflammatory drugs would be beneficial, especially for low risk MDS patients who have not yet progressed. Low-risk MDS is particularly difficult to treat as transfusions, EPO, and lenalidomide (for del 5q patients), work to manage anemia, but are temporary, resulting in responses in only 30% of patients for up to a year. It is likely that ant-inflammatory therapies in these patients would be well tolerated as they do not specifically target normal hematopoiesis. Biologics such as Enbrel, which work as a TNFα decoy receptor, may prove to be therapeutically useful to slow the progression of MDS. Targeting the TGF-β family of receptors, which normally inhibits erythropoiesis, with the ligand trap luspatercept (ACE-536) has also had some success in low-risk MDS patients. An early trial showed that patients with ringed-sideroblasts and high EPO had response rates of approximately 50%

versus 12% with placebo. While it is unclear precisely how luspatercept impacts erythropoiesis, its early success points to the importance of cytokines and the red cell compartment in managing disease (352)

REFERENCES

1. Kerr JFR, Wyllie AH CA (1972) Apoptosis: A Basic Biological Phenomenon with Wideranging Implications in Tissue Kinetics. *Br J Cancer* 26(239):239–257.
2. Sulston JE, Schierenberg E, White JG T (1983) The embryonic cell lineage of the nematode Caenorhabditis elegans. *Dev Biol* 100(1):64–119.
3. Horvitz HR EH (1986) Genetic Control of Programmed Cell Death in the Nematode C. elegans. *Cell* 44:817–829.
4. Tsujimoto Y, Gorham J, Cossman J, Jaffe E CC (1985) The t(14;18) chromsome translocations involved in B-cell neoplasms result from mistakes in VDJ joining. *Science (80-)* 229(4720):1390–1393.
5. Cleary ML, Smith SD SJ (1986) Cloning and Structural Analysis of cDNAs for bcl-2 and a Hybrid bcl-2/lmmunoglobulin Transcript Resulting from the t(14;18) Translocation. *Cell* 47:19–28.
6. Bakhshi A, Wright JJ, Graninger W, Seto M, Owens J, Cossman J, Jensen JP, Goldman P KS (1987) Mechanism of the t(14;18) chromosomal translocation: structural analysis of both derivative 14 and 18 reciprocal partners. *Proc Natl Acad Sci* 84:2396–2400.
7. Vaux DL, Cory S AJ (1988) Bcl-2 gene promotes haemopoietic cell survival and cooperates with c-myc to immortalize pre-B cells. *Nature* 335:440–442.
8. McDonnell TJ, Deane N, Platt FM, Nunez G, Jaeger U, McKearn JP KS (1989) Bcl-2-immunoglobulin transgenic mice demonstrate extended B cell survival and follicular lymphoproliferation. *Cell* 57(1):79–88.
9. Oltval ZN, Milliman CL KS (1993) Bcl-2 heterodimerizes in vivo with a conserved homolog, Bax, that accelerates programmed cell death. *Cell* 74(4):P609-619.
10. Hengartener MO HH (1994) C. elegans cell survival gene ced-9 encodes a functional homolog of the mammalian proto-oncogene bcl-2. *Cell* 76:665–676.
11. Youle, Richard J SA (2008) The BCL-2 protein family: opposing activities that mediate death. *Nat Rev Mol Cell Biol* 9(1):47–59.
12. Kale J, Osterlund EJ, Andrews DW (2018) BCL-2 family proteins: Changing partners in the dance towards death. *Cell Death Differ* 25(1):65–80.
13. Adams JM, et al. (2005) Differential Targeting of Prosurvival Bcl-2 Proteins by Their BH3-Only Ligands Allows Complementary Apoptotic Function. *Mol Cell* 17(3):393–403.
14. Kong W, et al. (2018) Experimental Characterization of the Binding Affinities between Proapoptotic BH3 Peptides and Antiapoptotic Bcl-2 Proteins. *ChemMedChem* 13(17):1763–1770.
15. Certo M, et al. (2006) Mitochondria primed by death signals determine cellular addiction to antiapoptotic BCL-2 family members. *Cancer Cell* 9(5):351–365.
16. Deng J, et al. (2007) BH3 Profiling Identifies Three Distinct Classes of Apoptotic Blocks to Predict Response to ABT-737 and Conventional Chemotherapeutic Agents. *Cancer Cell* 12(2):171–185.
17. Oltersdorf T, et al. (2005) An inhibitor of Bcl-2 family proteins induces regression of solid tumours. *Nature* 435(7042):677–681.
18. Zhu M, et al. (2015) Targeting BCL2 with Venetoclax in Relapsed Chronic Lymphocytic Leukemia. *N Engl J Med* 374(4):311–322.
19. Kantarjian H, et al. (2016) Efficacy and Biological Correlates of Response in a Phase II Study of Venetoclax Monotherapy in Patients with Acute Myelogenous Leukemia. *Cancer Discov* 6(10):1106–1117.

20. Scorrano L, et al. (2002) A distinct pathway remodels mitochondrial cristae and mobilizes cytochrome c during apoptosis. *Dev Cell* 2(1):55–67.
21. Yamaguchi R, et al. (2008) Opa1-Mediated Cristae Opening Is Bax/Bak and BH3 Dependent, Required for Apoptosis, and Independent of Bak Oligomerization. *Mol Cell* 31(4):557–569.
22. Zou H, Li Y, Liu X, Wang X (1999) An APAf-1 · cytochrome C multimeric complex is a functional apoptosome that activates procaspase-9. *J Biol Chem* 274(17):11549–11556.
23. Ferreira KS, et al. (2012) Caspase-3 feeds back on caspase-8, Bid and XIAP in type I Fas signaling in primary mouse hepatocytes. *Apoptosis* 17(5):503–515.
24. Du C, Fang M, Li Y, Li L, Wang X (2000) Smac, a Mitochondrial Protein that Promotes Cytochrome c–Dependent Caspase Activation by Eliminating IAP Inhibition. 102:33–42.
25. Ishihara Y, Shimamoto N (2006) Involvement of endonuclease G in nucleosomal DNA fragmentation under sustained endogenous oxidative stress. *J Biol Chem* 281(10):6726–6733.
26. Szabo C, et al. (2003) Intranuclear localization of apoptosis-inducing factor (AIF) and large scale dna fragmentation after traumatic brain injury in rats and in neuronal cultures exposed to peroxynitrite. *J Neurochem* 82(1):181–191.
27. Scaffidi C, Schmitz I, Zha J, Korsmeyer SJ, Krammer PH PM (1999) Differential Modulation of Apoptosis Sensitivity in CD95 Type I and Type II Cells. *J Biol Chem* 274(32):22532–22538.
28. Özören N, El-Deiry WS (2002) Defining characteristics of types I and II apoptotic cells in response to TRAIL. *Neoplasia* 4(6):551–557.
29. Stennicke HR, Jurgensmeier JM, Shin H, Deveraux Q, Wolf BB, Yang X, Zhou Q, Ellerby MH, Ellerby LM, Bredesen D, Green DR, Reed JC, Froelich CJ SG (1998) Pro-caspase-3 is a major physiologic targe of caspase-8. *J Biol Chem* 273:27084–27090.
30. Reiner U. Jänicke‡, Patrick Ng MLS and AGP (1998) Caspase-3 Is Required for α-Fodrin Cleavage but Dispensable for Cleavage of Other Death Substrates in Apoptosis. *J Biol Chem* (273):15540–15545.
31. Choudhary GS, et al. (2015) Cyclin E/Cdk2-dependent phosphorylation of Mcl-1 determines its stability and cellular sensitivity to BH3 mimetics. *Oncotarget* 6(19):16912–16925.
32. Megyesi J, Hodeify R, Seng N, Price P, Tarcsafalvi A (2016) Cdk2 phosphorylation of Bcl-xL after stress converts it to a pro-apoptotic protein mimicking Bax/Bak. *Cell Death Discov* 2(1):1–9.
33. Bassik MC, Scorrano L, Oakes SA, Pozzan T, Korsmeyer SJ (2004) Phosphorylation of BCL-2 regulates ER Ca2+ homeostasis and apoptosis. *EMBO J* 23(5):1207–1216.
34. Hill JA, et al. (2012) Exercise-induced BCL2-regulated autophagy is required for muscle glucose homeostasis. *Nature* 481(7382):511–515.
35. Letai A, et al. (2018) Phosphorylation switches Bax from promoting to inhibiting apoptosis thereby increasing drug resistance. *EMBO Rep* 19(9):e45235.
36. Zinkel SS, et al. (2005) A role for proapoptotic BID in the DNA-damage response. *Cell* 122(4):579–591.
37. Kamer I, et al. (2005) Proapoptotic BID is an ATM effector in the DNA-damage response. *Cell* 122(4):593–603.

38. Danial NN, et al. (2003) BAD and glucokinase reside in a mitochondrial complex that integrates glycolysis and apoptosis. *Nature* 424(6951):952–6.
39. Gross A, et al. (1999) Caspase cleaved BID targets mitochondria and is required for cytochrome c release, while BCL-X(L) prevents this release but not tumor necrosis factor-R1/Fas death. *J Biol Chem* 274(2):1156–1163.
40. Alnemri ES, et al. (2002) Caspase Cleavage Enhances the Apoptosis-Inducing Effects of BAD. *Mol Cell Biol* 21(9):3025–3036.
41. Kirsch DG, et al. (2002) Modulation of cell death by Bcl-xL through caspase interaction. *Proc Natl Acad Sci* 95(2):554–559.
42. Dijkers PF, Medema RH, Lammers JWJ, Koenderman L, Coffer PJ (2000) Expression of the pro-apoptotic Bcl-2 family member Bim is regulated by the forkhead transcription factor FKHR-L1. *Curr Biol* 10(19):1201–1204.
43. Nakano K, Vousden KH (2001) PUMA, a novel proapoptotic gene, is induced by p53. *Mol Cell* 7(3):683–694.
44. Cregan SP, et al. (2010) Neuronal Apoptosis Induced by Endoplasmic Reticulum Stress Is Regulated by ATF4-CHOP-Mediated Induction of the Bcl-2 Homology 3-Only Member PUMA. *J Neurosci* 30(50):16938–16948.
45. Degterev A, et al. (2005) Chemical inhibitor of nonapoptotic cell death with therapeutic potential for ischemic brain injury. *Nat Chem Biol* 1(2):112–119.
46. Stanger BZ, Leder P, Lee TH SB (1995) RIP: a novel protein containing a death domain that interacts with Fas/APO-1 (CD95) in yeast and causes cell death. *Cell* 81(4):513–523.
47. Stanger B, Kim E, Seedt B (1995) RIP A Novel Protein Containing a Death Domain. *Cell* 81.
48. Holler N, et al. (2000) Fas triggers an alternative, caspase-8-independent cell death pathway using the kinase RIP as effector molecule. *Nat Immunol* 1(6):489–495.
49. Hitomi J, et al. (2008) Identification of a Molecular Signaling Network that Regulates a Cellular Necrotic Cell Death Pathway. *Cell* 135(7):1311–1323.
50. Tait SWG, et al. (2013) Widespread Mitochondrial Depletion via Mitophagy Does Not Compromise Necroptosis. *Cell Rep* 5(4):878–885.
51. Zhang DW, shao J, Lin J, Zhang B, Lu B-J, Lin S-C, Dong M-Q HJ (2009) RIP3, an Energy Metabolism Regulator That Switches TNF-Induced Cell Death from Apoptosis to Necrosis. *Science (80-)* 325.
52. Sun X, et al. (1999) RIP3 , a Novel Apoptosis-inducing Kinase *. 274(24):16871–16875.
53. Cai Z, et al. (2014) Plasma membrane translocation of trimerized MLKL protein is required for TNF-induced necroptosis. *Nat Cell Biol* 16(1):55–65.
54. Dovey CM, et al. (2018) MLKL Requires the Inositol Phosphate Code to Execute Necroptosis. *Mol Cell* 70(5):936–948.e7.
55. Gong YN, et al. (2017) ESCRT-III Acts Downstream of MLKL to Regulate Necroptotic Cell Death and Its Consequences. *Cell* 169(2):286–300.e16.
56. Pasparakis M, Vandenabeele P (2015) Necroptosis and its role in inflammation. *Nature* 517(7534):311–320.
57. Van Coillie S, et al. (2018) Ubiquitin-Mediated Regulation of RIPK1 Kinase Activity Independent of IKK and MK2. *Mol Cell* 69(4):566–580.e5.
58. Surinova S, et al. (2015) LUBAC-Recruited CYLD and A20 Regulate Gene Activation and Cell Death by Exerting Opposing Effects on Linear Ubiquitin in Signaling Complexes. *Cell Rep* 13(10):2258–2272.
59. Zhu K, et al. (2018) Necroptosis promotes cell-autonomous activation of

proinflammatory cytokine gene expression article. *Cell Death Dis* 9(5). doi:10.1038/s41419-018-0524-y.
60. Kaczmarek A, Vandenabeele P, Krysko D V. (2013) Necroptosis: The Release of Damage-Associated Molecular Patterns and Its Physiological Relevance. *Immunity* 38(2):209–223.
61. Shlomovitz I, et al. (2019) Necroptosis directly induces the release of full-length biologically active IL-33 in vitro and in an inflammatory disease model. *FEBS J* 286(3):507–522.
62. Fernández-Majada V, et al. (2011) FADD prevents RIP3-mediated epithelial cell necrosis and chronic intestinal inflammation. *Nature* 477(7364):330–334.
63. van Loo G, et al. (2011) The Adaptor Protein FADD Protects Epidermal Keratinocytes from Necroptosis In Vivo and Prevents Skin Inflammation. *Immunity* 35(4):572–582.
64. Heckmann BL, Tummers B, Green DR (2019) Crashing the computer: apoptosis vs. necroptosis in neuroinflammation. *Cell Death Differ* 26(1):41–52.
65. Kelliher MA, et al. (1998) The death domain kinase RIP mediates the TNF-induced NF-κB signal. *Immunity* 8(3):297–303.
66. King KY, Goodell MA (2011) Inflammatory modulation of HSCs: Viewing the HSC as a foundation for the immune response. *Nat Rev Immunol* 11(10):685–692.
67. Varfolomeev EE1, Schuchmann M, Luria V, Chiannilkulchai N, Beckmann JS, Mett IL, Rebrikov D, Brodianski VM, KemVarfolomeev EE1, Schuchmann M, Luria V, Chiannilkulchai N, Beckmann JS, Mett IL, Rebrikov D, Brodianski VM, Kemper OC, Kollet O, Lapidot T, Soff WD (1998) Targeted disruption of the mouse Caspase 8 gene ablates cell death induction by the TNF receptors, Fas/Apo1, and DR3 and is lethal prenatally. *Immunity* 9(2):267–76.
68. Upton JW, et al. (2011) RIP3 mediates the embryonic lethality of caspase-8-deficient mice. *Nature* 471(7338):368–372.
69. Dillon CP, et al. (2012) Survival Function of the FADD-CASPASE-8-cFLIPLComplex. *Cell Rep* 1(5):401–407.
70. Cripps JG, et al. (2014) RIPK1 Blocks Early Postnatal Lethality Mediated by Caspase-8 and RIPK3. *Cell* 157(5):1189–1202.
71. Feng S, et al. (2007) Cleavage of RIP3 inactivates its caspase-independent apoptosis pathway by removal of kinase domain. *Cell Signal* 19(10):2056–2067.
72. Pop C, et al. (2011) FLIP L induces caspase 8 activity in the absence of interdomain caspase 8 cleavage and alters substrate specificity . *Biochem J* 433(3):447–457.
73. Qin ZH, et al. (2001) Pro-caspase-8 Is Predominantly Localized in Mitochondria and Released into Cytoplasm upon Apoptotic Stimulation. *J Biol Chem* 276(11):8079–8086.
74. Gonzalvez F, et al. (2008) Cardiolipin provides an essential activating platform for caspase-8 on mitochondria. *J Cell Biol* 183(4):681–696.
75. Poreba M, et al. (2018) Caspase selective reagents for diagnosing apoptotic mechanisms. *Cell Death Differ*:1–16.
76. Heise N, et al. (2015) NEMO Prevents Steatohepatitis and Hepatocellular Carcinoma by Inhibiting RIPK1 Kinase Activity-Mediated Hepatocyte Apoptosis. *Cancer Cell* 28(5):582–598.
77. Billen LP, Shamas-Din A, Andrews DW (2008) Bid: A Bax-like BH3 protein. *Oncogene* 27(S1):S93–S104.
78. Wang K, Yin XM, Chao DT, Milliman CL, Korsmeyer SJ (1996) BID: A novel BH3 domain-only death agonist. *Genes Dev* 10(22):2859–2869.

79. Luo X, Budihardjo I, Zou H, Slaughter C, Wang X (1998) Bid, a Bcl2 interacting protein, mediates cytochrome c release from mitochondria in response to activation of cell surface death receptors. *Cell* 94(4):481–490.
80. Li H, Zhu H, Xu C-J, Yuan J (1998) Cleavage of BID by Caspase 8 Mediates the Mitochondrial Damage in the Fas Pathway of Apoptosis. *Cell* 94:491–501.
81. Wei MC1, Lindsten T, Mootha VK, Weiler S, Gross A, Ashiya M, Thompson CB KS (2000) tBID, a membrane-targeted death ligand, oligomerizes BAK to release cytochrome c. *Genes Dev* 14(16):2060–2071.
82. Ruffolo SC1, Breckenridge DG, Nguyen M, Goping IS, Gross A, Korsmeyer SJ, Li H, Yuan J SG (2000) No BID-dependent and BID-independent pathways for BAX insertion into mitochondria. *Cell Death Differ* 7(11):1101–1108.
83. Korsmeyer SJ, et al. (2000) Pro-apoptotic cascade activates BID, which oligomerizes BAK or BAX into pores that result in the release of cytochrome c. *Cell Death Differ* 7(12):1166–1173.
84. Mcdonnell JM, et al. (1999) Solution Structure of the Proapoptotic Molecule BID : A Structural Basis for Apoptotic Agonists and Antagonists. 96:625–634.
85. Chou JJ, et al. (1999) Solution Structure of BID , an Intracellular Amplifier of Apoptotic Signaling. 96:615–624.
86. Kyoung JO, et al. (2005) Conformational changes in BID, a pro-apoptotic BCL-2 family member, upon membrane binding: A site-directed spin labeling study. *J Biol Chem* 280(1):753–767.
87. Shamas-Din A, et al. (2013) TBid undergoes multiple conformational changes at the membrane required for bax activation. *J Biol Chem* 288(30):22111–22127.
88. Lutter M, et al. (2000) Cardiolipin provides specificity for targeting of tBid to mitochondria. *Nat Cell Biol* 2(10):754–761.
89. Kim T, et al. (2004) Bid – Cardiolipin Interaction at Mitochondrial Contact Site Contributes to Mitochondrial Cristae Reorganization and Cytochrome c Release. 15(July):3061–3072.
90. Tae-Hyoung Kim, Yongge Zhao, Wen-Xing Ding, Jin Na Shin, Andrew A. Amoscato X-MY (2004) Bid-Cardiolipin Interaction at Mitochondrial Contact Site Contributes to Mitochondrial Cristae Reorganization and Cytochrome c Release. *Mol Biol Cell* 15:3061–3072.
91. Grinberg M, et al. (2005) Mitochondrial Carrier Homolog 2 Is a Target of tBID in Cells Signaled To Die by Tumor Necrosis Factor Alpha. 25(11):4579–4590.
92. Gross A, et al. (2012) Molecular Basis of the Interaction between Proapoptotic Truncated BID (tBID) Protein and Mitochondrial Carrier Homologue 2 (MTCH2) Protein. *J Biol Chem* 287(18):15016–15023.
93. Maryanovich M, et al. (2015) An MTCH2 pathway repressing mitochondria metabolism regulates haematopoietic stem cell fate. *Nat Commun* 6(12):7901.
94. Cogliati S, et al. (2013) Mitochondrial cristae shape determines respiratory chain supercomplexes assembly and respiratory efficiency. *Cell* 155(1):160–171.
95. Yin XM, et al. (1999) Bid-deficient mice are resistant to Fas-induced hepatocellular apoptosis. *Nature* 400(6747):886–891.
96. Lacronique V , Mignon A , Fabre M , Viollet B , Rouquet N , Molina T , Porteu A , Henrion A , Bouscary D , Varlet P , Joulin V KA (1996) Bcl-2 protects from lethal hepatic apoptosis induced by an anti-Fas antibody in mice. *Nat Med* 2(1):80–86.
97. Zinkel SS, et al. (2003) Proapoptotic BID is required for myeloid homeostasis and tumor suppression. *Genes Dev* 17(2):229–239.
98. Liu Y, Vaithiyalingam S, Zinkel SS, Shi Q, Chazin WJ (2011) BID Binds to

Replication Protein A and Stimulates ATR Function following Replicative Stress. *Mol Cell Biol* 31(21):4298–4309.
99. Liu Y, Bertram C, Shi Q, Zinkel S (2010) Proapoptotic Bid mediates the Atr-directed DNA damage response to replicative stress. *Cell Death Differ* 18(10):841–852.
100. Liu Y, Aiello A, Zinkel SS (2012) Bid protects the mouse hematopoietic system following hydroxyurea-induced replicative stress. *Cell Death Differ* 19(10):1602–1612.
101. Matise L, et al. (2010) A role for proapoptotic Bax and Bak in T-cell differentiation and transformation. *Blood* 116(24):5237–5246.
102. Barry M, et al. (2000) Granzyme B short-circuits the need for caspase 8 activity during granule-mediated cytotoxic T-lymphocyte killing by directly cleaving Bid. *Mol Cell Biol* 20(11):3781–94.
103. Linder S, et al. (2002) Calpain-Mediated Bid Cleavage and Calpain-Independent Bak Modulation: Two Separate Pathways in Cisplatin-Induced Apoptosis. *Mol Cell Biol* 22(9):3003–3013.
104. Cirman T, et al. (2004) Selective Disruption of Lysosomes in HeLa Cells Triggers Apoptosis Mediated by Cleavage of Bid by Multiple Papain-like Lysosomal Cathepsins. *J Biol Chem* 279(5):3578–3587.
105. Zha J1, Weiler S, Oh KJ, Wei MC KS (2000) Posttranslational N-myristoylation of BID as a molecular switch for targeting mitochondria and apoptosis. *Science (80-)* 290(5497):1761–1765.
106. Desagher S, et al. (2001) Phosphorylation of Bid by Casein Kinases I and II Regulates Its Cleavage by Caspase 8. 8:601–611.
107. Wang P, et al. (2014) Phosphorylation of the Proapoptotic BH3-Only Protein Bid Primes Mitochondria for Apoptosis during Mitotic Arrest. *Cell Rep* 7(3):661–671.
108. Yang E1, Zha J, Jockel J, Boise LH, Thompson CB KS (1995) Bad, a heterodimeric partner for Bcl-XL and Bcl-2, displaces Bax and promotes cell death. *Cell* 80(2):285–291.
109. Szlyk B, et al. (2014) A phospho-BAD BH3 helix activates glucokinase by a mechanism distinct from that of allosteric activators. *Nat Struct Mol Biol* 21(1):36–42.
110. Giménez-Cassina A, Danial NN (2015) Regulation of mitochondrial nutrient and energy metabolism by BCL-2 family proteins. *Trends Endocrinol Metab* 26(4):165–75.
111. Odumade OA, et al. (2010) The Proapoptotic Function of Noxa in Human Leukemia Cells Is Regulated by the Kinase Cdk5 and by Glucose. *Mol Cell* 40(5):823–833.
112. Ludwinski MW1, Sun J, Hilliard B, Gong S, Xue F, Carmody RJ, DeVirgiliis J CY (2009) Critical roles of Bim in T cell activation and T cell-mediated autoimmune inflammation in mice. *J Clin Invest* 119(6):1706–1713.
113. Mattoo AR1, Pandita RK2, Chakraborty S2, Charaka V2, Mujoo K2, Hunt CR2 PT (2017) MCL-1 Depletion Impairs DNA Double-Strand Break Repair and Reinitiation of Stalled DNA Replication Forks. *Mol Cell Biol* 37(3).
114. Dremina ES1, Sharov VS, Kumar K, Zaidi A, Michaelis EK SC (2004) Anti-apoptotic protein Bcl-2 interacts with and destabilizes the sarcoplasmic/endoplasmic reticulum Ca2+-ATPase (SERCA). *Biochem J* 383(3):361–370.
115. Pattingre S1, Tassa A, Qu X, Garuti R, Liang XH, Mizushima N, Packer M, Schneider MD LB (2005) Bcl-2 antiapoptotic proteins inhibit Beclin 1-dependent autophagy. *Cell* 122(6):927–936.

116. Maiuri MC1, Le Toumelin G, Criollo A, Rain JC, Gautier F, Juin P, Tasdemir E, Pierron G, Troulinaki K, Tavernarakis N, Hickman JA, Geneste O KG (2007) Functional and physical interaction between Bcl-X(L) and a BH3-like domain in Beclin-1. *EMBO J* 26(10):2527–2539.
117. Germain M SR (2011) MCL-1 regulates the balance between autophagy and apoptosis. *Autophagy* 7(5):549–551.
118. Karbowski M1, Norris KL, Cleland MM, Jeong SY YR (2006) Role of Bax and Bak in mitochondrial morphogenesis. *Nature* 7112(7112):658–662.
119. Cleland MM, et al. (2011) The Soluble Form of Bax Regulates Mitochondrial Fusion via MFN2 Homotypic Complexes. *Mol Cell* 41(2):150–160.
120. Karbowski M1, Lee YJ, Gaume B, Jeong SY, Frank S, Nechushtan A, Santel A, Fuller M, Smith CL YR (2002) Spatial and temporal association of Bax with mitochondrial fission sites, Drp1, and Mfn2 during apoptosis. *J Cell Biol* 159(6):931–8.
121. Jagasia R1, Grote P, Westermann B CB (2005) DRP-1-mediated mitochondrial fragmentation during EGL-1-induced cell death in C. elegans. *Nature* 433(7027):754–60.
122. McNally MA, Soane L, Roelofs BA, Hartman AL, Hardwick JM (2013) The N-terminal helix of Bcl-xL targets mitochondria. *Mitochondrion* 13(2):119–124.
123. Chen Y-B, et al. (2011) Bcl-xL regulates mitochondrial energetics by stabilizing the inner membrane potential. *J Cell Biol* 195(2):263–76.
124. Almeida A, et al. (2015) Regulation of Bcl-xL-ATP Synthase Interaction by Mitochondrial Cyclin B1-Cyclin-Dependent Kinase-1 Determines Neuronal Survival. *J Neurosci* 35(25):9287–9301.
125. Perciavalle RM, et al. (2012) Anti-apoptotic MCL-1 localizes to the mitochondrial matrix and couples mitochondrial fusion to respiration. *Nat Cell Biol* 14(6):575–583.
126. Thomas RL, et al. (2013) Loss of MCL-1 leads to impaired autophagy and rapid development of heart failure. *Genes Dev* 27(12):1365–1377.
127. Wang X, et al. (2013) Deletion of MCL-1 causes lethal cardiac failure and mitochondrial dysfunction. *Genes Dev* 27(12):1351–1364.
128. Escudero S, et al. (2018) Dynamic Regulation of Long-Chain Fatty Acid Oxidation by a Noncanonical Interaction between the MCL-1 BH3 Helix and VLCAD. *Mol Cell* 69(5):802–819.e1.
129. Mannella CA (2006) Structure and dynamics of the mitochondrial inner membrane cristae. *Biochim Biophys Acta* 1763(5–6):542–548.
130. Mannella CA1, Lederer WJ JM (2013) The connection between inner membrane topology and mitochondrial function. *J Mol Cell Cardiol* (62):51–57.
131. Zick M, Rabl R, Reichert AS (2009) Cristae formation-linking ultrastructure and function of mitochondria. *Biochim Biophys Acta - Mol Cell Res* 1793(1):5–19.
132. Hackenbrock CR (1966) Ultrastructural bases for metabolically linked mechanical activity in mitochondria. I. Reversible ultrastructural changes with change in metabolic steady state in isolated liver mitochondria. *J Cell Biol* 30(2):269–297.
133. Mannella CA (2008) Structural diversity of mitochondria: Functional implications. *Ann N Y Acad Sci* 1147:171–179.
134. Wallace DC, et al. (2015) Trans-mitochondrial coordination of cristae at regulated membrane junctions. *Nat Commun* 6(1):4–11.
135. Martinou J-C, et al. (2011) Dual Role of Mitofilin in Mitochondrial Membrane Organization and Protein Biogenesis. *Dev Cell* 21(4):694–707.
136. Harner M, et al. (2011) The mitochondrial contact site complex, a determinant of

mitochondrial architecture. *EMBO J* 30(21):4356–4370.
137. Hoppins S, et al. (2011) A mitochondrial-focused genetic interaction map reveals a scaffold-like complex required for inner membrane organization in mitochondria. *J Cell Biol* 195(2):323–340.
138. Frezza C, et al. (2006) OPA1 Controls Apoptotic Cristae Remodeling Independently from Mitochondrial Fusion. *Cell* 126(1):177–189.
139. Varanita T, et al. (2015) The Opa1-dependent mitochondrial cristae remodeling pathway controls atrophic, apoptotic, and ischemic tissue damage. *Cell Metab* 21(6):834–844.
140. Paumard P, et al. (2002) The ATP synthase is involved in generating mitochondrial cristae morphology. *EMBO J* 21(3):221–230.
141. Dudkina N V., Boekema EJ, Peters K, Kouřil R, Braun H-P (2009) Structure and function of mitochondrial supercomplexes. *Biochim Biophys Acta - Bioenerg* 1797(6–7):664–670.
142. Davies KM1, Anselmi C, Wittig I, Faraldo-Gómez JD KW (2012) Structure of the yeast F1Fo-ATP synthase dimer and its role in shaping the mitochondrial cristae. *Proc Natl Acad Sci* 109(34):13602–13607.
143. DeVay RM, et al. (2009) Coassembly of Mgm1 isoforms requires cardiolipin and mediates mitochondrial inner membrane fusion. *J Cell Biol* 186(6):793–803.
144. Malhotra A, et al. (2011) Cardiolipin Affects the Supramolecular Organization of ATP Synthase in Mitochondria. *Biophys J* 100(9):2184–2192.
145. Friedman JR, Mourier A, Yamada J, Michael McCaffery J, Nunnari J (2015) MICOS coordinates with respiratory complexes and lipids to establish mitochondrial inner membrane architecture. *Elife* 2015(4):1–61.
146. Song Z, Chen H, Fiket M, Alexander C, Chan DC (2007) OPA1 processing controls mitochondrial fusion and is regulated by mRNA splicing, membrane potential, and Yme1L. *J Cell Biol* 178(5):749–755.
147. Agier V, et al. (2012) Defective mitochondrial fusion, altered respiratory function, and distorted cristae structure in skin fibroblasts with heterozygous OPA1 mutations. *Biochim Biophys Acta - Mol Basis Dis* 1822(10):1570–1580.
148. Mannella CA1, Pfeiffer DR, Bradshaw PC, Moraru II, Slepchenko B, Loew LM, Hsieh CE, Buttle K MM (2001) Topology of the mitochondrial inner membrane: dynamics and bioenergetic implications. *IUMBM Life* 3–5:93–100.
149. Kolwicz SC, Purohit S, Tian R (2013) Cardiac metabolism and its interactions with contraction, growth, and survival of cardiomyocytes. *Circ Res* 113(5):603–616.
150. Lesnefsky EJ, Moghaddas S, Tandler B, Kerner J, Hoppel CL (2001) Mitochondrial Dysfunction in Cardiac Disease: Ischemia–Reperfusion, Aging, and Heart Failure. *J Mol Cell Cardiol* 33(6):1065–1089.
151. Murphy E, et al. (2016) *Mitochondrial Function, Biology, and Role in Disease: A Scientific Statement from the American Heart Association* doi:10.1161/RES.0000000000000104.
152. El-Hattab AW, Scaglia F (2016) Mitochondrial Cardiomyopathies. *Front Cardiovasc Med* 3(July):25.
153. Bourke JP, et al. (2012) Cardiac involvement in mitochondrial DNA disease: clinical spectrum, diagnosis, and management. *Eur Heart J* 33(24):3023–3033.
154. Liu S, et al. (2016) Executive Summary: Heart Disease and Stroke Statistics—2016 Update. *Circulation* 133(4):447–454.
155. Buysschaert I, et al. (2010) A variant at chromosome 9p21 is associated with recurrent myocardial infarction and cardiac death after acute coronary syndrome:

The GRACE genetics study. *Eur Heart J* 31(9):1132–1141.
156. Nikpay M, et al. (2015) A comprehensive 1,000 Genomes-based genome-wide association meta-analysis of coronary artery disease. *Nat Genet* 47(10):1121–30.
157. Murphy AN, et al. (2008) hNOA1 Interacts with Complex I and DAP3 and Regulates Mitochondrial Respiration and Apoptosis. *J Biol Chem* 284(8):5414–5424.
158. Ballinger SW, et al. (2002) Mitochondrial integrity and function in atherogenesis. *Circulation* 106(5):544–549.
159. Yu E, Mercer J, Bennett M (2012) Mitochondria in vascular disease. *Cardiovasc Res* 95(2):173–182.
160. Canto JG1, Rogers WJ, Goldberg RJ, Peterson ED, Wenger NK, Vaccarino V, Kiefe CI, Frederick PD, Sopko G ZZNI (2012) Association of age and sex with myocardial infarction symptom presentation and in-hospital mortality. *JAMA Cardiol* 307(8):813–822.
161. Lesnefsky EJ, Chen Q, Hoppel CL (2016) Mitochondrial Metabolism in Aging Heart. *Circ Res* 118(10):1593–1611.
162. Klipstein-Grobusch K, et al. (2018) Dietary antioxidants and risk of myocardial infarction in the elderly: the Rotterdam Study. *Am J Clin Nutr* 69(2):261–266.
163. Leopold JA (2015) Antioxidants and coronary artery disease: From pathophysiology to preventive therapy. *Coron Artery Dis* 26(2):176–183.
164. Niccoli G, Scalone G, Crea F (2015) Acute myocardial infarction with no obstructive coronary atherosclerosis: Mechanisms and management. *Eur Heart J* 36(8):475–481.
165. Karamanlidis G, Bautista-Hernandez V, Fynn-Thompson F, Del Nido P, Tian R (2011) Impaired mitochondrial biogenesis precedes heart failure in right ventricular hypertrophy in congenital heart disease. *Circ Hear Fail* 4(6):707–713.
166. Farrell SW, et al. (2019) Association of All-Cause and Cardiovascular Mortality With High Levels of Physical Activity and Concurrent Coronary Artery Calcification. *JAMA Cardiol* 75231. doi:10.1001/jamacardio.2018.4628.
167. Ascensão A, Ferreira R, Magalhães J (2007) Exercise-induced cardioprotection - biochemical, morphological and functional evidence in whole tissue and isolated mitochondria. *Int J Cardiol* 117(1):16–30.
168. Frasier CR, Moore RL, Brown DA (2011) Exercise-induced cardiac preconditioning: how exercise protects your achy-breaky heart. *J Appl Physiol* 111(3):905–915.
169. Gustafsson ÅB, Gottlieb RA (2006) Bcl-2 family members and apoptosis, taken to heart. *Am J Physiol Physiol* 292(1):C45–C51.
170. Brocheriou V1, Hagège AA, Oubenaïssa A, Lambert M, Mallet VO, Duriez M, Wassef M, Kahn A, Menasché P GH (2000) Cardiac functional improvement by a human Bcl-2 transgene in a mouse model of ischemia/reperfusion injury. *J Genet Med* 2(5):326–333.
171. Capano M, Crompton M (2006) Bax translocates to mitochondria of heart cells during simulated ischaemia: involvement of AMP-activated and p38 mitogen-activated protein kinases. *Biochem J* 395(1):57–64.
172. Chen M, et al. (2001) Bid is Cleaved by Calpain to an Active Fragment in Vitro and during Myocardial Ischemia/Reperfusion. *J Biol Chem* 276(33):30724–30728.
173. Riddle-Taylor E, et al. (2007) Mutations to bid cleavage sites protect hepatocytes from apoptosis after ischemia/reperfusion injury. *Transplantation* 84(6):778–785.
174. Reimer KA, Rasmussen MM, Jennings RB (1973) Reduction by propranolol of

myocardial necrosis following temporary coronary artery occlusion in dogs. *Circ Res* 33(3):353–363.
175. Nakayama H, et al. (2007) Cardiomyocyte Necrosis As a Primary Mediator of Heart Failure. *Jci* 117(9):2431–2444.
176. Lim SY, Davidson SM, Mocanu MM, Yellon DM, Smith CCT (2007) The cardioprotective effect of necrostatin requires the cyclophilin-D component of the mitochondrial permeability transition pore. *Cardiovasc Drugs Ther* 21(6):467–469.
177. Smith CCT, et al. (2007) Necrostatin: A potentially novel cardioprotective agent? *Cardiovasc Drugs Ther* 21(4):227–233.
178. Marella F.T.R. de Bruijn, Nancy A. Speck, 1 Marian C.E. Peeters and ED (2000) Definitive hematopoietic stem cells first develop within the major arterial regions of the mouse embryo. *EMBO J* 19(11):2465–2474.
179. Hanna K. A. Mikkola SHO (2006) The journey of developing hematopoietic stem cells. *Development* 133:3733–3744.
180. Pinho S, Frenette PS (2019) Haematopoietic stem cell activity and interactions with the niche. *Nat Rev Mol Cell Biol* (In press). doi:10.1038/s41580-019-0103-9.
181. Morrison SJ, Scadden DT (2014) The bone marrow niche for haematopoietic stem cells. *Nature* 505(7483):327–334.
182. Terhorst C, et al. (2005) SLAM Family Receptors Distinguish Hematopoietic Stem and Progenitor Cells and Reveal Endothelial Niches for Stem Cells. *Cell* 121(7):1109–1121.
183. Veis DJ1, Sorenson CM, Shutter JR KS (1993) Bcl-2-deficient mice demonstrate fulminant lymphoid apoptosis, polycystic kidneys, and hypopigmented hair. *Cell* 75(2):229–240.
184. Rinkenberger JL1, Horning S, Klocke B, Roth K KS (2000) Mcl-1 deficiency results in peri-implantation embryonic lethality. *Genes Dev* 14(1):23–7.
185. Motoyama N, Wang F, Roth KA, Sawa H, Nakayama K, Nakayama K, Negishi I, Senju S, Zhang Q, Fujii S et al. (1995) Massive cell death of immature hematopoietic cells and neurons in Bcl-x-deficient mice. *Science (80-)* 267(5203):1506–1510.
186. Wagner KU, Claudio E, Rucker EB 3rd, Riedlinger G, Broussard C, Schwartzberg PL, Siebenlist U HL (2000) Conditional deletion of the Bcl-x gene from erythroid cells results in hemolytic anemia and profound splenomegaly. *Dev Biol* 127(22):4949–4958.
187. Delbridge ARD, Opferman JT, Grabow S, Strasser A (2015) Antagonism between MCL-1 and PUMA governs stem/progenitor cell survival during hematopoietic recovery from stress. *Blood* 125(21):3273–3280.
188. Koury MJ BM (1990) Erythropoietin retards DNA breakdown and prevents programmed death in erythroid progenitor cells. *Science (80-)* 248(4953):378–381.
189. Gregoli PA BM (1997) The roles of Bcl-X(L) and apopain in the control of erythropoiesis by erythropoietin. *Blood* 90(2):630–640.
190. Dzierzak E, Philipsen S (2013) Erythropoiesis: Development and differentiation. *Cold Spring Harb Perspect Med* 3(4):1–16.
191. Rhodes MM, Kopsombut P, Bondurant MC, Price JO KM (2008) Adherence to macrophages in erythroblastic islands enhances erythroblast proliferation and increases erythrocyte production by a different mechanism than erythropoietin. *Blood* 111(3):1700–1708.
192. Socolovsky M, et al. (2001) Ineffective erythropoiesis in Stat5a-/-5b-/- mice due to decreased survival of early erythroblasts. *Blood* 98(12):3261–3273.

193. Rhodes MM, et al. (2012) Bcl-x L prevents apoptosis of late-stage erythroblasts but does not mediate the antiapoptotic effect of erythropoietin Bcl-x L prevents apoptosis of late-stage erythroblasts but does not mediate the antiapoptotic effect of erythropoietin. 106(5):1857–1863.
194. Porpiglia E, et al. (2011) Contrasting dynamic responses in vivo of the Bcl-xL and Bim erythropoietic survival pathways. *Blood* 119(5):1228–1239.
195. Strasser A, et al. (2017) The BH3-only proteins BIM and PUMA are not critical for the reticulocyte apoptosis caused by loss of the pro-survival protein BCL-XL. *Cell Death Dis* 8(7):e2914.
196. Kim C, et al. (2014) Cutting Edge: RIPK1 Kinase Inactive Mice Are Viable and Protected from TNF-Induced Necroptosis In Vivo. *J Immunol* 193(4):1539–1543.
197. Mocarski ES, et al. (2014) Cutting Edge: RIP1 Kinase Activity Is Dispensable for Normal Development but Is a Key Regulator of Inflammation in SHARPIN-Deficient Mice. *J Immunol* 192(12):5476–5480.
198. Pasparakis M, et al. (2014) Hematopoietic RIPK1 deficiency results in bone marrow failure caused by apoptosis and RIPK3-mediated necroptosis. *Proc Natl Acad Sci* 111(40):14436–14441.
199. Dokal I, Vulliamy T (2010) Inherited bone marrow failure syndromes. *Haematologica* 95(8):1236–1240.
200. Montalban-Bravo G, Garcia-Manero G (2018) Myelodysplastic syndromes: 2018 update on diagnosis, risk-stratification and management. *Am J Hematol* 93(1):129–147.
201. Bejar R, Steensma DP (2019) Recent Developments in Myelodysplastic Syndromes [Working Title]. *Recent Dev Myelodysplastic Syndr [Working Title]* 124(18):2793–2804.
202. Dayyani F, et al. (2010) Cause of Death in Patients with Lower-Risk Myelodysplastic Syndrome. *Cancer* 116(9):2174–2179.
203. Raza A, et al. (1995) Apoptosis in bone marrow biopsy samples involving stromal and hematopoietic cells in 50 patients with myelodysplastic syndromes. *Blood* 86(1):268–276.
204. Thompson JE, Conlon JP, Yang X, Sanchez PV CM (2007) Enhanced growth of myelodysplastic colonies in hypoxic conditions. *Exp Hematol* 35(1):21–31.
205. Kitagawa M, Saito I, Kuwata T, Yoshida S, Yamaguchi S, Takahashi M, Tanizawa T, Kamiyama R HK (1997) Overexpression of tumor necrosis factor (TNF)-alpha and interferon (IFN)-gamma by bone marrow cells from patients with myelodysplastic syndromes. *Leukemia* 11(12):2049–2054.
206. Sharma P, Pollyea DA (2018) Shutting Down Acute Myeloid Leukemia and Myelodysplastic Syndrome with BCL-2 Family Protein Inhibition. *Curr Hematol Malig Rep* 13(4):256–264.
207. Higgins JM, et al. (2014) Age-Related Clonal Hematopoiesis Associated with Adverse Outcomes. *N Engl J Med* 371(26):2488–2498.
208. Steensma DP, et al. (2017) Perspectives Clonal hematopoiesis of indeterminate potential and its distinction from myelodysplastic syndromes. 126(1):9–17.
209. Saleheen D, et al. (2017) Clonal Hematopoiesis and Risk of Atherosclerotic Cardiovascular Disease. *N Engl J Med* 377(2):111–121.
210. Gary D. Friedman, Arthur L. Klatsky, and A. B. Siegelaub (1974) The Leukocyte Count as a Predictor of Myocardial Infarction. *N Engl J Med* 290(1275–1278).
211. Soehnlein O, Swirski FK (2013) Hypercholesterolemia links hematopoiesis with atherosclerosis. *Trends Endocrinol Metab* 24(3):129–136.

212. S Ishibashi, M S Brown, J L Goldstein, R D Gerard, R E Hammer and JH (1993) Hypercholesterolemia in low density lipoprotein receptor knockout mice and its reversal by adenovirus-mediated gene delivery. *J Clin Invest* 92:883–893.
213. Beyer S, Kowala MC, Gu C, Valentine M, Recce R (2002) Characterization of atherosclerosis in LDL receptor knockout mice: macrophage accumulation correlates with rapid and sustained expression of aortic MCP-1/JE. *Atherosclerosis* 149(2):323–330.
214. Sano S, et al. (2018) Tet2-Mediated Clonal Hematopoiesis Accelerates Heart Failure Through a Mechanism Involving the IL-1β/NLRP3 Inflammasome. *J Am Coll Cardiol* 71(8):875–886.
215. Tall AR, et al. (2016) LNK/SH2B3 Loss of Function Promotes Atherosclerosis and Thrombosis. *Circ Res* 119(6):91–103.
216. Amrein PC, et al. (2017) Risk and timing of cardiovascular death among patients with myelodysplastic syndromes. *Blood Adv* 1(23):2032–2040.
217. Zhang Q, et al. (2015) Tet2 is required to resolve inflammation by recruiting Hdac2 to specifically repress IL-6. *Nature* 525(7569):389–393.
218. Rauh MJ, Wells RA, Cull AH, Buckstein R, Snetsinger B (2017) Tet2 restrains inflammatory gene expression in macrophages. *Exp Hematol* 55:56–70.e13.
219. Chen S, et al. (2018) Inhibition of Inflammatory Signaling in Tet2 Mutant Preleukemic Cells Mitigates Stress-Induced Abnormalities and Clonal Hematopoiesis. *Cell Stem Cell* 23(6):833–849.e5.
220. Schuringa JJ, et al. (2010) Bone marrow dysfunction in chronic heart failure patients. *Eur J Heart Fail* 12(7):676–684.
221. Visscher PM, et al. (2017) 10 Years of GWAS Discovery: Biology, Function, and Translation. *Am J Hum Genet* 101(1):5–22.
222. Denny JC, et al. (2010) PheWAS: Demonstrating the feasibility of a phenome-wide scan to discover gene-disease associations. *Bioinformatics* 26(9):1205–1210.
223. Robinson JR, Denny JC, Roden DM, Van Driest SL (2018) Genome-wide and Phenome-wide Approaches to Understand Variable Drug Actions in Electronic Health Records. *Clin Transl Sci* 11(2):112–122.
224. Roden DM, et al. (2008) Development of a large-scale de-identified DNA biobank to enable personalized medicine. *Clin Pharmacol Ther* 84(3):362–9.
225. Farrall M (2004) Quantitative genetic variation: a post-modern view. *Hum Mol Genet* 13(90001):1R–7.
226. Consortium TGte, et al. (2015) The Genotype-Tissue Expression (GTEx) pilot analysis: Multitissue gene regulation in humans. *Science (80-)* 348(6235):648–660.
227. Consortium G (2017) Genetic effects on gene expression across human tissues. doi:10.1038/nature24277.
228. Gamazon, Eric R., Ayellet V. Segrè M van de B (2018) Using an atlas of gene regulation across 44 human tissues to illuminate complex 2 disease- and trait-associated variation. *Nat Genet* 50(July). doi:10.1038/s41588-018-0154-4.
229. Gamazon ER, et al. (2015) A gene-based association method for mapping traits using reference transcriptome data. *Nat Genet* 47(9):1091–1098.
230. Lange LA, et al. (2014) Whole-exome sequencing identifies rare and low-frequency coding variants associated with LDL cholesterol. *Am J Hum Genet* 94(2):233–245.
231. Moslehi J, et al. (2018) Bid maintains mitochondrial cristae structure and function and protects against cardiac disease in an integrative genomics study. *Elife* 7(Imm):1–36.
232. Nakatani BY, Ogryzko V (2003) [37] Immunoaffinity Purification of Mammalian

Protein Complexes. *Methods* 370(1989):430–444.
233. Gundersen HJ JE (1987) The efficiency of systematic sampling in stereology and its prediction. *J Microsc* 147((Pt 3)):229–63.
234. Brookes PS, Shiva S, Patel RP D-UV (2002) Measurement of mitochondrial respiratory thresholds and the control of respiration by nitric oxide. *Methods Enzymol* (359):305–319.
235. Palmer W (1977) Biochemical Interfibrillar Muscle*. *Biol Chem* 236(2):8731–8739.
236. Wieckowski MR, Giorgi C, Lebiedzinska M, Duszynski J, Pinton P (2009) Isolation of mitochondria-associated membranes and mitochondria from animal tissues and cells. *Nat Protoc* 4(11):1582–90.
237. Calvo SE, Clauser KR, Mootha VK (2016) MitoCarta2.0: An updated inventory of mammalian mitochondrial proteins. *Nucleic Acids Res* 44(D1):D1251–D1257.
238. Wittig I, Braun H-P, Schägger H (2006) Blue native PAGE. *Nat Protoc* 1(1):418–428.
239. Veksler VI, Kuznetsov A V., Sharov VG, Kapelko VI, Saks VA (1987) Mitochondrial respiratory parameters in cardiac tissue: A novel method of assessment by using saponin-skinned fibers. *BBA - Bioenerg* 892(2):191–196.
240. Lark DS, et al. (2016) Direct real-time quantification of mitochondrial oxidative phosphorylation efficiency in permeabilized skeletal muscle myofibers. (32):239–245.
241. Torres JM, et al. (2016) Integrative cross tissue analysis of gene expression identifies novel type 2 diabetes genes. 1–33.
242. Nielsen JB, et al. (2018) Biobank-driven genomic discovery yields new insight into atrial fibrillation biology. *Nat Genet*. doi:10.1038/s41588-018-0171-3.
243. Bauer F, et al. (2009) Obesity genes identified in genome-wide association studies are associated with adiposity measures and potentially with nutrient-specific food preference 1 – 3. (3). doi:10.3945/ajcn.2009.27781.INTRODUCTION.
244. Locke AE, et al. (2015) Genetic studies of body mass index yield new insights for obesity biology. *Nature* 518(7538):197–206.
245. Schunkert H, et al. (2011) Large-scale association analysis identifies 13 new susceptibility loci for coronary artery disease. *Nat Genet* 43(4):333–338.
246. Bastarache L, et al. (2013) Systematic comparison of phenome-wide association study of electronic medical record data and genome-wide association study data. *Nat Biotechnol* 31(12):1102–1110.
247. Wei W, Bastarache LA, Carroll RJ, Marlo JE, Denny C (2017) Evaluating phecodes , clinical classification software , and ICD-9-CM codes for phenome- wide association studies in the electronic health record. 1–16.
248. Stitziel, Nathan O., Stirrups, Kathleen E., Nicholas, G.D. Masca, Erdmann, Janette, Ferrario, Paola G., Konig Inke R., Weeke Peter E et al. (2016) Coding Variation in ANGPTL4, LPL, and SVEP1 and the Risk of Coronary Disease. *N Engl J Med* 374(12):1134–1144.
249. Beran M, et al. (2011) Tet2 Loss Leads to Increased Hematopoietic Stem Cell Self-Renewal and Myeloid Transformation. *Cancer Cell* 20(1):11–24.
250. Hackenbrock CR (1966) Ultrastructural bases for metabolically linked mechanical activity in mitochondria. I. Reversible ultrastructural changes with change in metabolic steady state in isolated liver mitochondria. *J Cell Biol* 30(2):269–297.
251. Cogliati S, Enriquez JA, Scorrano L (2016) Mitochondrial Cristae: Where Beauty Meets Functionality. *Trends Biochem Sci* 41(3):261–273.
252. Rampelt H, Zerbes RM, Laan M Van Der, Pfanner N (2016) Role of the

mitochondrial contact site and cristae organizing system in membrane architecture and dynamics. *BBA - Mol Cell Res* 1864(4):26–28.
253. Lapuente-brun E, et al. (2013) Supercomplex Assembly Determines Electron Flux in the Mitochondrial Electron Transport Chain. (June):1567–1571.
254. Moslehi J, Depinho RA, Sahin E (2012) Telomeres and mitochondria in the aging heart. *Circ Res* 110(9):1226–1237.
255. Wallace DC (2013) A mitochondrial bioenergetic etiology of disease. *J Clin Invest* 123(4):1405–1412.
256. Picard M, Wallace DC, Burelle Y (2016) The rise of mitochondria in medicine. *Mitochondrion* 30:105–116.
257. Hardwick JM, Chen Y bei, Jonas EA (2012) Multipolar functions of BCL-2 proteins link energetics to apoptosis. *Trends Cell Biol* 22(6):318–328.
258. Zinkel S, Gross A, Yang E (2006) BCL2 family in DNA damage and cell cycle control. *Cell Death Differ* 13(8):1351–1359.
259. Maryanovich M, et al. (2012) The ATM–BID pathway regulates quiescence and survival of haematopoietic stem cells. *Nat Cell Biol* 14(5):535–541.
260. Shamas-Din A, et al. (2014) Multiple partners can kiss-and-run: Bax transfers between multiple membranes and permeabilizes those primed by tBid. *Cell Death Dis* 5(6):e1277-9.
261. K. S, et al. (2014) The breathing heart - Mitochondrial respiratory chain dysfunction in cardiac disease. *Int J Cardiol* 171(2):134–143.
262. Guarani V, et al. (2015) QIL1 is a novel mitochondrial protein required for MICOS complex stability and cristae morphology. *Elife* 4(MAY):1–23.
263. Meyers DE, Basha HI, Koenig MK (2013) Mitochondrial cardiomyopathy: pathophysiology, diagnosis, and management. *Tex Heart Inst J* 40(4):385–94.
264. Brown DA, et al. (2017) Expert consensus document: Mitochondrial function as a therapeutic target in heart failure. *Nat Rev Cardiol* 14(4):238–250.
265. RE B, Thomas W, O'Neal R (1958) An Electron Microscopic Study of Myocardial Ischemia in the Rat. *Circ Res* VI:699–709.
266. Breckenridge R (2010) Heart failure and mouse models. 143:138–143.
267. GOLDBERG LI, BLOODWELL RD, BRAUNWALD E, MORROW AG (1960) The direct effects of norepinephrine, epinephrine, and methoxamine on myocardial contractile force in man. *Circulation* 22(December):1125–1132.
268. Di Bella G, et al. (2013) Scar extent, left ventricular end-diastolic volume, and wall motion abnormalities identify high-risk patients with previous myocardial infarction: A multiparametric approach for prognostic stratification. *Eur Heart J* 34(2):104–111.
269. Hull TD, et al. (2016) Heme oxygenase-1 regulates mitochondrial quality control in the heart. 1(2):1–17.
270. Talman V, Ruskoaho H (2016) Cardiac fibrosis in myocardial infarction—from repair and remodeling to regeneration. *Cell Tissue Res* 365(3):563–581.
271. Hahn A, et al. (2016) Structure of a Complete ATP Synthase Dimer Reveals the Molecular Basis of Inner Mitochondrial Membrane Morphology. *Mol Cell* 63(3):445–456.
272. Schägger H, Pfeiffer K (2001) The Ratio of Oxidative Phosphorylation Complexes I-V in Bovine Heart Mitochondria and the Composition of Respiratory Chain Supercomplexes. *J Biol Chem* 276(41):37861–37867.
273. Gamazon ER, Park DS (2016) SNP-based heritability estimation : measurement noise , population stratification and stability.

274. Battle A, et al. (2013) Characterizing the genetic basis of transcriptome diversity through RNA-sequencing of 922 individuals. *Genome Res* (650):1–38.
275. Sudlow C, et al. (2015) UK Biobank : An Open Access Resource for Identifying the Causes of a Wide Range of Complex Diseases of Middle and Old Age. 1–10.
276. Clohessy JG, Zhuang J, De Boer J, Gil-Gómez G, Brady HJM (2006) Mcl-1 interacts with truncated bid and inhibits its induction of cytochrome c release and its role in receptor-mediated apoptosis. *J Biol Chem* 281(9):5750–5759.
277. Anand SS, et al. (2008) Risk factors for myocardial infarction in women and men: Insights from the INTERHEART study. *Eur Heart J* 29(7):932–940.
278. Socolovsky M, et al. (2007) Negative Autoregulation by FAS Mediates Robust Fetal Erythropoiesis. *PLoS Biol* 5(10):e252.
279. Rickard JA, et al. (2014) TNFR1-dependent cell death drives infammation in Sharpin-defcient mice. *Elife* 2014(3):1–23.
280. Ganesan S, et al. (2014) Caspase-8 and RIP kinases regulate bacteria-induced innate immune responses and cell death. *Proc Natl Acad Sci* 111(20):7391–7396.
281. Oberst A, et al. (2011) Catalytic activity of the caspase-8-FLIP L complex inhibits RIPK3-dependent necrosis. *Nature* 471(7338):363–368.
282. Dickens LS, et al. (2012) A Death Effector Domain Chain DISC Model Reveals a Crucial Role for Caspase-8 Chain Assembly in Mediating Apoptotic Cell Death. *Mol Cell* 47(2):291–305.
283. Weinlich R, Dillon CP, Green DR (2011) Ripped to death. *Trends Cell Biol* 21(11):630–637.
284. Zhou W, Yuan J (2014) Necroptosis in health and diseases. *Semin Cell Dev Biol* 35:14–23.
285. Danial NN, Korsmeyer SJ (2004) Cell death: critical control points. *Cell* 116:205–219.
286. Takeuchi O, et al. (2005) Essential role of BAX,BAK in B cell homeostasis and prevention of autoimmune disease. *Proc Natl Acad Sci* 102(32):11272–11277.
287. Kinney MC, Zinkel SS, Rebel VI, Scott LM, Zhou T (2015) Revisiting the case for genetically engineered mouse models in human myelodysplastic syndrome research. *Blood* 126(9):1057–1068.
288. Green DR (2018) An Element of Life. *Cell* 172(3):389–390.
289. Zha J, et al. (2002) Differential Modulation of Apoptosis Sensitivity in CD95 Type I and Type II Cells. *J Biol Chem* 274(32):22532–22538.
290. Moquin D, et al. (2009) Phosphorylation-Driven Assembly of the RIP1-RIP3 Complex Regulates Programmed Necrosis and Virus-Induced Inflammation. *Cell* 137(6):1112–1123.
291. Vanlangenakker N, Vanden Berghe T, Vandenabeele P (2012) Many stimuli pull the necrotic trigger, an overview. *Cell Death Differ* 19(1):75–86.
292. Kerbauy DB, Deeg HJ (2007) Apoptosis and antiapoptotic mechanisms in the progression of myelodysplastic syndrome. *Exp Hematol* 35(11):1739–1746.
293. Venugopal P, et al. (2002) Correlation of tumor necrosis factor α (TNFα) with high Caspase 3-like activity in myelodysplastic syndromes. *Cancer Lett* 140(1–2):201–207.
294. Masala E, et al. (2012) Distinct Signal Transduction Abnormalities and Erythropoietin Response in Bone Marrow Hematopoietic Cell Subpopulations of Myelodysplastic Syndrome Patients. *Clin Cancer Res* 18(11):3079–3089.
295. Metcalf D, et al. (2014) RIPK1 Regulates RIPK3-MLKL-Driven Systemic Inflammation and Emergency Hematopoiesis. *Cell* 157(5):1175–1188.

296. Zou J, Shi Q, Chen H, Juskevicius R ZS (2019) Programmed Necrosis is Upregulated in Low-grade Myelodysplastic Syndromes and May Play a Role in the Pathogenesis. *Haematologica*:In revision.
297. Greenberg P, et al. (2018) Clinical effectiveness and safety of erythropoietin-stimulating agents for the treatment of low- and intermediate-1−risk myelodysplastic syndrome: a systematic literature review. *Br J Haematol* (December 2018):134–160.
298. Zinkel SS, et al. (2018) Increased Ripk1-mediated bone marrow necroptosis leads to myelodysplasia and bone marrow failure in mice. *Blood* 133(2):107–120.
299. Yang L, Qian Y, Eksioglu E, Epling-Burnette PK, Wei S (2015) The inflammatory microenvironment in MDS. *Cell Mol Life Sci* 72(10):1959–1966.
300. Wegner KW, Saleh D, Degterev A (2017) Complex Pathologic Roles of RIPK1 and RIPK3: Moving Beyond Necroptosis. *Trends Pharmacol Sci* 38(3):202–225.
301. Fitzgerald KA, et al. (2017) Dendritic Cell RIPK1 Maintains Immune Homeostasis by Preventing Inflammation and Autoimmunity. *J Immunol* 200(2):737–748.
302. Weiss G, Goodnough LT (2005) Anemia of Chronic Disease. *N Engl J Med* 352(10):1011–1023.
303. Rusten LS, Eirik S (1995) Tumor Necrosis Factor (TNF)-a Directly Inhibits Human Erythropoiesis In Vitro: Role. *J Biol Chem* 85(4):989–996.
304. Tanyong DI, Panichob P, Kheansaard W, Fucharoen S (2015) Effect of Tumor Necrosis Factor-Alpha on Erythropoietinand Erythropoietin Receptor-Induced Erythroid Progenitor Cell Proliferation in β Thalassemia/Hemoglobin E Patients. *Turkish J Hematol* 32(4):304–310.
305. Hotz MJ, et al. (2018) Red blood cells homeostatically bind mitochondrial DNA through TLR9 to maintain quiescence and to prevent lung injury. *Am J Respir Crit Care Med* 197(4):470–480.
306. Karsten E, Breen E, Herbert BR (2018) Red blood cells are dynamic reservoirs of cytokines. *Sci Rep* 8(1):1–12.
307. Böing AN, Nieuwland R, Tuip-De Boer A, Juffermans NP, Straat M (2015) Extracellular Vesicles from Red Blood Cell Products Induce a Strong Pro-Inflammatory Host Response**,** Dependent on Both Numbers and Storage Duration. *Transfus Med Hemotherapy* 43(4):302–305.
308. Triviai I, et al. (2018) ASXL1/EZH2 mutations promote clonal expansion of neoplastic HSC and impair erythropoiesis in PMF. *Leukemia* 33(1):99–109.
309. Zhou Y, et al. (2016) ASXL1 plays an important role in erythropoiesis. *Sci Rep* 6(1):1–11.
310. Zhao X, et al. (2013) Deletion of Asxl1 results in myelodysplasia and severe developmental defects in vivo. *J Exp Med* 210(12):2641–2659.
311. Qu X, et al. (2018) TET2 deficiency leads to stem cell factor–dependent clonal expansion of dysfunctional erythroid progenitors. *Blood* 132(22):2406–2417.
312. Gallagher PG, et al. (2017) Distinct roles for TET family proteins in regulating human erythropoiesis. *Blood* 129(14):2002–2012.
313. Saito K, et al. (2017) Impact of TET2 deficiency on iron metabolism in erythroblasts. *Exp Hematol* 49:56–67.e5.
314. Kim SY, et al. (2014) Myelodysplastic syndrome evolving from aplastic anemia treated with immunosuppressive therapy: Efficacy of hematopoietic stem cell transplantation. *Haematologica* 99(12):1868–1875.
315. Montoro J, et al. (2018) Autoimmune disorders are common in myelodysplastic syndrome patients and confer an adverse impact on outcomes. *Ann Hematol* 97(8):1349–1356.

316. Kistner EO, et al. (2006) A Genome-Wide Association Study Identifies IL23R as an Inflammatory Bowel Disease Gene. *Science (80-)* 314(5804):1461–1463.
317. Auton A, et al. (2015) A global reference for human genetic variation. *Nature* 526(7571):68–74.
318. Cogle CR (2015) Incidence and Burden of the Myelodysplastic Syndromes. *Curr Hematol Malig Rep* 10(3):272–281.
319. Wolach O, Stone R (2016) Autoimmunity and inflammation in myelodysplastic syndromes. *Acta Haematol* 136(2):108–117.
320. Lutter M, Perkins GA, Wang X (2001) The pro-apoptotic Bcl-2 family member tBid localizes to mitochondrial contact sites. *BMC Cell Biol* 2. doi:10.1186/1471-2121-2-22.
321. Hu X, Han Z, Wyche JH, Hendrickson EA (2003) Helix 6 of tBid is necessary but not sufficient for mitochondrial binding activity. *Apoptosis* 8(3):277–289.
322. Aouacheria A, Rech de Laval V, Combet C, Hardwick JM (2013) Evolution of Bcl-2 homology motifs: Homology versus homoplasy. *Trends Cell Biol* 23(3):103–111.
323. Steven W. Muchmore, Michael Sattlert, Heng Liangt, Robert P. Meadows, John E. Harlant, Ho Sup Yoont, David Nettesheimt, Brian S. Chang, Craig B. Thompson, Sui-Lam Wongll'II S-CN& SWF (1996) X-ray and NMR structure of human Bcl-xL an inhibitor of programmed cell death. *Nature* 381:335–341.
324. Shortridge MD, Powers R (2009) Structural and Functional Similarity between the Bacterial Type III Secretion System Needle Protein PrgI and the Eukaryotic Apoptosis Bcl-2 Proteins. *PLoS One* 4(10). doi:10.1371/journal.pone.0007442.
325. Petros AM, Olejniczak ET, Fesik SW (2004) Structural biology of the Bcl-2 family of proteins. *Biochim Biophys Acta - Mol Cell Res* 1644(2–3):83–94.
326. Nunnari J, Suomalainen A (2012) Mitochondria: In sickness and in health. *Cell* 148(6):1145–1159.
327. Zhang M, Zheng J, Nussinov R, Ma B (2017) Release of Cytochrome C from Bax Pores at the Mitochondrial Membrane /631/114/2397 /639/638/440/56 /119/118 article. *Sci Rep* 7(1):1–13.
328. Asciolla JJ, Renault TT, Chipuk JE (2012) Examining BCL-2 Family Function with Large Unilamellar Vesicles. *J Vis Exp* (68):2–7.
329. Strauss M, Hofhaus G, Schröder RR, Kühlbrandt W (2008) Dimer ribbons of ATP synthase shape the inner mitochondrial membrane. *EMBO J* 27(7):1154–1160.
330. Hui G, Stephanie A. B, John L. R (2017) Atomic model for the dimeric Fo region of mitochondrial ATP synthase. *Science (80-)* 4815(October):936–940.
331. Kang Y, Fielden LF, Stojanovski D (2018) Mitochondrial protein transport in health and disease. *Semin Cell Dev Biol* 76:142–153.
332. Lindsten T, et al. (2000) The Combined Functions of Proapoptotic Bcl-2 Family Members Bak and Bax Are Essential for Normal Development of Multiple Tissues cells within both the central nervous and hematopoi- etic systems. Thus, Bax and Bak have overlapping roles in the regulation . *Mol Cell* 6:1389–1399.
333. Rusten LS JS (1995) Necrosis Factor (TNF)-alpha directly inhibits human erythropoiesis in vitro: Role of p55 and p75 TNF Receptors. *Blood* 85(4):989–996.
334. Meisel M, et al. (2018) Microbial signals drive pre-leukaemic myeloproliferation in a Tet2-deficient host. *Nature* 557(7706):580–584.
335. Drexler HG, Dirks WG, MacLeod RAF (2009) Many are called MDS cell lines: One is chosen. *Leuk Res* 33(8):1011–1016.
336. Benito AI, et al. (2003) NOD/SCID mice transplanted with marrow from patients with myelodysplastic syndrome (MDS) show long-term propagation of normal but

not clonal human precursors. *Leuk Res* 27(5):425–436.
337. Glover J, et al. (2018) Cytokines increase engraftment of human acute myeloid leukemia cells in immunocompromised mice but not engraftment of human myelodysplastic syndrome cells. *Haematologica* 103(6):959–971.
338. Medyouf H, et al. (2014) Myelodysplastic cells in patients reprogram mesenchymal stromal cells to establish a transplantable stem cell niche disease unit. *Cell Stem Cell* 14(6):824–837.
339. Wong E, et al. (2019) A highly efficient and faithful MDS patient-derived xenotransplantation model for pre-clinical studies. *Nat Commun* 10(1):1–14.
340. Lin JR, et al. (2018) Highly multiplexed immunofluorescence imaging of human tissues and tumors using t-CyCIF and conventional optical microscopes. *Elife* 7:1–46.
341. Yang J, et al. (2018) Age-related inflammatory bone marrow microenvironment induces ineffective erythropoiesis mimicking del(5q) MDS. *Leukemia* 32(4):1023–1033.
342. Montecino-rodriguez E, et al. (2013) Causes , consequences , and reversal of immune system aging Find the latest version : Review series Causes , consequences , and reversal of immune system aging. *J Clin Invest* 123(3):958–965.
343. Mohanty JG, Nagababu E RJ (2014) Red blood cell oxidative stress impairs oxygen delivery and induces red blood cell aging. *Front Physiol*.
344. Fibach E RE (2008) The role of oxidative stress in hemolytic anemia. *Curr Mol Med* 8(7):609–619.
345. S G (2008) Oxidative stress in the regulation of normal and neoplastic hematopoiesis. *Antioxid Redox Signal* 10(11):1923–1940.
346. Yang X, et al. (2008) ABT-263: A Potent and Orally Bioavailable Bcl-2 Family Inhibitor. *Cancer Res* 68(9):3421–3428.
347. Roberts AW1, Seymour JF, Brown JR, Wierda WG, Kipps TJ, Khaw SL, Carney DA, He SZ, Huang DC, Xiong H, Cui Y, Busman TA, McKeegan EM, Krivoshik AP, Enschede SH HR (2012) Substantial susceptibility of chronic lymphocytic leukemia to BCL2 inhibition: results of a phase I study of navitoclax in patients with relapsed or refractory disease. *J Clin Oncol* 30(5):488–496.
348. Roberts AW, Davids MS SJ (2016) New Agents to Treat Chronic Lymphocytic Leukemia. *N Engl J Med* 374(22):2186–2187.
349. Opferman JT, Kothari A (2018) Anti-apoptotic BCL-2 family members in development. *Cell Death Differ* 25(1):37–45.
350. Reidel V, et al. (2018) Selective inhibition of BCL-2 is a promising target in patients with high-risk myelodysplastic syndromes and adverse mutational profile. *Oncotarget* 9(25):17270–17281.
351. Campos L, et al. (2002) Expression and prognostic significance of Bcl-2 family proteins in myelodysplastic syndromes. *Am J Hematol* 70(2):115–125.
352. Fenaux P, Kiladjian JJ, Platzbecker U (2019) Luspatercept for the treatment of anemia in myelodysplastic syndromes (MDS) and primary myelofibrosis (PMF). *Blood* 133(8):blood-2018-11-876888.